Modelling and Simulation of the Electrodeposition Process on Open-Porous Media

Dissertation

zur Erlangung des Grades

des Doktors der Ingenieurwissenschaften

der Naturwissenschaftlich-Technischen Fakultät

der Universität des Saarlandes

von

Christine Grill, M. Sc.

Saarbrücken

2023

Tag des Kolloquiums:	18. Juli 2024
Dekan:	Prof. Dr.-Ing. Michael Vielhaber
Berichterstatter:	Prof. Dr.-Ing. Stefan Diebels
	Prof. Dr.-Ing. Amsini Sadiki
Vorsitz: Prof.	Dr.-Ing. Christian Motz
Akad. Mitarbeiter:	Dr.-Ing. Niklas König

Danksagung

Die vorliegende Arbeit entstand während meiner Tätigkeit als wissenschaftliche Mitarbeiterin am Lehrstuhl für Technische Mechanik (LTM) unter der Leitung von Prof. Dr.-Ing. Stefan Diebels an der Universität des Saarlandes. Finanziell wurde diese Arbeit vom Landesforschungsförderungsprogramm (LFFP) der Staatskanzlei des Saarlandes unterstützt.

An erster Stelle möchte mich bei meinem Doktorvater Prof. Dr.-Ing. Stefan Diebels für die langjährige Unterstützung bedanken. Die Unterstützung, die ich in meiner gesamten Zeit beginnend als studentische Hilfskraft, über Bachelor- und Masterarbeit hinaus bis zu meiner Zeit als Doktorandin erfahren habe, hat mich in meiner persönlichen Entwicklung in vielerlei Hinsicht vorangebracht und wachsen lassen.

An zweiter Stelle danke ich Prof. Dr. rer. nat. Amsini Sadiki von der TU Darmstadt für die Übernahme des Zweitgutachtens.

Ein ganz besonderer Dank geht auch an Prof. Dr.-Ing. Dr. rer. nat. Anne Jung. Durch ihre zahlreichen Ideen und Anregungen und unsere fachlichen Diskussionen hat sie mich auf meinem gesamten Weg als Doktorandin in großem Maße unterstützt.

Zusätzlich bedanke ich mich bei allen Mitarbeitern des Lehrstuhls für Technische Mechanik, die mich während meiner Zeit am Lehrstuhl begleitet haben. Durch viele fachliche und auch mal fachfremde Diskussionen und das stets angenehme Arbeitsklima haben sie maßgeblich zu dieser Arbeit beigetragen. Vielen Dank an Dr.-Ing. Tobias Scheffer, der mich schon während meines Studiums am Lehrstuhl gefördert hat. Ebenfalls vielen Dank an Dr.-Ing. Ralf Derr und Dr.-Ing. Thomas Bleistein, die mich in den ersten Monaten als wissenschaftliche Mitarbeiterin unterstützt haben. Zudem möchte ich Dr.-Ing. Prateek Sharma hervorheben, der neben vielen Diskussionen auch bei der Korrektur dieser Arbeit geholfen hat und mir oft einen neuen Blickwinkel aufgewiesen hat. Meinen zwei weiteren Bürokollegen Dr.-Ing. Martin Reis und Selina Neuhaus, M.Sc. möchte ich ebenfalls von ganzem Herzen danken. Ohne euch hätte die Arbeit nur halb so viel Spaß gemacht. Ich werde noch häufig an die zwar oft stressige, aber wegen euch allen auch sehr schöne Zeit am Lehrstuhl zurückdenken.

Abschließend geht mein Dank an meine Familie und Freunde, die mich in den letzten Jahren immer wieder unterstützt haben und viel Verständnis für meine Arbeit aufbringen mussten. Ganz besonders möchte ich mich bei meinem Mann Tobi bedanken. Mit seiner Unterstützung hat er mit am wesentlichsten zur Fertigstellung dieser Arbeit beigetragen.

Vielen Dank!

Saarbrücken, 2023 Christine Grill

Zusammenfassung

Durch die Endlichkeit von Materialien und Energie ist eine ressourceneffiziente Nutzung dieser Rohstoffe unabdingbar. Mittels Elektrodeposition mit Nickel nanokristallin beschichtete Hybridschäume meistern durch ihre hervorragenden mechanischen Eigenschaften bei gleichzeitig geringem Gewicht diese Herausforderung der Ressourcenschonung. Bedingt durch Stofftransportlimitierungen kommt es während des Beschichtungsprozesses zu einer inhomogenen Schichtdickenverteilung und somit zu einem inhomogenen Materialverhalten. Zur Vermeidung von inhomogenen Beschichtungsdicken wird in dieser Arbeit dieser Elektrodepositionsprozess auf Schäumen untersucht. Dazu wird der Prozess abstrahiert. Die dominierenden Stofftransportprozesse der Ionenbewegung, deren Einfluss aufeinander sowie ihr Einfluss auf die Ionenkonzentration wurden in einem beidseitig gekoppelten Modell diskutiert. Für die Modellierung des Einflusses der Beschichtungsdicke auf den Prozess erfolgt eine Geometriestudie zur Vereinfachung der komplexen Schaumstruktur. Mittels eines für das einseitig gekoppelte Modell generierten expliziten FD-Codes werden die Ergebnisse aus der Simulation den Ergebnissen aus dem Experiment bezüglich der Beschichtungshomogenität gegenübergestellt. Der Einfluss verschiedener Parameter auf die Ergebnisse in der Simulation sowie die Unterschiede zwischen Experiment und Simulation werden mit Hilfe eines Design of Experiment untersucht.

Abstract

As materials and energy are finite resources, it is essential to use these raw materials efficiently. Hybrid foams coated with electrodeposited nanocrystalline nickel master this challenge of resource efficiency perfectly by combining excellent mechanical properties with low weight. Due to mass transport limitations, an inhomogeneous coating thickness distribution and, thus, inhomogeneous material characteristics appear during the electrodeposition process. With the aim of achieving a homogeneous coating thickness, this electrodeposition process on hybrid foams is examined in this thesis. For this purpose, the process is abstracted and divided into the mass transport processes dominating the ion movement, their influence on each other, as well as their influence on the local ion concentration in a two-sided coupled model. A geometry study is carried out to simplify the complex foam structure to model the back-coupling. An explicit FD code is developed for the one-sided coupled model, assuming a linear relationship between the ion concentration and the coating homogeneity, and the results of the simulations are compared with the results from the experiments. The experimental results are discussed using a Design of Experiment, and the influence of various parameters on the results in the simulation is investigated.

Contents

1

Introduction

1.1 Motivation

Cellular structures like foams consist of a connected network of lattices with open and closed faces pin-jointed or rigidly bonded at their edges. However, the term cellular solids means different things to different people. For non-scientists, foams are soft, flexible objects which can be used for packaging, padding and cleaning. Food scientists think of bread, cake, meringue, or mousse. For natural scientists, cellular solids are materials like wood, coral, or bone. For engineers, they are essential in lightweight structures, energy management, insulation, and filtration [11], as with the foams examined in this thesis. In general, they are inspired by nature, and the artificial foams are made of metal or synthetics for industrial applications. Foams made of metal are called metal foams and are an essential representative of artificial cellular structures. They are often made of aluminium (Al) due to its low density, low melting point and low price compared to other lightweight metals [11]. Additionally, metal and synthetic foams can be coated with a metallic layer. The metallic layer improves the mechanical properties further and can be applied, for instance, by an electrochemical coating process. For the material labelling of coated foams, also called hybrid foams, the coating material is mentioned first and the substrate material second. Thus, Ni-coated Al-foams are called Ni/Al-foams. The foam to be coated is called substrate, and the coated foams are called hybrid foams. Nickel (Ni) is suitable for the coating due to its outstanding mechanical properties. Nanocrystalline Ni applied as an electrochemical coating impresses with extraordinary mechanical properties such as high hardness [9, 128], high yield strength [119, 172], fracture strength [9, 50], wear resistance [146], corrosion re-

sistance [65], and catalyst properties [104, 135, 170]. Hence, it is particularly useful as a coating material. The small grain sizes in the nanometre range achieved during the electrodeposition process further improve the material behaviour due to the Hall-Petch relationship [95, 100, 117]. In addition, the coating enhances the mechanical properties and functionalises the inner surface of the substrate. In general, the inner surface of the foams is extensive in relation to the volume [59, 141, 142], due to the porous structure. In the past, Al-foams were already electrochemically coated with nanocrystalline Ni-tungsten (NiW) in 2008 by Boonyongmaneerat et al. [23] to enhance their mechanical properties. Even with a low coating thickness, a positive effect on the absolute stiffness, strength, and energy absorption was determined [23, 85]. Moreover, Bouwhuis et al. [25] confirmed the results of Boonyongmaneerat et al. [23] with Ni-coated Al-foams in 2009. However, the coated foams showed a low coating homogeneity across their geometry. The coating thickness in the middle of the foam is approximately 10 % of the coating thickness at the outer foam surface. This coating inhomogeneity is caused by mass transport limitation and electromagnetic shielding (Figure 1.1). According to

Figure 1.1: Coated foam with significant coating thickness inhomogeneities, Bouwhuis et al. [25]

a study by Bele et al. [13], cells in the middle of the foam failed first due to the thin coating thickness. Thus, the achievable peak compressive strength is strongly limited by the non-uniform coating [13]. This observation was confirmed by Lausic et al. [105] at the same time. A Ni layer of $24 - 72\,\mu m$ leads to an increase in strength in the range of $2.3 - 5.2\,MPa$ when loaded parallel to the coating gradient and an increase in strength of $4.0 - 10.5\,MPa$ when loaded perpendicular to the coating gradient [105].

The specific strength and stiffness could be increased by 240 % for parallel and 540 % for perpendicular loading, respectively [104]. To improve the homogeneity of the coating thickness, Jung et al. [86, 87] developed a sacrificial anode in cage form. Coating thickness homogeneities of up to 80 % in relation to the maximum coating thickness were achieved by flowing the electrolyte through the foam [86, 87].
For cost reasons, the substrate made of Al can be substituted by a substrate of polyurethane (PU). The substitution is possible because the coating carries most of the total stress, even under tension. This observation was shown in simulations of microtensile tests on coated single struts [82]. The more cost-efficient PU-foams have poorer mechanical properties than Al-foams but this is of low influence on the properties of the Ni/PU hybrid foams. An additional advantage is the lower number of preparation steps (one step for the pretreatment of PU-foams, eight steps for the pretreatment of Al-foams). So, a cost reduction of 85 % per absorbed energy unit can be achieved when using Ni/PU-foams compared to Ni/Al-foams [82]. In contrast to Al, PU has to be coated with graphite in the first processing step as a non-conductive material. Due to graphite's lower conductivity than Al, the mass transport limitation processes have a more substantial effect on the inhomogeneity of the coating thickness in Ni/PU-foams compared to Ni/Al-foams. For the coating of Ni/PU-foams, optimising the process parameters of the electrodeposition process to achieve homogeneous coating thicknesses is even more relevant than Ni/Al hybrid foams. The foams examined in this thesis are both Ni/Al and Ni/PU hybrid foams. In the following, all chemical elements are abbreviated according to the standard regulation of the International Union of Pure and Applied Chemistry (IUPAC).

1.2 Objectives and Structure of the Thesis

First, in **chapter 2**, the bulk material of porous structures is considered in terms of its various properties. Different ways of producing porous structures are also explained with advantages and disadvantages. Furthermore, fields of application of porous structures are shown.
In **chapter 3**, different coating possibilities of porous structures are presented. The most suitable electrodeposition process is examined with regard to different physical and chemical processes. This is followed by an explanation of the four main reasons for mass transport: convection, diffusion, migration, and reaction including experimental data from literature [57]. The experimental setup used at that time is discussed concerning the Design of Experiment (DoE), as well as the possible evaluations of the DoE.
In **chapter 4**, the processes occurring during the electrodeposition process are modelled in a one-sided model. This model takes into consideration the influence of the convection, diffusion, migration and reaction on the coating thickness. Moreover, the chemical background of the electrodeposition process is given.
The partial differential equation (PDE) resulting from the model is classified, and the most prevalent discretisation possibilities are compared in **chapter 5**. The continuous PDE is discretised and transformed into the implemented code through an explicit finite difference scheme.
In **chapter 6**, benchmark tests are used to validate the code for the four dominant mass transport processes.
The coating thickness influences the geometry parameters, and the geometry parameters influence the mass transport. This relationship shows that the electrodeposition process is not only a one-sided coupled problem but a fully coupled problem. For the modelling of the back-coupling, firstly, the representative volume element (RVE) of foams is determined in **chapter 7**, and this is followed by an examination of the influence of the coating thickness on various geometry parameters with the utilisation of computed tomography (CT) data. In addition, the geometry of different stackable unit cells with the real foam structure is examined as a function of the coating thickness. By using several regular unit cells, the numerical calculation of foams can be performed more efficiently than with the use of irregular RVEs. Based on the results of the unit cells, a model can be chosen to describe the permeability of the foams. This chapter also examines the cross-sectional area as a function of the coating thickness.
The results obtained in the previous chapters are used in **chapter 8** to simulate the one-sided coupled model. Besides a simple comparison of the results between experiment and simulation, the DoE is applied and evaluated in terms of two target variables. The

first target variable is the difference between the experimental results of the electrodeposition process described in [57] and the simulations based on the model presented in this thesis. The second target variable is the difference between the maximum and the minimum coating thickness obtained in the simulations in this thesis. The effects and interactions of the influencing variables, for example, velocity and current density, on the target variables are also determined by evaluating the DoE. For the sake of completeness, a sensitivity analysis is executed for the parameters velocity, diffusion constant, electrical field and sink constant, as well as an examination of further parameters, followed by a stability analysis.

Chapter 9 summarises all gained knowledge and gives an outlook on further fields to be examined in the domain of simulations of the electrodeposition process on open-porous metal foams to improve the coating thickness homogeneity.

2

Porous Structures

Porous structures are not a modern invention. The first mention of porous metals was in 77 AD in literature describing the so-called granulation process, which Etruscan goldsmiths used to make fine jewellery [133]. At the beginning of the 20th century, porous metals were used as sinter powders and grids in commercial and technical applications [30, 126]. A patent was granted in France in 1925 for producing a structure with high porosity by foaming a material, which is still used today [116] for metal foam production. The commercialisation of what is now called metal foam started in the late 1950s through research and development [106]. The reason for this development is the large inner surface area, the high stiffness-to-weight ratio when loaded in bending, and good permeability in the case of open-porous structures. Properties like this ensure that there is continued interest in researching into such materials.

2.1 Structural Properties

The properties of porous structures are linked to other parameters than is the case with completely dense, monolithic materials. These properties depend on the topology (connectivity) [10], material [10], pore size [40, 66, 122, 152, 155], pore distribution [40, 66, 122, 152, 155], density [40, 66, 122, 152, 155] and the shape of nodes and struts [10] in open-cell foams. Porous structures can be categorised in the geometry of the cell structure, the size scale, and the mechanical properties.

2.1.1 Cell Structures

The terms stochastic and periodic structures characterise porous materials according to their geometry (Figure 2.1). In stochastic structures, the struts are randomly distributed, and in periodic structures, the struts are arranged in a regularly repeated unit cell. Foams can also be categorised as open-cells (Figure 2.1 a) and c)) or closed-cells (Figure 2.1 b)). In open-cells, the cells are connected by open faces. The inspiration for open-cell foams are bones and sponges [11, 12]. In closed-cells, the cells are separated by walls [11]. They are inspired by cork [11, 12]. Both are stochastic structures, foams with open-cells as well as foams with closed-cells. Stochastic open-cell structures consist of several nodes and struts. Periodic structures comprise micro lattices and micro trusses (Figure 2.1 c)), i.e., 3D structures consisting of a unit cell repeated several times. Periodic cellular structures can also consist of honeycombs (Figure 2.1 d)). Honeycombs are only arranged in two dimensions and resemble real honeycombs built by bees. The last possible structure of cellular materials is an auxetic structure (Figure 2.1 e), a planar auxetic structure). These are two- or three-dimensionally arranged unit or stochastic cells. When elongated, they expand transversely to the direction of elongation, resulting in a negative Poisson's ratio.

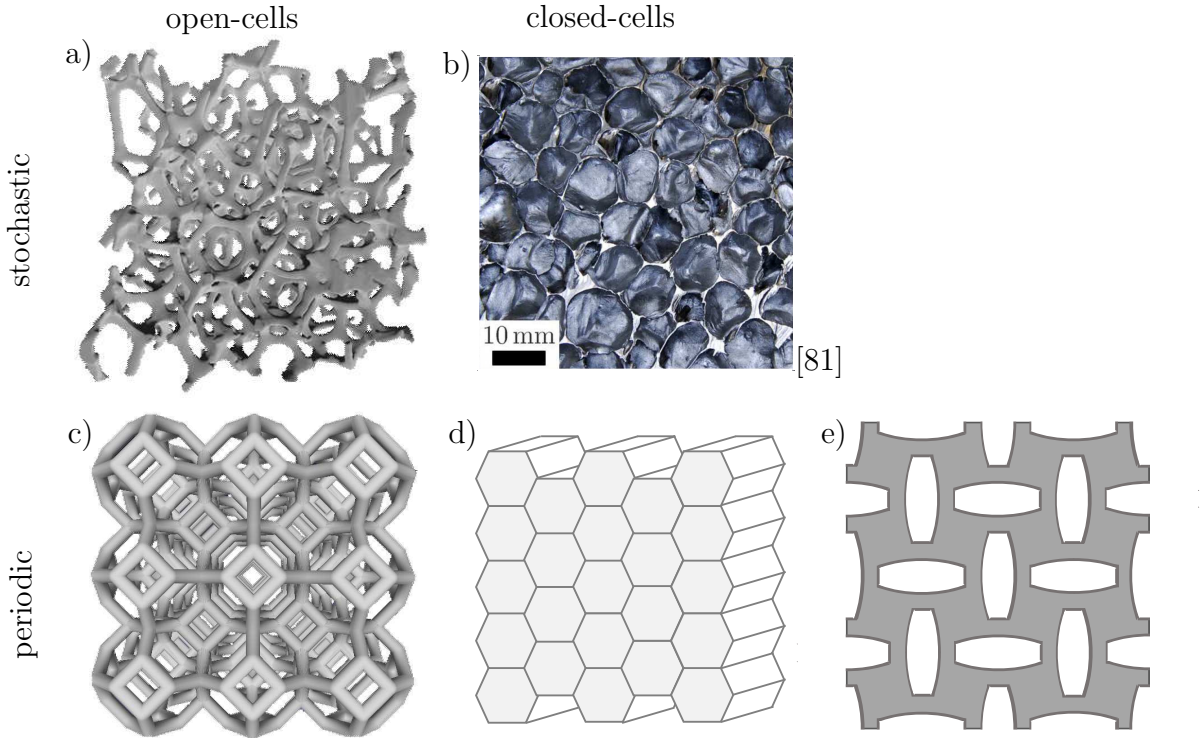

Figure 2.1: Various porous structures sorted into stochastic and regular cells. a) open-cell metal foam b) closed-cell metal foam c) micro lattices/micro trusses d) honeycombs e) auxetic structures

2.1.2 Hierarchical Structure

Porous structures can also be classified in hierarchical terms defining different spatial scales (Figure 2.2). A distinction is made between the macro, meso and micro-scale. On the macro-scale, the whole component or the entire sample (Figure 2.2 a)) is considered. On this scale, the foam is perceived as a homogeneous continuum with its effective properties, which are comparable with the properties of completely dense monolithic materials [10]. The meso-scale contains single pores (Figure 2.2 b)) or only a small number of pores, whereas the micro-scale covers the material properties and grain structure of individual struts (Figure 2.2 c)). A change in the meso and microstructure influences the macroscopic material parameters of the entire foam. In the mesostructure, the parameters pore size, porosity and in the case of coated foams, the coating thickness can be changed. In the microstructure, the strut geometry and the material can be varied. Therefore, each scale is essential for a complete characterisation of the foams. This thesis focuses on the macro-scale for the modelling and the simulation of the electrodeposition process, and the meso and micro-scale for the geometrical analysis.

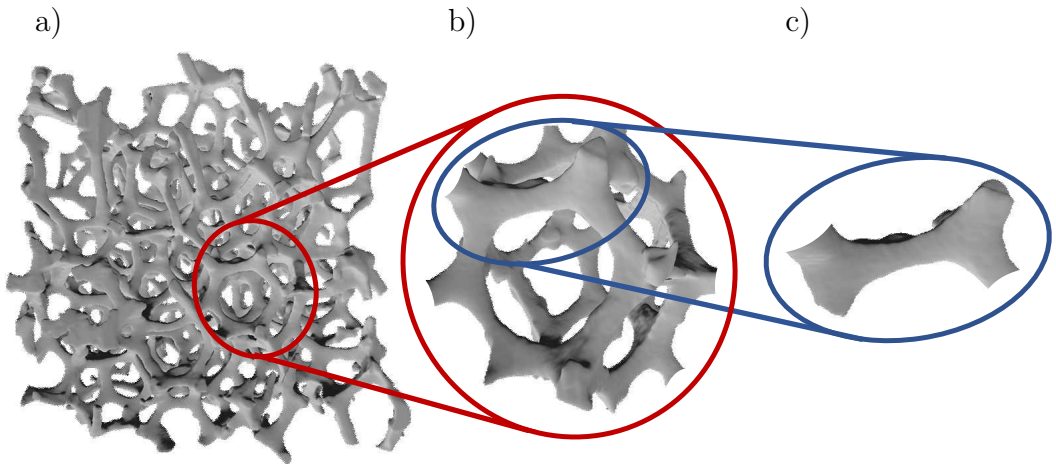

Figure 2.2: Different scales of metal foams a) Macro-scale or sample b) Meso-scale or one pore c) One strut

2.1.3 Mechanical Properties

A distinction can be made between isotropic, anisotropic and orthotropic, which is a special case of anisotropic materials, if porous media are classified according to the macro-scale's mechanical properties. Isotropic structures show no directional dependence in their properties. Cork, as an anisotropic structure, shows axis-symmetric behaviour. Orthotropy is a particular form of anisotropy. Orthotropic structures show

the same material behaviour as anisotropic structures, but only when rotated around the orthotropic axis [12]. Wood, for example, consists of long fibres aligned in one direction and shows a particular orthotropic behaviour, namely transversal isotropy. The pores of metal foams are slightly elliptical due to the manufacturing process, which leads to marginally pronounced orthotropic properties. This elliptical manner was confirmed in the research by Andrews [6], where the cells had a principle axis of 3 mm and 4.5 mm depending on the direction of measurement [6]. This directional dependency is also present in naturally occurring materials. Strength and stiffness vary by a factor of 2 for cork, depending on the direction of loading, and for wood by a factor of 10 [12]. However, metal foams are usually considered to have an isotropic material behaviour.

2.2 Manufacturing Processes

This work focuses mainly on the coating process of open-porous metal and PU foams. For the sake of clarity, the production process of the foams, creating the substrate of hybrid foams, will be discussed first. The coating process for archiving the hybrid foams is discussed in more detail in **chapter 3**.

2.2.1 Metal Foams

Literature distinguishes between nine different processes for producing metal foams. The five processes used commercially are:

1 **Gas injection:** Melted Al or a melted Al alloy is mixed with ceramic particles. Bubble-forming gas or water is injected into the melt to produce pores. This process produces foams with closed-cells and a low relative density ($0.03 - 0.1$). It is the most cost-effective method, and mainly Al-SiC or Al-Al_20_3 alloys are used to produce Al-foams [11].

2 **Gas-releasing particle decomposition in the melt:** Molten metal alloys are mixed with a foaming agent. When heated above 465 °C, the foaming agent starts to decompose, producing large amounts of hydrogen gas, and generating bubbles. The molten alloy is cooled down while controlling the overpressure so that the hydrogen cannot escape and the bubbles do not coalesce or collapse. Only closed-cell Al-foams are produced with this method [11].

3 **Gas releasing particle decomposition in semi-solid materials:** Mixed metal alloy powders with a foaming agent (TiH_2) are solidified and extruded into dense rods or sheets. They are placed in a mould and heated. The foaming agent decomposes

to form bubbles with high internal pressure. The remaining metal alloy fills the mould and obtains the same geometry as the mould. This process produces closed-cell foams with a relative density of approximately 0.08 and cell diameters of $1 - 5\,\text{mm}$ and applies to Al, Zn, Fe, Pb and Au[11].

4 **Casting using a polymer or wax die:** An open-porous polymer foam with the desired geometry is embedded in casting sand in a mould. When the mould is baked, the casting material hardens, and the polymer template decomposes and finally evaporates. A negative image of the open-porous foam remains, which is filled with a liquid metal alloy or a metal powder slurry. After cooling, the casting materials are removed, and the metal foam is created equivalent to the original polymer foam. This process produces open-porous metal foams made of Al, Cu, Mg, NiCr, and stainless steel [11].

5 **Metal deposition on cellular preforms:** An open-cell polymer foam is introduced into a reactor. Ni carbonyl is passed through the reactor, which results in Ni deposition at 100°C on the polymer foam. After reaching the intended coating thickness, the polymer foam is burnt out by heating the air. This method produces open-cell metal foams with hollow struts. The foams consist of Ni or Ti [11].

In addition to the commercially used processes described above, there are four other processes, namely gas expansion at high pressure, production using a hollow sphere structure, co-compaction or casting of two materials, one of which can be leached out, and eutectic solidification of gas-metal.
Processes 1 to 3 produce closed-cell metal foams. Processes 4 and 5 create open-cell metal foams, whereby process 5 only produces hollow struts. The advantages of process 4 are the precise control of production parameters, which can be tailored for foam usage. These production parameters are alloy, geometry, density, and cell structure. Additionally, the metal foam produced is an exact copy of the polymer foam, and accordingly, it is possible to produce complex component geometries. Depending on the process, it is also feasible to produce stable structures and an application-optimised pore size distribution. Furthermore, solid components can be bonded directly to the foam during the casting process. Disadvantages of the process are the high effort and the price due to the mould production.
The foams examined in this thesis were all produced using process 4.

2.2.2 PU-Foams

The production of open-porous PU-foams is very similar to production process 2 of Al-foams. Polyol and isocyanates are mixed in a mould with a blowing agent. This process results in a block of foam, which has to be stirred and cooled for about one day. After this process, the PU-foam has closed pores, as for the Al-foams in the production process. To open the pores, the PU foam is reticulated several times. A gas (e. g. oxyhydrogen gas) is injected into the foam and detonated for reticulation. The detonation finally opens the cell walls. Repeated reticulation converts a closed-cell PU-foam into an open-cell PU-foam. Then, the foam is permeable. The production process of open-cell porous PU-foams is much more cost-efficient than the production process of open-cell porous metal foams. This cost-efficiency is due to the production process 4 of the Al-foams, where a PU-foam is needed for creating the mould.

2.3 Applications of Metal Foams

Due to their extraordinary appearance, excellent mechanical properties and lightweight, metal and PU-foams are used in various fields. They are widely used in structural damping, thermal and electrical insulation, packaging, buoyancy, filters, membranes, and substrates such as ink carriers. A detailed list of the various applications is given in Table 2.1.
Despite the extensive range of possible applications, metal foams have been used so far almost exclusively in niches. This niche usage is due to the high production costs. Metal foams have to compete with already established and, therefore, cheaper materials. In contrast to metal foams, the established materials are not multi-functional. Metal foams combine several properties such as mechanical properties, crash absorber function and a high inner surface. By using the multi-functionality of metal foams, the usage of additional materials and, therefore also, costs can be reduced. However, challenges have to be successfully dealt with, such as poor reproducibility and high material costs of the foams. Only then can metal foams be made available to a broad market. Another way to make metal foams more attractive to the broad market is to exploit their multi-functionality, which can be achieved by using electrodeposition to apply a coating, for example. Applying the coating can produce an active surface and enhance the material properties.

Table 2.1: Properties and resulting applications for metal and PU-foams

properties	reasons for application	application
structural usage [59]	- large static and cyclic loads for a long period of time - high stiffness-to-weight ratio when loaded by bending - absorption of high impact energies [7, 106]	- space vehicle [3] - ski - racing yachts - portable buildings - crash/energy absorbers [11] - lightweight construction materials - orthopaedic applications [7]
thermal insulation [59]	low thermal mass [7, 106]	- disposable coffee cups - booster rockets for space shuttle - modern buildings - cork to save the bark
electrical insulation [7]	low loss factor per unit volume	- artificial skins [59] - radio transmitters - antistatic shields - sensors
packaging [59]	- energy absorption of impacts [7] - light weight - nearly constant stress level during large deformations	- shipping materials
buoyancy [11, 59]	- closed-cells: retain buoyncy, even when highly damaged - unaffected by extended immersion in water	- marine bouyancy - flotation in boats - modern sailboat design
other applications - filters [11, 59] - carriers [59] - membranes[59] - miscellaneous	for example: high inner surface [7]	- water cleaners [8] - carriers for inks [59] - carriers for dyes [59] - carrier for lubricants [59] - water-repellent membranes - stopper for bottles [59] - bulletin boards [59] - non-slip surfaces [59] - sound absorption [3] - scaffolds - heat-exchangers [7] - electrodes [11] - catalysts [59]

3

Electrodeposition Process

Functionalisation of the inner surface is essential for exploiting the potential of open-cell metal and polymer foams. In addition, the properties of the substrate are improved, or the substrate obtains new properties through a coating. According to DIN 8580, coating processes are one of the six manufacturing processes [1] along with primary shaping, forming, separating, joining and changing material properties. For coating processes, a distinction is made between the initial states of the coating material. The coating material can be in gaseous or vapour form, in liquid, pulpy or paste-like form. It can be in a solid (powdery or granular) state or an ionised state [1]. The challenge in foam coating is the microheterogeneous structure and the demand for a homogeneous coating thickness. Therefore, the choice of coating processes is very limited.

3.1 Coating of Foams

Coating foams can improve their properties enormously. Catalytic flow processes, surface functionalisation, corrosion resistance or mechanical properties can be improved. Particularly marked improvements in the mechanical properties can be achieved in terms of hardness, yield strength, fracture strength and wear resistance. The following describes various coating processes established for coating open-cell foams.

3.1.1 Possible Options for Foam Coating

There exist five different ways to apply the coating:

1 Foam immersed in liquid dispersion of fine metal particles, dried and sintered

2 Thermal spraying processes such as high-velocity flame spraying

3 Vapour phase deposition

4 Electrodeposition

5 Dipping foam into a melt of another metal with a lower melting point (= Hot Dip Coating)

Processes 1, 2 and 3 are applicable for fragile foam structures. However, processes 1 and 2 can only produce very thin coating thicknesses. Process 3 is costly because only very thin coatings can be applied in one single step. In process 5, the coating thickness is difficult to adjust. Processes 3 and 4 are the only processes that produce a nanocrystalline metallic coating and thus better mechanical properties according to the Hall-Petch relationship [95, 100, 117]. A nanocrystalline coating further improves mechanical properties and is preferable to a conventional coating. Regarding these points, process 4 shows the highest potential to improve mechanical behaviour. Therefore, the electrodeposition process is the central point of this thesis.

3.2 Electrodeposition Process

Electrodeposition is the process of passing an electric current through an electrolytic bath to create a coating by electrochemical deposition of metallic substrates. It is derived from electroplating, discovered by the Italian doctor Luigi Galvani in 1790. With the help of the electrodeposition process, coating thicknesses with an accuracy of less than one micrometre can be achieved on a flat surface [95, 100, 117, 147]. Furthermore, the initial compressive modulus and the peak compressive strength can be enhanced [105]. The electrodeposition process also influences the functionalisation of the inner surface and, additionally, the overall shape of the compression-strain curve [105]. The process is mainly influenced by the local electrolyte concentration (= the local ion concentration), the local current density, the hydrogen evolution, the convection of the electrolyte, and the different active areas within the medium to be coated [147]. For the substrate material, aluminium is suitable due to its low density, combined with good mechanical properties and favourable price compared to other lightweight metals [11]. Nevertheless, it has low stiffness and low strength in relation to other materials, such as, for example, Ni. For this reason, even thin Ni-coatings are sufficient to influence mechanical properties significantly. The coating material has evolved over time. In 2008, Boonyongmaneerat et al. [23] coated Al-foams with nanocrystalline Ni-W and found a positive effect on absolute stiffness, strength, and energy absorption at low coating thicknesses due to the coating. In further research, these results were also

Table 3.1: Number of pre-treatments steps for the electrodeposition on PU-foams

step	solution	duration
1	dip-coating in conductive layer (Cu or Graphit)	5 s
2	removing excessed lacquer by compressed airflow	15 s

Table 3.2: Number of pre-treatments steps for the electrodeposition on Al-foams

step	pickling solution composition	duration
1	alkaline pickling NaOH(20 %)	2 min
2	acid deoxidation HNO_3 (37 %)	1 min
3	zincate pickling first	1 min
4	dissolution of Zn layer HNO_3 (37 %)	15 s
5	zincate pickling second	1 min
6	dissolution of Zn layer HNO_3 (37 %)	15 s
7	zincate pickling third	1 min
8	electroless copper plating 200 g/l $CuSO_4 \times H_2O$ 50 g/l H_2SO_4	1.5 min

found to apply to a coating with nanocrystalline Ni [25, 85]. Furthermore, it was shown that a limitation in mass transport occurs within the foam due to the electromagnetic shielding. This mass transport limitation results in a coating thickness of 10 % in the middle of the foam in relation to the maximum coating thickness (Figure 1.1). The coating inhomogeneity also has a noticeable effect on the mechanical properties. For non-uniformly coated foams, the achievable peak compressive strength is severely limited [13]. Using a caged sacrificial anode and flowing the electrolyte through the foam, Jung et al. [86, 87] achieved a homogeneity in the coating thickness of 80 %of the maximum coating thickness. Finite-Element-Simulations of micro-tensile tests revealed an almost complete stress absorption by the coating [82], whereas the mechanical properties of the substrate have almost no influence. This led to the replacement of the Al substrate by a PU substrate. For a coating of the PU foam via electrodeposition, the foam only has to be dip-coated in a conductive layer of graphite. This means that there are two pre-treatment steps for the PU hybrid foams production (Table 3.1) in contrast to the eight pre-treatment steps for the Al hybrid foams production (Table 3.2).

3.2.1 Electrochemical Cell

Electrochemical coating cells are used for electrodeposition. The coating cell consists of two electrodes, a positively charged anode and a negatively charged cathode. The electrodes are placed in an electrolyte and are connected to a current source. With the current source cut off, the system is at equilibrium potential. If the current source

is switched on, there is an increase in potential, called overpotential. For current to flow within the electrolyte, the externally applied potential has to be higher than the equilibrium potential. Then, the electrodeposition process starts working. At the anode, the anode material, in this thesis, a metal (Me), reacts to form positively charged ions (Me^{z+}) and electrons (e^-)

$$Me \rightarrow Me^{z+} + ze^- \,. \tag{3.1}$$

The positively charged ions move from the anode to the cathode through the electrolyte. There, the ions react with the electrons to form the anodic material

$$Me^{z+} + ze^- \rightarrow Me \,. \tag{3.2}$$

Thus, the anodic material is reduced at the anode while the cathode is coated with the anodic material by oxidation of the metal ions (Figure 3.2). During the electrodeposition process, different reactions take place, depending on the distance to the electrode surface. A rough guide for this distance is a value of 1000 $\mathring{A}$ from the electrode surface. The so-called bulk electrolyte is located at a distance of more than 1000 $\mathring{A}$ from the electrode surface. In the bulk electrolyte, there are three or four dominant reasons for ionic movement:

1 applied pump = convection (Figure 3.1 a))

2 gradient of the ion concentration = diffusion (Figure 3.1 b))

3 potential gradient = migration (Figure 3.1 c))

4 ion consumption = reaction (Figure 3.1 d)).

A connected pump transports the electrolyte in the cell considered in this thesis. Therefore, all four reasons for the ion movement have to be considered.
The ion flux $\mathbf{j}^{\text{flux}}$ within the bulk electrolyte (mechanisms 1 to 4) can be described by the Nernst-Planck equation:

$$\mathbf{j}^{\text{flux}} = \underbrace{\frac{zF}{RT} Dc \operatorname{grad} \Phi}_{\text{migration}} + \underbrace{D \operatorname{grad} c}_{\text{diffusion}} - \underbrace{c\mathbf{v}}_{\text{convection}} + \underbrace{\sigma}_{\text{reaction}} \,. \tag{3.3}$$

F is the Faraday constant, z the valence of the ions, R the gas constant, T the temperature, D the diffusion coefficient, c the ion concentration, Φ the electrical potential, $\mathbf{v}$ the velocity of the bulk electrolyte and σ the reaction term. The operator grad defines the spatial gradient of its argument. Due to the relatively small potential difference,

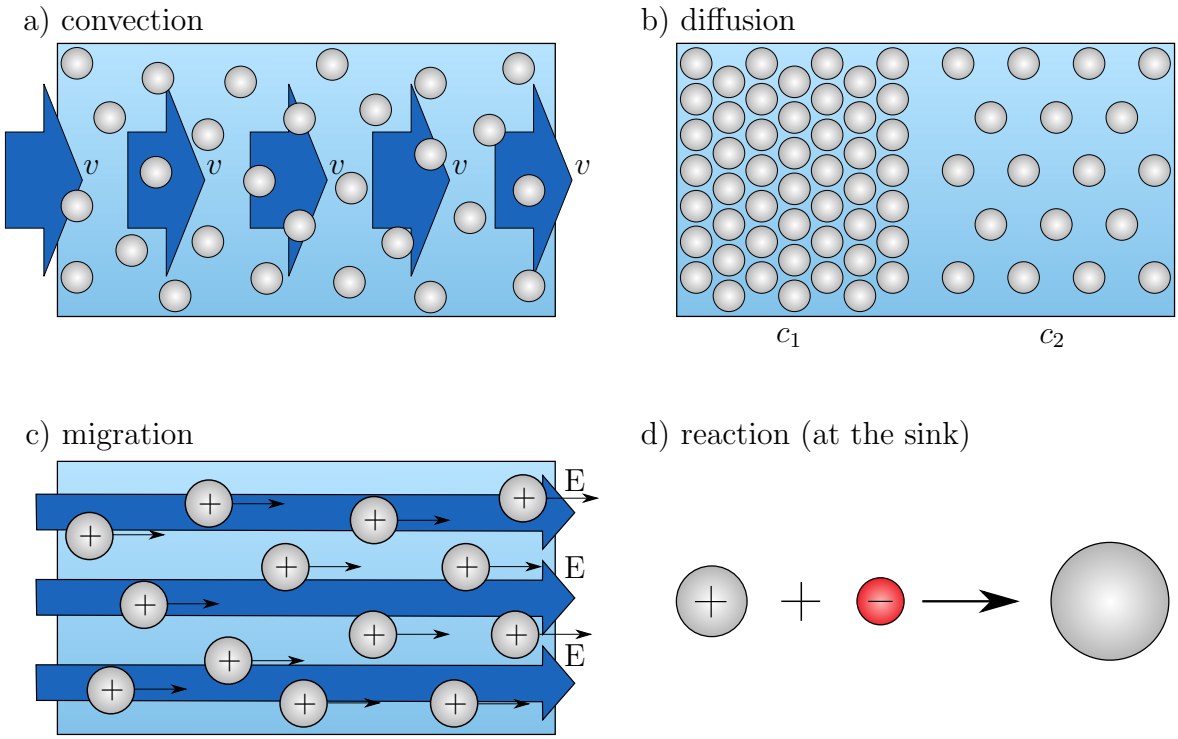

Figure 3.1: Mass transport due to a) convection, b) diffusion, c) migration and d) reaction

convection, diffusion, and reaction dominate the movement within the bulk electrolyte [144]. The actual reaction in the electrodeposition process occurs around the electrode surface at approximately 1000 $\mathring{A}$. In this region, the following four mechanisms can be distinguished:

1 the ion transport in the electrolyte,

2 the discharge reaction immediately in front of the electrode,

3 the breaking of ionic bonds near the electrode,

4 growth of a thin film on the electrode surface.

This region can be divided into two layers, the electrolytic double layer and the diffusion layer [31] (Figure 3.3 and 3.4). The diffusion layer modelling developed in this thesis only concerns the mass transport processes in the area of the bulk electrolyte. All mechanisms in the boundary layer between the electrode surface and 1000 $\mathring{A}$ to the electrode surface are neglected. Nevertheless, these mechanisms are briefly presented since knowing the chemical reactions immediately in front of the electrode surface is important for choosing the experimental setup and the parameters used in the experiment.

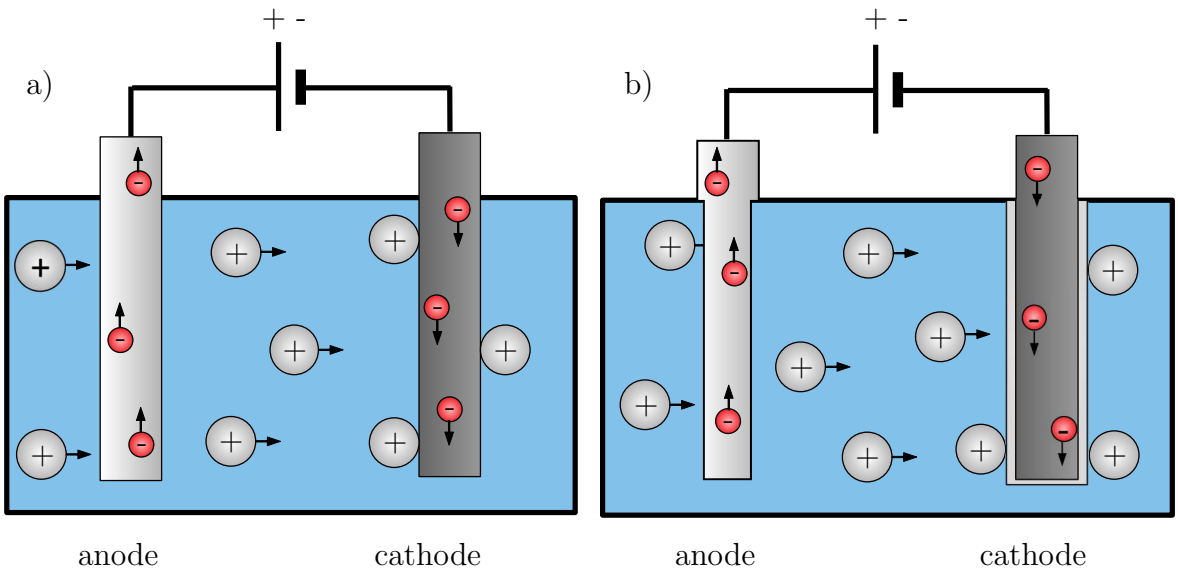

Figure 3.2: a) Electrodeposition cell at beginning of the process, b) electrodeposition cell after some time

3.2.2 Electrolytic Double Layer

To describe the main processes of electrochemical reactions, it is essential to explain the mechanisms between the metal electrode and the electrolyte. The distance between the metal electrode and the bulk electrolyte is called the electrolytic double layer (Figure 3.3). Historically, the first model of the electrolytic double layer was developed by Helmholtz [69] in 1853 and is hence called the inner and outer Helmholtz layer. This was followed by the models of Gouy-Chapman (1910 [60] & 1913 [32]), Stern [159] (1924), Grahame [61] (1947), Bockris-Müller-Devanathan [18] (1963), Trasatti/Buzzanca [156] (1971), Conway [37, 38] (1975-1980) and Marcus [115] (1992), which included increasingly complex process models progressively. Concerning the complexity of the chemical processes presented here, Stern's model is more than adequate and will therefore be considered in more detail (Figure 3.3). According to Stern's model, adsorbed and mobile ions can be found in the electrolytic double layer. Non-specifically adsorbed ions (Figure 3.3) have an intact solvate shell (layer of water molecules) and the boundary of the outer Helmholtz surface passes through their centres. Non-specifically adsorbed ions are bound to the surface via electrostatic forces. Specifically adsorbed ions (Figure 3.3) have partially stripped off their solvate shell and form a chemical bond with the surface. The boundary of the inner Helmholtz layer passes through their midpoints.

3.2.3 Nernst Equation

During the electrodeposition process, the Ni electrode is positioned in the electrolyte, which is enriched with Ni ions. Due to the potential difference within the system, solely

the anode material deposits on the cathode and the cathode material does not deposit on the anode. The reaction only proceeds in one direction. The potential of the metal electrode can be determined experimentally on the one hand and on the other hand via Nernst's equation

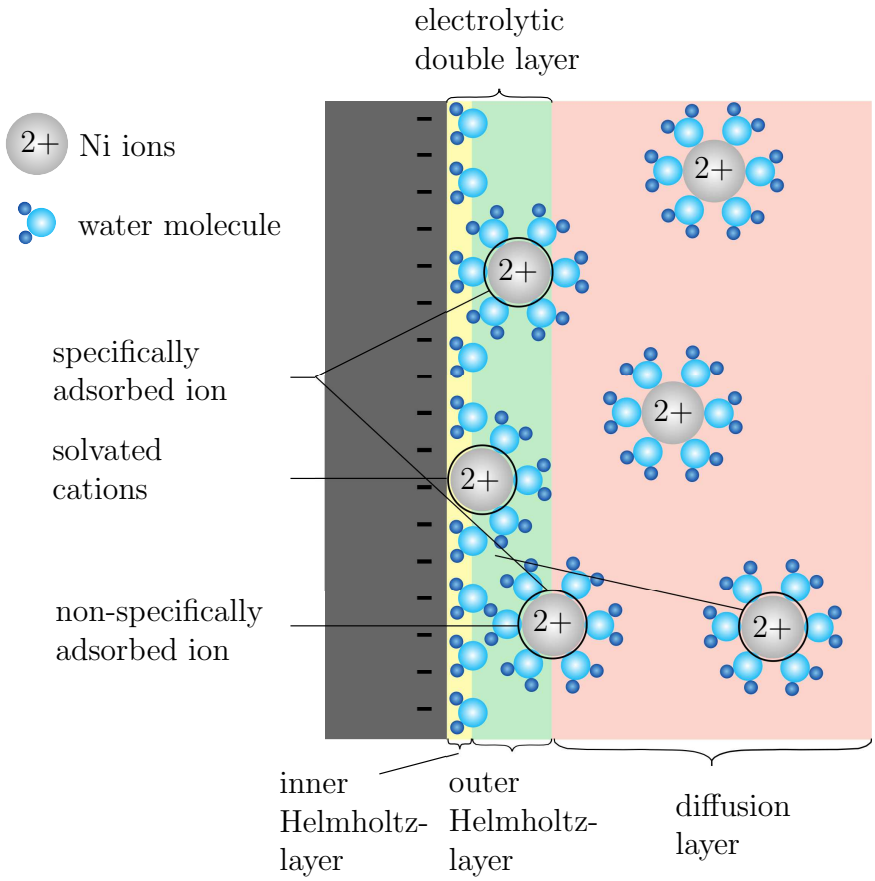

Figure 3.3: Different ions in different layers in front of the electrode

$$E = E^0 + \frac{RT}{zF} \ln \frac{a_{Me^{z+}}}{a_{Me}} . \tag{3.4}$$

The Nernst equation depends on the standard electrode potential E^0, the number of exchanged electrons z, the activity of the deposited metal a_{Me} and the activity of the metal ions in the electrolyte $a_{Me^{z+}}$. Ni is the coating material in this work, so the valence z can be replaced by 2, and the metal Me by Ni. The activity of the phase a_{Me}, being a pure phase, can be assumed to be 1 [14]. In contrast, $a_{Me^{z+}}$ is dependent on the ion concentration.

3.2.4 Direct and Pulsed Electrodeposition

For a mechanical application of metal foams, it is essential to have homogeneous material parameters and also a homogeneous coating thickness of the hybrid foams. There

exist different ways of homogenising the coating thickness. On the one hand, the current density can be reduced, but this leads to longer coating times. On the other hand, the type of current applied can be changed (Figure 3.4 a) and b)). In the case of electrodeposition with direct current (DC) (Figure 3.4 a)), the current is initially cut off. While the current is cut off, the concentration within the foam corresponds to the concentration c_0 of the bulk electrolyte. Switching the current on, the concentration distribution changes. The ions inside the foam are very quickly deposited, and the concentration inside the foam reaches $c = 0$. At the outer foam boundary, the concentration is lower than the concentration of the bulk electrolyte and, at the same time, higher than the concentration inside the foam. The concentration is c_a at the boundary. Outside the foam and at a certain distance from the foam boundary, the ion concentration is again c_0 equal to the concentration in the bulk electrolyte. With the current switched on for a longer time, the ion concentration distribution in the bulk electrolyte and directly at the boundary does not change during DC. Within the foam, ions are delivered and also gradually deposited. The concentration falls from the outer boundary to the centre of the foam. This decrease in ion concentration leads to a coating thickness inhomogeneity during the electrodeposition process. To improve the homogeneity, the electrodeposition process is often carried out with a pulsed current (PED). In the initial state, the current is off. When the current is switched on, the ion distribution inside and outside the foam behaves analogously to DC's ion distribution. However, with PED the current is then cut off after a short time. When this happens, no more ions are deposited, and the ions are redistributed in the electrolyte by the mass transport processes convection, diffusion, and migration. Because the current is switched off, no ions are deposited, and no reaction occurs. Again, there is a homogeneous ion concentration of c_0 over the complete foam. Thus, the foam is coated more homogeneously with the help of PED than with DC. The modulation of the current signal for the electrodeposition process is executed in the experiments in this thesis, as shown in Figure 3.4 b), using a square wave pulse. Important quantities are the pulse duration of the switched-on current t_{on} and the duration of the cut off current t_{off}. The maximum current, also called amplitude, is denoted by I_P, and the mean current is I_m

$$I_m = I_P \frac{t_{on}}{t_{on} + t_{off}} \,. \tag{3.5}$$

The mean current is responsible for the deposition rate and corresponds to the current at the electrodeposition process with DC. Another important quantity is the duty cycle, which is the ratio of the switched-on time to the total time (=sum of the switched-on and cut off time)

$$d = \frac{t_{on}}{t_{on} + t_{off}} = \frac{t_{on}}{t_{total}} \,. \tag{3.6}$$

The mass of the deposited material m and hence the coating thickness can be calculated in the experiment using the molar mass M of Ni, the deposition time t, the current I during the deposition, the number of electrons z transferred during the electrodeposition and the Faraday constant F

$$m = \frac{M\ I\ t}{z\ F}\,. \tag{3.7}$$

For electrodeposition with DC, I corresponds to the current. For the electrodeposition process with PED, I corresponds to the average current I_m. This variation of the current signal leads to a change in the concentration immediately in front of the electrode surface, the so-called diffusion layer.

3.2.5 Diffusion Layer

Two popular models exist to describe the ion concentration in front of the electrode. One for DC [75] and one for PED [76]. For DC, the electrolyte concentration increases linearly from the cathode in the direction of the bulk electrolyte to the concentration $c = c_0$ (Figure 3.4). The area with increasing concentration is the thickness of the hydrodynamically established Nernst diffusion layer δ_N. For PED, two diffusion layers exist to describe the true ion concentration. One is the thickness of the pulsating diffusion layer δ_P (closer to the electrode), and the other is the thickness of the stationary diffusion layer δ_S (further away from the electrode). The ion concentration increases linearly towards the bulk electrolyte to $c = c_0$. The concentration slope in the pulsating diffusion layer is higher than for the stationary diffusion layer. The PED model also takes into consideration the ion concentration increase in front of the electrode after the current cut off. The dotted trends are the concentration profiles at times $t_1 < t_2 < t_3$ in δ_P (Figure 3.4). The diffusion layer's concentration has to be increased to increase the mass transport. One way to increase mass transport is to increase the velocity of the electrolyte flow. Increasing the electrolyte flow improves the mass transport and, thus, the electrochemical conversion.

3.3 Description of the Experimental Setup

3.3.1 Coating Setup

Coating thickness inhomogeneities are higher in PU-foams due to the higher mass transport limitations than in Al-foams. Therefore, the experiments to validate the simulations are carried out on 20 ppi PU-foams (Schaumstoff Direkt Rüdiger Nolte,

Enger, Germany) instead of Al-foams. The cylindrical samples (diameter: 70 mm and height: 20 mm) are coated with a graphite layer (CRC Industries Deutschland GmbH, Iffezheim, Germany) in a dip coating step due to their non-existing conductivity. The dip coating results in closed faces, which can be opened by blowing the foams with

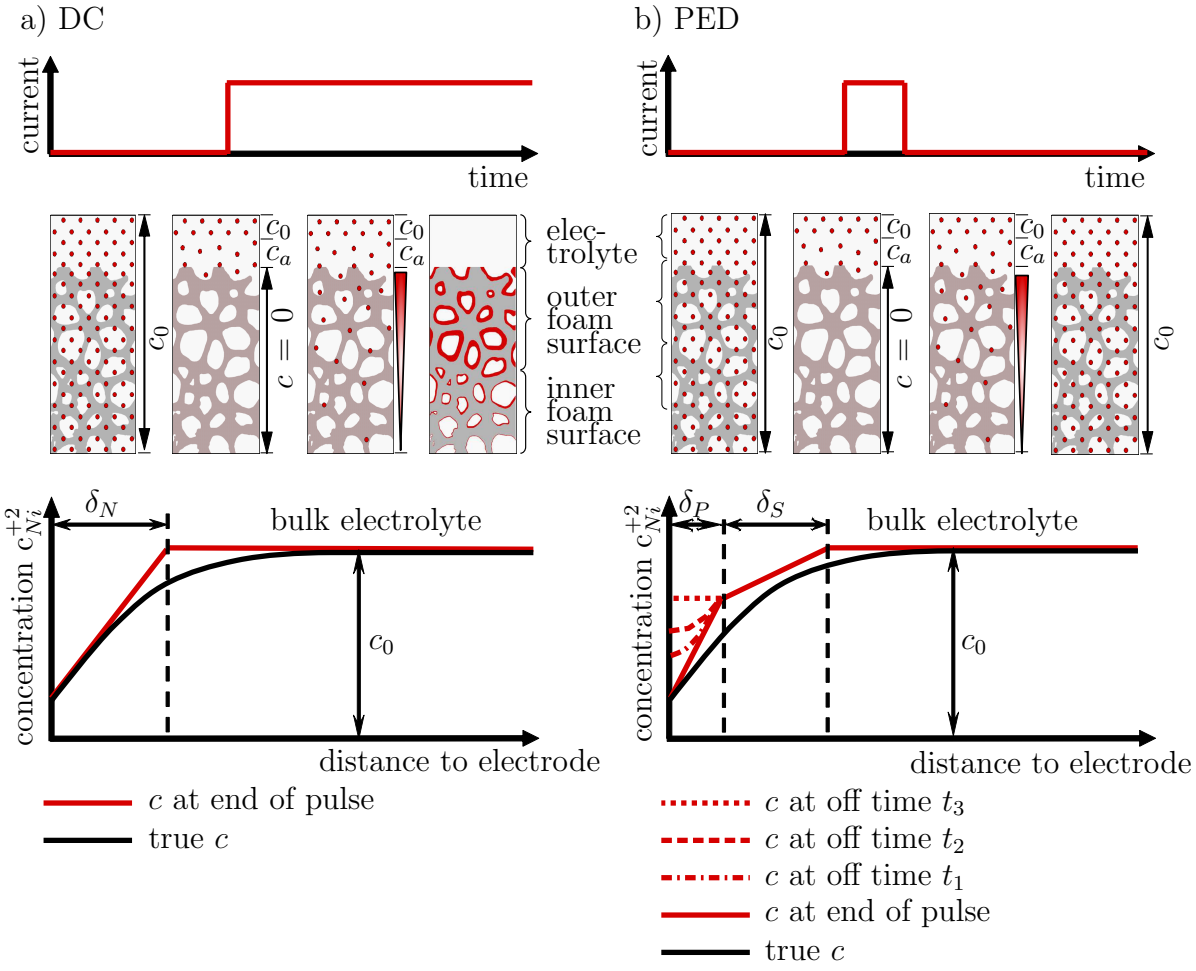

Figure 3.4: Current over time, ion concentration in the electrolyte and in the foam for different times and concentration profiles a) concentration profile for electrodeposition with DC after [89] and [75], b) concentration profile for electrodeposition with PED, doted lines at off time for $t_1 < t_2 < t_3$ after [89] and [75]

compressed air. This blowing has the advantage that it allows for controlled drying and a very thin graphite layer. For the electrodeposition process, a flow-through reactor [57, 62] (Figure 3.5) is used. It is an improvement of the electrodeposition cell invented from Keck [92] in 2017. The Keck cell was a development of the caged anode of Jung [86] to achieve better coating homogeneity and better adjustable and measurable experimental parameters. The reactor has a cylindrical shape, which results in a more uniform flow and easier measurement of various parameters during the process. Additionally, the flow through can be increased by a pump, and mass transport limitations can consequently be reduced [87]. Another advantage of the cylindrical shape is that it makes it easier to control electrolyte flow. The controlled electrolyte flow results in

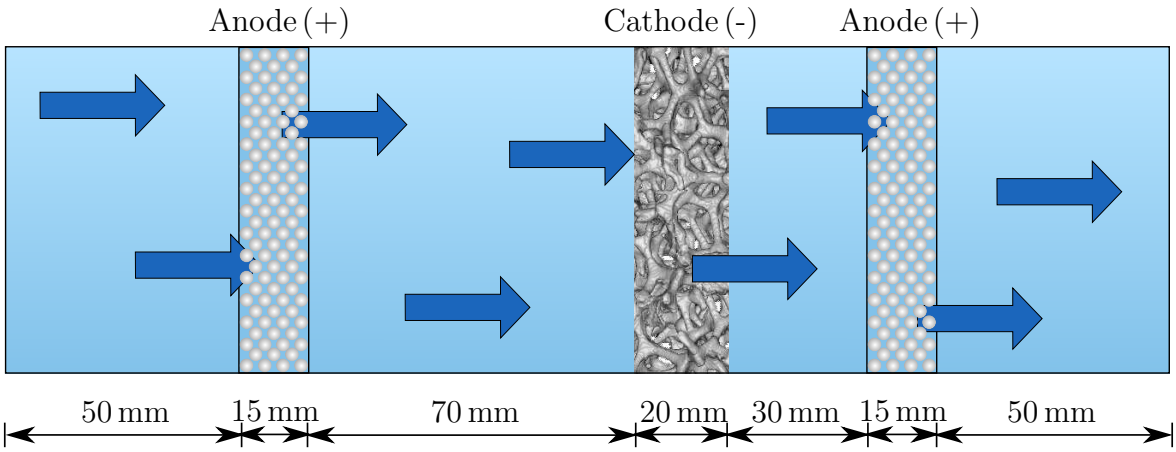

Figure 3.5: Schematic illustration of the flow cell used in the experiments including the two anodes with the Ni pellets, the cathode, and the flow direction

better transferability of the experiment into the simulation. The flow-through reactor consists of a tube with two cylindrical anodes between which the cathode is attached in the form of a cylindrical PU-foam. In front of the first anode is an inlet and behind the second anode is the electrolyte outlet. The foam is placed nearer to the second than to the first anode. This placement prevents mass transport limitations at the back side of the foam. The electrolyte is a commercial Ni sulphamate electrolyte (Enthone GmbH, Langenfeld, Germany) with a Ni concentration of 110 g/l, used at a pH of 3.5 and a temperature of 50 °C. The electrolyte is pumped through the reactor from a storage vessel using a diaphragm pump, filtered and returned to the reservoir. The sacrificial anodes consist of titanium anode bags containing Ni pellets (A.M.P.E.R.E. GmbH, Dietzenbach, Germany). A pulsed current is better than a direct current to avoid mass transport limitations. However, since the experiments are to be used to validate the modelling and simulation, the experiments are carried out with DC and PED. The target coating thickness of the Ni on the foam is 70 μm. For the validation of the simulation and the difference between the simulation and experiment, different parameters will be varied and evaluated with respect to the differences in the coating thickness. These parameters are presented in more detail in **chapter 8**.

3.3.2 Difference between Al and PU as Foam Materials

Traditionally, only Al-foams were used for the coating process. Al is characterised by a favourable price combined with good mechanical properties and low weight. However, Al-foams are still relatively expensive at about 90,000 €/m³. Studies by Jung and Diebels [82] showed that almost all the stress was transmitted by the coating and only minimal stress by the substrate foam. These results have led to the coat-

ing of PU-foams in addition to Al-foams. PU-foams are much cheaper at $1,500\,€/m^3$. Therefore, a coating of PU instead of Al-foams brings immense cost advantages, with $88,500\,€/m^3$. Another clear advantage of coating PU instead of Al-foams is the number of preparation steps. When coating Al-foams, 8 preparation steps are necessary. In sum, the duration of the preparation steps takes about 84 minutes (Table 3.2) resulting in a process of 20 seconds . When coating PU foams, only two preparatory steps are necessary (Table 3.1). One disadvantage of coating PU-foams is their lack of conductivity. For this reason, PU-foams are made conductive, for example, by dipping them in graphite. However, due to this low conductivity compared to Al-foams, PU-foams are even more vulnerable to forming coating thickness inhomogeneities. These thickness inhomogeneities can be prevented to a very large extent by determining optimal process parameters. However, determination of the parameters in experiments is very extensive due to the many influencing factors and is thus highly time-consuming. By modelling and simulating the electrodeposition process, the examination of the process parameters on the coating thickness homogeneity and, thus, the determination of optimal process parameters can be performed with less time and less resource input. For this reason, the modelling approach to the electrodeposition process is presented in detail in the following chapters and is later implemented into simulation software. The results of the simulations will be compared to experiments conducted using the following methods.

3.3.3 Coating Thickness Measurement

To measure the coating thickness homogeneity in the experiments, the cylindrical samples are cut each into 25 cuboids of size $10 \times 10 \times 20\,\mathrm{mm}^3$. The coating thickness of each cuboid was measured at the top, middle and bottom plane, meaning that each cuboid has to be cut in the middle. In each of the three planes, optical microscopy (Leica Microsystems GmbH, Wetzlar, Germany) measured the coating thickness at the 25 locations. The coating thickness inhomogeneity is highest in the middle of the foam. For this reason, only the results of the cuboids at locations 3, 8, 11, 12, 13, 14, 15, 18 and 23 (Figure 3.6) are considered, with the focus on cuboid number 13 of the samples. In the following, the coating homogeneity is calculated with the help of the maximum and actual coating thickness of each experiment

$$\text{coating homogeneity } [\%] = \frac{\text{actual coating thickness}}{\text{maximum coating thickness}}\,. \tag{3.8}$$

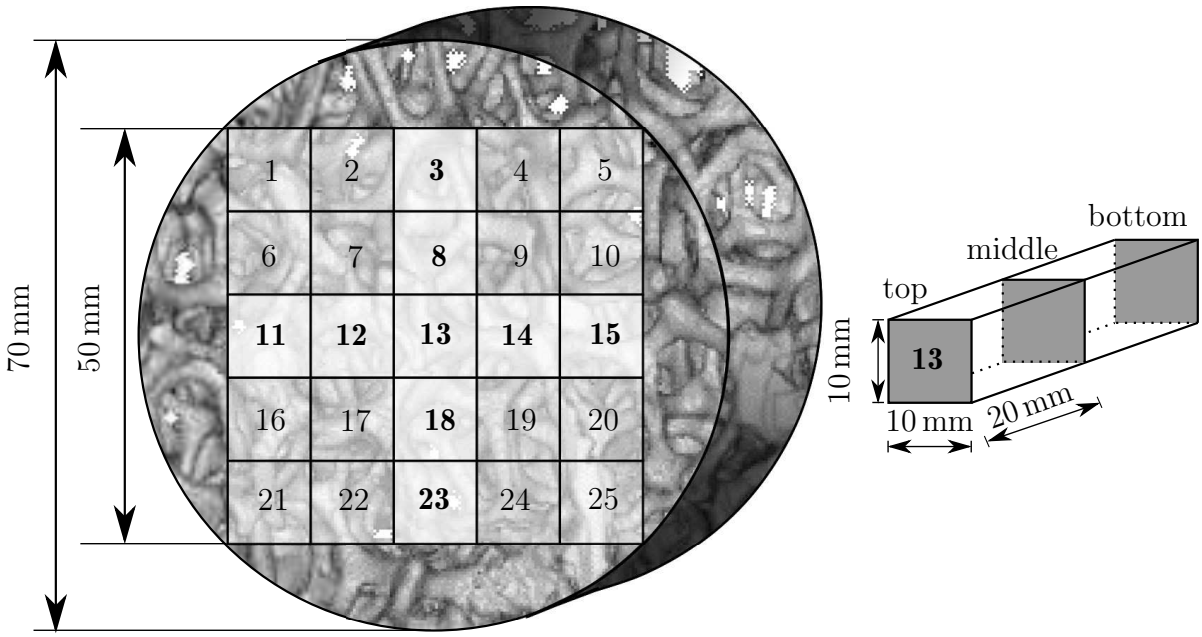

Figure 3.6: Cutting and numbering of the foam specimen for measuring the coating thickness on the top, the middle, and bottom of the specimen

3.4 Experimental Results

Experimental results were obtained in the context of the bachelor thesis by Fries [57] and are listed in detail in the appendix (Table A.1). Results are evaluated in comparison to the results of the simulation and can be found in **chapter 8**.

3.5 Design of Experiment

Mainly due to the worldwide standardised procedure [24], statistical experimental design is becoming increasingly essential [151], especially in the presentation of results. Using a statistical experimental design, the number of experiments to be conducted can be significantly reduced. The basis is a system with input variables and output (Figure 3.7), whereby a distinction is made between input variables that can be specifically changed and input variables that cannot be specifically changed or are unknown. The influencing variables are called parameters in modelling, and the parameters considered in statistical experimental design are called factors. The factors can be set to concrete values in the experimental design, the so-called steps or levels. Each factor is tested on at least two different levels.

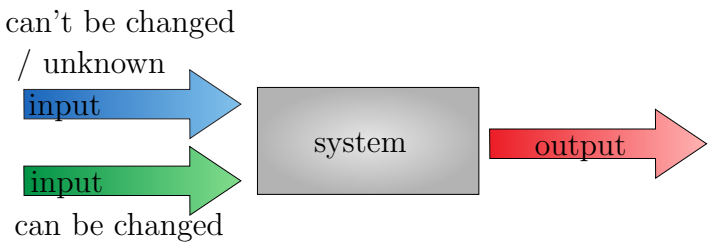

Figure 3.7: Simplification of an arbitrary system with different inputs and an output

The step distances chosen should not be too small since small step distances are physically accompanied by minor physical effects [151], providing there are no instabilities in the system. The effect characterises the average change of the target variable (= output) as a result of a step variation. For this reason, the steps chosen should be as large as possible, but instability of the system should be avoided. Additionally, the steps should be in an adjustment range which is realistic for the application. The different levels have a uniform notation called coding. Conventions provide the codes $-/+$, $-1/+1$, or $1/2$ to describe two levels or stages. In this thesis, the code $-1/+1$ is used. One example of statistical experimental design is factorial experimental design. Here, a distinction is made between the full factorial experimental design and the partial factorial experimental design. In the full factorial experimental design, measured values of the target variable are recorded for all combinations of factor levels. In partial factorial experimental design, the measured values of the target variable are recorded only for a selected subset of the combinations. Full factorial design can be thought of as a hyper cube (Figure 3.8 shows the visualisation for three factors) that describes the minimum resolution, the 1st order plan (corner point test). This minimum resolution can be extended by a star (star point test) and a centre (centre point test) to a second order plan. Second order plans are necessary to capture the non-linear connections for each factor in at least three steps.

All combinations are tested in full-factorial experimental design, whereby the number of experiments is minimised. This minimalisation is the unique characteristic of full-factorial experimental design. Generally, in parameter studies one parameter is varied per experiment (one-factor or parameter-at-a-time method). This one-factor method leads to a vast number of experiments. Compared to the one-factor method, the effects of the individual factors and the interactions of the factors can be determined more easily in statistical experimental design. For this reason, a full factorial experimental design in cube form (corner point tests) is used to determine two target variables [55, 150]. These are, on the one hand, the coating homogeneity and, on the other hand, the difference between the results from simulation and experiment concerning the coating homogeneity. This experimental design is referred to as the DoE in the following. The DoE is explained using the example of Table 3.3 and shows the DoE varying three factors at two levels. These are qualitative levels which are replaced by

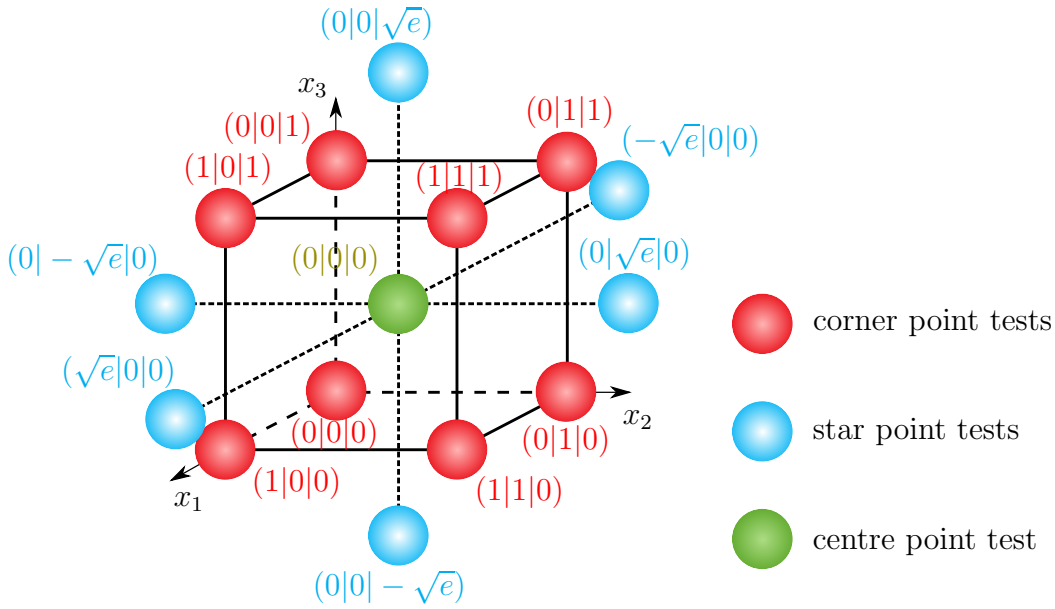

Figure 3.8: Different types of experimental designs, the corner point test (red), the star point (blue) test and the centre point test (red)

quantitative values in the practical implementation. In addition to the single interaction and the influence of every individual parameter, the interaction between the parameters is also considered. The number of experiments corresponds to the $2^3 = 8$ (level to the power of factors) factor level combinations with the target quantity y. In general, the number of experiments which have to be performed is N. N is the number of levels N_L to the power of the number of factors N_F to be varied

$$N = N_L^{N_F} \,. \tag{3.9}$$

Table 3.3: Full factorial Testing Design with 3 factors (A, B and C) and 2 levels/ steps (-1, $+1$) and one target value y

experiment n	A	B	C	AB	AC	BC	ABC	y
1	-1	-1	-1	$+1$	$+1$	$+1$	-1	y_1
2	$+1$	-1	-1	-1	-1	$+1$	$+1$	y_2
3	-1	$+1$	-1	-1	$+1$	-1	$+1$	y_3
4	$+1$	$+1$	-1	$+1$	-1	-1	-1	y_4
5	-1	-1	$+1$	$+1$	-1	-1	$+1$	y_5
6	$+1$	-1	$+1$	-1	$+1$	-1	-1	y_6
7	-1	$+1$	$+1$	-1	-1	$+1$	-1	y_7
8	$+1$	$+1$	$+1$	$+1$	$+1$	$+1$	$+1$	y_8

One requirement for experimental test design is orthogonality and balance. Orthogonality of the experimental design is achieved if no combination of two columns of the table (Table 3.3) correlates with each other, which equals linear independence. To prove

the orthogonality of an experimental design, the dot product of two column vectors of the influencing factors A, B and C have to result in the value 0

$$\begin{aligned} A \cdot B &= (-1)(-1) + (+1)(-1) + (-1)(+1) + (+1)(+1) \\ &\quad + (-1)(-1) + (+1)(-1) + (-1)(+1) + (+1)(+1) \\ &= 1 - 1 - 1 + 1 + 1 - 1 - 1 + 1 \\ &= 4 - 4 = 0\,, \end{aligned} \tag{3.10}$$

$$\begin{aligned} B \cdot C &= (-1)(-1) + (-1)(-1) + (+1)(-1) + (+1)(-1) \\ &\quad + (-1)(+1) + (-1)(+1) + (+1)(+1) + (+1)(+1) \\ &= 1 + 1 - 1 - 1 - 1 - 1 + 1 + 1 \\ &= 4 - 4 = 0\,, \end{aligned} \tag{3.11}$$

$$\begin{aligned} A \cdot C &= (-1)(-1) + (+1)(-1) + (-1)(-1) + (+1)(-1) \\ &\quad + (-1)(+1) + (+1)(+1) + (-1)(+1) + (+1)(+1) \\ &= 1 - 1 + 1 - 1 - 1 + 1 - 1 + 1 \\ &= 4 - 4 = 0\,. \end{aligned} \tag{3.12}$$

Due to the orthogonality of the vectors A, B and C, this set of vectors is a basis and every element of the vector space of this basis may be written in a unique way as a finite liner combination of A, B and C.
To demonstrate the balance of the experimental test design, the adjustment of a factor showed no effect on the other two factors. So if, for example, the level of factor A is changed, there exist the same number of experiments for each level for factors B and C

$$\begin{array}{ccc} A- & B- & C- \\ A- & B+ & C- \\ A- & B- & C+ \\ A- & B+ & C+ \end{array} \quad \Leftrightarrow \quad \begin{array}{ccc} A+ & B- & C- \\ A+ & B+ & C- \\ A+ & B- & C+ \\ A+ & B+ & C+ \end{array}\,, \tag{3.13}$$

$$\begin{array}{ccc} A- & B- & C- \\ A+ & B- & C- \\ A- & B- & C+ \\ A+ & B- & C+ \end{array} \quad \Leftrightarrow \quad \begin{array}{ccc} A- & B+ & C- \\ A+ & B+ & C- \\ A- & B+ & C+ \\ A+ & B+ & C+ \end{array}\,, \tag{3.14}$$

$$\begin{array}{lll} A- & B- & C- \\ A+ & B- & C- \\ A- & B+ & C- \\ A+ & B+ & C- \end{array} \quad \Leftrightarrow \quad \begin{array}{lll} A- & B- & C+ \\ A+ & B- & C+ \\ A- & B+ & C+ \\ A+ & B+ & C+ \end{array} \quad . \tag{3.15}$$

The DoE evaluations show the orthogonality and balance of the test, which is thus well suited for the evaluation of experiments. The so-called effect characterises the influence of a single factor on the system. The effect is the difference between the mean value of the setting $+1$ and the mean value of the setting -1 [123]. Thus, the effect E_A of factor A on the target value y is calculated, for example,

$$\begin{aligned} E_A &= E_A^{+1} - E_A^{-1} \\ &= \frac{y_2 + y_4 + y_6 + y_8}{4} - \frac{y_1 + y_3 + y_5 + y_7}{4} . \end{aligned} \tag{3.16}$$

Whereas the index of y represents the number of the experiment. Effects E_B and E_C of the factors B and C respectively are calculated analogously, whereby the indices change according to the sign in the DoE

$$\begin{aligned} E_B &= E_B^{+1} - E_B^{-1} \\ &= \frac{y_3 + y_4 + y_7 + y_8}{4} - \frac{y_1 + y_2 + y_5 + y_6}{4} , \end{aligned} \tag{3.17}$$

$$\begin{aligned} E_C &= E_C^{+1} - E_C^{-1} \\ &= \frac{y_5 + y_6 + y_7 + y_8}{4} - \frac{y_1 + y_2 + y_3 + y_4}{4} . \end{aligned} \tag{3.18}$$

For the graphical representation of the effects, the mean value of the results of the setting $+1$ and the results of the setting -1 follows in a point, and the effect thus corresponds to the slope of the straight line through these points (Figure 3.9 i), iii) and v)). In addition to the effects, the interactions of the factors can also be described using the DoE. The interaction of factor A on factor B can be calculated as the difference between the target of A^{+1} and A^{-1} multiplied by B^{+1}, subtracted by the difference between the target of A^{+1} and A^{-1} multiplied with B^{-1}

$$\begin{aligned} I_{A-B} &= AB^{+1} - AB^{-1} \\ &= (A^{+1}B^{+1} - A^{-1}B^{+1}) - (A^{+1}B^{-1} - A^{-1}B^{-1}) \\ &= (\frac{y_4 + y_8}{2} - \frac{y_3 + y_7}{2}) - (\frac{y_2 + y_6}{2} - \frac{y_1 + y_5}{2}) . \end{aligned} \tag{3.19}$$

For the graphical representation, the four points $A^{+1}B^{+1}$, $A^{-1}B^{+1}$, $A^{+1}B^{-1}$ and $A^{-1}B^{-1}$

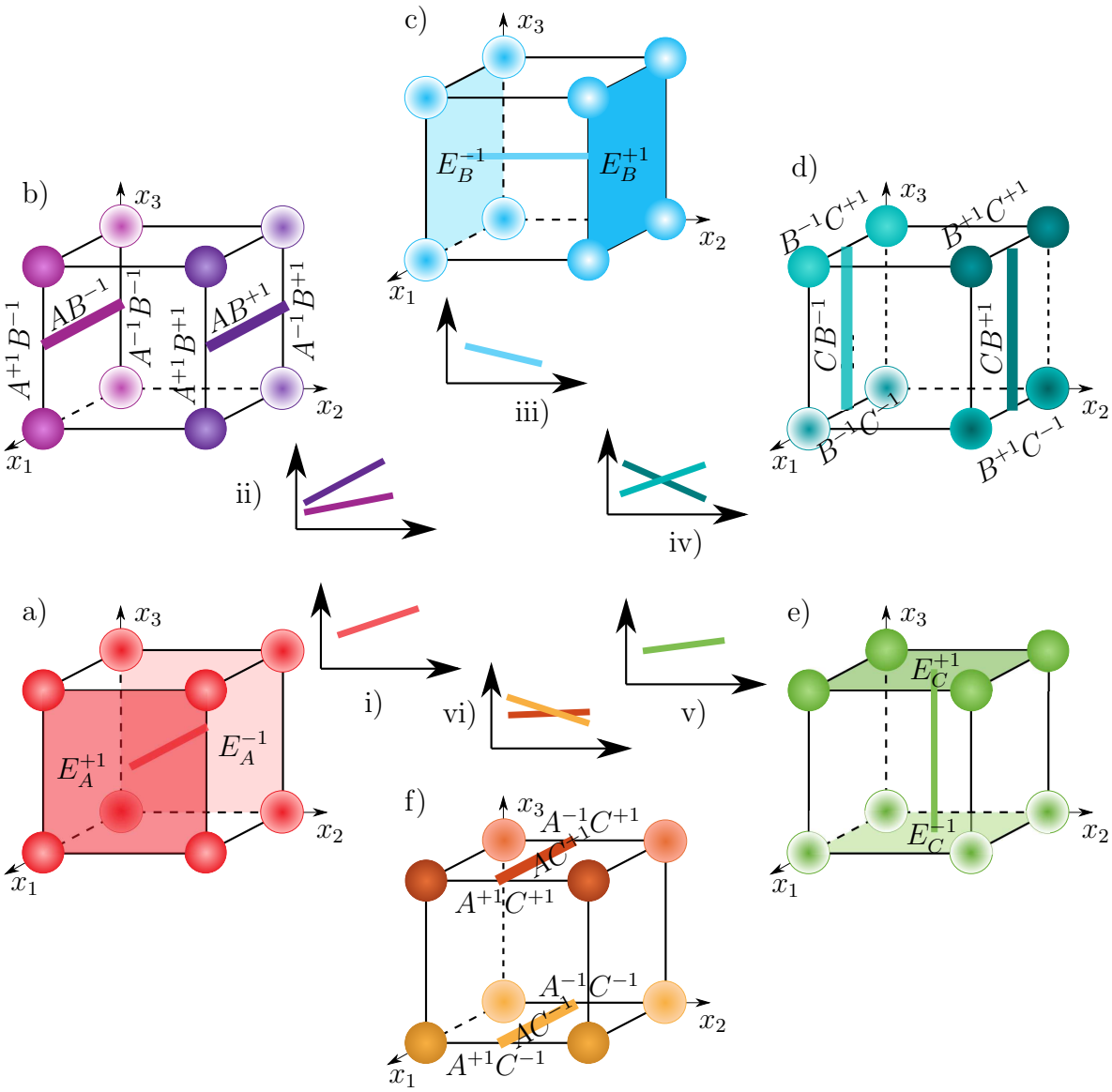

Figure 3.9: Analysis of the DoE: influence of the parameters on the target variable (a), c) and e)) and influence of the parameters on each other in relation to the target variable (b), d) and f)); i) to vi): Interpretation of the evaluation as straight lines in a coordinate system

are the starting and ending points of two straight lines (connecting $A^{-1}B^{+1}$ and $A^{+1}B^{+1}$ as well as connecting $A^{-1}B^{-1}$ and $A^{+1}B^{-1}$). The magnitude of the interaction can be read as the difference in the slope of the two straight lines (Figure 3.9 ii), iv), vi)).

4

Modelling the Electrodeposition Process

Modelling is "the mathematical way to describe a real-world problem", according to Rienstra [139]. It uses mathematical tools to describe a model that will help to find solutions. In general, the level of accuracy of models should be limited; a model should be as complex as necessary but at the same time as simple as possible. According to Steiner [157] and Ortlieb [127] (Figure 4.1), the modelling process can be seen as a cycle. A mathematical problem (Fig. 4.1 ②) is created by modelling (Fig. 4.1 Ⓐ),

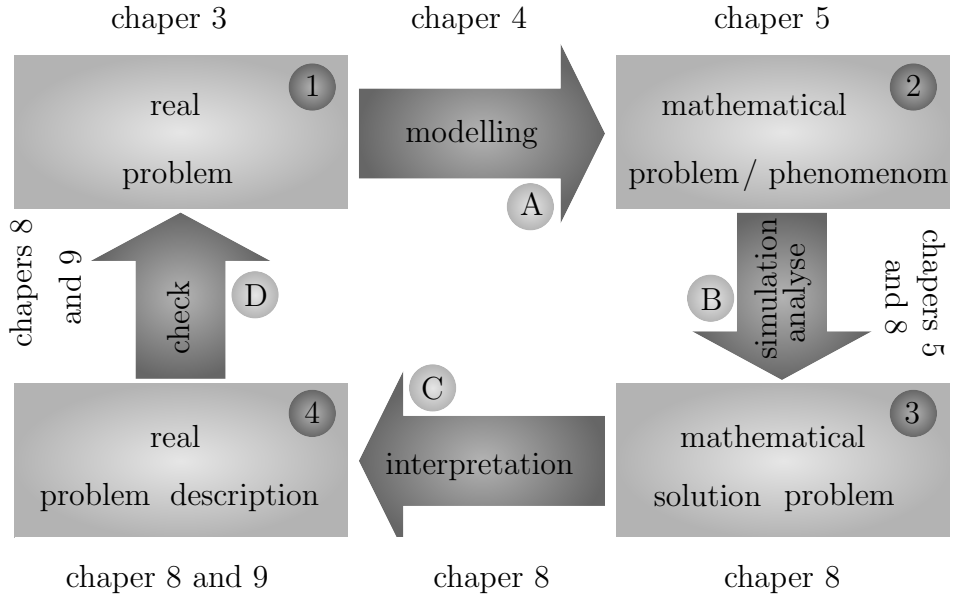

Figure 4.1: Closed circuit for the procedure of the approach to modelling and simulation of a real problem

starting from a real problem (Fig. 4.1 ①). Via analysis and simulation (Fig. 4.1 Ⓑ),

the solution (Fig. 4.1 ③) of the mathematical problem has to be interpreted (Fig. 4.1 Ⓒ) against the real problem. What follows is the verification (Fig. 4.1 Ⓓ) of the real solution with respect to the initial problem, this real problem has to be translated into a mathematical problem, and this mathematical problem has to be solved. According to figure 4.1, the real problem in this thesis is the electrodeposition process, which was discussed in detail in **chapter 3**.
In this chapter, the modelling of the electrodeposition process on open-cell foams is evaluated. Since the two steps, translation into a mathematical problem and solution utilising simulation, are at first glance very closely linked, they are described together in the section on research literature. The theoretical background to the analysis and simulation of the mathematical problem to find the mathematical solution will be discussed in more detail in **chapter 5**. The simulation analysis can be found in **chapters 5 and 8**. The mathematical solution of the problem, as well as the interpretation, are examined in **chapter 8**, and the real problem description and the check can also be found in **chapter 8 and 9**.

4.1 Modelling of Electrodeposition in Literature

The electrodeposition process is ancient and can be used in many areas. As a result, it has already been covered extensively in research. The process has also been modelled and simulated many times. Nevertheless, there has been no research on the electrodeposition process on stochastically porous materials, including convection, diffusion, migration and reaction, under consideration of the many parameters considered in this thesis. In literature so far, it has been examined on different spatial scales, concerning different physical conditions, with regard to different applications and with the help of different mathematical models, simulation schemes, and programmes. An attempt is made to list everything as precisely as possible, but this also means that some papers about different approaches have been listed twice.
First, the general electrodeposition process was modelled and simulated for different surfaces like a planar surface [118, 162, 179, 181], microscopically [39, 109, 113], considering surface roughness [169] or crystal orientation [109]. In addition, dendritic growth or nucleation on planar surfaces [5, 36, 149, 169, 176] were examined. For example, the electrodeposition process for wavers, the filling of small holes [19, 20, 26, 52, 175] and regular structures [176] was simulated. Attempts to model and simulate the electrodeposition process on complex and irregular structures like foams have, up to now, only been made by Jung et al. [84] and Grill et al. [62–64].
Different approaches can be used for the modelling. On the one hand, a phase-field modelling approach may be taken [36, 52, 67, 149], using at least two phases. On

the other hand, a combination of convection, diffusion, migration, and reaction can be used. Additionally, the electrodeposition process was described by different authors only by diffusion [134, 164], by the combination of diffusion-convection [51, 97, 168], diffusion-reaction [5, 52, 84, 88, 140] and diffusion-migration [33, 67, 153]. Moreover, the electrodeposition process was also studied by combining diffusion-migration-reaction [154], convection-diffusion-reaction [113], convection-diffusion-migration [34, 35, 167, 171, 178, 179] and convection-diffusion-migration-reaction [63, 64, 114, 175]. The convection was sometimes caused by the rotation of the electrode [34, 51, 98, 113, 114, 178]. These mathematical models were solved using finite differences [34, 63, 64, 98, 134, 136, 167, 178], finite elements [33, 84], finite volume [51, 114, 167] and Monte Carlo [113] methods.

4.2 Model Used in Implementation

For the implementation, the modelling should be as simple as possible and still represent all relevant mechanisms at the same time. Since metal foams are complex microheterogeneous materials, consideration of the electrodeposition process on the micro level would be very complex and would require immense computing capacity. For improving coating thickness homogeneity, consideration of the macro level is sufficient. This means that computing capacity can be saved. In chapter 3.2.1 the different mechanisms of ion movement at different distances from the electrode surface have already been presented. Since the electrodeposition process is only considered macroscopically at this point, the mechanisms at a distance of 1000 $\mathring{A}$ from the electrode surface can be neglected. Accordingly, only the movement of the ions in the bulk electrolyte is modelled. For the gradient of the ion concentration, in other words, diffusion, an approach following Fick's diffusion is used [54]. Fick's diffusion describes the mass transport $\mathbf{j}^{fl}$ as

$$\mathbf{j}^{fl} = -D \operatorname{grad} c\,, \tag{4.1}$$

with the diffusion constant D and the concentration c. For the gradient of the potential, an approach based on Farraday's law is used, where mass transport is defined as

$$\mathbf{j}^{fl} = -z\ F\ v^{\text{ion}}\ c\ \operatorname{grad}\Phi \tag{4.2}$$

with the mobility v^{ion} of the ions and the electric potential Φ. If the Nernst-Einstein equation

$$D = RTv^{\text{ion}} \tag{4.3}$$

$$v^{\text{ion}} = \frac{D}{RT} \tag{4.4}$$

is included in this approach, whereby D equals the diffusion constant from the diffusion part, the result is

$$\mathbf{j}^{fl} = -\frac{z\ F}{R\ T}\ D\ c\ \operatorname{grad}\Phi\ . \tag{4.5}$$

The so-called reaction term σ is used for ion consumption. A positive σ describes a source, a negative σ a sink. For this, a simple linear approach is used

$$\sigma = -a\ c\,, \tag{4.6}$$

with the sink constant a. Consequently, a high amount is deposited at a high concentration. The electrolyte is pumped through the open-cell foam during electrodeposition to prevent mass transport limitations. This movement is called convection and is described by the equation

$$\mathbf{j}^{fl} = \mathbf{u}\ c \tag{4.7}$$

with the velocity v of the electrolyte. The equations (4.1), (4.5) and (4.7) can be written into the continuity equation which is based on the mass conservation equation

$$\frac{\partial c}{\partial t} + \operatorname{div}\mathbf{j}^{fl} = \sigma\,. \tag{4.8}$$

The first term on the left-hand side of the equation (4.8) is the temporary change in concentration at one point. The second term on the left side of the equation is the transport term, and the term on the right side of the equation is the sink term. All terms together represent the mass balance. The modelling approach to be implemented results in the governing equation

$$\frac{\partial c}{\partial t} = -\operatorname{div}(\mathbf{u}c) + \operatorname{div}(D\operatorname{grad}c) + \operatorname{div}\left(\frac{z\ F}{R\ T}D\ c\operatorname{grad}\Phi\right) - a\ c\,. \tag{4.9}$$

Reasons for the local change in concentration are the flow term and the source term, resulting in a one-way coupling. However, the electrodeposition process is not just a one-sided coupled problem. In this fully coupled problem as it is, the coating thickness, in turn, influences the porosity, which influences the permeability, inner surface area and bulk volume, which, finally, have an influence on the convection, migration and reaction.

4.3 Modelling Approaches for $\mathbf{u}$ of the Convection, $\operatorname{grad}\Phi$ of the Migration and a of the Reaction

4.3.1 $\mathbf{u}$ of the Convection

An electrolyte flows through the open-porous foam in the electrodeposition process on foams. During this coating process, a change in coating thickness leads directly to a change in geometry and, consequently, in the pore space. This change in geometry leads to a change in permeability and, finally, to a change in velocity. Darcy's law describes a correlation between the pressure gradient and the velocity.

Darcy's law

Darcy's law is a phenomenological law and was discovered in 1856 by Darcy [44] while studying the flow of water through sand. He found that there is a linear relationship between the flow rate q $[{}^{m^3}/_{m^2\ s}]$ and the quotient of the height difference $h_2 - h_1$ and the length L of a sand-filled tube (Figure 4.2 a)). The proportionality factor K corresponds to the permeability of the fluid flowing through the pipe

$$q = -K\frac{h_2 - h_1}{L} \tag{4.10}$$

and is a function of the porosity Θ which results in $K = K(\Theta)$. Over time, Darcy's law was rather generalised and changed in its notation into

$$\mathbf{q} = -\frac{K}{\mu}(\operatorname{grad} p - \rho\mathbf{g}) \tag{4.11}$$

with the dynamic viscosity of the fluid μ, the pressure p, the density of the fluid ρ and the gravity $\mathbf{g}$. If the experimental setup is arranged horizontally, the gravity $\mathbf{g}$ is omitted. $\mathbf{q}$ and p are averaged values over a particular volume of the material. This is why the flow u within the pipe is regarded to be macroscopically homogeneous (Figure 4.2 a)) instead of the microscopic flow v in the pore channel. Darcy's law is a special solution of the Navier-Stokes equation [124]. For this reason the Darcy's law only applies to a laminar flow (Figure 4.2 b)) and describes an average velocity in a certain cross-section of the porous sample. According to investigations by Seguin et al. [148], the fluid flow through a foam can be regarded as laminar. If a turbulent flow prevails within the porous medium to be flowed through, Darcy's law can be extended by a Brinkman [27], or Forchheimer [174] term for non-linear flow [101]. In laminar

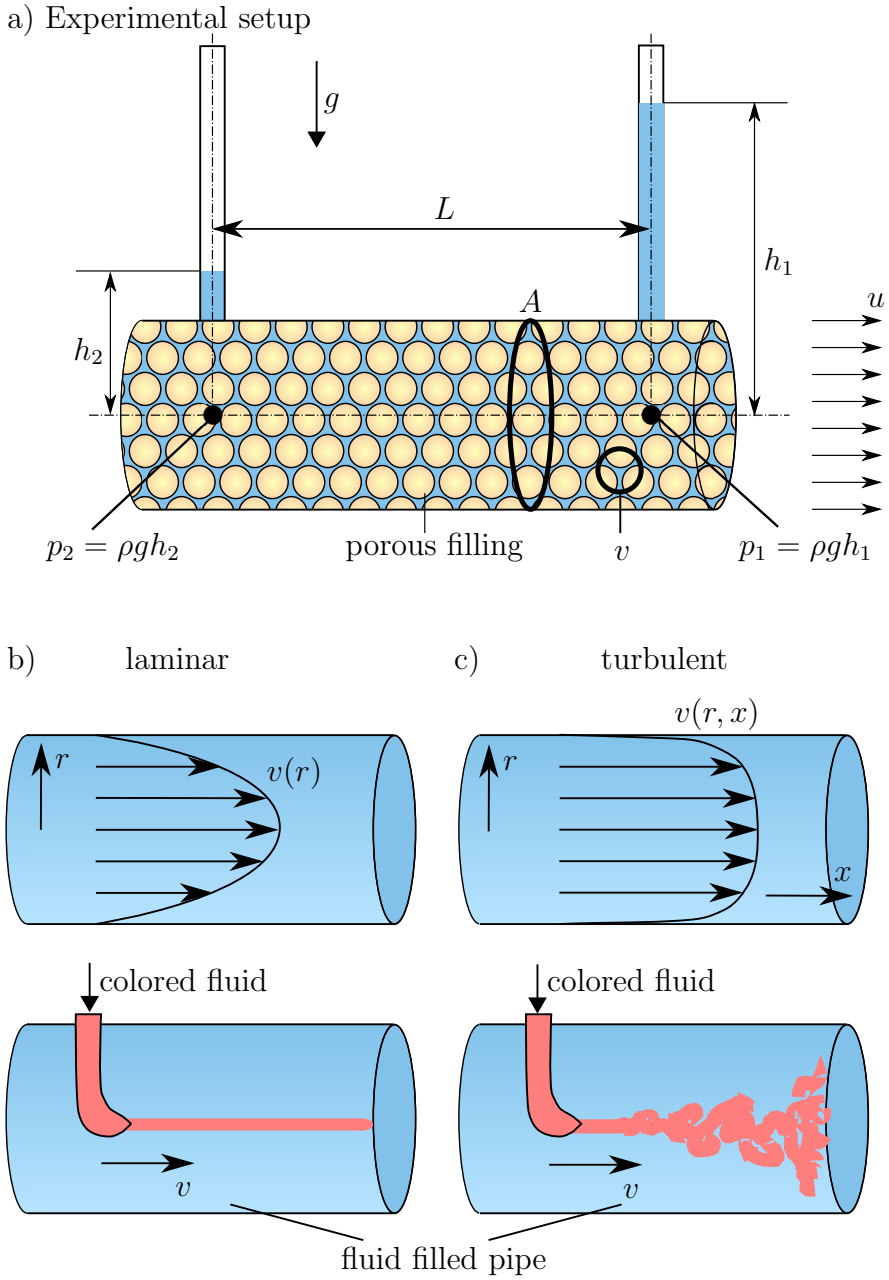

Figure 4.2: a) Experimental set-up by Henry Darcy when discovering Darcy's law, v is macroscopically homogeneous, u is the flow in the pore channel = microscopic b) appearance of the microscopic velocity u profile with laminar flow, here Darcy's law is valid, c) appearance of the microscopic velocity u profile with turbulent flow, here Darcy's law has to be extended

flow, the macroscopically observable flow is in parallel layers. Microscopically, there is a random exchange of momentum between the individual layers, which is the reason for the internal friction [182]. If, in contrast, visible exchange occurs macroscopically (Figure 4.2 c), the term turbulent flow is used, whereby it is a matter of transient, vortex-like random movements [182]. This thesis assumes a laminar flow through the foam without considering a Brinkman or Forchheimer term.

4.3.2 $\operatorname{grad}\Phi$ of the Migration

Due to the geometry change during the electrodeposition process, the inner surface also changes in addition to the permeability. The inner surface influences the electric current density $\mathbf{j}^{el}$. The electric current density is defined in physics as the amount of current flowing through a conductor of cross-sectional area A_{cs}

$$\mathbf{j}^{el} = \frac{\mathbf{I}}{A_{\text{cs}}}\,. \tag{4.12}$$

Area A_{cs} is perpendicular to the direction of movement of the ions. In electroplating theory and thus also for electrodeposition, the active area A_{active} is taken as A_{cs} (Figure 4.3). During the experiment, a constant current density is regulated, and a

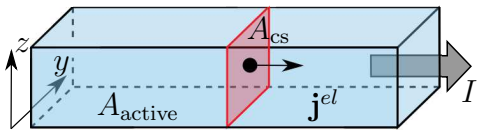

Figure 4.3: Difference between active and cross-sectional area

geometry change causes a change in the current I. The current I and the electric current density $\mathbf{j}^{el}$ are proportionally related to the electrical field $\mathbf{E}$ by the electric conductivity σ_E

$$\mathbf{j}^{el} = \sigma_E \mathbf{E} \tag{4.13}$$

and the electric field $\mathbf{E}$ is the negative gradient of the electric potential Φ

$$-\operatorname{grad}\Phi = \mathbf{E}\,. \tag{4.14}$$

Thus, the change of the geometry causes a change of the active area in the foam, which influences the electrodeposition process via the migration part. The change of the active area in relation to the coating thickness is examined in **chapter 7**. For the simulation of the electrodeposition process, this change was not taken into account.

4.3.3 a of the Reaction

The coating thickness influences the current density, and the current density influences the sink term. The sink term is assumed to be linear, and the sink constant is defined as a mass change per time according to equation (4.8). According to the Faraday law of electrolysis [53], the electric charge quantity Q can be defined as the product of the ion quantity n, the ion valence number z and the Faraday constant F

$$Q = \int \mathbf{I} dt = nzF\,. \tag{4.15}$$

Replacing Q by the product between current $\mathbf{I}$ and time t under the assumption of a constant current and replacing the amount of substance n by the quotient between the deposited mass m and the molar mass M, the following relation is obtained by rearranging the terms

$$\frac{m}{t} = \frac{MI}{zF}\,. \tag{4.16}$$

Combined with equation 4.8, it results in

$$a = \frac{\Delta m^{\mathrm{rel}}}{t} = \frac{MI}{zF} \tag{4.17}$$

which shows that the current change caused by the geometry change also influences the sink constant and, thus, the sink term. Δm^{rel} can be calculated via the volume change during the electrodeposition process for the calculation of a in the simulation. Weighing the sample from the experiment is also possible. However, an experiment would first have to be carried out before any simulation and the experiment's sample will not have an homogeneous coating thickness, which is the case in the calculated volume change. The volume change examination is executed in **chapter 7**. In this work, back-coupling is considered in observing various parameters, but is not considered in the simulation. Figure 4.4 shows the complex coupling of all parameters.

4.3.4 Relationship between Concentration Distribution and Coating Thickness

The simulation aims to predict the parameters for the experiment required to obtain a homogeneous coating thickness. So far, the model only shows a connection between the influencing variables in the area of convection, diffusion, migration and reaction to the concentration. Consideration of the actual coating thickness was not performed. This thesis assumes a linear relationship between the concentration of the Ni ions and the

coating thickness homogeneity. This means that the ion concentration distribution at time t shows the coating thickness homogeneity at time t. In this way, the complexity of the model can be reduced. The linear relationship between ion concentration and coating thickness homogeneity corresponds to an incremental view and should be a good approximation while neglecting the back-coupling. Finally, a homogeneous ion concentration has to be achieved to predict a homogeneous coating thickness. Therefore, a homogenisation of the ion concentration is the aim of the following chapters.

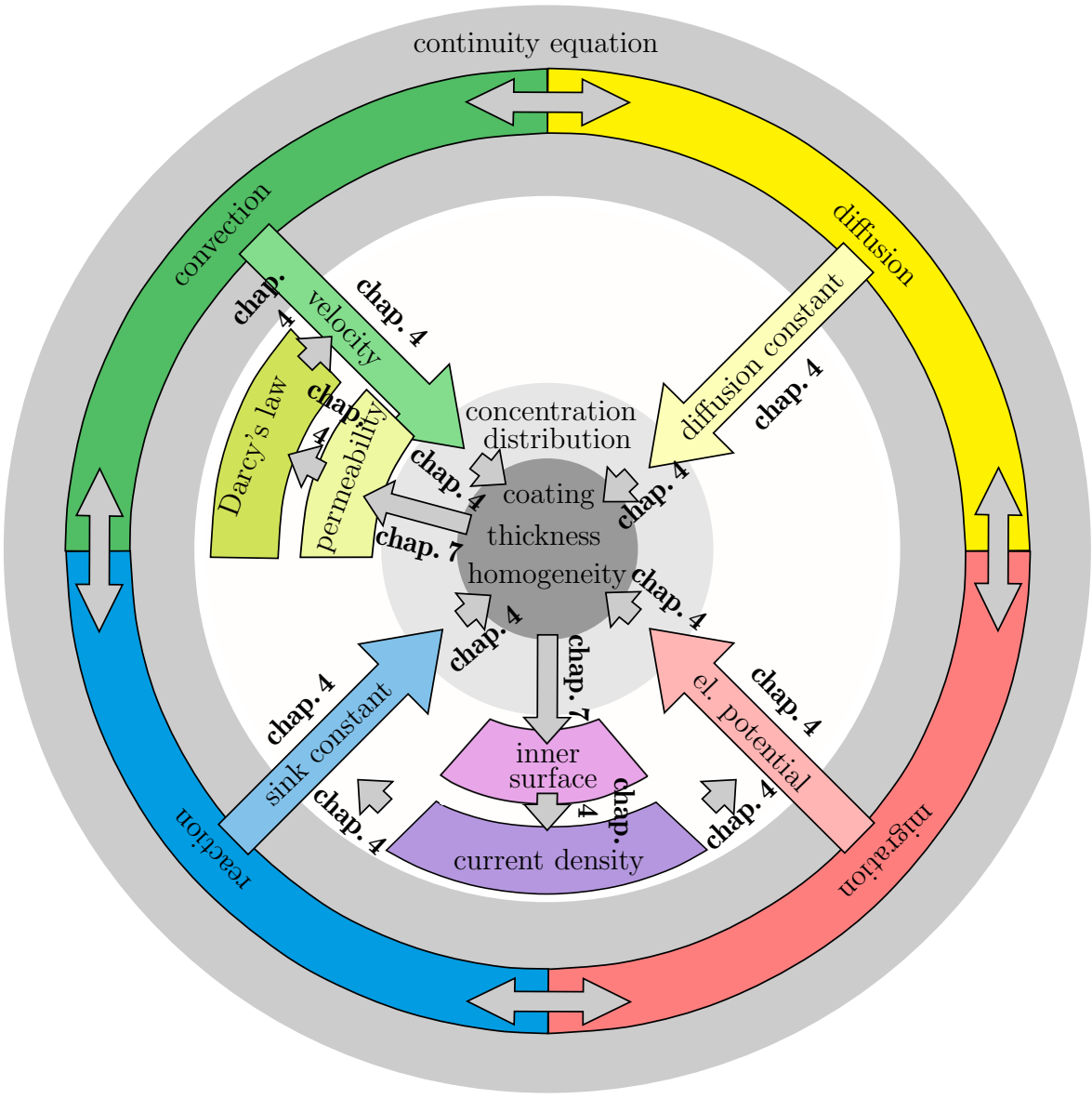

Figure 4.4: Influences of the interrelationships of the transport mechanisms and the geometry parameters on each other

5

Numerical Background

According to Figure 4.1, the analysis of the real problem and the mathematical, phenomenological representation of the problem through modelling should lead to a mathematical solution with the help of analysis and simulation. Numerical methods are used to perform the simulations. There are various methods for solving differential equations like equation (4.9) that can be applied to obtain the solution to this problem. Some of these methods fit better with some type of PDE while other methods fit better with some sample geometries. For this reason, the differential equation to be solved is first analysed in this chapter. Afterwards, various methods of solving differential equations and finding the most suitable solving strategy are presented. Finally, the numerical methods used in the simulation and the procedure for obtaining the solution of the PDE are presented.

5.1 Classification of the PDE

The different types of PDEs can be classified depending on their properties, which helps to find the best numerical solving method for each equation.

Order

Firstly, differential equations are classified according to the order, i.e. according to the highest-order partial derivative appearing in them. The differential equation (4.9) is rewritten into a simplified two-dimensional representation to determine its order. For this purpose, the velocity is divided in the x-direction (u_{X}) and in the y-direction (u_{Y})

with D assumed as constant

$$\begin{aligned}\frac{\partial c}{\partial t} =& -\frac{\partial u_\mathrm{X}}{\partial x}c - \frac{\partial c}{\partial x}u_\mathrm{X} - \frac{\partial u_\mathrm{Y}}{\partial y}c - \frac{\partial c}{\partial y}u_\mathrm{Y} \\ &+ D\frac{\partial c}{\partial x} + D\frac{\partial^2 c}{\partial x^2} + D\frac{\partial c}{\partial y} + D\frac{\partial^2 c}{\partial y^2} \\ &+ \frac{zF}{RT}D\frac{\partial^2 \Phi}{\partial x^2}c + \frac{\partial c}{\partial x}\frac{zF}{RT}D\frac{\partial \Phi}{\partial x} + \frac{zF}{RT}D\frac{\partial^2 \Phi}{\partial y^2}c + \frac{\partial c}{\partial y}\frac{zF}{RT}D\frac{\partial \Phi}{\partial y} \\ &- ac\,. \end{aligned} \tag{5.1}$$

For better readability,

$$\frac{\partial\,(\cdot)}{\partial t} = (\cdot)_t \tag{5.2}$$

can be rewritten. Applying this to equation (5.1) results in

$$\begin{aligned}c_t =& Dc_{xx} + Dc_{yy} \\ &+ (-u_\mathrm{X} + \frac{zF}{RT}D\Phi_x)c_x + (-u_\mathrm{Y} + \frac{zF}{RT}D\Phi_y)c_y \\ &+ (-u_{\mathrm{X}x} - u_{\mathrm{Y}y} + \frac{zF}{RT}D\Phi_{yy} + \frac{zF}{RT}D\Phi_{xx} - a)c\,. \end{aligned} \tag{5.3}$$

The highest-order partial derivative appearing in equation (5.3) is second-order in space and first-order in time. Therefore, equation (4.9) is a second-order PDE in space and a first-order PDE in time.

Linearity

A second possible classification of differential equations is linearity. If all terms are only linear in the searched quantity and its derivatives, as is the case in this thesis with the concentration, the equation is linear. If there is a dependence of the coefficients and the required quantity, the PDE is non-linear. A PDE is also non-linear if the searched quantity and its derivatives are of an order higher than 1 in the PDE. The coefficients of the PDE (4.9) namely D, u_X, u_Y, z, F, R and T do not depend on the concentration, and the sink term has a linear approach. Therefore, equation (4.9) is a linear PDE.

Type

In addition to order and linearity, second-order linear PDEs can also be classified in terms of the type of their solution. The PDE itself does not have to be solved for this classification, but the discriminants' size has to be determined. For this purpose, the pre-factors of the partial derivatives of the canonical form of a linear second-order PDE

with three independent variables are considered

$$\lambda_1(x,y,t)c_{tt} + \lambda_2(x,y,t)c_{xx} + \lambda_3(x,y,t)c_{yy} = U(c,c_x,c_y,c_t,x,y,t)\,. \tag{5.4}$$

U has to be linear in c, c_x, c_y and c_t. With the help of the canonical form, the following definition can be made. The PDE is

- **elliptic**, if and only if all λ_i have the same sign [158]
- **hyperbolic**, if and only if one λ_i has the opposite sign of the other λ_i [158]
- **parabolic**, if and only if one λ_i is zero and the other λ_i have the same sign [158].

Looking at equation (5.3), $\lambda_1 = 0$, $\lambda_2 = D$ and $\lambda_3 = D$. As per definition, the canonical form of equation (5.3) gives a parabolic form of the PDE. The parabolic form indicates that the solution of the model evolves to a steady state. The PDE is only parabolic if it is first-order in time and second-order in space, which it is in this thesis.

5.2 Predominating Mass Transport Mechanism

In addition to these very general classifications of PDE, the dominant mass transport mechanism can be determined for convection-diffusion-reaction systems. To distinguish whether a process is dominated by convection or diffusion, the dimensionless Péclet number was introduced [180]. The Péclet number is the quotient between the convective and diffusive transport rates

$$\mathrm{Pe} = \frac{\text{convective transport rate}}{\text{diffusive transport rate}} = \frac{Lu}{D} \tag{5.5}$$

with the velocity u, the characteristic length L and the diffusion constant D. In literature, there exist six different possibilities for calculating the characteristic length in metal foams, whereas the most common derivations are, that the characteristic length equals the pore diameter or the ratio between volume and surface area [74]. Here, the characteristic length corresponds to the pore diameter. In the application considered in this thesis, the thickness of the cylindrical foam is considered. Depending on the value of the Péclet number, three different cases can be distinguished (Figure 5.1). A thought experiment is used for this purpose. In this experiment, an ion source spreading with a diffusion constant D and exposed to a velocity u is considered and the ratio u to D is changed (Figure 5.1).

Pe $\rightarrow$ 0

If the Péclet number approaches zero (Figure 5.1 a)), either the velocity u is approximately zero, or the diffusivity is infinite. Thus, the process is diffusion dominant. Consequently, the concentration profile in parallel and perpendicular flow direction is identical, and convection does not affect the concentration distribution. The concentration distribution around the ion source evolutes circular and increases towards the source.

Pe $\approx$ 1

With a Péclet number in the order of one (Figure 5.1 b)), the process is neither convection nor diffusion dominant. In the flow direction, both convection and diffusion mass transport mechanisms are active, which is why the concentration profile is elongated in the flow direction. Perpendicular to the flow direction, the active mass transport mechanism is only diffusion, and the concentration profile is slightly flattened in this direction.

Pe $\rightarrow \infty$

If the Péclet number tends towards infinity (Figure 5.1 c)), either the velocity is approximately infinite, or the diffusion constant goes to zero. Thus, the process is convection dominant. In this case, the concentration profile is only elongated in the flow direction, and an evolution of the concentration profile perpendicular to the flow direction does not occur.

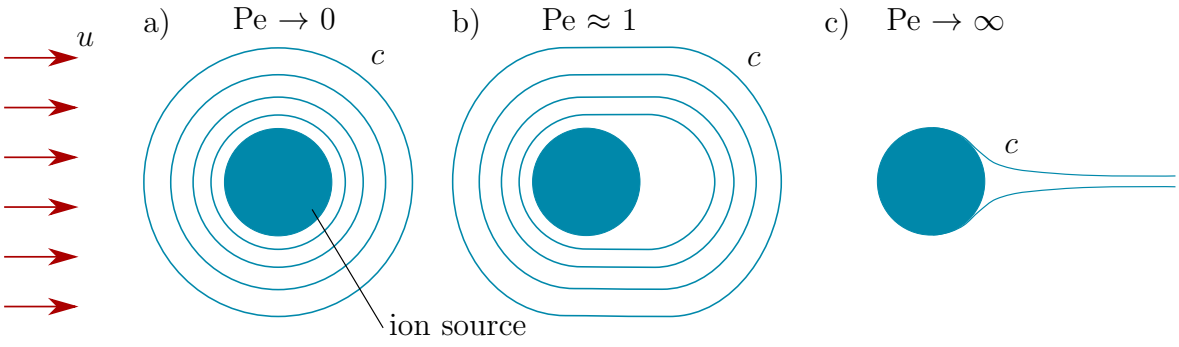

Figure 5.1: Different concentration profiles for different Péclet-Numbers, starting from an ion source, a) diffusion predominated flow, b) convection and diffusion predominated flow, c) convection predominated flow

According to the experimental setup and experimental design presented in **chapter 3**, only the parameter u is varied, considering the parameters L, u and D. The parameters L and D remain constant. The parameter u varies between the values $u_{\text{min}} = 0.00466\,\text{m/s}$ and $u_{\text{max}} = 0.01863\,\text{m/s}$. L =pore diameter= $0.0061\,\text{m}$ and

$D = 0.000096^{m}/_{s^2}$ (the exact derivation of these values can be found in **chapter 7** and **chapter 8**). This results in the two Péclet numbers $\mathrm{Pe}_{\min} = 0.309$ and $\mathrm{Pe}_{\max} = 1.234$. Accordingly, the problem is neither convection nor diffusion dominated in the parameter range considered in this thesis.

5.3 Mathematical Computation Tools

The equation (4.9) is a linear PDE of second-order in its continuous form. Solving this equation analytically is, with regard to the closed form solution, impossible and computationally very intensive, except for special boundary conditions. For this reason, the differential equation is converted from a continuous form into a discrete form, which can then be solved numerically. There are different approaches to transforming the mathematical differential equation into a discrete form. The best known are

- Finite Difference Method (FDM)
- Finite Volume Methode (FVM)
- Finite Element Method (FEM) .

FDM The FDM is the oldest method for the numerical solution of PDEs and was probably developed by Euler in 1768 [17]. In the FDM, all derivatives in the differential equations are replaced by so-called difference schemes, resulting in a set of algebraic equations. The equations contain the unknown variables of the corresponding mesh points (Figure 5.5 a)) in dependence on a certain number of values of neighbouring points. The difference schemes result from a Taylor series expansion or a polynomial fitting. The Taylor series is usually truncated after two or three terms. The more terms are included, the more precise the solution is, but the higher the computational costs and there can occur stability problems. Advantages of FDM are the simplicity of implementation on regular grids and the possibility of achieving higher order approximations and, thus, higher accuracy in a simple way. However, the FDM results can violate the conservation laws of classical physics, such as energy and mass balance. Consequently, FDM is not conservative in general. Furthermore, using FDM's advantages with simple implementation requires a structured grid, so it should only be used for relatively simple geometries.

FVM In FVM, the computational domain is discretised by finite volumes (control volumes), which have a polygonal or polyhedral shape (Figure 5.5 b)). For each control volume, the conservation equations are formulated in integral form. The conservation

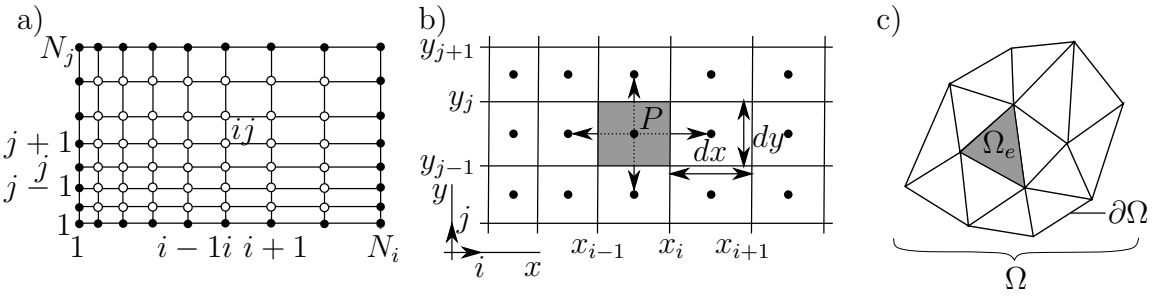

Figure 5.2: a) typical cartesian grid of the FDM for 2D, b) typical control volume and the notation for a cartesian mesh in 2D of the FVM, c) typical computational mesh for the FEM in 2D

equations are usually available directly from the corresponding continuum mechanical conservation laws. With the FVM, the conservation laws of classical physics are fulfilled, and it is comparatively intuitive to understand. In contrast, the FVM is complex to implement but precisely for higher order approaches.

FEM In the FEM, the calculation domain is divided into a finite number of sub-parts of simple shapes, such as cuboids or tetrahedra (Figure 5.5 c)). These discrete subparts are called finite elements. Their physical behaviour can be calculated with shape functions for the searched quantity. The shape functions have to fulfil problem and therefore PDE dependent continuity conditions, and the elements react to forces and boundary conditions, whereby the physical behaviour of the entire body is simulated. With the FEM, the weak form of conservation laws of classical physics are always fulfilled. The use of the weak form leads to reduced requirements for differentiability. The FEM is a powerful solution method since the solutions only have to be differentiable ones. In contrast, the FEM quickly becomes more complicated than the FDM and FVM and is additionally more complicated to implement than the FDM.

Choice of Method In this thesis the electrodeposition process is examined on a macroscopic scale concerning the coating thickness homogeneity of the foams. The unique geometry of the microheterogeneous structure of the sample is not taken into account. This non-consideration corresponds to the Darcy's law, where only the the macroscopic velocity, consequently the average over the velocities in all pore channels, is considered. Therefore, the regarded sample in the simulation has a cylindrical shape. The observation of a cylindrical sample by means of FDM is theoretically possible, however, due to the rotational symmetry of the sample, it is feasible to simulate a cross-section of the sample, consequently a rectangle. This simplifies the simulation from a 3D sample to a 2D sample. Although the modelling should be as simple as possible, it is non-trivial even in its simplest form due to the one-side coupling of convection,

diffusion, migration, and reaction. For this reason and because of its simplicity, the FDM is particularly suitable for implementation. Since a simple geometric shape of the sample is examined, the disadvantages of FDM regarding specimen geometry are negligible.

5.4 Finite Difference Method

Using the FDM for the solution calculation of the model, a sequence of operations has to be completed to discretise the continuous equation [173].

- Replacing the geometry with discrete points
- Replacing the derivatives with finite differences
- Setting up the associated linear system of equations
- Solving the linear system of equations with a suitable method
- Interpolation between the discrete points if a continuous solution is to be obtained

There are two systematic error sources in the solution of mathematical models by the FDM. On the one hand, the geometry is only described by a finite number of discrete grid points and not continuously. On the other hand, instead of the physical model equation (PDE), a discretised differential equation [173] is solved.

5.4.1 Replacing Geometry with Discrete Points

Grid

First, the domain of the body of interest Ω has to be discretised or subdivided. The finite difference uses, therefore, a so-called grid which contains nodes or points. Ω is discretised in each spatial direction and in time in uniformly spaced nodess to create this grid. For a $\Omega = [0,T] \times [0,X] \times [0,Y]$ in a two-dimensional space, each of the intervals $[0,X] \times [0,Y]$ is discretised into N_i+1 grid points in the x-direction and N_j+1 grid points in the y-direction into the grid W (Figure 5.5)

$$W = [w_{0,0},\, w_{0,1},\, \ldots,\, w_{0,x_{N_i}},\, w_{1,0},\, w_{1,1}\, \ldots, w_{i,j},\, \ldots,\, w_{N_i,N_j}]\,. \tag{5.6}$$

If the grid points are equally spaced in both directions, so $\Delta x = {}^{X}/_{N_i}$ and $\Delta y = {}^{Y}/_{N_j}$ respectively, it is called equidistant. The spatial discretisation in x- and y-direction can be executed independently. Additionally, the time in the interval $[0,T]$ is also

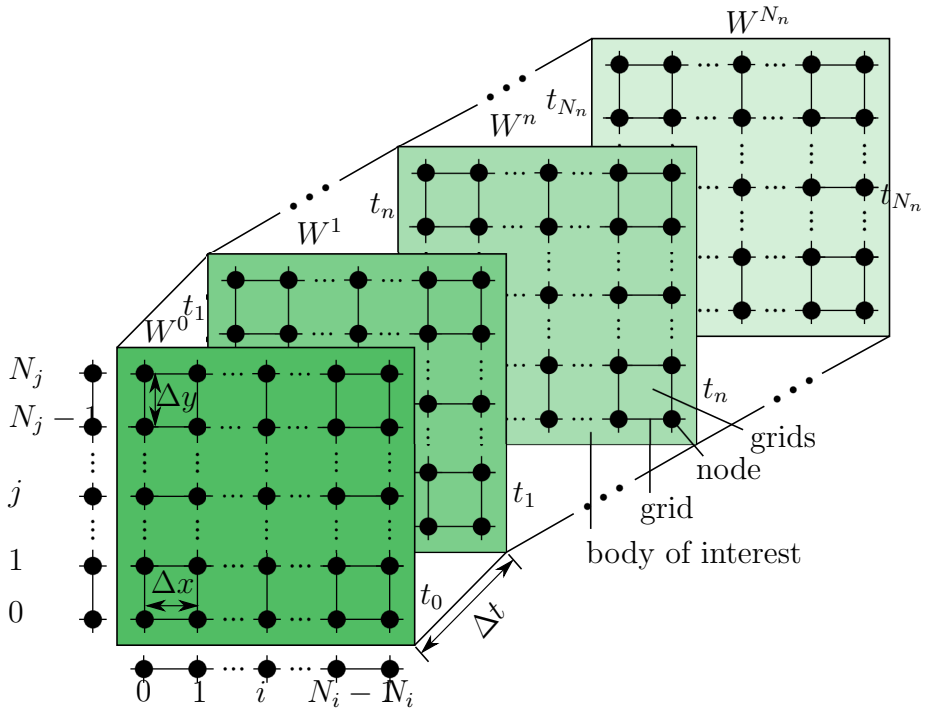

Figure 5.3: Finite difference grid for several time steps with spatial discretisation in x, y for each time step

discretised into $N_n + 1$ different grid points with the time step size $\Delta t = {}^{T}/_{N_n}$. The grid W in the range $[0, X] \times [0, Y]$ thus exists for each time step n, so that the final solution over the entire grid at each time step is given as

$$\mathbf{W} = [W^0, W^1, \ldots, W^n, \ldots, W^{N_n}]\,. \tag{5.7}$$

The numerical solution of the differential equation is an approximation of the exact solution. It is obtained using a discrete representation of the differential equation at the grid point $w_{i,j}$ in the discrete spatial grid at every time step n. The numerical solution is hence a set of countable values. With a sufficiently fine grid, i.e. small step sizes Δx, Δy and Δt, the numerical solution approximates the analytical solution of the differential equations

$$W^n \approx w(x, y, t)\,. \tag{5.8}$$

5.4.2 Discretisation

To transform the continuous differential equation into a discretisation at different grid points, the partial differential quotients have to be converted into difference quotients.

The choice of the difference quotients can be taken based on the orders of each partial derivative appearing in the PDE to be discretised and the required truncation error. The derivation of these difference quotients is carried out with the help of the Taylor series expansion.

Different Differential Quotients

These have first been derived to replace the partial derivatives with difference quotients, which is executed via the general Taylor series expansion

$$w(x) = \sum_{n=0}^{\infty} \frac{(x - x_i)^n}{n!} \left(\frac{\partial^n w}{\partial x^n} \right) \tag{5.9}$$

evaluated at the point x_i. The derivation can be found in numerous books on numerical mathematics. As an example, the used difference is shown here in the x-direction

$$\left(\frac{\partial w}{\partial x} \right) = \underbrace{\frac{w_{i+1} - w_i}{\Delta x}}_{\text{forward difference}} \underbrace{- \frac{\Delta x}{2} \left(\frac{\partial^2 w}{\partial x^2} \right) - \frac{(\Delta x)^2}{6} \left(\frac{\partial^3 w}{\partial x^3} \right) - \dots}_{\text{truncation error } \mathcal{O}(\Delta x)} \tag{5.10}$$

$$\left(\frac{\partial w}{\partial x} \right) = \underbrace{\frac{w_i - w_{i-1}}{\Delta x}}_{\text{backward difference}} \underbrace{- \frac{\Delta x}{2} \left(\frac{\partial^2 w}{\partial x^2} \right) - \frac{(\Delta x)^2}{6} \left(\frac{\partial^3 w}{\partial x^3} \right) - \dots}_{\text{truncation error } \mathcal{O}(\Delta x)} \tag{5.11}$$

$$\left(\frac{\partial w}{\partial x} \right) = \underbrace{\frac{w_{i+1} - w_{i-1}}{2\Delta x}}_{\text{central quotient}} - \underbrace{\frac{(\Delta x)^2}{6} \left(\frac{\partial^3 w}{\partial x^3} \right)}_{\text{truncation error } \mathcal{O}(\Delta x)^2} + \dots \tag{5.12}$$

$$\left(\frac{\partial^2 w}{\partial x^2} \right) = \underbrace{\frac{w_{i+1} - 2w_i + w_{i-1}}{\Delta x^2}}_{\text{central quotient}} - \underbrace{\frac{(\Delta x)^2}{6} \left(\frac{\partial^3 w}{\partial x^3} \right)}_{\text{truncation error } \mathcal{O}(\Delta x)^2} + \dots . \tag{5.13}$$

The equations (5.10), (5.11) and (5.12) show the difference schemes to describe a first-order partial quotient. Equation (5.12) is obtained by eliminating $\partial^2 w / \partial x^2$ from equations (5.10) and (5.11). The equations (5.10) and (5.11) are first-order approximations, and equation (5.12) is a second-order approximation. The equations (5.10) and (5.11) include not only the current position but also its left or right neighbour. Thus, information is transported specifically in one direction, corresponding to convection or migration transport. In equation (5.12), both neighbouring points left and right from the central point in space are considered, but not the current one. This corresponds to a symmetrical transport of information. Therefore, this type of difference quotient is not applicable to a convection term. Equation (5.13) is a second-order difference quotient (Figure 5.4). For the calculation, as with equation (5.12), its left and right

neighbour is included in addition to the current position. Here (equation (5.13)), as well as in equation (5.12), symmetrical transport takes place, including the current position. Therefore, equation (5.13) is suitable for describing the diffusion process, which is also symmetrically.

Explizit and Implizit

A distinction can be made between explicit methods on the one hand and implicit methods on the other hand, depending on the type of discretisation. In explicit methods, the new point w_{i+1} is calculated from known points such as w_i, w_{i-1}, and so on. An example of an explicit method is the forward difference quotient. In implicit methods, the point w_{i+1} is also used in the calculation rule. For this reason, systems of equations have to be solved for the calculation in implicit methods. An example of an implicit method is the backward difference quotient. On the negative side, implicit methods are usually slower, due to the calculation of the system of equations. On the positive side, they are more stable and larger time-step sizes can be chosen.

Discretisation in Time

There exists also a discretisation in time besides the already discussed discretisation in space. There can also be distinguished between implicit and explicit procedures. In explicit procedures, the variables from known points in time w^n, w^{n-1} are used to calculate the variable at the searched point in time w^{n+1}. In implicit methods, the time w^{n+1} is also used in the calculation rule. For this reason, systems of equations have also to be solved in the discretisation in time for implicit methods.

Upwind-Scheme

The discretisation methods presented are not always stable when treating hyperbolic partial differential equations such as convection problems. For this reason, the so-called upwind scheme was invented by Courant [42] in 1952. The simplest upwind scheme is called the first-order upwind scheme, consisting of the forward and backward difference quotient depending on the flow direction. The upwind scheme is implicit or explicit in space, depending on the sign of the velocity, and always explicit in time. Therefore, no system of equations has to be solved when using the upwind scheme.
Even though the forward and the backward difference quotient have a larger error than the central difference quotient, the method is more suitable due to the higher stability. The choice of the difference quotient depends on the direction in which the information is transported. As an example, the upwind scheme is explained by a linear convection

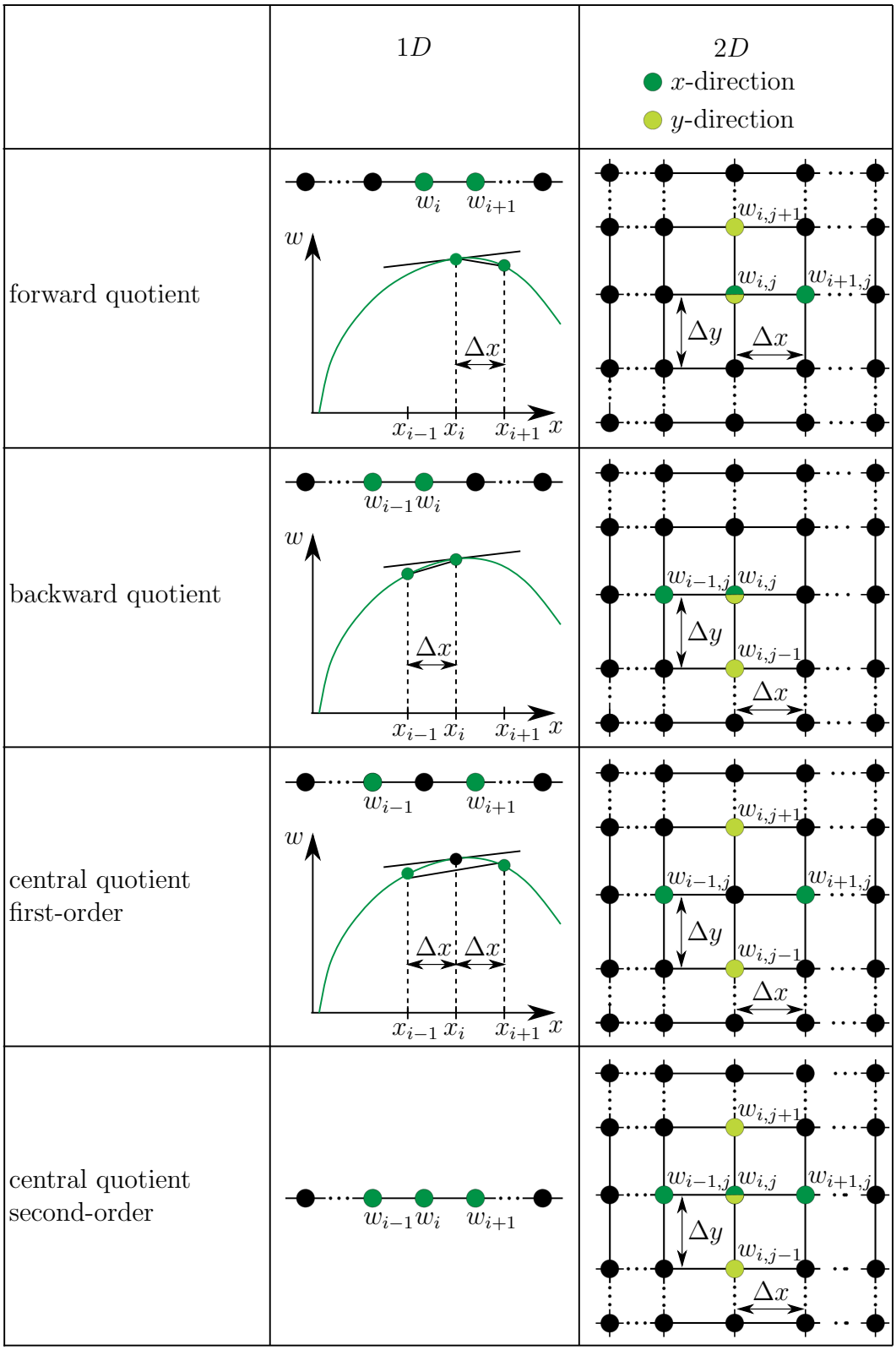

Figure 5.4: Required grid points for the discretisation for the forward, backward and central first-order difference quotient and central second-order difference quotient

equation, which describes the wave propagation in the x-direction with the velocity u

$$\frac{\partial w}{\partial t} + u\frac{\partial w}{\partial x} = 0\,. \tag{5.14}$$

The transport of information takes place in the direction of the characteristic. If u is larger than 0, the backward difference quotient is used. For example, the information of the current position and the upstream position is transported in the x-direction

$$\frac{w_i^{n+1} - w_i^n}{\Delta t} + u\frac{w_i^n - w_{i-1}^n}{\Delta x} = 0 \text{ for } u > 0\,. \tag{5.15}$$

Thus, in accordance with the principle of ion transport, the information can be transported forward by convection, which has also given the process its name. If u is less than 0, the forward difference quotient is used, i.e., the information from the current position and the downstream position is transported in the x-direction

$$\frac{w_i^{n+1} - w_i^n}{\Delta t} + u\frac{w_{i+1}^n - w_i^n}{\Delta x} = 0 \text{ for } u < 0\,. \tag{5.16}$$

Again, the information is transported in the flow direction according to the ion transport by convection. Since the convection runs in the negative x-direction, the difference quotient is called the backward quotient. The forward difference quotient, an explicit scheme, is used for the discretisation in time. Since only information from the current time step is used to calculate the new time step, it is an explicit scheme. The Upwind-Scheme discretisation can also be interpreted differently.

$$\begin{aligned} u < 0 \qquad \frac{w_{i+1}^n - w_i^n}{\Delta x} &= \frac{2w_{i+1}^n - 2w_i^n}{2\Delta x} + \frac{w_{i-1}^n}{2\Delta x} - \frac{w_{i-1}^n}{2\Delta x} \\ &= \frac{w_{i+1}^n - w_{i-1}^n}{2\Delta x} + \frac{w_{i+1}^n - 2w_i^n + w_{i-1}^n}{2\Delta x} \end{aligned} \tag{5.17}$$

$$\begin{aligned} u > 0 \qquad \frac{w_i^n - w_{i-1}^n}{\Delta x} &= \frac{2w_i^n - 2w_{i-1}^n}{2\Delta x} + \frac{w_{i+1}^n}{2\Delta x} - \frac{w_{i+1}^n}{2\Delta x} \\ &= \frac{w_{i+1}^n - w_{i-1}^n}{2\Delta x} - \frac{w_{i+1}^n - 2w_i^n + w_{i-1}^n}{2\Delta x} \end{aligned} \tag{5.18}$$

The reason for the higher stability compared to the central differences becomes clear by rewriting the equation (5.17)

$$\frac{w_{i+1}^n - w_i^n}{\Delta x} = \underbrace{\frac{w_{i+1}^n - w_{i-1}^n}{2\Delta x}}_{\text{first-order central quotient}} + \underbrace{\frac{\Delta x}{2}}_{\text{pre-factor}} \underbrace{\frac{w_{i+1}^n - 2w_i^n + w_{i-1}^n}{\Delta x^2}}_{\text{second-order central quotient}}\,. \tag{5.19}$$

A product of a discretisation dependent pre-factor and the second-order central quotient

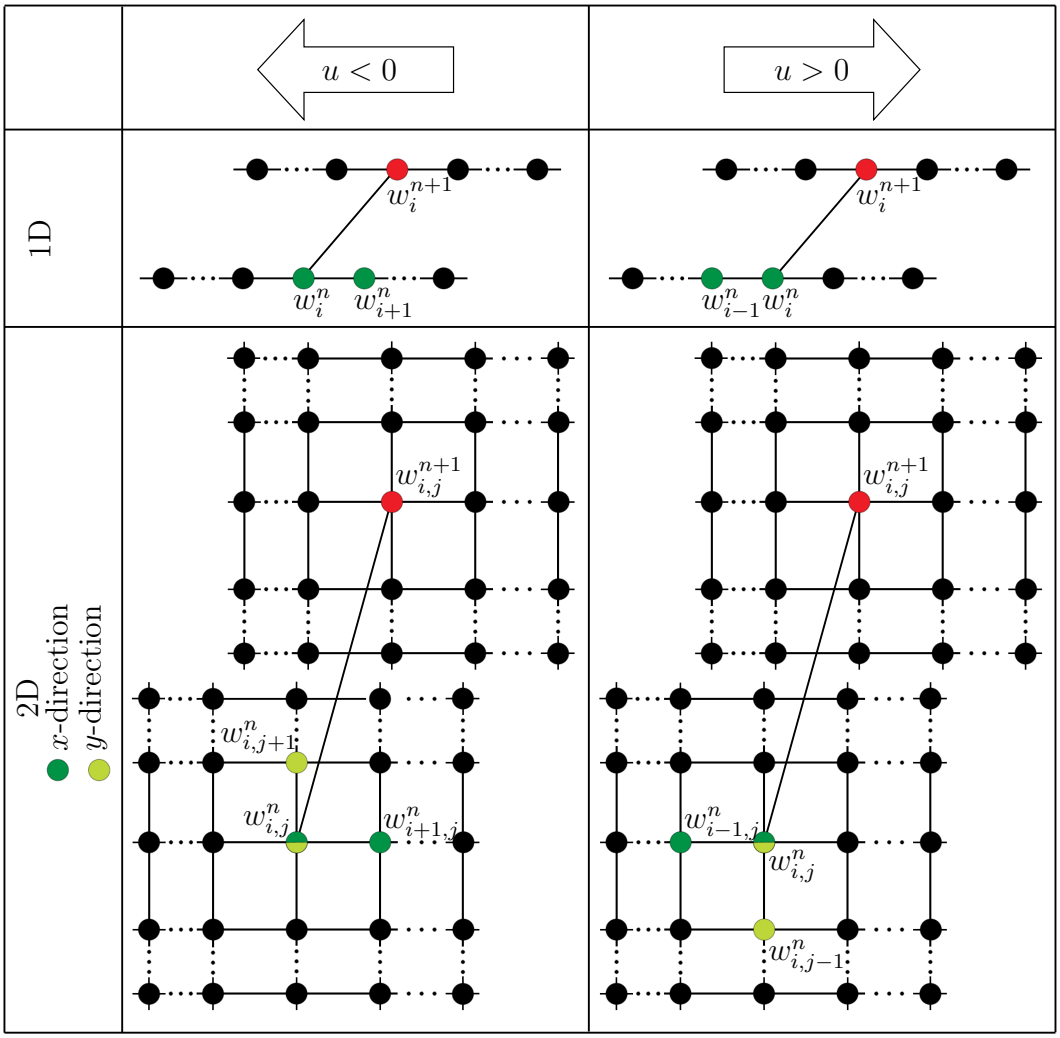

Figure 5.5: First-order upwind scheme for 1D and 2D

is added to the first-order central quotient. The pre-factor and the second-order central quotient generate an artificial diffusivity. The procedure is nevertheless consistent since the artificial diffusivity also tends to zero with $\Delta x \to 0$. The equations (5.15) and (5.16) can be combined to the compact form of the upwind scheme, which describes the case $u > 0$ and the case $u < 0$. In the x-direction

$$u\frac{\partial w}{\partial x} = u_i^n \frac{w_{i+1}^n - w_{i-1}^n}{2\Delta x} + \frac{|u_i^n|}{2}\frac{w_{i+1}^n - 2w_i^n + w_{i-1}^n}{\Delta x} \tag{5.20}$$

and in the y-direction

$$u\frac{\partial w}{\partial y} = u_j^n \frac{w_{j+1}^n - w_{j-1}^n}{2\Delta y} + \frac{|u_j^n|}{2}\frac{w_{j+1}^n - 2w_j^n + w_{j-1}^n}{\Delta y}\,. \tag{5.21}$$

The upwind scheme is conditionally stable due to the Courant-Friedrichs-Lewy condi-

tion ($\mathrm{CFL_u}$) in the x-direction

$$\left|\frac{u\Delta t}{\Delta x}\right| \leq 1 \tag{5.22}$$

and the y-direction

$$\left|\frac{u\Delta t}{\Delta y}\right| \leq 1\,, \tag{5.23}$$

which have to be fulfilled [41] by appropriate choiced for Δx, Δy and Δt. There exists a second CFL-condition ($\mathrm{CFL_D}$) concering the diffusion [41]. The diffusion with the second order central difference quotient is stable for

$$\left|\frac{D\Delta t}{\Delta x^2}\right| \leq 1 \tag{5.24}$$

and the y-direction

$$\left|\frac{D\Delta t}{\Delta y^2}\right| \leq 1\,. \tag{5.25}$$

5.4.3 Replacing the Derivatives with Finite Differences

To discretise the continuous function (5.1), the equations (5.10), (5.11), (5.12), (5.13), (5.20) and (5.21) can be used. A closer look at the equation (5.1) reveals that the components of migration have a similar character as the components of convection. For this reason, the migration is also discretised with the help of the upwind scheme, and thus a divergence of the solution caused by the migration part is prevented

$$\begin{aligned}
\frac{c_{i,j}^{n+1}-c_{i,j}^{n}}{\Delta t} &= D_{i,j}^{n}\frac{c_{i+1,j}^{n}-2c_{i,j}^{n}+c_{i-1,j}^{n}}{\Delta x^2} + D_{i,j}^{n}\frac{c_{i,j+1}^{n}-2c_{i,j}^{n}+c_{i,j-1}^{n}}{\Delta y^2} \\
&+ \left(-u_{\mathrm{X}_{i,j}}^{n} + \frac{zF}{RT}D_{i,j}^{n}\frac{\partial\Phi}{\partial x}\right)\frac{c_{i+1,j}^{n}-c_{i-1,j}^{n}}{2\Delta x} \\
&+ \frac{|-u_{\mathrm{X}_{i,j}}^{n} + \frac{zF}{RT}D_{i,j}^{n}\frac{\partial\Phi}{\partial x}|}{2}\frac{c_{i+1,j}^{n}-2c_{i,j}^{n}+c_{i-1,j}^{n}}{\Delta x} \\
&+ \left(-u_{\mathrm{Y}_{i,j}}^{n} + \frac{zF}{RT}D_{i,j}^{n}\frac{\partial\Phi}{\partial y}\right)\frac{c_{i,j+1}^{n}-c_{i,j-1}^{n}}{2\Delta y} \\
&+ \frac{|-u_{\mathrm{Y}_{i,j}}^{n} + \frac{zF}{RT}D_{i,j}^{n}\frac{\partial\Phi}{\partial y}|}{2}\frac{c_{i,j+1}^{n}-2c_{i,j}^{n}+c_{i,j-1}^{n}}{\Delta y} \\
&+ \left(-\frac{\partial u_{\mathrm{X}}^{n}}{\partial x} - \frac{\partial u_{\mathrm{Y}}^{n}}{\partial y} + \frac{zF}{RT}D_{i,j}^{n}\frac{\partial\Phi_{\mathrm{X}^2}}{\partial^2 x} + \frac{zF}{RT}D_{i,j}^{n}\frac{\partial\Phi_{\mathrm{Y}^2}}{\partial^2 y} - a_{i,j}^{n}\right)c_{i,j}^{n}\,.
\end{aligned} \tag{5.26}$$

This equation is re-sorted according to the different spatial nodes to be evaluated

$$
\begin{aligned}
\frac{c_{i,j}^{n+1}}{\Delta t} = & \\
& + c_{i,j-1}^{n} \left(\frac{D_{i,j}^{n}}{\Delta y^2} + \frac{u_{\mathrm{Y}_{i,j}}^{n}}{2\Delta y} - \frac{zF}{RT}\frac{D_{i,j}^{n}}{2\Delta y}\frac{\partial \Phi}{\partial y} + \frac{|-u_{\mathrm{Y}_{i,j}}^{n} + \frac{zF}{RT} D_{i,j}^{n}\frac{\partial \Phi}{\partial y}|}{2\Delta y} \right) \\
& + c_{i-1,j}^{n} \left(\frac{D_{i,j}^{n}}{\Delta x^2} + \frac{u_{\mathrm{X}_{i,j}}^{n}}{2\Delta x} - \frac{zF}{RT}\frac{D_{i,j}^{n}}{2\Delta x}\frac{\partial \Phi}{\partial x} + \frac{|-u_{\mathrm{X}_{i,j}}^{n} + \frac{zF}{RT} D_{i,j}^{n}\frac{\partial \Phi}{\partial x}|}{2\Delta x} \right) \\
& + c_{i+1,j}^{n} \left(\frac{D_{i,j}^{n}}{\Delta x^2} - \frac{u_{\mathrm{X}_{i,j}}^{n}}{2\Delta x} + \frac{zF}{RT}\frac{D_{i,j}^{n}}{2\Delta x}\frac{\partial \Phi}{\partial x} + \frac{|-u_{\mathrm{X}_{i,j}}^{n} + \frac{zF}{RT} D_{i,j}^{n}\frac{\partial \Phi}{\partial x}|}{2\Delta x} \right) \\
& + c_{i,j+1}^{n} \left(\frac{D_{i,j}^{n}}{\Delta y^2} - \frac{u_{\mathrm{Y}_{i,j}}^{n}}{2\Delta y} + \frac{zF}{RT}\frac{D_{i,j}^{n}}{2\Delta y}\frac{\partial \Phi}{\partial y} + \frac{|-u_{\mathrm{Y}_{i,j}}^{n} + \frac{zF}{RT} D_{i,j}^{n}\frac{\partial \Phi}{\partial y}|}{2\Delta y} \right) \\
& + c_{i,j}^{n} \left(\frac{1}{\Delta t} - \frac{2D_{i,j}^{n}}{\Delta x^2} - \frac{2D_{i,j}^{n}}{\Delta y^2} - \frac{|-u_{\mathrm{X}_{i,j}}^{n} + \frac{zF}{RT} D_{i,j}^{n}\frac{\partial \Phi}{\partial x}|}{\Delta x^2} - \frac{|-u_{\mathrm{Y}_{i,j}}^{n} + \frac{zF}{RT} D_{i,j}^{n}\frac{\partial \Phi}{\partial y}|}{\Delta y^2} \right. \\
& \qquad \left. - \frac{\partial u_{\mathrm{X}}}{\partial x} - \frac{\partial u_{\mathrm{Y}}}{\partial y} + \frac{zF}{RT} D_{i,j}^{n}\frac{\partial \Phi_{\mathrm{X}^2}}{\partial^2 x} + \frac{zF}{RT} D_{i,j}^{n}\frac{\partial \Phi_{\mathrm{Y}^2}}{\partial^2 y} - a_{i,j}^{n} \right) .
\end{aligned}
\tag{5.27}
$$

5.4.4 Boundary and Initial Conditions

Independent of whether an explicit or an implicit procedure is used, boundary and initial conditions can be used from the mathematical side to obtain a unique solution to a problem, such as solving a PDE. Additionally, they are circumstances in the application that can only be influenced with a high amount of effort or cannot be changed at all. For this reason, the boundary and initial conditions will first be discussed with regard to the numerical solution of the problem. This will be necessary for understanding the benchmark tests. This general view is followed by the interpretation and the physical meaning of boundary and initial conditions.

General Information

Different boundary conditions or initial conditions can be applied depending on the experiment's setting. Only by setting the boundary conditions a well-posed problem can be obtained. According to Hadamard [68], a well-posed problem must have a solution (existence). This solution has to be unique (uniqueness) and has to depend continuously on the input data (stability). In literature, a distinction is made between different boundary conditions and initial conditions depending on the transport direction. For

boundary conditions, only the nodes at the edge of the grid are considered. For initial conditions, only the nodes in the first time step are considered. Two types of boundary conditions and the initial condition are briefly presented here.

- boundary conditions
  - Dirichlet condition
    The Dirichlet condition gives a real number as a solution at the edge of the grid to the known function $f(x, y, t)$ of the problem

$$w(x, y, t) = f(x, y, t) \quad \forall (x, y, t) \text{ in } \partial\Omega\,. \tag{5.28}$$

  - Neumann condition
    The Neumann condition gives a real number $f^n_{i,j}$ as values of the first derivative of the solution $w^n_{i,j}$ of the problem at the edge of the grid

$$\frac{\partial w(x, y, t)}{\partial n} = f(x, y, t) \quad \forall (x, y, t) \text{ in } \partial\Omega\,, \tag{5.29}$$

    where n is the unit normal to the boundary surface, i.e. the normal component of the associated flux.
- initial condition
  The initial condition gives the real number $f(x, y, 0)$ as the solution to the unknown function $w(x, y, 0)$ of the problem at the beginning of the process at time $t = 0$, consequently the initial time step

$$w(x, y, 0) = f(x, y, 0) \tag{5.30}$$

Interpretation Concerning the Experimental Setup

The foam to be coated is placed in a flow cell (Figure 3.5 and 5.6), following the application of the electrodeposition process with the setup presented in **chapter 3**. Only the 2D problem is considered, due to the homogeneity of the flow velocity and the experimental setup (Figure 3.5). The experiment starts when the current is switched on. So, at the beginning of the experiment, no ions have been consumed, and the concentration in the entire bulk electrolyte is c_0. Consequently, the experimental setup's initial condition equals the value c_0. During the experiment, ions are consumed within the foam. Here, it is the task of the model to predict the ion concentration. In contrast, factual statements can be made on the outer foam surface. Edge 1 is permanently in contact with the electrolyte flowing in the cell. A concentration on edge 1 is assumed which corresponds to the concentration c_0, assuming an infinitely high ion reservoir in the

electrolyte outside the specimen, represented by the Ni pellets used in the experiment. Although edges 2 and 3 are at the boundary edges of the flow cell, a small gap is unavoidable in the experimental setup. As a result, the electrolyte also flows behind these edges. The initial concentration c_0 is also assumed as a boundary condition, assuming only marginal ion consumption in relation to the electrolyte flowing behind. There is another layer of Ni pellets behind the foam to avoid a too low ion concentration just at the edge 4 and thus at the end of the foam. This counteracts a depletion of the electrolyte. Therefore, the boundary condition can also be assumed to be c_0 at this edge. In sum, a constant ion concentration of c_0 is assumed as the initial condition as well as the boundary conditions at edge 1, 2, 3 and 4, which equals the concentration of the bulk electrolyte.

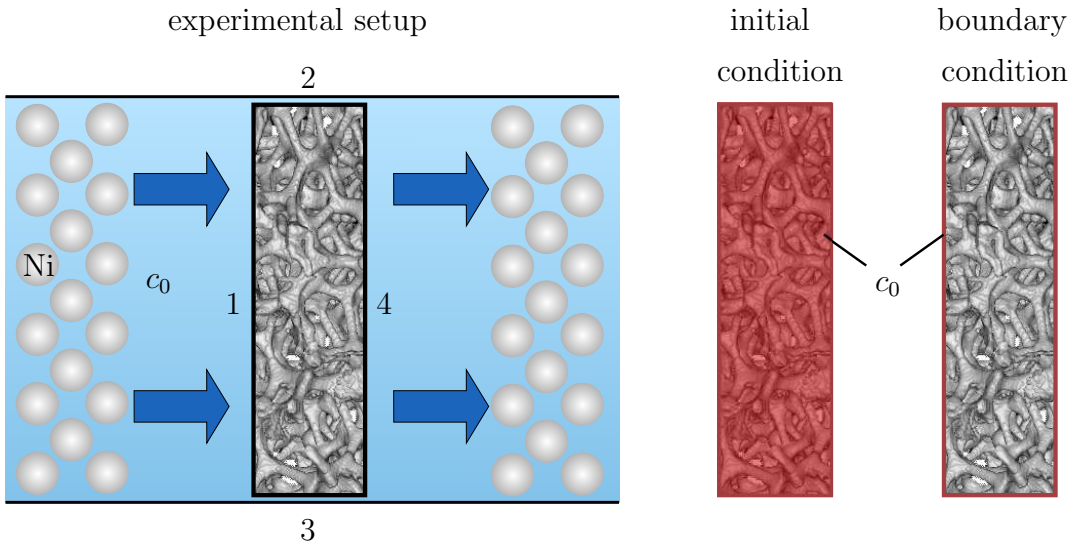

Figure 5.6: Experimental setup, cut through the cylindrical setup, analogue Figure 3.5, and the resulting initial and boundary conditions

5.4.5 Initial Problem and Boundary Value Problem

A distinction is made between an initial problem and a boundary value problem, depending on the type of the given boundary values. In an initial problem, an initial condition is given. An explicit procedure is appropriate for the solution with this type of problem, since all further values can be calculated in a simple manner from the given first value. In a boundary value problem, the values at the boundary are given as boundary conditions and the values in the middle have to be calculated. An implicit method is appropriate in this type of problem, since a system of equations has to be solved anyway due to the predefined boundary values. The problem considered in this paper is an initial value problem in time. Consequently, no system of equations has to be solved.

6

Validation of the Ion Flux Code

Before the code developed in the previous chapters can be used, it has to be checked for correctness and accuracy. This procedure is called validation. It is by definition of the IEEE Standard Glossary of Software Engineering Terminology, the "process of evaluating a system or component during or at the end of the development process to determine whether it satisfies specified requirements" [2]. The code developed is validated with regard to all four included ion movement parts: convection, diffusion, migration, and reaction.

6.1 Benchmark Tests

Due to the impossibility of solving equation (4.9), it is not possible to validate all the included parts in combination with each other. So, the convection, diffusion, migration, and reaction part is validated separately and checked for accuracy with analytical solutions. The type of analytical solution varies for all four parts, as does the manner of verification. The validation of a numerical solution using an initial value problem of an already known analytical solution is called a benchmark test. Benchmark tests are used to examine the numerical solution of the developed code against an analytical solution in terms of qualitative and quantitative differences.

6.1.1 Diffusion

Diffusion is essential in various fields, such as heat or mass transport. For this reason, several analytical solutions start from different given initial conditions. The Benchmark

test with the Dirac delta function δ at $x = x_0$ and $y = y_0$ with a real constant M is usually used as the initial condition

$$f(x, y, t = 0) = M\delta(y - y_0)\delta(x - x_0) \tag{6.1}$$

which results in the analytical solution with the diffusion constant D as

$$f(x, y, t) = \frac{M}{\sqrt{(4\pi Dt)}} e^{-\frac{x^2+y^2}{4Dt}} . \tag{6.2}$$

The Dirac delta function assumes an infinitely high value at $t = 0$. The infinitely high value is not feasible in the numerical implementation. For this reason, another initial condition was chosen at this point, namely a cosine function

$$f(x, y, t = 0) = \cos(x)\cos(y) , \tag{6.3}$$

which results in the solution

$$f(x, y, t) = \exp(-2Dt)\cos(x)\cos(y) , \tag{6.4}$$

with the diffusion constant D. The initial condition was set on the domain $\Omega = [0, 1] \times [0, 1]$ and a spatial discretisation of $\Delta x = 0.001\,\text{m}$ as well as $\Delta y = 0.001\,\text{m}$ was chosen. Neumann boundary conditions were applied at all the edges. The numerical results of the simulation and the analytical results were compared (Figure 6.1) after $t = 10\,\text{s}$. At first glance, the result from simulation and analytical solutions agree quantitatively and qualitatively. For a better comparison between the simulation and analytical results of

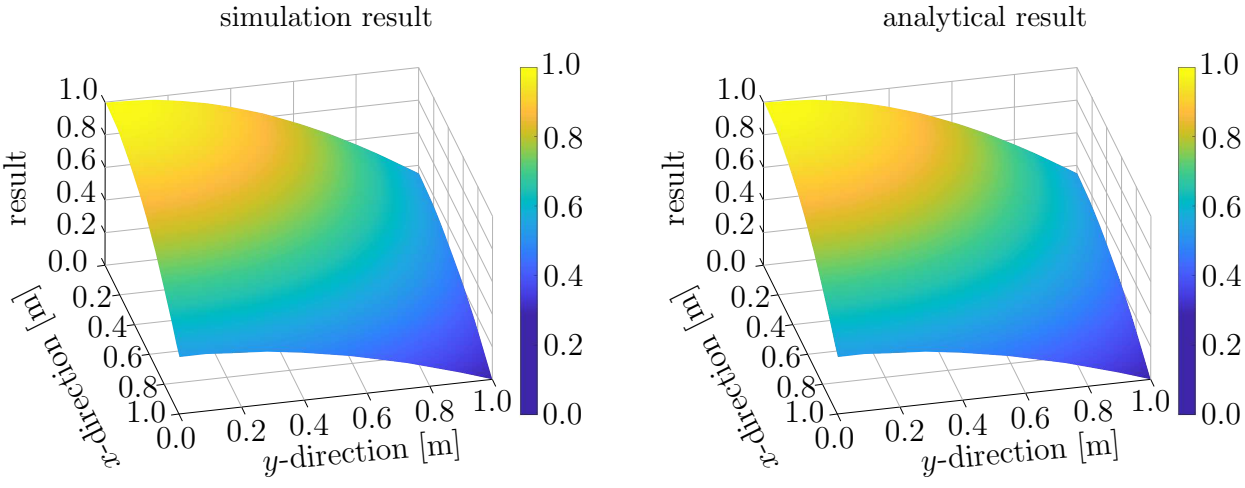

Figure 6.1: Result of the test function after $t = 10\,\text{s}$ for $\Delta t = 0.001\,\text{s}$, $\Delta x = 0.001\,\text{m}$ and $\Delta y = 0.001\,\text{m}$

Figure 6.1, the error is shown in Figure 6.2. The error is the result of the numerical simulation subtracted from the result of the analytical solution. The maximum error, the minimum error and the mean error over all grid points were plotted for different time steps and spatial discretisations of Δx and Δy. The time step size was varied ($\Delta t = [0.0001\,\text{s}, 0.001\,\text{s}, 0.01\,\text{s}, 0.1\,\text{s}, 0.25\,\text{s}, 0.5\,\text{s}, 0.75\,\text{s}, 1\,\text{s}]$) while the spatial discretisation was kept constant at $\Delta x = \Delta y = 0.01\,\text{m}$ (Figure 6.2). The error is plotted quantitatively for the different spatial discretisations (Figure 6.2 top-left), and the error is also plotted qualitatively (Figure 6.2 bottom-left). The time step size refinement is accompanied by a maximum and an average error reduction. The deviation of the minimum values, on the other hand, increases with a refinement of the time step size. This deviation is caused by a slightly shifted curve that occurs when the time steps are refined. In

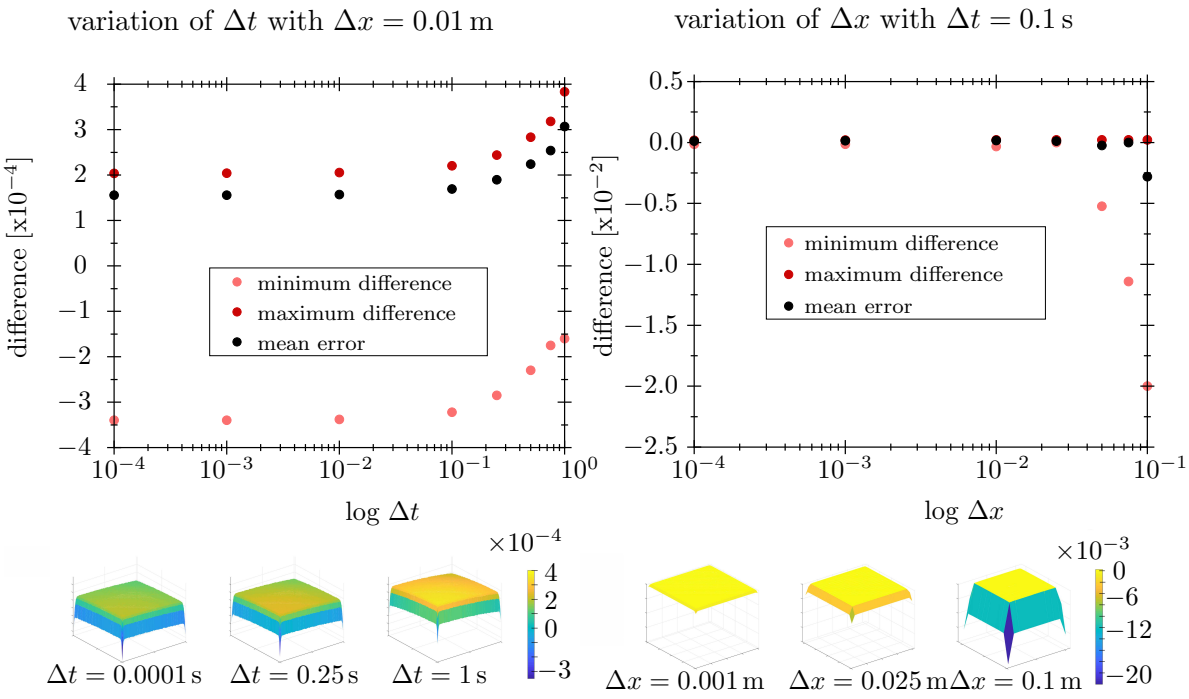

Figure 6.2: Minimum, maximum and mean error of the benchmark test for different spatial discretisations and time step sizes, quantitative and qualitative, Δt in s, Δx in m

addition to the variation of the time step size, the spatial discretisation is varied for fixed $\Delta t = 0.1\,\text{s}$ ($\Delta x = [0.0001\,\text{m}, 0.001\,\text{m}, 0.01\,\text{m}, 0.025\,\text{m}, 0.05\,\text{m}, 0.075\,\text{m}, 0.1\,\text{m}]$) (Figre 6.2 right). Varying the discretisation, all errors, i.e., the difference of the maximum values, the difference of the minimum values as well as the mean difference over all values, decrease with a refinement of the spatial step size (Figure 6.2 right).

6.1.2 Convection

In comparison to the validation of diffusion, convection verification is much simpler. The convection can be rewritten as

$$u_x = \frac{x}{t} \tag{6.5}$$

through the "Method of Characteristics". The two easy-to-define parameters position x and time t are connected by the velocity u_x to be set. A region $\Omega = [0,1] \times [0,1]$ is considered with Neumann boundary conditions. An initial value of $z = 100\,\mathrm{g/l}$ is set in the domain zero, and this initial value point moves with a velocity of $u_x = 0.1\,\mathrm{m/s}$ in the positive x-direction. The value $z = 100\,\mathrm{g/l}$ was chosen because it approximately corresponds to the initial condition of $c = 110\,\mathrm{g/l}$ in the simulation of the electrodeposition process. This peak has to take a time of $t = 5\,\mathrm{s}$ to travel the distance $x = 0.5\,\mathrm{m}$ from the centre to the edge. The shape and the maximum values of the transported profile should stay constant. The profile is shown in Figure 6.3. In the upper left image, the initial value at $t = 0\,\mathrm{s}$ of $z = 100\,\mathrm{g/l}$ can be seen in the centre of the domain. In the lower left figure, the same time step is shown in the top view and on the bottom in the form of a cut across the centre of the domain. The figure shows, from left to right, the

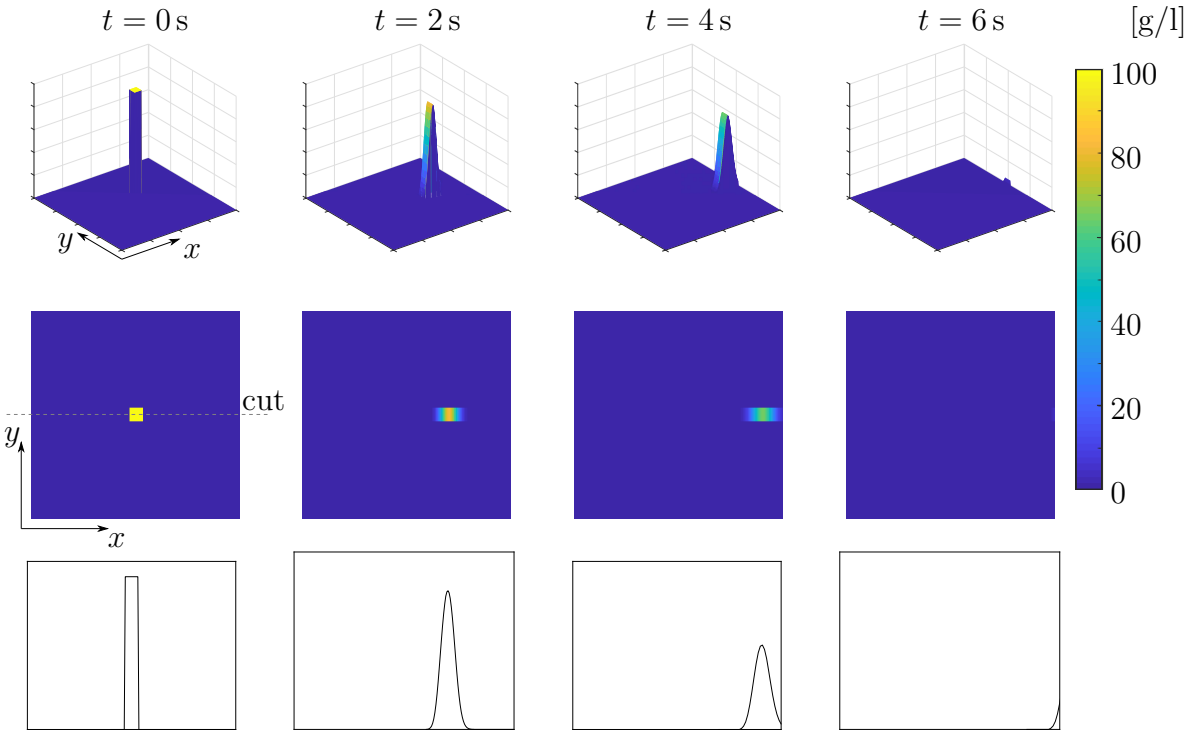

Figure 6.3: Appearance and location of the peak for different time steps, top: 3D view, middle: top view, bottom: cut through the top view

development of the solution during time. The point moves according to the direction

of the velocity in positive x-direction and is hardly visible at time $t = 6\,\mathrm{s}$ because it leaves the domain. However, in addition to the position of the peak, the height and size of the peak change. This change comes from the implementation of the convection part with the upwind scheme, which adds a virtual diffusivity. This virtual diffusivity blurs the clear edge in the velocity direction, which reduces the peak's height. The area under the curve keeps constant. Δx and Δt are varied to check the diffusivity dependence with the time step size. The parameter Δt varies between the values $[0.001\,\mathrm{s}, 0.002\,\mathrm{s}, 0.005\,\mathrm{s}, 0.01\,\mathrm{s}, 0.02\,\mathrm{s}, 0.05\,\mathrm{s}, 0.1\,\mathrm{s}, 0.2\,\mathrm{s}, 0.5\,\mathrm{s}]$ and the parameter Δx varies between the values $[0.001\,\mathrm{m}, 0.002\,\mathrm{m}, 0.005\,\mathrm{m}, 0.01\,\mathrm{m}, 0.02\,\mathrm{m}, 0.05\,\mathrm{m}, 0.1\,\mathrm{m}]$.
The upwind scheme is stable only for a CFL value ≤ 1. For this reason, the CFL value for a velocity of $u_x = 0.1\,\mathrm{m/s}$ is listed for the different values of Δt and Δx in Table 6.1. The parameter study is evaluated only for the values marked in green for a CFL value ≤ 1. The results of this parameter study are shown in Figure 6.4. The figure shows

Table 6.1: CFL values for different time steps and space increments for a velocity of $u_x = 0.1\,\mathrm{m/s}$

$u = 0.1\,\mathrm{m/s}$		Δt [s]								
		0.5	0.2	0.1	0.05	0.02	0.01	0.005	0.002	0.001
Δx [m]	0.1	0.5	0.2	0.1	0.05	0.02	0.01	0.005	0.002	0.001
	0.05	1	0.4	0.2	0.1	0.04	0.02	0.01	0.004	0.002
	0.02	2.5	1	0.5	0.25	0.1	0.05	0.025	0.01	0.005
	0.01	5	2	1	0.5	0.2	0.1	0.05	0.02	0.01
	0.005	10	4	2	1	0.4	0.2	0.1	0.04	0.02
	0.002	25	10	5	2.5	1	0.5	0.25	0.1	0.05
	0.001	50	20	10	5	2	1	0.5	0.2	0.1

how the peak has changed after time $t = 1\,\mathrm{s}$. The initial condition is identical with the initial condition of Figure 6.3 and the velocity equals still $u_x = 0.1\,\mathrm{m/s}$. As expected, the accuracy of the solution increases when the spatial discretisation is refined. The diffusivity, the widening of the profile, increases with the time step size, and the value of the peak decreases as the time step size is refined. For the CFL value of 1, the peak value is conserved in each case, and the diffusivity goes to zero. However, in general, no prediction about the accuracy of the numerical solution can be made via the CFL value. The CFL value is only used to check the stability of the method. Additionally, in Figure 6.5, the time needed to transport the peak can be seen. The peak at time $t = 5$ is just at the expected location of $x = 1$ for all simulations.
The trend of the convection was also checked in negative x-direction (u_x =-0.1) as well as in positive and negative y-direction ($u_y = 0.1$ and $u_y = -0.1$). The results agree with the results in the positive x-direction and can be found in the appendix. In addition, the results were checked by coupling the velocity in x- and y-direction with

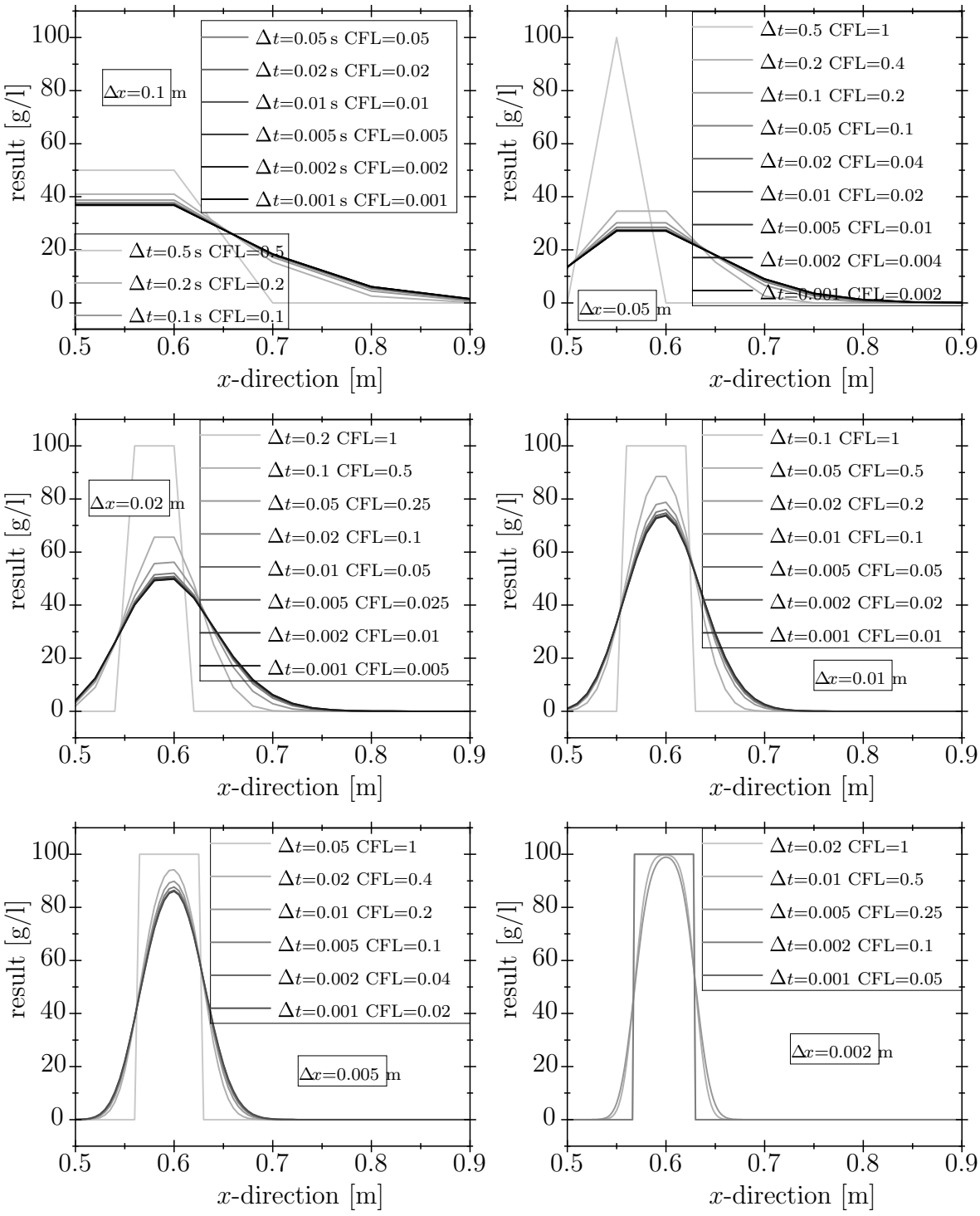

Figure 6.4: Trend of the profile for different discretisation sizes of Δx and Δt and the corresponding different CFL values for a velocity of $u_x = 0.1\,\mathrm{m/s}$ after a duration of $t = 1\,\mathrm{s}$, with the initial profile of Figure 6.3 bottom left

all possible combinations of positive and negative x- and y-directions. These also agree totally with the previous results and can be found in the appendix to complete the presented results. Likewise, the areas under the profiles match in each case.

6.1.3 Migration

As explained in the previous chapter, the appearance of the migration part with respect to variable c is analogous to the appearance of variable c in the convection part. For this reason, the product $(^{zF}/_{RT} D \operatorname{grad} \Phi)$ can be replaced by a fictitious velocity u. To verify the code, the parameters z, F, R, T, D and $\operatorname{grad} \Phi$ were chosen to be equivalent to the velocity, giving $u = 0.1\,{}^{\mathrm{m}}/_{\mathrm{s}}$. Thus, migration results can be directly checked with the results of convection. They agree one-to-one with the convection results, therefore, they are not explicitly shown here. The results can be found in the appendix.

6.1.4 Reaction

A distinction between a source and a sink term can be made for the reaction term. In a source term, ions are produced; in a sink term, the ions are consumed. Only a sink

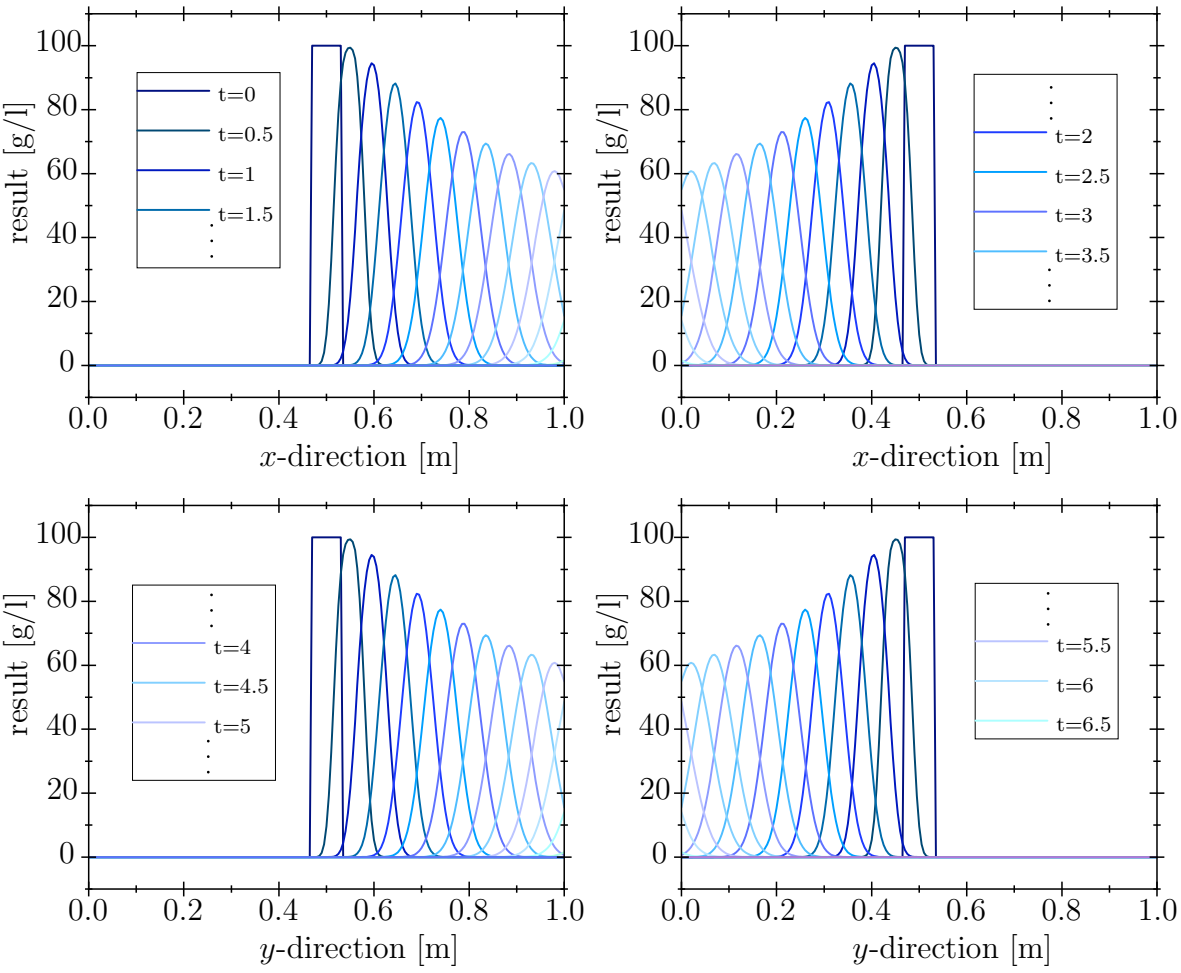

Figure 6.5: Profile of the peak at different times, top in x-direction, bottom in y-direction, left with an velocity >0, right with an velocity <0, all four legends belong together and describe all four figures, t in [s]

part is considered in the model presented in this thesis. The implementation of the linear sink part is validated in the following.

Sink Term

A closer look at its implementation is needed to validate the accuracy of the sink term. A reduction of equation (5.27) concerning the sink term results in

$$c_{ij}^{n+1} = c_{ij}^{n} \left(1 - a\Delta t\right) . \tag{6.6}$$

If this equation is executed m times with a constant time step Δt, it results in

$$c_{ij}^{n+m} = c_{ij}^{n} \left(1 - a\Delta t\right)^{m} . \tag{6.7}$$

This equation is based on the equation of exponential decay. The sink constant a can be interpreted as a fractional decrease of the initial value. If the parameter a is multiplied by 100%, one obtains the percentage decrease a^* of the initial value

$$a^* = a100\% . \tag{6.8}$$

For the sink term verification, a peak of size $100\,\mathrm{g/l}$ was set as the initial condition in the middle of the domain $\Omega = [0,1] \times [0,1]$. The peak height was measured for different time step sizes with a spatial discretisation of $\Delta x = \Delta y = 0.01\,\mathrm{m}$. In Figure 6.6, top-left, the peak maximum profile is plotted for a time duration of $t = 100$. At first glance, the numerical and analytical solutions match each other (Figure 6.6 top-left). For this reason, in Figure 6.6 top-right, the difference between analytical and numerical solution is plotted in % with respect to the analytical solution. The error increases with time and as the time step size is refined. Here, the error runs into an equilibrium state and remains below 0.8 % for $t = 100$. The increase of the error when the time step size is refined can be explained by the increase in calculation steps. For a time step size of $\Delta t = 1$, significantly fewer computational steps have to be performed to reach the final time of 100 than for the time step size $\Delta t = 0.001$. This shows equation (6.7). If Δt becomes smaller, m becomes larger to reach a desired time t. Therefore, more data savings have to be made and as there is a small error with each saving, the error increases at the same time as the Δt becomes smaller [43]. Figure 6.6 bottom also shows the top view of the peak at different time steps. As expected, there is no diffusivity as seen for the convection.

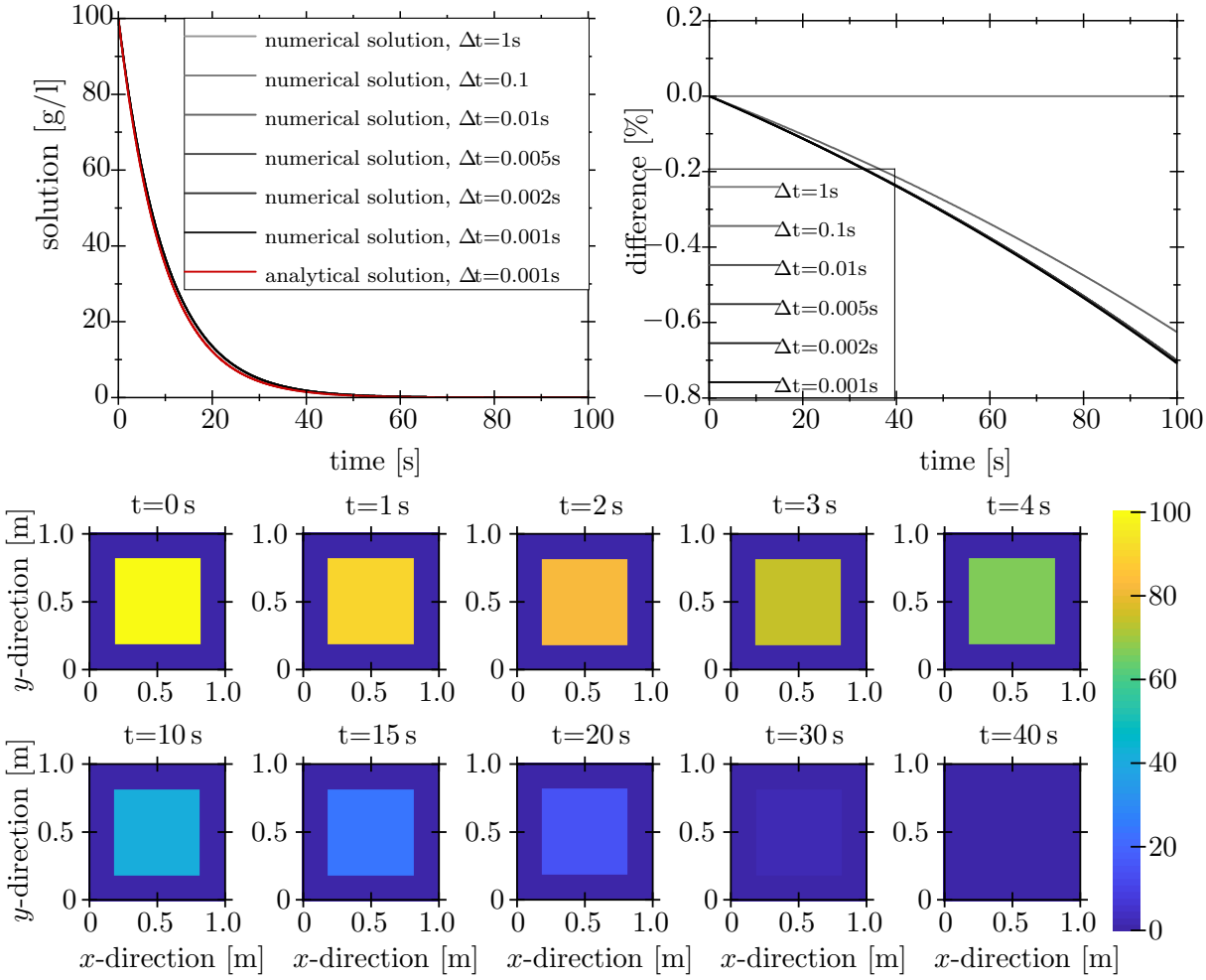

Figure 6.6: Change of the concentration profile over time with a sink constant of $a = 0.1$.

6.2 Conclusion

After checking all four model parts with regard to their correctness and error, conclusions can be made regarding the parameters which have to be chosen. These parameters are time step size, spatial discretisation and CFL value. For diffusion, the spatial discretisation size chosen should be as small as possible and the time step size as large as possible. This result is in partial agreement with the result for the convection. For the convection, the time step size should also be kept as large as possible regarding the CFL, but a sufficiently fine spatial step size has to be chosen to increase the accuracy of the results. The results for migration correspond to the results of the convection. For the reaction, only the time step size influences the accuracy. The time step size chosen has to be as large as possible, and in general, the calculating time interval has to be as small as possible. This influences the choice of the parameters in the following. For a given velocity, both the value for the time step size and the value for the spatial step size can be varied for the choice of the CFL value ≤ 1. Here it is necessary to try

to set the CFL value at 1, the time step size as large as possible, and keep the spatial step size as small as possible.

7

Coating Thickness Influence on the Geometry Parameters

The electrodeposition process is a fully coupled problem, as shown in Figure 4.4. The coating of the foam causes a change in geometry parameters, which in return influences the model components convection, migration, and reaction. Thus, the inner surface influences the current density and, consequently, the sink constant and the electric potential. The relative volume change has an influence on the sink constant and consequently the sink term, and the porosity has an influence on the permeability and hence on the velocity. Therefore, the influence of the coating thickness on these different geometry parameters has to be examined. Additionally, an RVE is determined in this chapter to be able to describe the stochastic structure of the foams with less computational effort.

7.1 Influence of the Coating Thickness on Several Geometry Parameters

Determining the specific surface area and volume of foams using conventional methods is complex due to the microheterogeneous structure. In addition, these parameters also have to be examined in relation to the coating thickness. This coating thickness variation would result in producing foams with different coating thicknesses for each pore size, consequently in lots of foams which have to be produced. Additionally, an analysis of the geometry has to be performed. Since this procedure is very time-,

cost- and resource-intensive, computer tomography (CT) data is used in this study. The further processing of the CT data is executed with the help of the open-source program Fiji [143].

7.1.1 Geometry Analysis using Fiji

CT data (Frauenhofer IZFP Saarbrücken) is used to evaluate the specific surface area and the specific bulk volume as a function of the coating thickness and to determine the RVE. After converting the CT data into a .tiff-format, the data can be post-processed. This post-processing can involve a virtual coating, virtual cutting into smaller cubes and virtual measuring of the specific surface area and the specific bulk volume. The post-processing is executed with the help of the open-source program Fiji. Fiji is the acronym for (=**F**iji **i**s **j**ust **i**mageJ). It was originally evolved from ImageJ, an image processing and editing program used for medical and scientific image analysis. ImageJ was extended by many plugins to combine many tools for analysing images of biological samples in one single software [143, 145] for the development of Fiji. Fiji is an open-source program under the GNU General Public Licence. Thus, everyone can contribute with plugins, tutorials, and patches.
The foams are cut into smaller cubes using the "Crop 3D" function from the "Stacks" plugin in order to determine the RVE with Fiji. The MorpholibJ plugin [107] is used to determine the specific surface area and the specific bulk volume of the foams. Using the "Analyze Regions 3D" function of the same plugin, both the specific surface area and the specific bulk volume can be determined. The MorpholibJ plugin [107] is also used for the virtual coating of the foams. The foams can be virtually coated or virtually eroded using the "Dilation" or "Erosion" operation using the Morphological Filters (3D) function. Different element shapes with different radii in x, y and z directions can be selected for this virtual coating. The "Ball" setting with a voxel radius of 1 in all three spatial directions was used for the dilated element shape for the results considered in this work. A voxel is equivalent in 3D computer graphics to a pixel in a 2D bitmap. The virtual coating process was repeated voxel by voxel until the foam reached the desired virtual coating thickness. The RVEs have to be determined first for the geometric quantities of interest, namely the specific surface area and the specific bulk volume. This procedure ensures, that the selected digitised samples are large enough to reflect the geometry parameters correctly.

7.1.2 RVE

The RVE was defined for the first time, in a mechanical context, by Hill [70]. There, the RVE is defined as "structurally entirely typical of the whole mixture on average,

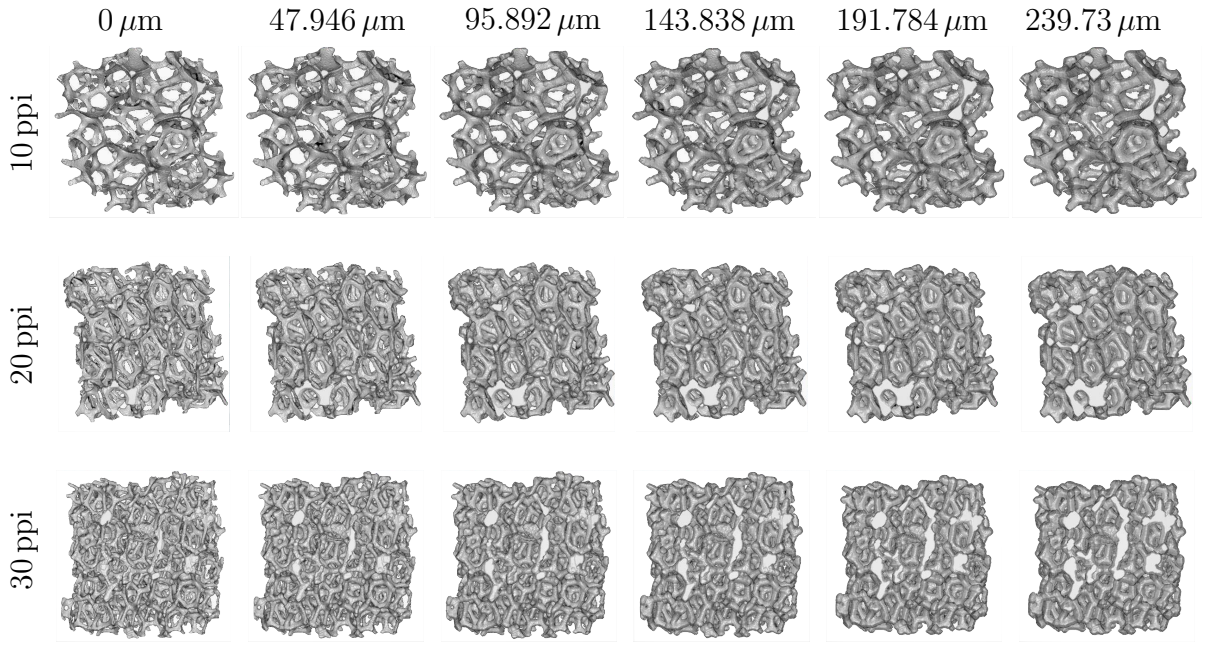

Figure 7.1: Appearance of foams of different pore sizes with different coating thicknesses, each foam has a size of approx. $16 \times 16 \times 16\,\mathrm{mm}^3$

and contains a sufficient number of inclusions for the apparent overall moduli to be effectively independent of the surface values of traction and displacement, so long as these values are 'macroscopically uniform'". A newer definition by Drugen et al. [47] is used, since the RVE in this thesis does not deal with the mechanical properties. There, the RVE is defined as "the smallest material volume element of the composite for which the usual spatially constant 'overall modulus' macroscopic constitutive representation is a sufficiently accurate model to represent mean constitutive response". In summary: The smallest volume from which the value of a special parameter no longer changes corresponds to the RVE of this parameter. The geometric properties of the entire sample can be determined based on the results of the sample in the size of the RVE. The RVE can differ for different properties. The CT image of Al foams (Frauenhofer IZFP Saarbrücken, resolution of 23.973658 μm) is virtually cut into different-sized cubes of edge lengths ranging from 0.48 mm to 6.89 mm to determine the RVE regarding inner surface area and bulk volume. No part of the foams is used twice for each edge length. The geometry parameters of specific surface area and specific bulk volume are determined for each cube edge length. Scattering in the values for the specific surface area and the specific bulk volume occurs for edge lengths smaller than the edge length of the RVE. For edge lengths larger than or equal to the RVE, the specific surface area and bulk volume values equal one single value, respectively. The smallest edge length without a value scattering corresponds to the RVE. The edge length of the cut cube pieces varies for the different pore sizes (Figure 7.2). For foams of pore size 10 ppi, the edge length is between 0.96 mm and 6.89 mm, for foams of pore size 20 ppi between

0.48 mm to 6.89 mm and for foams of edge length 30 ppi between 0.48 mm and 5.75 mm (Figure 7.2). This is because the RVE for the 10 ppi foams is in any case larger than the RVE for the 20 ppi and 30 ppi foams. Figure 7.3 a) shows the specific bulk volume

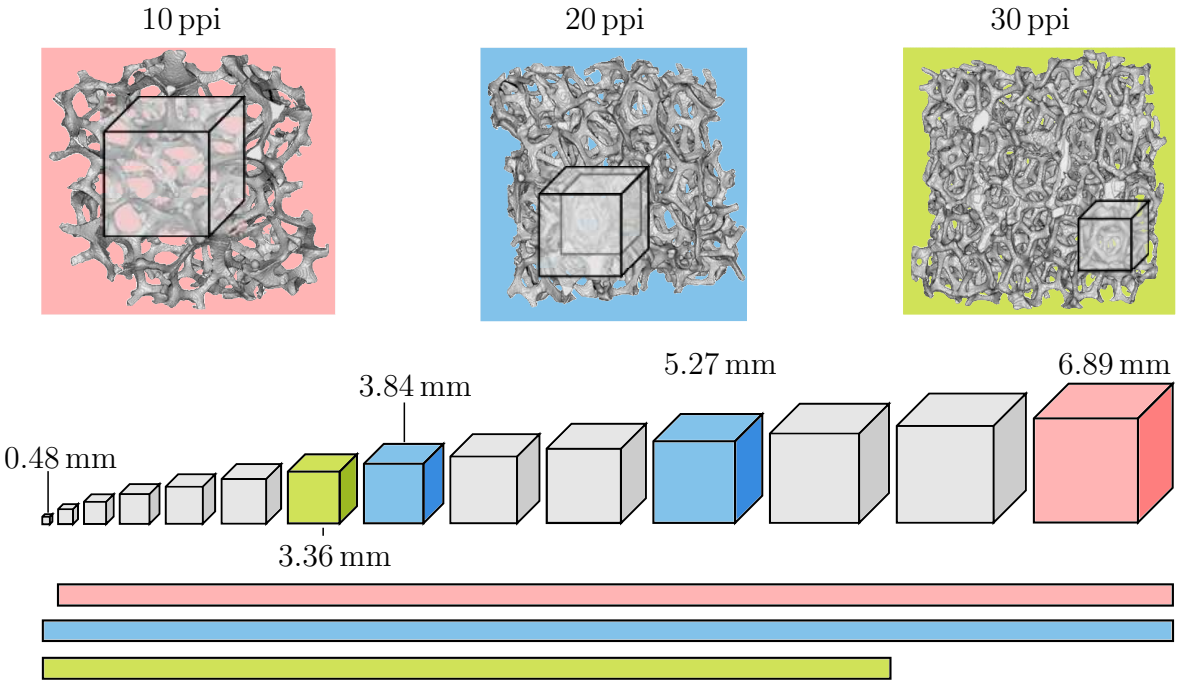

Figure 7.2: Different edge sizes for foams with different ppi numbers for the evaluation of the RVE; the size of the RVE of the specific surface area and the specific volume are coloured, the RVE of the inner surface and the RVE of the inner bulk volume differ for the 20 ppi foam

for different edge lengths of the cut cubes for the different pore sizes 10 ppi, 20 ppi and 30 ppi. The specific bulk volume was normalised by the total volume of the cubes for better comparability. Three different foams were evaluated for each pore size. The scatter of the specific bulk volume values decreases as edge length increases. The value zero is reached more often for smaller edge lengths. This phenomenon is due to the size of the foam cubes in relation to the total foam and individual pores. The cube size is completely inside a pore. For a 30 ppi foam, the value 1 is reached more often. This is due to the randomly chosen cubes, which are almost entirely within a node or strut. For a clearer view, Figure 7.3 b) first shows the region of an edge length larger than two. Here, the different values for the specific bulk volume of the different pore sizes can be seen better, and the scattering of the values of the individual pore sizes to each other is clearly visible. Thus, the RVE for the 10 ppi foams can be determined on a cube of an edge length of 6.89 mm, the RVE for 20 ppi foams is a cube of an edge length of 5.27 mm and the RVE for 30 ppi foams is a cube of an edge length of 3.36 mm. As the pore size increases, so does the size of the RVE. This fact could be predicted from Figure 7.2.

a) for all edge lengths

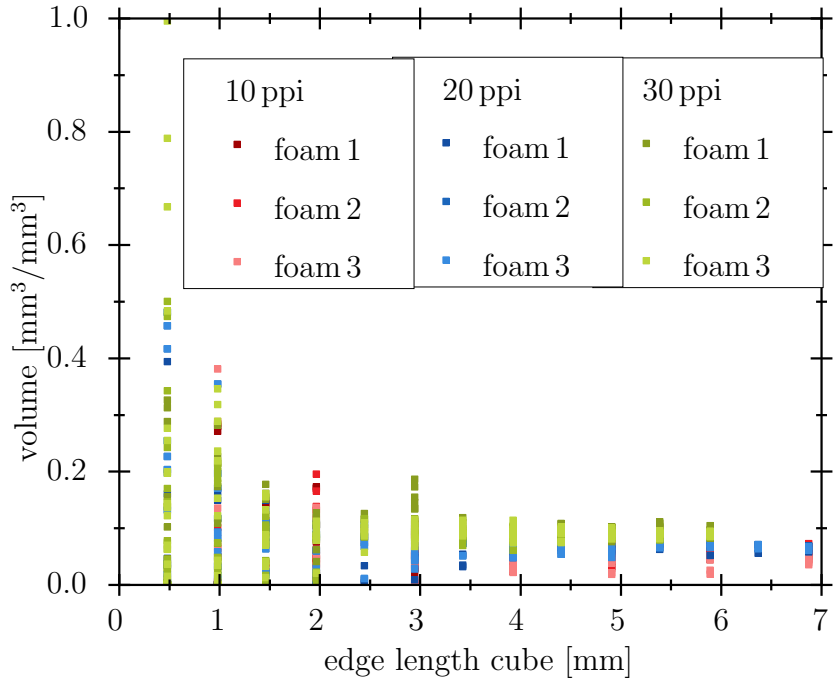

b) for all edge lengths larger than 2 mm

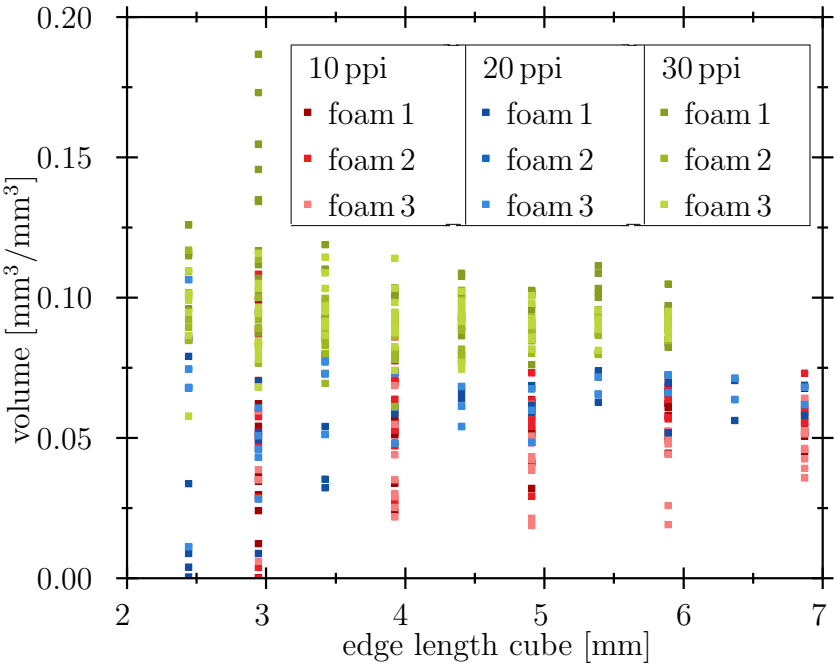

Figure 7.3: Specific bulk volume of the foams with the pore sizes 10 ppi, 20 ppi and 30 ppi for different cube edge lengths for RVE determination

Figure 7.4 a) shows the specific inner surface for different edge lengths of the cut-out cubes for the different pore sizes 10 ppi, 20 ppi and 30 ppi. The specific surface area was normalised to the cubes' total volume, and three different foams for each pore size were examined as with the specific bulk volume. The scattering of the values for the inner surface decreases with an increasing edge length (Figure 7.4). Figure 7.4 b) shows the scattering for edge lengths larger than one for a clearer representation.
Thus, the RVE for the 10 ppi foams can be determined to be a cube of an edge length of 6.89 mm, the RVE for 20 ppi foams is a cube of an edge length of 3.84 mm, and the RVE for a 30 ppi foam is a cube of an edge length of 3.36 mm. As the foams' pore size increases, so does the size of the RVE, similar to the RVE of the specific bulk volume. The RVE of the specific bulk volume also corresponds to the RVE of the inner surface for the foams of pore sizes 10 ppi and 30 ppi. For the foam of pore size 20 ppi, the RVEs differ. The choice of the cubes is not the reason for the different RVE sizes. The examination of the specific inner surface and specific bulk volume was performed on the same cubes. The RVE is cut out around one single pore (Figure 7.5) for each pore size for further examinations about the different 20 ppi RVE. The RVE for the 10 ppi and 30 ppi foams, as well as the RVE for the specific surface area for the 20 ppi foam, roughly correspond to the size of a pore. This suggests an overestimation of the size of the RVE concerning the specific surface area for 20 ppi and has to be investigated in further investigations.
Nevertheless, it can be concluded that sub volumes of $16 \times 16 \times 16\,\mathrm{mm}^3$ of the available CT data are large enough to represent the specific bulk volume and inner surface for the following investigations.

7.2 Unit Cells

Open-cell foams are microheterogeneous materials and, therefore, insufficiently suitable for simulation on the microscale due to the high computation time required. So, different unit cells are considered to simplify the complex structure of nodes and struts of different lengths and thicknesses. Unit cells are also a way of describing the microheterogeneous structure of the foams in addition to the RVE. The RVE of the unit cell equals to the unit cell, the RVE of a microheterogeneous structure does not have to be in the order of magnitude of a cell. The unit cells should have the same macroscopic properties as the microheterogeneous material. Thus, the macroscopic properties of the microheterogeneous material can be represented using the unit cells without knowing the exact appearance of the foam microstructure.

a) for all edge lengths

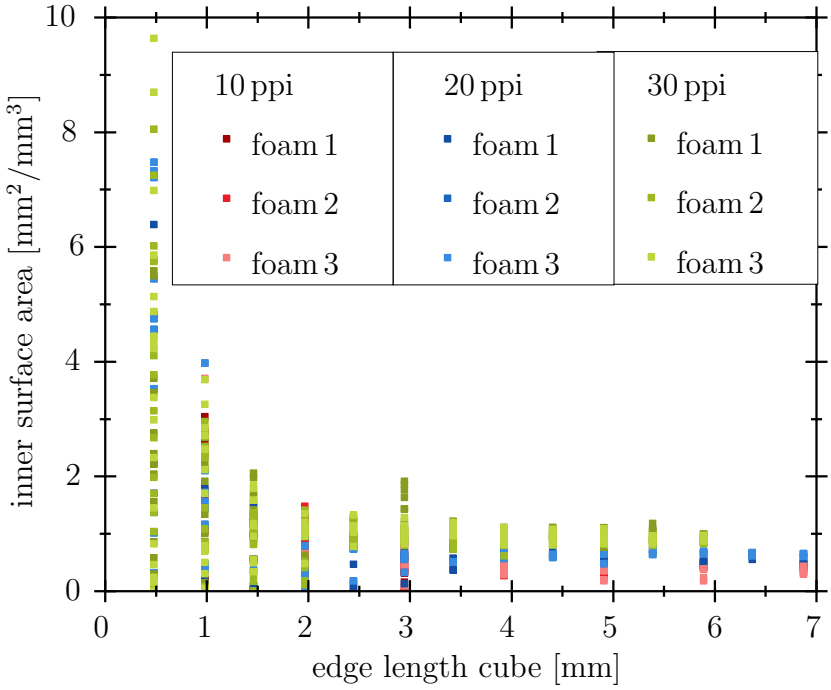

b) for all edge lengths larger than 1 mm

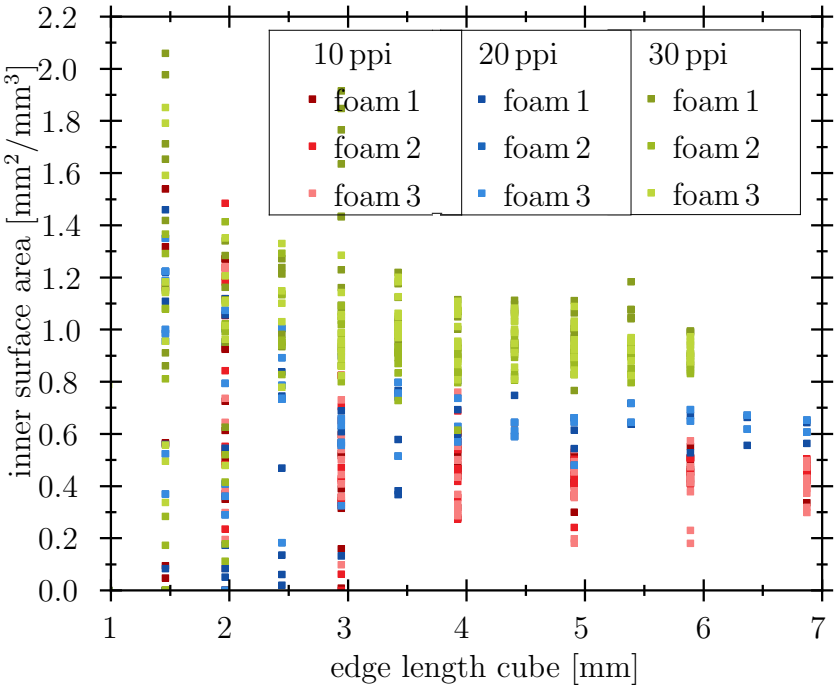

Figure 7.4: Inner surface of the foams with the pore sizes 10 ppi, 20 ppi and 30 ppi for different cube edge lengths for RVE determination

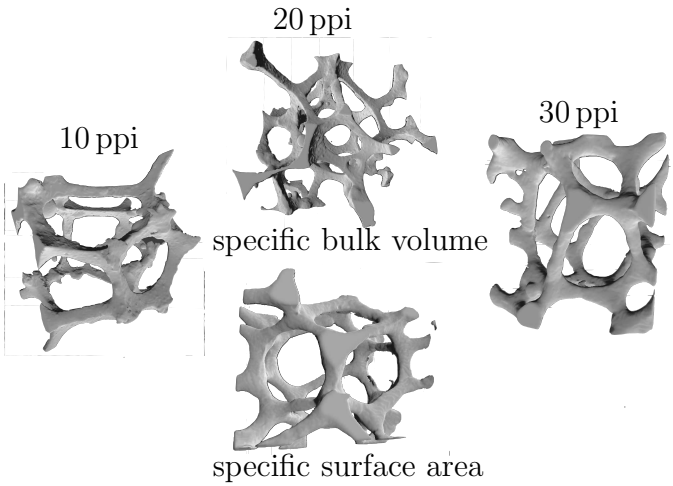

Figure 7.5: Size of the RVE of the different pore sizes. For the 20 ppi foam, the RVE of the specific bulk volume and specific surface area

In describing foamed materials, various unit cells are used in literature, such as

- Kelvin Cell [22, 79, 103, 129] (Figure 7.6 (a))
- Weaire-Phelan Cell [28, 103, 131] (Figure 7.6 (b))
- Pentagon dodecahedron [48, 72] (Figure 7.6 (c))
- Cut-Out Spheres Cell [99, 108, 160, 161] (Figure 7.6 (e)).

These unit cells are briefly presented here and then used to further analyse the geometry parameters like specific surface area and specific bulk volume. In addition, these parameters are examined as a function of the coating thickness and compared with the results of the specific surface area and the specific bulk volume of Al foams. The investigations are executed by using the image analysis tool Fiji.

Kelvin Cell

In 1887 Lord Kelvin developed the tetrakaidecaheron, or in short, the Kelvin Cell [165] (Figure 7.6 (a)), which was, according to the knowledge at that time, a space-filling structure with minimum surface area. The surface of the Kelvin cell consists of four squares and eight hexagons. If all edges of the Kelvin cell become struts and all vertices become nodes, then each node is connected with 3.5 struts on average.

Weaire-Phelan Cell

In 1993 Weaire and Phelan found another space-filling structure with an even smaller surface area than the Kelvin Cell [131] (Figure 7.6 (b)). The Weaire-Phelan Cell is an irregular pentagon dodecahedron with twelve irregular pentagons. If the edges are

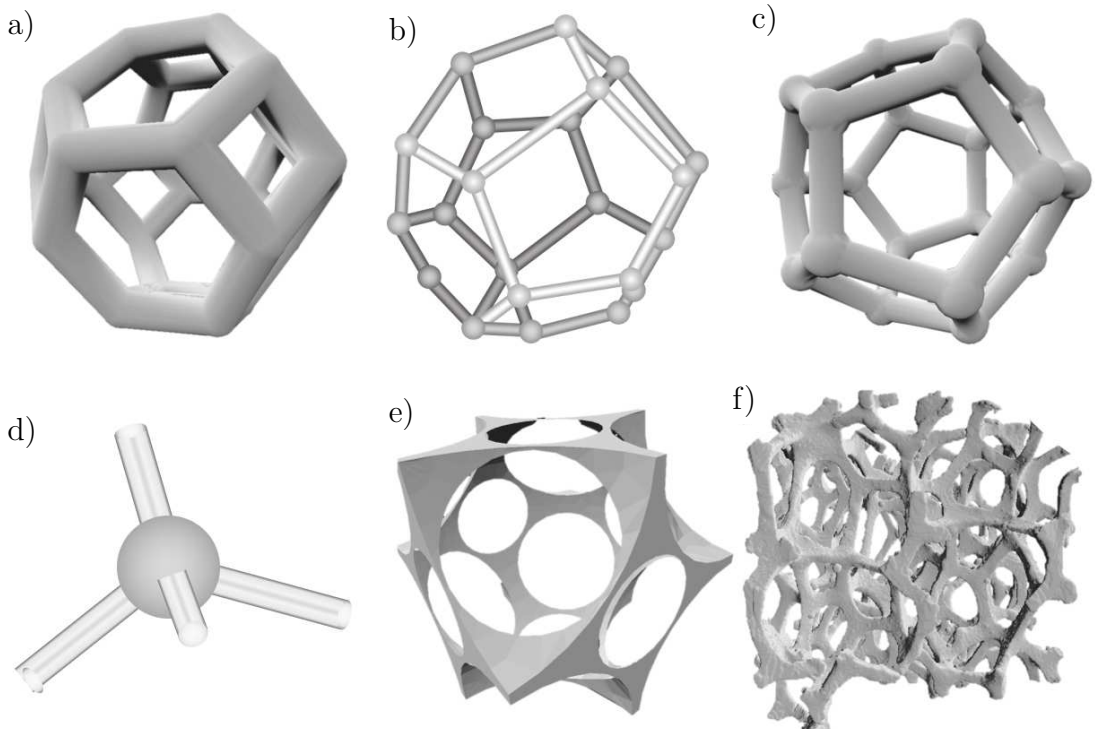

Figure 7.6: Different unit cells, a) Kelvin Cell with thin nodes, b) Weaire-Phelan Cell with thick nodes, c) Pentagon dodecahedron with thin nodes, d) Node Unit with thick node, e) Cut-Out Spheres Cell, f) real foam

assumed to be struts, and the corners are assumed to be nodes, each node is connected on average with 4 struts. The strut's length of the Weaire-Phelan cell varies.

Pentagon dodecahedron

The regular pentagon dodecahedron (Figure 7.6 (c)) is a body consisting of 12 congruent regular pentagons and correspondingly equal-length struts. Unlike the Weaire-Phelan cell, however, the pentagon dodecahedron is not space-filling.

Cut-Out Spheres Cell

The model of the Cut-Out Spheres Cell (Figure 7.6 (e)) is based on the manufacturing process of metal foams. One possible manufacturing method is the so-called placeholder method. This method uses spheres as placeholders and burns out after filling the mould with the desired material [96]. In the unit cell of the Cut-Out Spheres Cell, 9 spheres are cut out of one cube. The resulting geometry looks very similar to the geometry of the real metal foam.

7.2.1 Choice of Three Unit Cells to be Investigated

Some unit cells presented are more suitable than others. For comparing the different unit cells concerning geometry parameters like specific surface area and specific bulk volume. The Kelvin Cell is exceptionally suited due to its equal length struts and space-filling capability. In addition, surface area and volume can be calculated analytically for different coating thicknesses easily. The Weaire-Phelan Cell is slightly poorer suited due to its different strut lengths. For simplification, a minimisation of the geometric parameters like the strut length is of significant advantage for microscopic observation of the cells. This minimisation is not possible for the Weaire-Phelan Cell. The pentagon dodecahedron is also unsuitable because of the lack of space-filling ability. As a substitute for the Weaire-Phelan cell and the pentagon dodecahedron, the Node Unit is considered at this point. Due to its connectivity of 4, it is not space-filling. However, the geometry parameters of specific surface area and specific bulk volume are easy to calculate analytically. The number of nodes per volume can be calculated using the Weaire-Phelan cell, and parameters such as strut length can be calculated using the pentagon dodecahedron. The last structure presented here, the Cut-Out Spheres Cell, is also space-filling and has a periodic structure due to the fact that spheres of the same size are cut from one cube. For this reason, it is also well suited for analysing the geometry parameters, specific surface area and specific bulk volume. The geometry parameters of the unit cells are then compared with data from the virtually coated foams from the CT in chapter 7.2.3.

7.2.2 Choice of Parameters and Calculation Method

The required parameters (strut length, node radius, ...) for the calculation have to be identified before determining the specific surface area and the specific volume of the different unit cells. For the Kelvin Cell and Node Unit, different strut and node geometries can be used (Figure 7.7 a)). Different strut geometries can be used because the geometry of the strut cross-section is changing between a round and a triangular cross section (Figure 7.7 a)). At the same time, the size of the area of the cross-section also changes. However, the nodes are assumed to be spheres for both structures (Figure 7.7 b)). The cross-section of the struts should be as close as possible to the original geometry. When considering the strut cross-section of the real foams, the cross-section varies from strut to strut and from position to position in the strut (Figure 7.7 a)). Sometimes the cross-section of struts is more round and sometimes more triangular. For this reason, the Kelvin Cell and the Node Unit are examined with a round and a triangular strut cross-section, respectively (Figure 7.7 b)). Furthermore, for calculating the specific surface area and the specific bulk volume, more geometry parameters like

strut length and node size have to be investigated. The radius r_S and for triangular strut cross-section the side length a_S of the equilateral triangle have to be determined in addition for the round strut cross-section, for the foams with the pore sizes 10 ppi, 20 ppi and 30 ppi (Figure 7.7 b)). Jung et al. [83] examined several strut cross-sections for different pore sizes. The cross-sectional area of the struts varies depending on the position within the strut. In the centre of the strut, the cross-sectional area is usually the smallest and increases towards the nodes. Based on the sizes of the cross-sections determined by Jung [83], the radii for the round strut cross-sections and the side lengths for the triangular strut cross-sections were calculated.

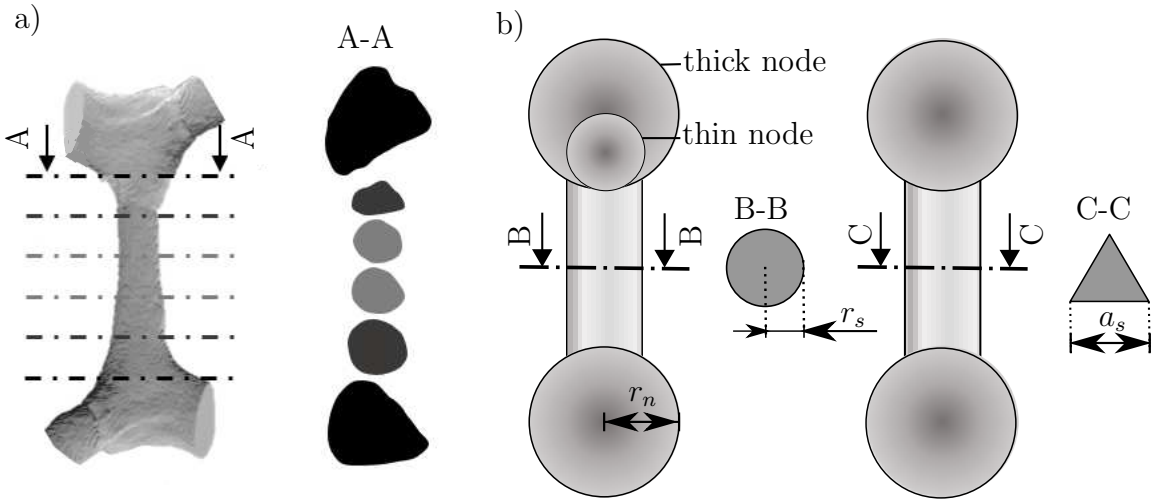

Figure 7.7: a) real strut with varying cross-sections at different points, b) strut in the calculation model with round and triangular cross-section

The results for the mean radius and mean side length of struts correspond to the strut radius r_S and strut side length l_S. The radii from the maximum strut cross-sections are used as the radii for the node r_n. Since sometimes larger and sometimes smaller nodes can be seen, a distinction is also made between thick and thin nodes for the Kelvin Cell and the Node Unit (Figure 7.7 b)). For thin nodes, the radius of the node is equal to the radius of the strut. For thick nodes, the radius of the node is equal to the radius calculated from the maximum cross-section of struts.

The inner surface and the specific bulk volume are calculated analytically. For this purpose, in the case of round cross-sections, the curvature of the node surface is taken into account when calculating the surface area and volume (Figure 7.8). This procedure is very complex for the struts with a triangular cross-section and is therefore not carried out in this thesis. It is carried out for the triangular struts in simplified form as an additional calculation method for the round struts (Figure 7.7). The calculation rule for an arbitrary structure is for the inner surface with n_n nodes and n_s struts with a node radius of r_n, a strut edge length a_s, a coating thickness b, connectivity of n_c and

a strut length of l_s for cells with triangular strut cross-section,

$$O^{\text{tri}} = n_n \underbrace{\left(4\pi \left(r_n + b\right)^2\right.}_{\text{surface sphere}} - n_c \underbrace{\left.\sqrt{3}/8 \left(a_s + b\right)^2\right)}_{\text{cross-section triangle}} + n_s \underbrace{\left(a_s + \frac{2b}{\sqrt{3}}\right)\left(l_s - b\right)}_{\text{surface strut}} \tag{7.1}$$

and for the specific bulk volume

$$V^{\text{tri}} = n_n \underbrace{\frac{4}{3}\pi \left(r_n + b\right)^3}_{\text{volume sphere}} + n_s \underbrace{\frac{\sqrt{3}}{4}\left(a_s + 2b\frac{3}{\sqrt{3}}\right)^2 \left(l_s - b\right)}_{\text{volume strut}} . \tag{7.2}$$

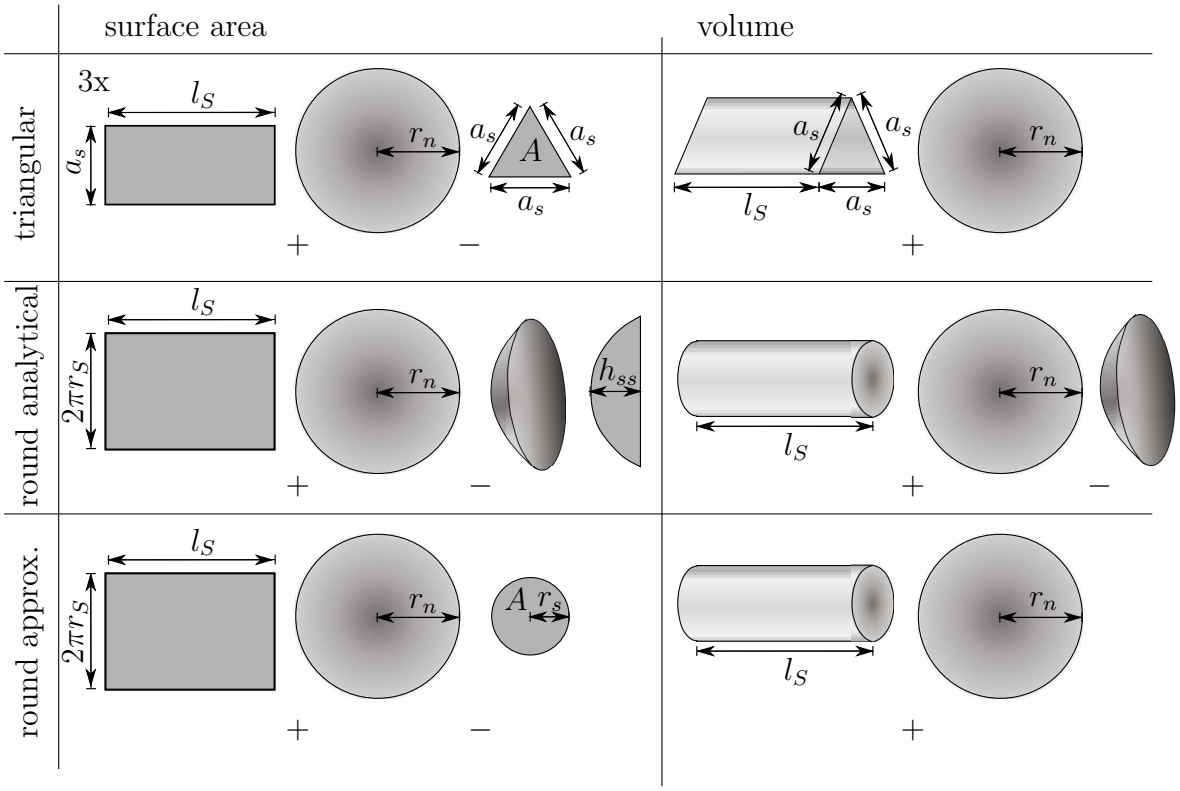

Figure 7.8: Components of the calculation formulas of the cells with triangular strut cross-section and round strut cross-section by means of analytical and approximated approach

The calculation is as follows for the inner surface area of the cells with a round strut cross-section with consideration of curvature

$$O^{\text{circ}}_{\text{analyt}} = n_n \underbrace{\left(4\pi \left(r_n + b\right)^2\right)}_{\text{surface sphere}} + n_s \underbrace{2\pi \left(r_s + b\right)\left(l_s - b\right)}_{\text{surface strut}}$$

$$-n_c \underbrace{\pi \left(r_n + b - \sqrt{(r_n+b)^2 - (r_s+b)^2} \right)^3 + (r_s+b)^2 \Bigg)}_{\text{surface sphere segment}}, \tag{7.3}$$

for the specific bulk volume

$$V_{\text{analyt}}^{\text{circ}} = n_n \underbrace{\frac{4}{3}\pi (r_n+b)^3}_{\text{volume sphere}} + n_s \underbrace{\frac{\sqrt{3}}{4} \left(a_s + 2b\frac{3}{\sqrt{3}} \right)^2 (l_s - b)}_{\text{volume strut}}$$

$$- n_c \frac{\pi}{3} \Big(\underbrace{(r_n + b - \sqrt{(r_n+b)^2 - (r_s+b)^2}}_{\text{height sphere segment } h_{ss}} \Big)^2 (3\,(r_s+b) \tag{7.4}$$

$$- \Big((r_n + b - \underbrace{\sqrt{(r_n+b)^2 - (r_s+b)^2}}_{\text{height sphere segment } h_{ss}})^3 + (r_s+b)^2 \Big) \Big) \Big) , \tag{7.5}$$

for the approximated calculation for the inner surface

$$O_{\text{approx}}^{\text{circ}} = n_n \underbrace{\left(4\pi (r_n+b)^2}_{\text{surface sphere}} - n_c \quad \underbrace{(r_n+b)^2}_{\text{cross-section strut}} \quad \Big) + n_s \underbrace{2\pi (r_s+b)(l_s-b)}_{\text{surface strut}} \tag{7.6}$$

and for the specific bulk volume

$$V_{\text{approx}}^{\text{circ}} = n_n \underbrace{\frac{4}{3}\pi (r_n+b)^3}_{\text{volume sphere}} + n_s \underbrace{\frac{\sqrt{3}}{4} \left(a_s + 2b\frac{3}{\sqrt{3}} \right)^2 (l_s - b)}_{\text{volume strut}} . \tag{7.7}$$

The calculated parameters for the foams of the different pore sizes are summarised in Table 7.1. With the help of the ppi number of the foams, the number of pores in a given volume, as well as the pore diameter, can be calculated. The number of nodes which have to be added by adding a pore (= nodes per additional pore) is about how many nodes of infinitely many unit cells exist in relation to the number of pores. This was estimated using CAD for the Kelvin Cell, and for the Node Unit, and was estimated starting from the Weaire-Phelan Cell.

The strut length of foams was measured firstly by Jung et al. [83] and secondly calculated based on the pore size (Table 7.1). Based on the different cross-sectional areas, different radii were calculated for struts with a round cross-section and edge lengths for struts with a triangular cross-section. The strut lengths measured from Jung were used to calculate the specific surface area and the specific bulk volume instead of the analytically calculated strut lengths, which were calculated with the pentagon dodecahedron. The CAD software FreeCAD calculates the inner surface and the specific

Table 7.1: Different geometry parameters for different pore sizes

			10 ppi	20 ppi	30 ppi
1	pore diameter d		8 mm	5.68 mm	4.6 mm
2	nodes per additional pore Node Unit		8	8	8
3	connectivity Node Unit $n_c^{\text{Node Unit}}$		4	4	4
4	nodes per additional pore Kelvin Cell		8	8	8
5	connectivity Kelvin Cell $n_c^{\text{Kelvin Cell}}$		3.5	3.5	3.5
6	length strut l_s measured in [83]		3.2 mm	2 mm	1.25 mm
7	length strut l_s calculated with pentagon dodecahedron		3.06 mm	2.17 mm	1.75 mm
8	cross-section A from [83] [mm]	from to	0.20 - 1.12	0.10 - 0.60	0.10 - 0.30
		average	0.50	0.25	0.10
9	edge length a_s derived from 8 [mm]	from to	0.48 - 1.13	0.34 - 0.83	0.34 - 0.59
		average	0.75	0.54	0.34
10	radius r_S derived from 8 [mm]	from to	0.25 - 0.0	0.18 - 0.44	0.18 - 0.30
		average	0.39	0.28	0.18

bulk volume of the Cut-Out Spheres Cell. The pore size can be taken directly from Table 7.1. The edge length of the original cuboid from which the spheres are cut out is selected so that the resulting cross-sectional area of the struts is approximately equal to the cross-sectional area of the struts measured.

7.2.3 Results of the Geometry Analysis

The specific surface area increases with the increasing coating thickness (Figure 7.9 a), c) and e)). For all three pore sizes, the specific surface area of the Node Unit is smaller than the specific surface area of the Kelvin Cell, regardless of the nodes and struts geometry. For the 10 ppi and 20 ppi foams, results of the real structure are in-between the Node Unit and Kelvin Cell results. The results of the real structure are the results of the measuring of the CT data via Fiji. For the 10 ppi foam, the Node Unit is closer to the real structure, and for the 20 ppi foam, the Kelvin Cell is closer. For the 30 ppi foam, all Unit Cells underestimate the curve of the specific surface area of the real foam. The slope of the curve of the Node Unit with thick nodes best matches the real curve. The results for the specific bulk volume from the Node Unit tend to be lower

than the Kelvin Cell results (Figure 7.9 b), d) and f)). For the 10 ppi foam, the curve of the real foam lies precisely on the Node Unit curve with thick nodes and triangular strut cross-section. For the 20 ppi foam, the Kelvin cell overestimates the curve of the real foam just for larger coating thicknesses and the Node Unit underestimates the curve of the real foam for a larger coating thickness. For the 30 ppi foam, all models underestimate the trend of the real foam. According to the slope, the curve of the Kelvin Cell with thick nodes and triangular cross-section of struts best matches the curve of the real foam.

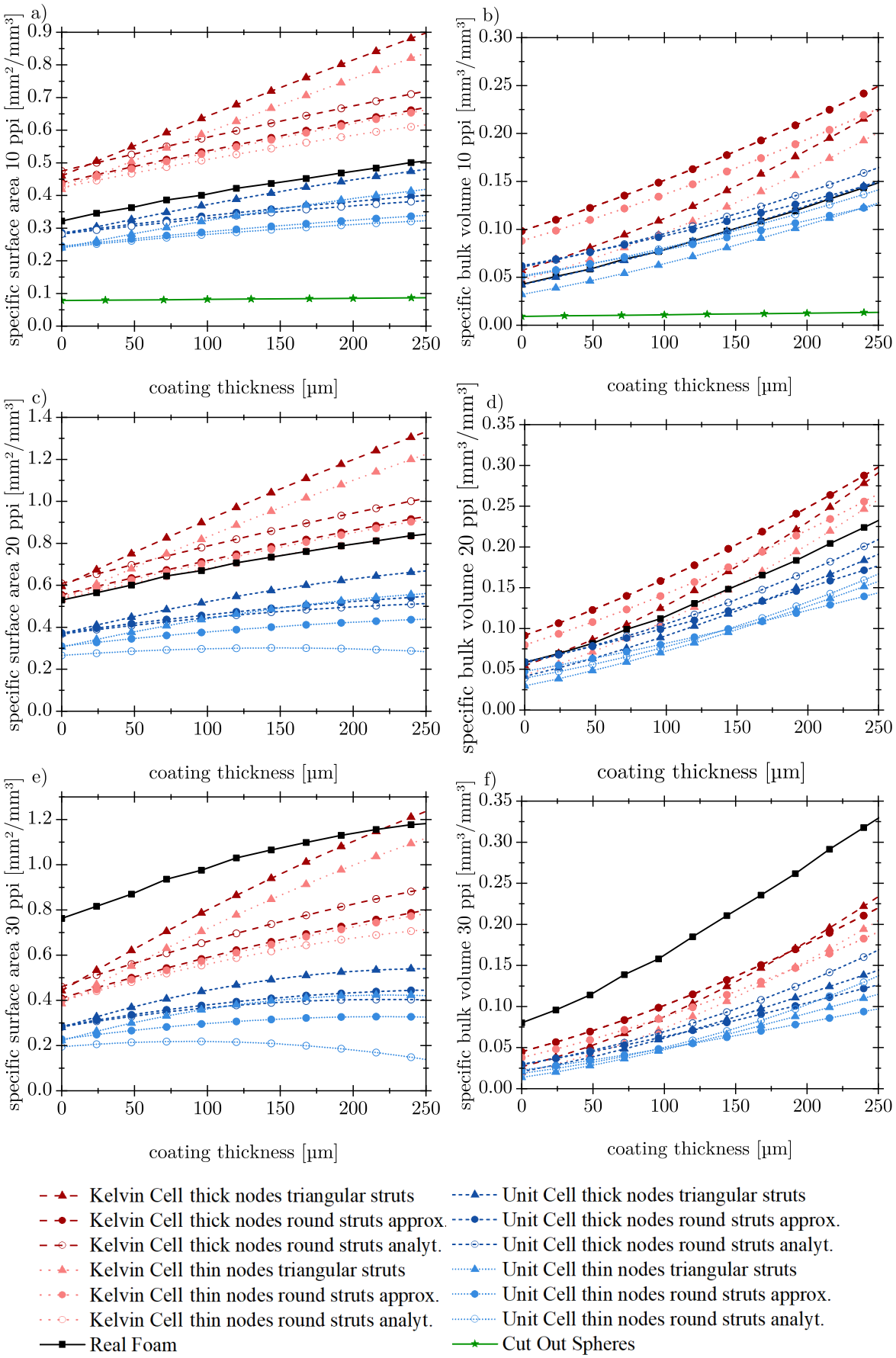

Figure 7.9: Specific surface area and specific bulk volume of the foams with the pore sizes 10 ppi, 20 ppi and 30 ppi for different coating thicknesses

Figure 7.10 shows the specific surface area for the three pore sizes and the best fitting Unit Cells with an constant additive offset applied. At least one unit cell can be found that reflects the variation of the surface area as a function of the coating thickness for each pore size.

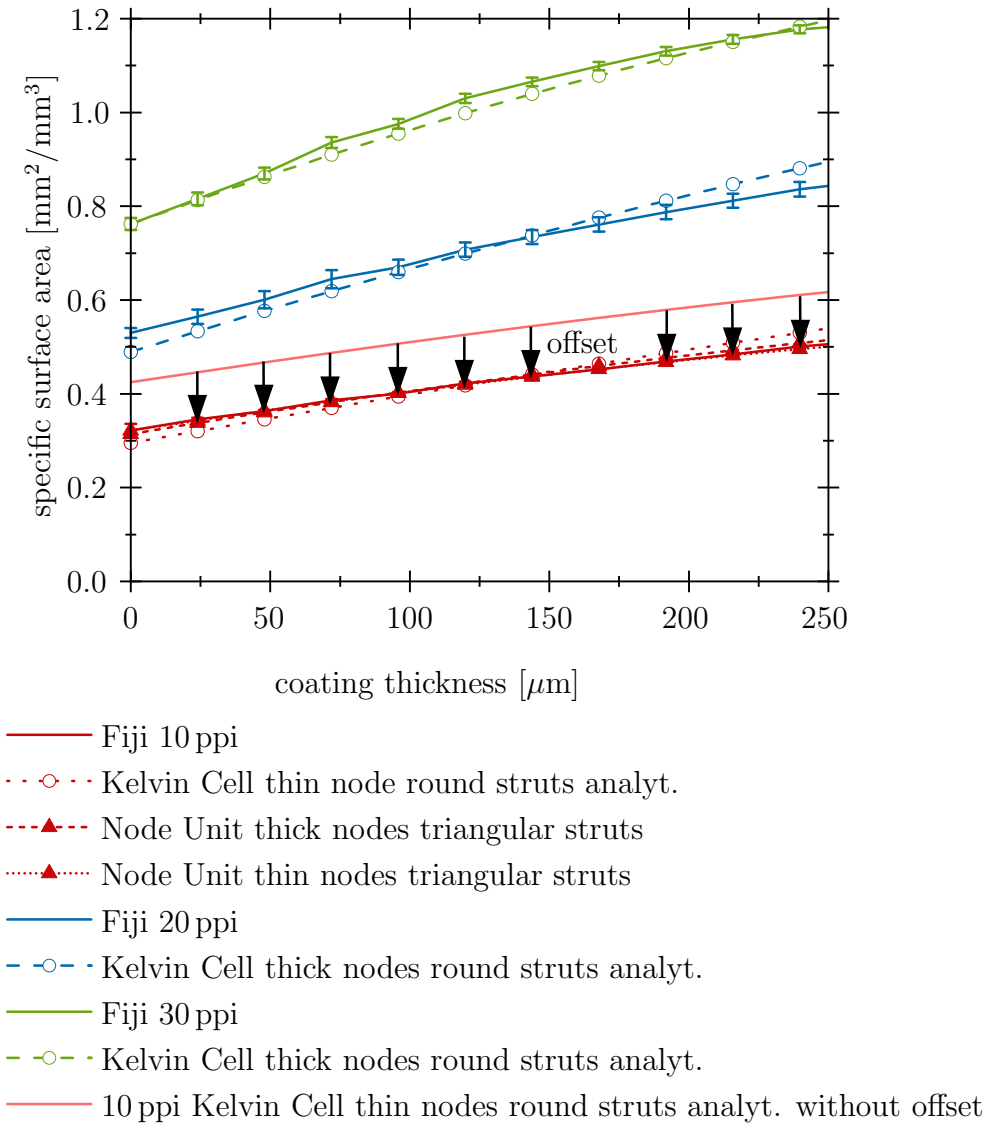

Figure 7.10: Specific surface area of the foams with the pore sizes 10 ppi, 20 ppi and 30 ppi with an constant additive offset to obtain the specific surface area of the real foam

A summary of which unit cell, which cross-section of struts, and which node size is best for representing a real foam can be estimated. The results can be found in Table 7.2. In general, the Node Unit and Kelvin Cell models are similarly well suited for surface area and bulk volume representation. In addition, both the triangular and round cross-sections of struts are suitable. For the specific surface area representation, the Node Unit with thin nodes and a triangular cross-section of struts and the Kelvin Cell with thin nodes and round cross-sections of struts are most suitable for analytical calculation.

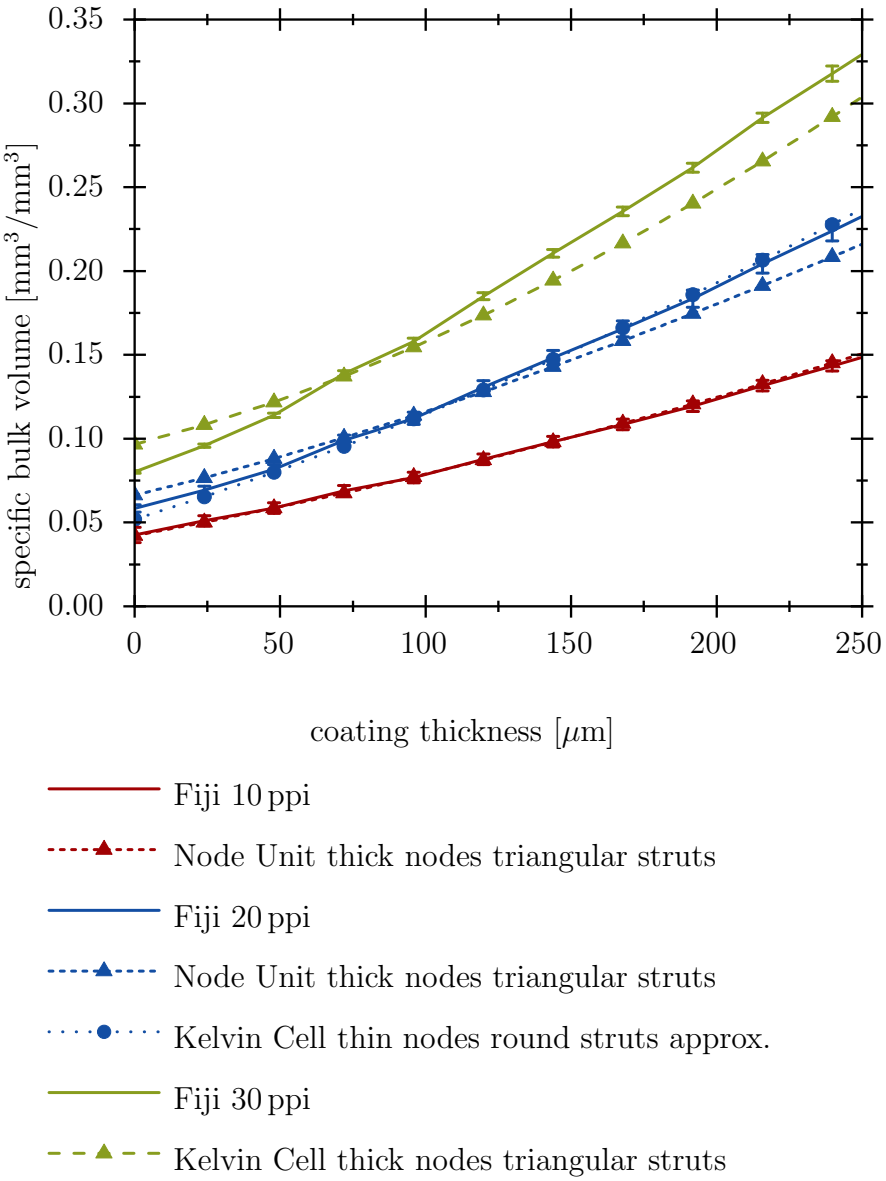

Figure 7.11: Specific bulk volume of the foams with the pore sizes 10 ppi, 20 ppi and 30 ppi with an constant additive offset to obtain the specific bulk volume of the real foam

The Node Unit with thick nodes and triangular strut cross-section is more suitable for the calculation of the specific bulk volume. The deviation of the models from the real foam is the smallest, and the largest for the 30 ppi foam for the 10 ppi foams.
To examine which of the selected parameters from Table 7.1 is the reason for the 30 ppi error offset, the number of pores, the strut length l_s as well as the node radius r_n were varied for the 30 ppi foam. The strut diameter was kept constant because the calculation of specific surface area and specific bulk volume does not consider the struts' intergrowth with increasing strut diameter. The results of this parameter study are shown for the specific surface area in Figure 7.12. The increase of the node diameter by

Table 7.2: Summary which unit cell with which cross-section of struts and with which node size best describes the geometry of the real foam, what is the real error, which is the relative minimum and maximum error in percent

	specific surface area [mm^2/mm^3]			specific bulk volume [mm^3/mm^3]		
	cell	node	strut	cell	node	strut
10 ppi	Kelvin Cell	thin	round analyt.	Node Unit	thick	triangular
	Offset:	-0.18 mm^2/mm^3		Offset:	0 mm^3/mm^3	
		-55.96% - -35.14%			0% - 0%	
	Kelvin Cell	thick	triangular			
	Offset:	0.03 mm^2/mm^3				
		9.32% - 5.86%				
	Node Unit	thin	triangular			
	Offset:	0.082 mm^2/mm^3				
		32.74% - 16.01%				
20 ppi	Node Unit	thin	triangular	Node Unit	thick	triangular
	Offset:	-0.12 mm^2/mm^3		Offset:	0.02 mm^3/mm^3	
		-22.64% - -14.07%			34.25% - 8.20%	
				Kelvin Cell		round approx.
				Offset:	-0.028 mm^3/mm^3	
					-47.95% - -11.47%	
30 ppi	Kelvin Cell	thick	round analyt.	Node Unit	thick	triangular
	Offset:	0.3 mm^2/mm^3		Offset:	0.07 mm^3/mm^3	
		39.35% - 25.25%			87.37% - 20.32%	

100 % for the Kelvin cell with round struts matches the analytical calculation and the trend of the real foam. Only considering the slope of the curve, the Kelvin Cell with round strut cross-section with approximated calculation is most suitable. However, a large offset would have to be applied in this case again. There are similar results for the specific surface area. If only the slope of the curves is taken into account, the Kelvin cell with a round strut cross-section and a doubled node diameter matches the real curve best. However, an offset has to be applied in this case as well. For low coating thicknesses, the Kelvin Cell is best suited with a round strut cross-section with approximated calculation with a doubling of the number of nodes and the associated doubling of the struts. For both geometrical parameters, the Node Unit and the Kelvin Cell models are well suited to reproduce the actual behaviour of the inner surface and the specific bulk volume when the parameters are varied for small coating thicknesses. However, the effect of the varying parameters for the specific surface area and the specific bulk volume differ. Moreover, all models overestimate the trend of the actual foam for higher coating thicknesses. For this reason, the intergrowth of the struts should be considered in future studies to achieve a more precise solution when considering coating thicknesses above 100 μm.

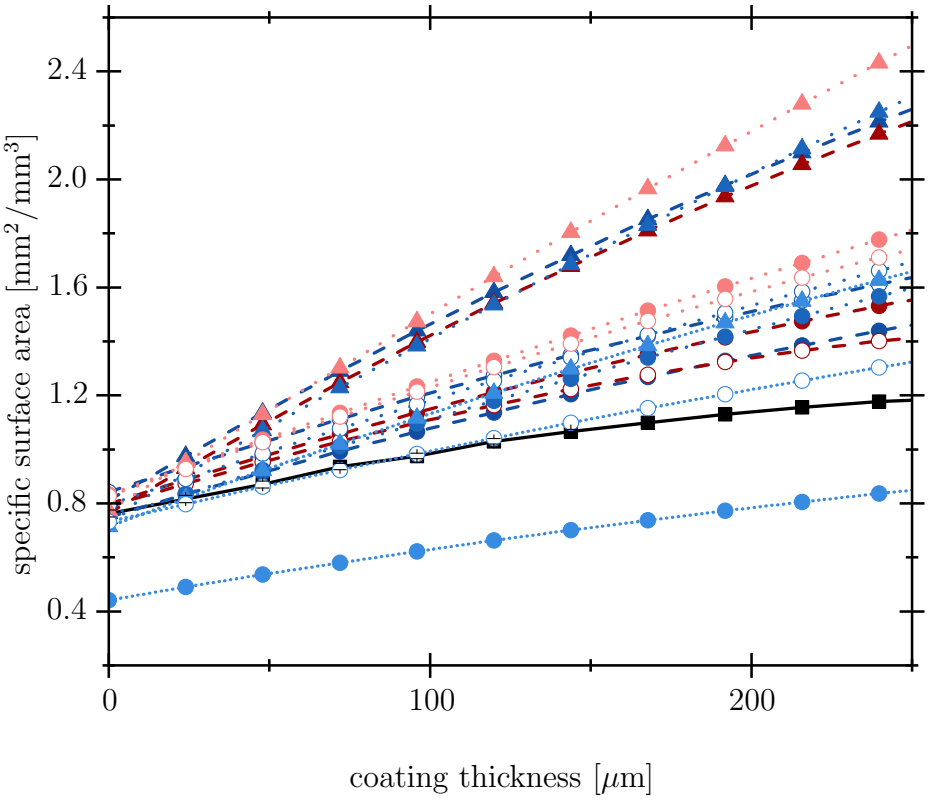

Fiji 30 ppi
Kelvin Cell thick nodes triangular struts, $n_S = 600$
Kelvin Cell thick nodes round struts approx., $n_S = 600$
Kelvin Cell thick nodes, round struts analyt., $n_S = 600$
Kelvin Cell thin nodes triangular struts, $n_S = 650$
Kelvin Cell thin nodes round struts approx., $n_S = 650$
Kelvin Cell thin nodes, round struts analyt., $n_S = 650$
Kelvin Cell thick nodes triangular struts, $l_S = 2.3$
Kelvin Cell thick nodes round struts approx., $l_S = 2.3$
Kelvin Cell thick nodes, round struts analyt., $l_S = 2.3$
Kelvin Cell thin nodes triangular struts, $l_S = 2.6$
Kelvin Cell thin nodes round struts approx., $l_S = 2.6$
Kelvin Cell thin nodes, round struts analyt., $l_S = 2.6$
Kelvin Cell thick nodes triangular struts, $r_S = 0.6$
Kelvin Cell thick nodes round struts approx., $r_S = 0.6$
Kelvin Cell thick nodes, round struts analyt., $r_S = 0.6$

Figure 7.12: Varying different parameters to obtain the real specific surface area of a 30 ppi foam without adding an offset

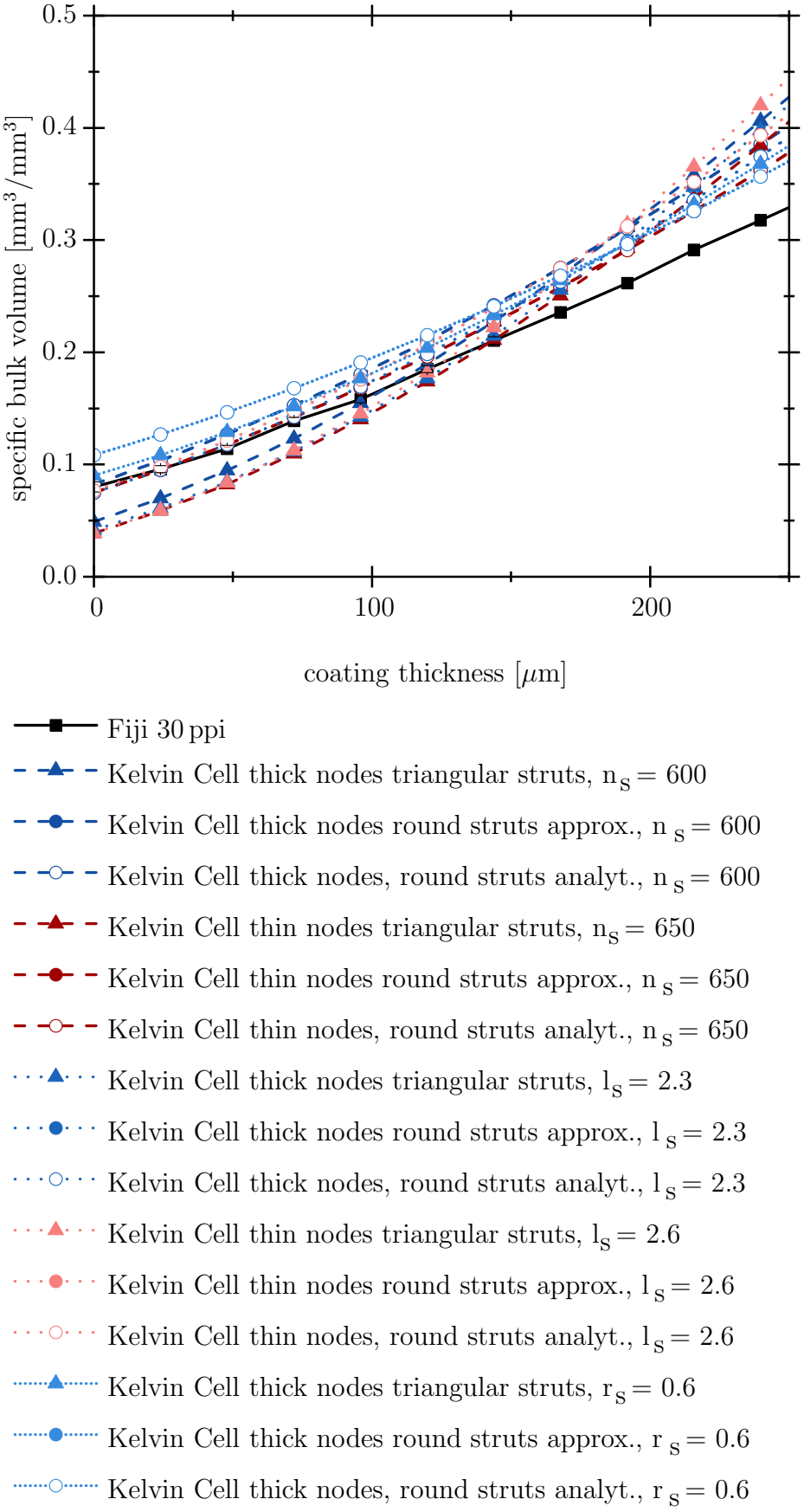

Figure 7.13: Varying different parameters to obtain the real specific bulk volume of a 30 ppi foam without adding an offset

7.3 Permeability

Only the influence of the coating thickness on the specific surface area and the specific bulk volume has been examined. In reality, the coating thickness also changes both the permeability of the foam and, finally, the flow velocity through the foam. The permeability is a value which can be derived from Darcy's law. It is defined as the quotient between the product of the flow rate Q, the dynamic viscosity η and the length l of the body flowed through divided by the product of the cross-sectional area A, which is flowed through and the pressure difference Δp (Figure 7.14)

$$K = \frac{Q\eta l}{A\Delta p}\,. \tag{7.8}$$

Permeability is not specific to the flow in foams. It is relevant to many different sciences that deal with the flow in porous media, such as in geology in the flowability of sand and for fibrous materials or metal foams in the form of heat exchangers and catalysts. To the author's knowledge, the permeability of foams as a function of different coating thicknesses has never been researched.

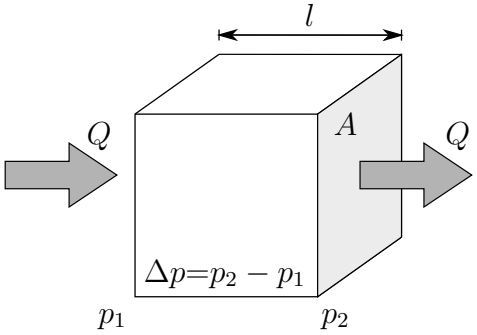

Figure 7.14: Definition of the permeability, with the flow rate Q, the length of a cube l, the pressure difference Δp and the surface area A

In the relevant literature, different models are used to describe the dependence of geometry parameters on permeability. Most models are based on the so called Kozeny-Carman equation, which is also often called the Ergun-like approach depending on the context in which the equation is used. According to this approach, permeability is the quotient of the product of the porosity ε raised to the power of three and the square of the mean grain diameter d_{grain} divided by the product of an empirical parameter A_K and the square of the difference between one and the porosity

$$K = \frac{\varepsilon^3 d_{\text{grain}}^2}{A_K(1-\varepsilon)^2}\,. \tag{7.9}$$

Other models refer to a uniform cell structure of cubically arranged struts [4, 56,

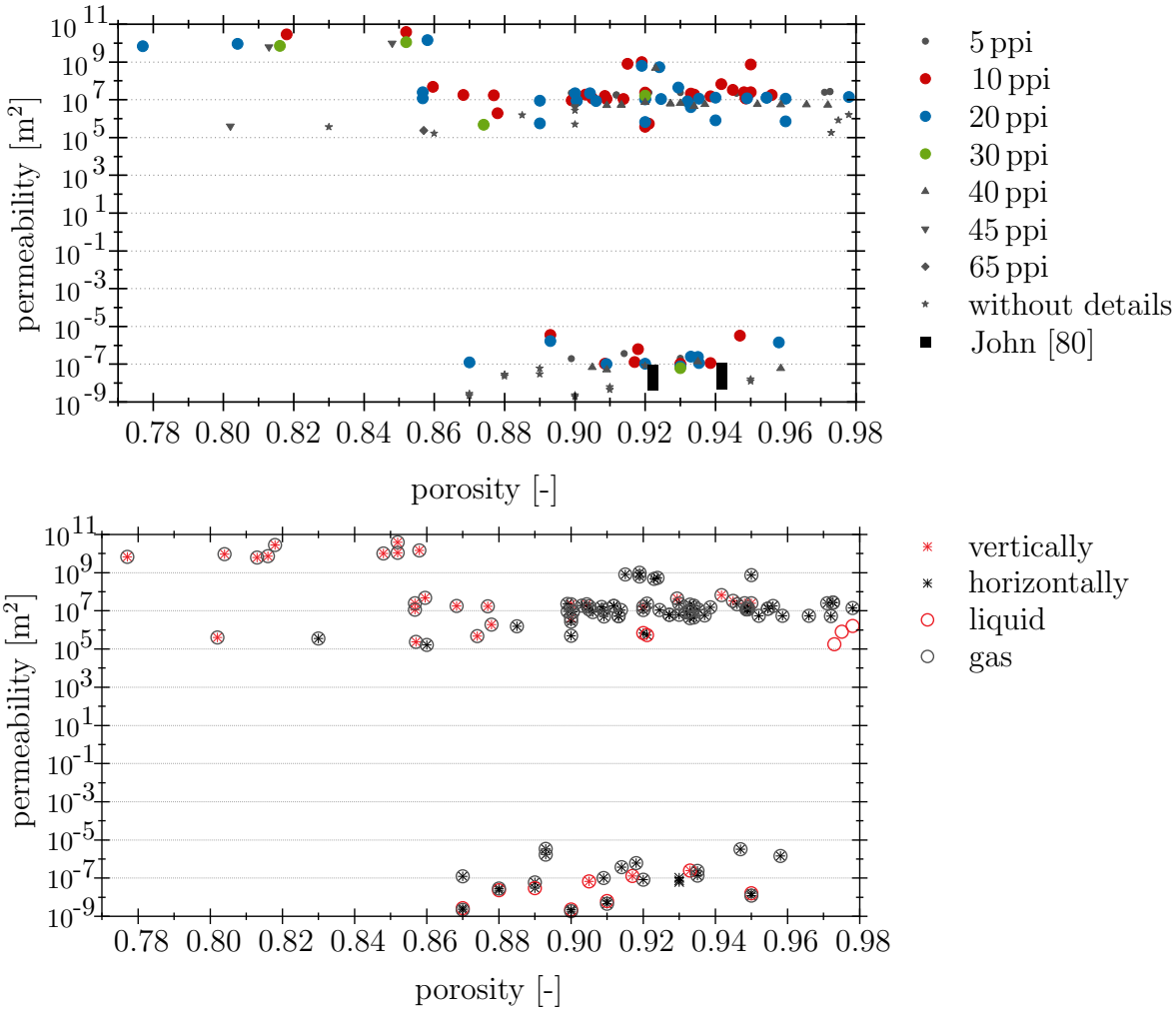

Figure 7.15: Permeability of different foams taken from literature showing the characteristic of measuring

71, 177], of other uniform cell structures [15], or are self-developed empirical models [46, 49, 58]. For the Ergun-like approach, the values of the empirical parameter A_K are sometimes set to a fixed value [58, 78, 93, 163, 166] in a range of [10^{-4}[166]−865[163]] and sometimes a custom calculation rule is used [59, 77, 101, 120, 121, 138]. To summarise which of the models describes the permeability in dependence of the coating thickness of the foams best, many values for the permeability of metal foams of different pore sizes and porosities from literature are plotted in Figure 7.15. The summary of these values with the respective literature can be found in the appendix. In general, the smaller the permeability value, the more impermeable the medium to flow through. At first glance, it is apparent that there are two data groups for permeability. In one point group, the permeability values are higher than 1, in the second point group, they are less than 1. Furthermore, neither the porosity nor the ppi number indicates the range of values for permeability. In Figure 7.15 top, all values are sorted according to the aggregate state of the medium (liquid or gas), as well as the arrangement of the testing

device (vertical or horizontal) to get an idea of what could be the reason for these two clouds. However, non of this characteristics does indicate the difference between these two data groups. For this reason, permeability measurements were carried out on 10 ppi and 30 ppi foams with water (liquid) and a vertically oriented experimental setup as part of a seminar paper by John [80]. The permeabilities obtained in this work are in the lower point cloud, so it is taken as the initial value for further research and only the lower point cloud is considered in the following figures. The Kozeny-Carman model (eq. (7.9)) with the porosity ε, the empirical parameter A_K (values between 10^{-4} [166] and 865 [163]) and the average particle diameter d is used. Furthermore, the following models are also used. The model of DuPlessis [132] is based on a uniform cell structure and uses both the pore diameter d_{pore} and the tortuosity χ. The Tortuosity is defined as the ratio of the average length $l_{\text{av.}}$ of the flow paths through a permeable medium, here the foam, to the straight-line length l, across the permeable medium (Figure 7.16)

$$\chi = \frac{l_{\text{av.}}}{l} \geq 1\,, \tag{7.10}$$

with

$$l_{\text{av.}} = \frac{1}{n}\sum_{i=1}^{n} l_n\,. \tag{7.11}$$

The higher the tortuosity, the more difficult it is to achieve a homogeneous coating, in the context of the electrodeposition process.

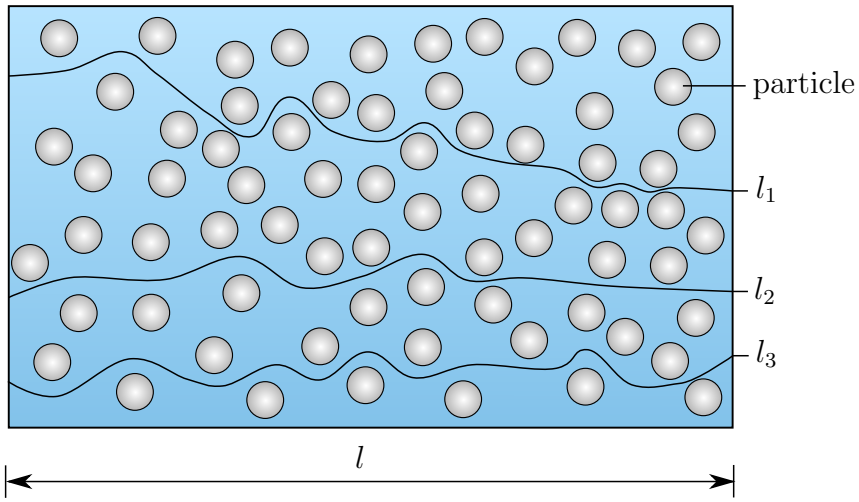

Figure 7.16: Definition of the tortuosity of a permeable media

The model of DuPlessis defines the Permeability as

$$K = \frac{\varepsilon^2 d_{\text{pore}}^2}{36\chi(\chi-1)}\,. \tag{7.12}$$

The model of Ahmed [4] also includes the ratio between node diameter to strut diameter

R and the ratio d_R of the strut radius r_s to strut length l_s

$$K = \frac{\varepsilon^{2.5}}{36\chi^{1.5}(\pi d_R + 4R^2 d_R^2 - \pi d_R^2(1+2R))} l_s^2 \,. \tag{7.13}$$

The Fourier-based model was introduced by Bhattacharya [15] with an additional calculation for tortuosity

$$\frac{1}{\chi} = \frac{3}{4\varepsilon}\left[1 - \left(1.18\sqrt{\frac{1-\varepsilon}{3\pi}}\frac{1}{G}\right)^2\right] \tag{7.14}$$

$$\tag{7.15}$$

with

$$G = 1 - \exp\left(-\frac{1-\varepsilon}{0.04}\right) \,. \tag{7.16}$$

In the model of Depois [45], a form factor a is introduced, which has a value of $a = 0.64$ for randomly packed spheres. It was invented for describing the flow through packed spheres. Therefore, the particle diameter $d_{particle}$ was also used

$$K = \frac{\varepsilon d_{particle}^2}{4\pi}\left(\frac{\varepsilon - a}{3(1-a)}\right)^{1.5} \,. \tag{7.17}$$

The Hooman [71] model requires a fitting factor

$$K \propto \frac{2 r_s d \varepsilon}{6} \,, \tag{7.18}$$

and the model of Yang [177] is given by

$$K = \frac{\varepsilon[1-(1-\varepsilon)^{1/3}]}{108[(1-\varepsilon)^{1/3} - (1-\varepsilon)]} d^2 \,. \tag{7.19}$$

The use of the empirical models is omitted here because they fit the known parameters permeability to porosity. For further analysis of the remaining non-empirical models, the node diameter is used instead of particle size. For tortuosity, the values are always calculated using the approximation of Bhattacharya [15].
The values from the models with the fitting parameters of Hooman and the Ergun-like approach hit the observed values the best due to the fitting parameters (Figure 7.17). In the Hooman model, the permeability increases with decreasing porosity, i.e., increasing coating thickness. The Ergun-like approach increases permeability with increasing porosity, which is physically correct. For this reason, the Ergun-like approach is the

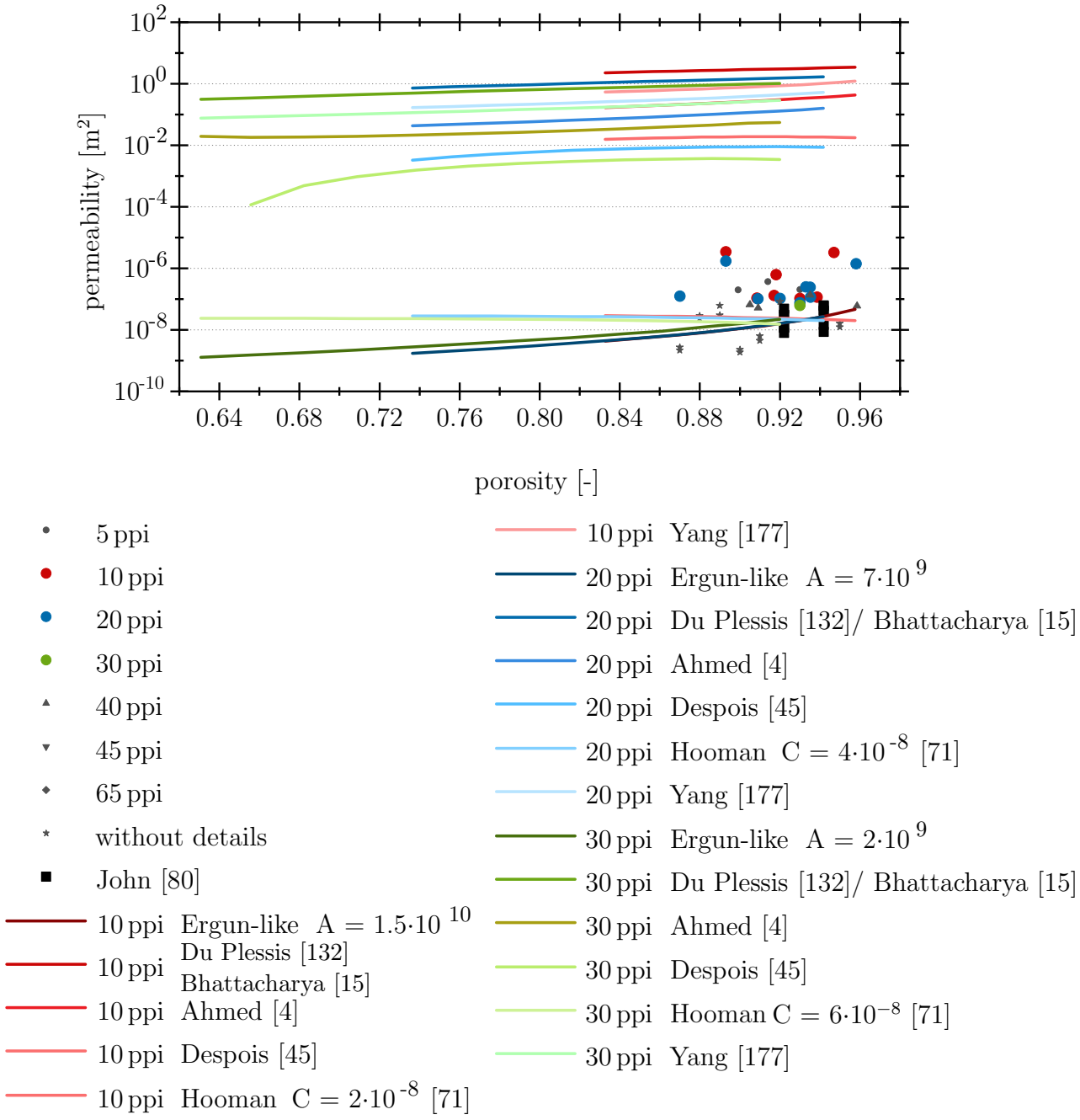

Figure 7.17: Different models for permeability in comparison to the permeability values from literature, zoom of the relevant permeability values

most suitable for representing permeability as a function of the coating thickness of all the considered models. This observation is independent of the pore size and thus valid for 10 ppi, 20 ppi and 30 ppi foams.

During the production of the foams, slightly elongated pores occur, resulting in a different geometry in one direction. To observe whether this elongation in geometry influences the flow rate, the cross-sectional area in all three spatial directions is examined.

7.4 Directional Dependency of the Cross-Sectional Area

Examination of the cross-sectional area should be carried out on the same foam in all three spatial directions to ensure better statistics. To achieve this, a non-destructive testing method has to be used. So, the testing is carried out virtually with the help of the open-source programme Fiji. The same foams already considered for the specific surface area and the specific bulk volume determination are used for examining the directional dependency of the cross-sectional area. The foams are rotated with the aid of the function "reslice" with a view into all three spatial planes. Using the function "histogram", the number of white voxels representing the void area is determined in relation to all voxels of the cross-sectional area. This examination is also carried out as a function of the virtual coating thickness with the help of CT data. A comparison of this data with the porosity is also made afterwards. With increasing coating thickness, the cross-sectional area decreases for all foams in all three spatial directions (Figure 7.18, 7.19 and 7.20). The largest variation in the cross-sectional area can be seen for the foams of pore size 10 ppi and the smallest for pore size 20 ppi. For all three pore sizes, cross-sectional area differences are seen between all three spatial directions. However,

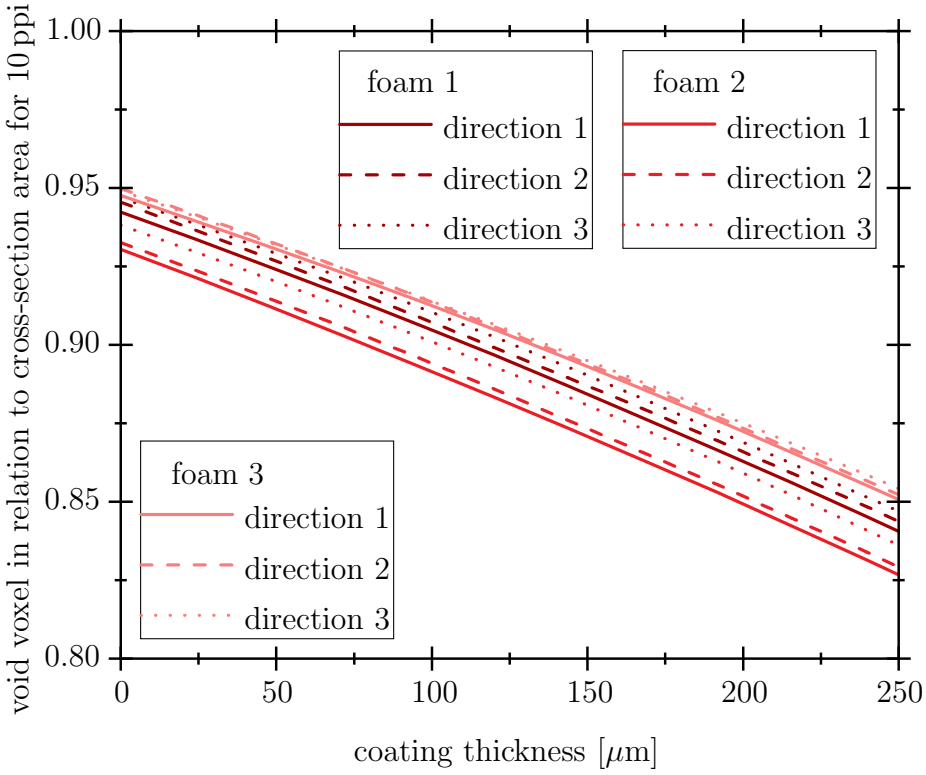

Figure 7.18: Influence of the flow direction of 10 ppi foams

the difference of the values between the spatial directions is smaller than the differences

between the three different foams for all three pore sizes examined. For this reason, it is assumed that the permeability is independent of the flow direction of the foams. Accordingly, the orientation of the foams during the coating process has no influence and does not have to be taken into account, i.e. the foam is isotropic concerning the permeability.

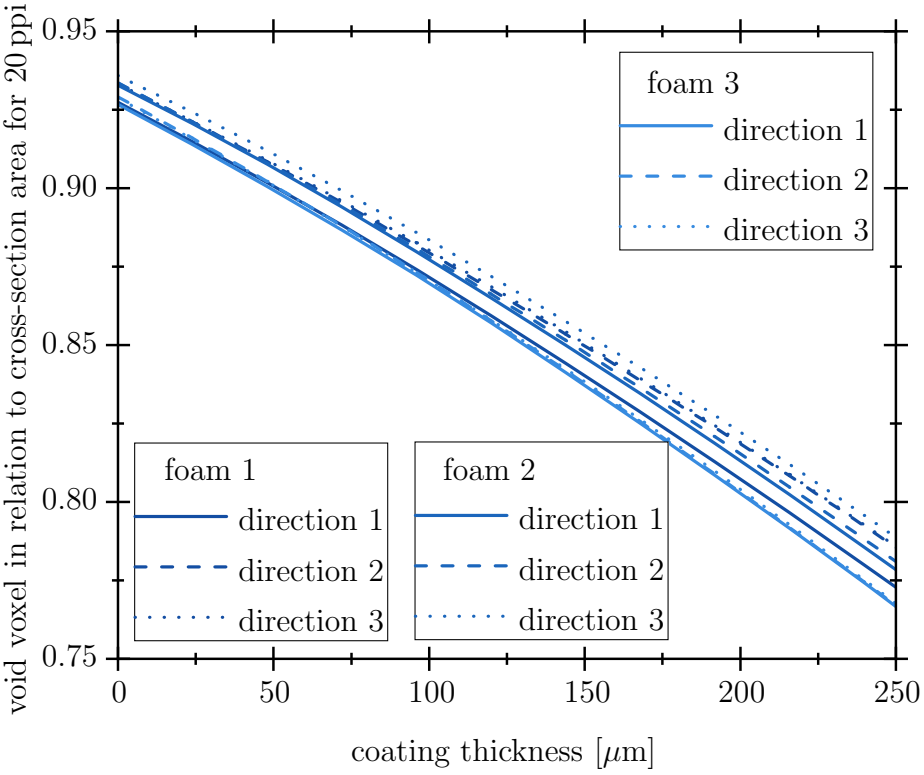

Figure 7.19: Influence of the flow direction of 20 ppi foams

At first glance, it appears that the ratio between the void voxels to the cross-section area corresponds to the porosity. For this reason, Figure 7.21 shows the mean value from Figures 7.18 to 7.20 and the porosity of the corresponding foams as a function of the coating thickness. The porosity values were again obtained with the help of Fiji. Figure 7.21 shows that although the values are similar, there is a deviation in size and slope. Nevertheless, if either the void voxel in relation to the cross-section area or the porosity is not known, the corresponding other value can give a rough indication of the order of magnitude.

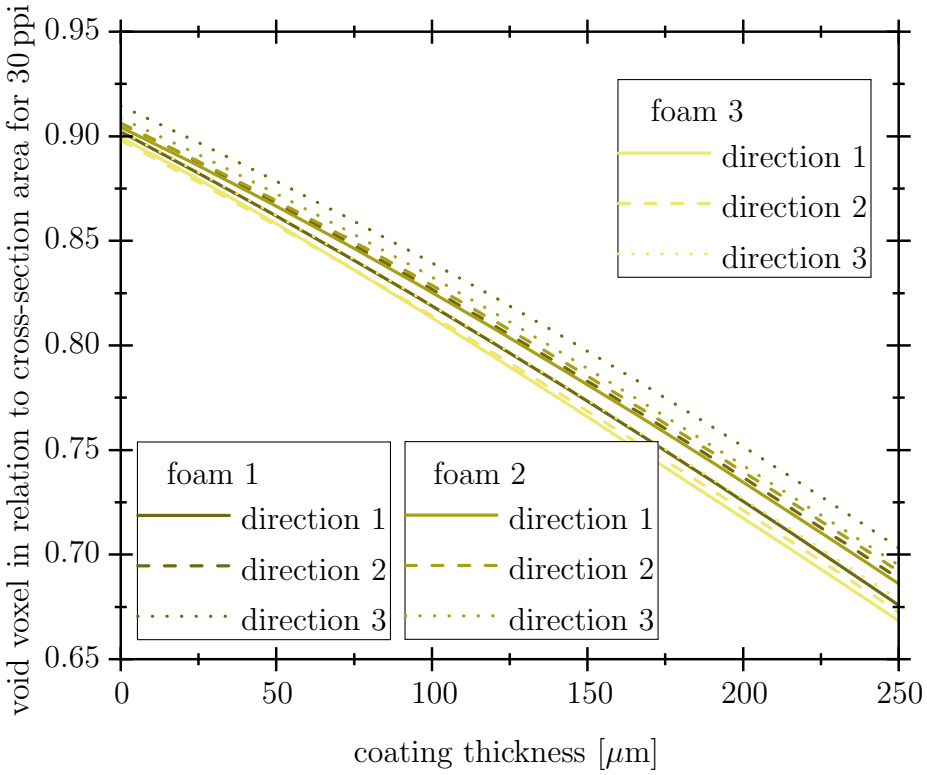

Figure 7.20: Influence of the flow direction of 30 ppi foams

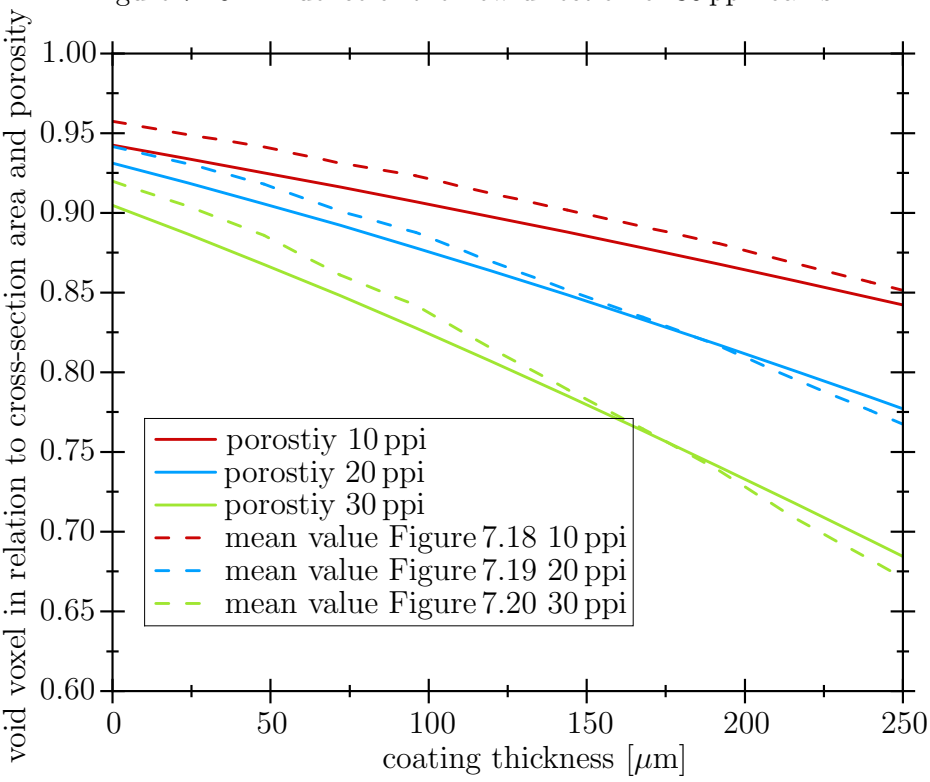

Figure 7.21: comparison between the relation between void voxel to cross-section and the porosity of 10 ppi, 20 ppi and 30 ppi foams

8

Simulation of One-Sided Coupling

Now that all the necessary prerequisites have been derived, and after much discussion about the back-coupling, the one-sided coupling is simulated in this chapter. The previously developed code to determine the ion concentration distribution is used in combination with the observed geometry parameters using 10 ppi, 20 ppi and 30 ppi for this purpose. The test plan created for the experiments in the DoE is used in the simulation. So, the modelling can be verified, and potential error sources between the experiment and simulation can be identified.

8.1 Transforming the Experimental Parameters to the Parameters in Simulation

In the simulation, the adjustable parameters differ from the experiment. Therefore, the parameters from the experiment have to be transformed into the parameters for the simulation. Table 8.1 summarises the different parameters and the different values in experiment and simulation. Concerning the pore size of the foam, there is no difference between experiment and simulation. However, the three dimensional foam used in the experiment is considered in two dimensions in the simulation (Figure 5.6). The foam diameter thus corresponds to the total width y in the simulation, and the foam height corresponds to the total length x in the simulation. The electrolyte has an ion concentration of 110 g/l, which is used as the initial and boundary conditions in the simulation. The temperature is given in unit °C in the experiment; in the simulation, it is converted to Kelvin K for inserting in equation 4.9. The pH value of the electrolyte is

essential for the experiment but is not relevant in the simulation. The parameters duty cycle, targeted coating thickness, and deposition time are related to the experiment. The higher the target thickness, the longer takes the deposition process. Moreover, the higher the duty cycle, the shorter the deposition time has to be. The parameters duty cycle and targeted coating thickness are also related in the simulation. They are summarised in the sink constant. The deposition time taken from the experiment is also used for the calculation of the sink constant. The description of the sink constant

Table 8.1: Adjustable parameters in experiment and simulation

Parameter	Experiment	Simulation
Pore size of foam	20 ppi	20 ppi
Diameter	0.07 m	$y = 70\,\text{mm}$
Height	0.02 m	$x = 20\,\text{mm}$
Concentration electrolyte	$110\,\text{g/l}$	initial condition boundary condition
Temperature	50°C	273 K
pH	3.5	not needed
Duty cycle	DC / PED	sink constant a
Targeted coating thickness	$70\,\mu\text{m}$	
Deposition time	from 51,240 s to 820,260 s	
Current	current density j^{el}	electrical field/ electrical potential
Velocity electrolyte	Volumetric flow rate Q	velocity u
Diffusion constant	not known	diffusion constant

corresponds to the relative deposited mass $m^{\text{rel.}}$ per time

$$a = \frac{\Delta m^{\text{rel.}}}{t}\, d = \frac{\rho^{\text{Ni}} \Delta V^{\text{rel.}}}{\rho^{\text{H}_2\text{O}} t}\, d\,. \tag{8.1}$$

To determine the relative deposited mass $m^{\text{rel.}}$ per time in relation to water, the ratio of the density of Ni ρ^{Ni} and water $\rho^{\text{H}_2\text{O}}$ is multiplied by the relative volume to be deposited $\Delta V^{\text{rel.}}$, and this result is multiplied by the duty cycle d. The value $\Delta V^{\text{rel.}} = 0.04053\,\text{mm}^3/\text{mm}^3$, derived in **Chapter 7** (Figure 7.11), is used for the relative volume change during the deposition process. There are two possibilities for the implementation of the pulsed current, comparable to the DC and PED in experiment (Figure 3.4).

Version I

In **Version I**, the sink constant a is calculated using the duty cycle $d = 0.25$ (eq. (8.1)). The sink constant is kept constant for the complete duration of the simulation (Figure 8.1).

Version II

When calculating the sink constant a, $d = 1$ is used. The value of the sink constant for the experiments considered here is four times higher than in the calculation in **Version I**. However, the sink constant in this version is simulated in a pulsed manner, exactly like the current (Figure 8.1) used in the experiment. Depending on the calculation

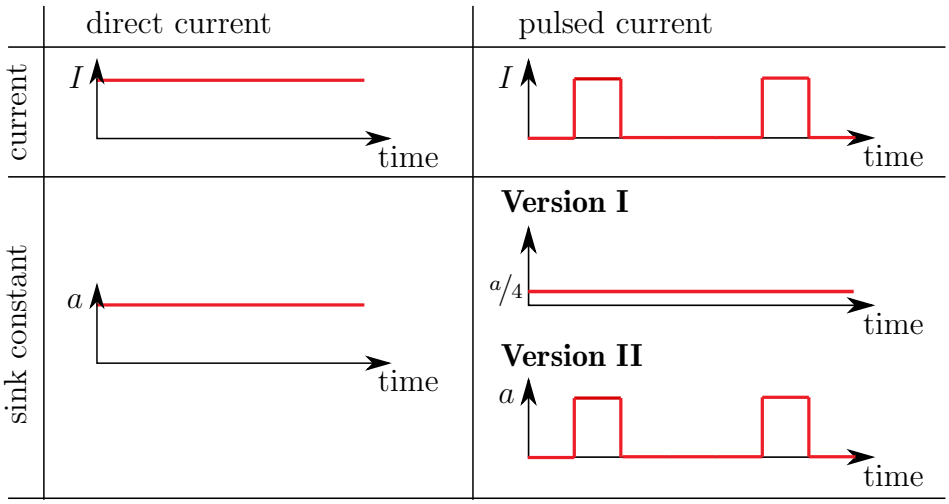

Figure 8.1: Different ways of applying the current on the sink constant, difference between **Version I** and **Version II** shown on the example d = 0.25

method used for the pulsed current and the deposition time, the values in Table 8.2 are obtained for the sink constant a for the desired coating thickness of 70 μm on a 20 ppi foam.

Table 8.2: Different values for a for the different durations and duty cycles of the electrodeposition process

DC		
t [s]	d [s]	a [1/s]
205,000	1	1.8
51,240	1	7.05

PED			
t [s]	d [s]	a [1/s]	**Version**
820,000	1	0.45	**I**
205,000	1	1.8	**I**
820,000	0.25	7.05	**II**
205,000	0.25	1.7625	**II**

In the experiment, the amplitude of the applied current is controlled by the current density. It amounts to either 1 $^{mA}/_{mm^2}$ or 4 $^{mA}/_{mm^2}$. However, the electric field is the

parameter used for the simulation rather than the current density. Conversion between the current density and the electric field is performed using the electric conductivity σ^{el}

$$\mathbf{j} = \sigma^{\mathrm{el}}\, \mathbf{E}\,. \tag{8.2}$$

Either, the value $\sigma^{\mathrm{el}}_{\mathrm{graphit}} = 3 \times 10^6\,{}^{\mathrm{S}}/_{\mathrm{m}}$ could be used, as the foam is dip coated in graphite, or $\sigma^{\mathrm{el}}_{\mathrm{Ni}} = 13.9\ 10^6\,{}^{\mathrm{S}}/_{\mathrm{m}}$ when it is already coated with Ni. It is assumed that a minimal coating with Ni is achieved very fast, and therefore, the duration of the deposition on graphite is very short. So, the value of the electrical conductivity for Ni is used in the simulation. Inserting the values, an electric field of $7.19\ 10^{-5}\,{}^{\mathrm{V}}/_{\mathrm{m}}$ for a current density of $1\,{}^{\mathrm{mA}}/_{\mathrm{mm^2}}$ and an electric field of $2.88\ 10^{-4}\,{}^{\mathrm{V}}/_{\mathrm{m}}$ for a current density of $4\,{}^{\mathrm{mA}}/_{\mathrm{mm^2}}$ is obtained.
Similarly, the volumetric flow rate Q from the experiment is converted to the velocity u in the simulation. This calculation is executed using the cross-sectional area A of the foam

$$u = \frac{Q}{A}\,. \tag{8.3}$$

For a foam of 20 ppi, the cross-sectional area in the uncoated state is 0.93 % as determined in **Chapter 7**. If this is related to the sample diameter, a volumetric flow rate of $Q = 1\,{}^{\mathrm{l}}/_{\mathrm{min}}$ in the experiment results in a velocity of $u = 0.00466\,{}^{\mathrm{m}}/_{\mathrm{s}}$ in the simulation and a volumetric flow rate of $Q = 4\,{}^{\mathrm{l}}/_{\mathrm{min}}$ results in a value of $u = 0.01863\,{}^{\mathrm{m}}/_{\mathrm{s}}$. To quantify the diffusion in the simulation, the value for the diffusion constant is taken from the relevant literature [144] and was set to $D = 0.000096\,{}^{\mathrm{m^2}}/_{\mathrm{s}}$.

8.2 General Simulation Results

The results of DoE experiment 1 and experiment 5 are discussed in detail to describe the results from the electrodeposition process simulation. The knowledge gained from this analysis then allows describing the remaining results more briefly. The parameters used for experiments 1 to 8 are summarised in Table 8.3, with the deviation of the sink constant for all the experiments with pulsed current.

8.2.1 Experiment 1 - Duty Cycle Equals 1

The results converge into a steady state after a time, when simulating experiment 1 from the DoE, using the parameters from Table 8.3, with a spatial step size of $\Delta x = \Delta y = 0.00025\,\mathrm{m}$, and a time step size of $\Delta t = 0.0001\,\mathrm{s}$. This time varies with different parameters, but it less than $4\,s$ in all simulations. The run into a steady state corresponds to the behaviour of the parabolic PDE already described in **Chapter 5**. The

Table 8.3: The different parameters used in simulation for the different experiments of the DoE

	$E = 7.19\ 10^{-5}\ \mathrm{V/m}$		
$u = 0.00466\ \mathrm{m/s}$	experiment 1	$t = 205,000\,\mathrm{s}$	$a = 1.8\ 1/\mathrm{s}$
	experiment 5	$t = 820,260\,\mathrm{s}$	$a = 0.45\ 1/\mathrm{s}$ DC
			$a = 1.8\ 1/\mathrm{s}$ PED
$u = 0.01863\ \mathrm{m/s}$	experiment 2	$t = 205,000\,\mathrm{s}$	$a = 1.8\ 1/\mathrm{s}$
	experiment 6	$t = 820,260\,\mathrm{s}$	$a = 0.45\ 1/\mathrm{s}$ DC
			$a = 1.8\ 1/\mathrm{s}$ PED
	$E = 2.88\ 10^{-4}\ \mathrm{V/m}$		
$u = 0.00466\ \mathrm{m/s}$	experiment 3	$t = 51,240\,\mathrm{s}$	$a = 7.05\ 1/\mathrm{s}$
	experiment 7	$t = 205,000\,\mathrm{s}$	$a = 1.7625\ 1/\mathrm{s}$ DC
			$a = 7.05\ 1/\mathrm{s}$ PED
$u = 0.01863\ \mathrm{m/s}$	experiment 4	$t = 51,240\,\mathrm{s}$	$a = 7.05\ 1/\mathrm{s}$
	experiment 8	$t = 205,000\,\mathrm{s}$	$a = 1.7625\ 1/\mathrm{s}$ DC
			$a = 7.05\ 1/\mathrm{s}$ PED

steady state is reached very fast in the simulation compared to the duration of the experiment to reach the desired coating thickness. This duration underlines the possibility of the approach of comparing the coating homogeneity with the ion concentration in the steady state.

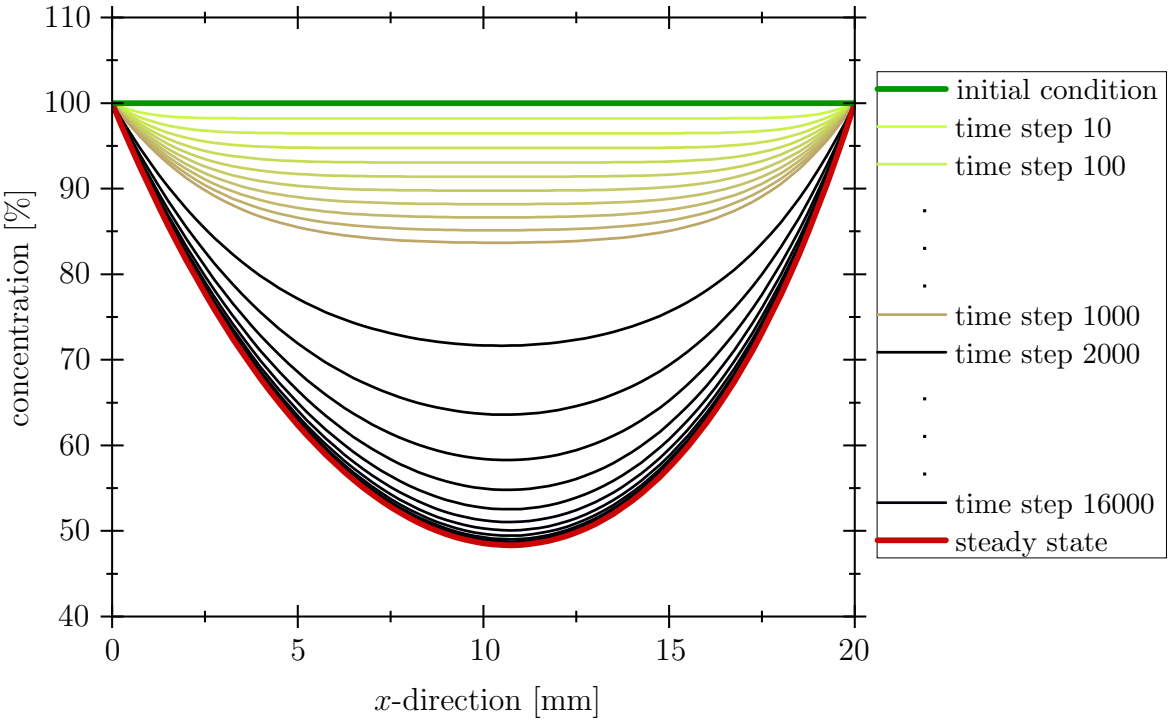

Figure 8.2: Concentration distribution at different time steps of experiment 1

8.2.2 Experiment 5 - Duty Cycle Equals 0.25

The simulation results of **Version I** as well as **Version II** (Figure 8.1) run into a steady state. For **Version I** exactly one steady state is reached (Figure 8.3 a)), for **Version II** several steady states are reached (Figure 8.3 b)). The simulation converges in this case in 200 steady states. The number of steady states for **Version II** depends on the number of time steps passing through a pulse duration. For this reason, the simulations in Figure 8.4 use the frequency of $f = 1250\,\mathrm{Hz}$ (8 time steps to pass one pulse) for the pulse of the PED instead of $f = 50\,\mathrm{Hz}$ (200 time steps to pass one pulse) for the pulse of the PED. This makes it easier to understand the reason for the different steady states. At the frequency of $f = 1250\,\mathrm{Hz}$, there are two time steps with a sink constant of $a = 1.8\,{}^{1}/_{\mathrm{s}}$ and 6 time steps with a sink constant of $a = 0\,{}^{1}/_{\mathrm{s}}$ (Figure 8.4). Consequently, the source is switched on for to time steps and switched off for 6 time steps. The figure shows the steady states of the time steps with the help of dividing with remainder by 8, which results in numbers from 0 to 7. Modulo 8 is the mathematical abbreviation for the calculation with the remainder 8. All steady states are reached within a time of less than $t < 4\,\mathrm{s}$, as in the simulations with DC. The average standard deviation with respect to the mean value over all measured values is 0.255%. Hence, the coating thickness distribution can also be determined for the PED using the concentration distribution in the different steady states. For the results of the PED, the mean value of all steady states is calculated. Also of interest is the question, what influence the phase of the on- and off-cycles has on the different steady states. In the first time step with the current switched on (steady state mod 8 = 0), the concentration distribution becomes smaller and reaches its minimum with the second time step (steady state mod 8 = 1) with the current switched on. If the current is then cut off again for time steps 3 to 8 (steady state mod 8 = 2-7), the ion distribution recovers from time step to time step and has its maximum in time step 8 (steady state mod 8 = 7). The mean value of the simulation with PED does not correspond exactly to the results of the simulation with the same parameters with DC and is discussed further in the comparison between simulation and experiment in Chapter 8.2.3. In general, however, this result shows that the simulation represents the effect of the PED.

8.2.3 Comparison of Experiment and Simulation Flow-Direction

The coating homogeneity of the foam is the highest in the flow direction in the electrodeposition process, according to Jung et al. [87]. For this reason, the model and the simulation are developed to represent the concentration distribution in the electrolyte flow direction. The experimental results 1 to 8 are compared with the corresponding simulations to validate the simulation results. In the simulation of the experiments

a) Version I

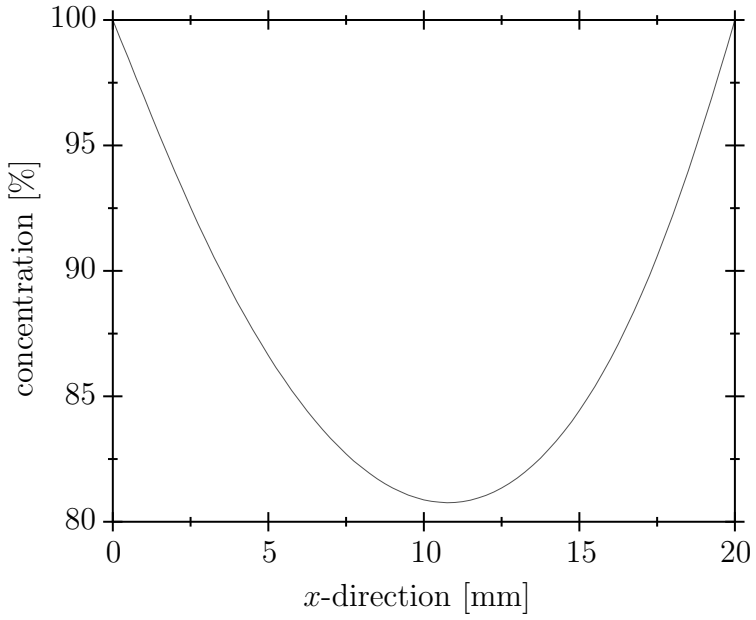

b) Version II

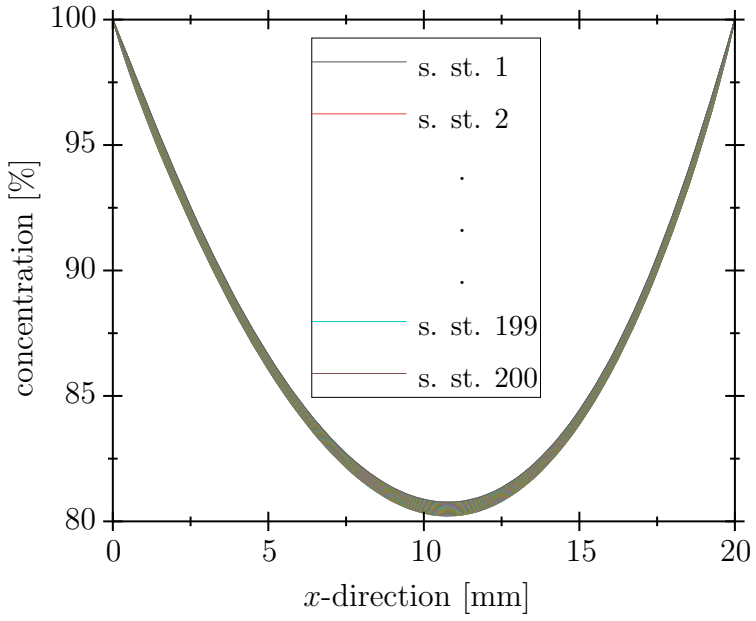

Figure 8.3: Concentration distribution of experiment 5, top: 1 steady state (s. st.) for sink constant, bottom: 200 steady states for sink constant

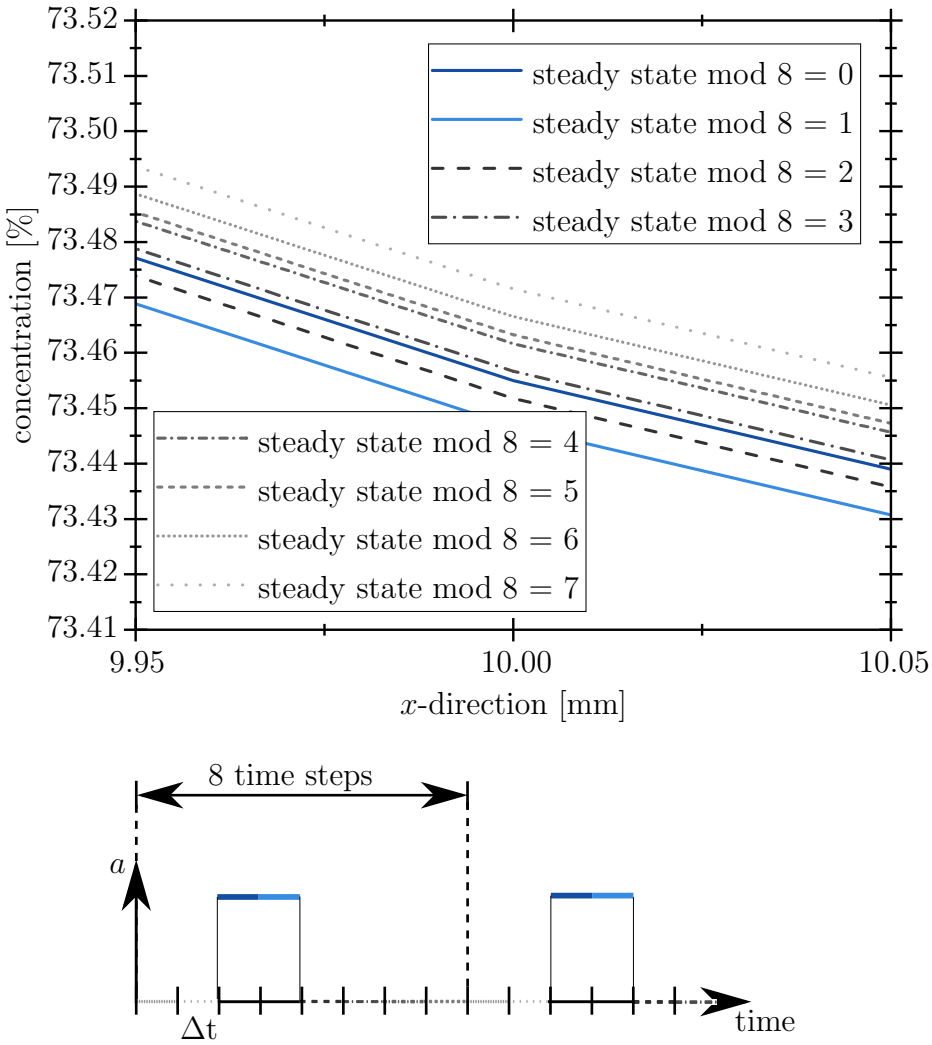

Figure 8.4: Top: Concentration distribution of different time steps of experiment 5 with f=1250 Hz converging into 8 steady states, Bottom: Assignment of the steady states to the different time steps within a pulse and assignment of the results by dividing with remainder

with PED, a distinction is made between the two variants for implementing the sink constants. Since in experiments 1 and 5, 2 and 6, 3 and 7, 4 and 8, only the type of applied current varies between DC and PED, these experiments are shown in one figure, respectively. For enhanced comparability between the experiment and simulation, the relative coating thickness of the experiment is compared with the relative concentration of the simulation. This study can also be evaluated with regard to the effects of the different parameters and the interactions of the parameters with each other caused of the DoE use. Figure 8.5 summarises the experimental design. However, in the first step, the experiment and simulation results are merely compared with one another.

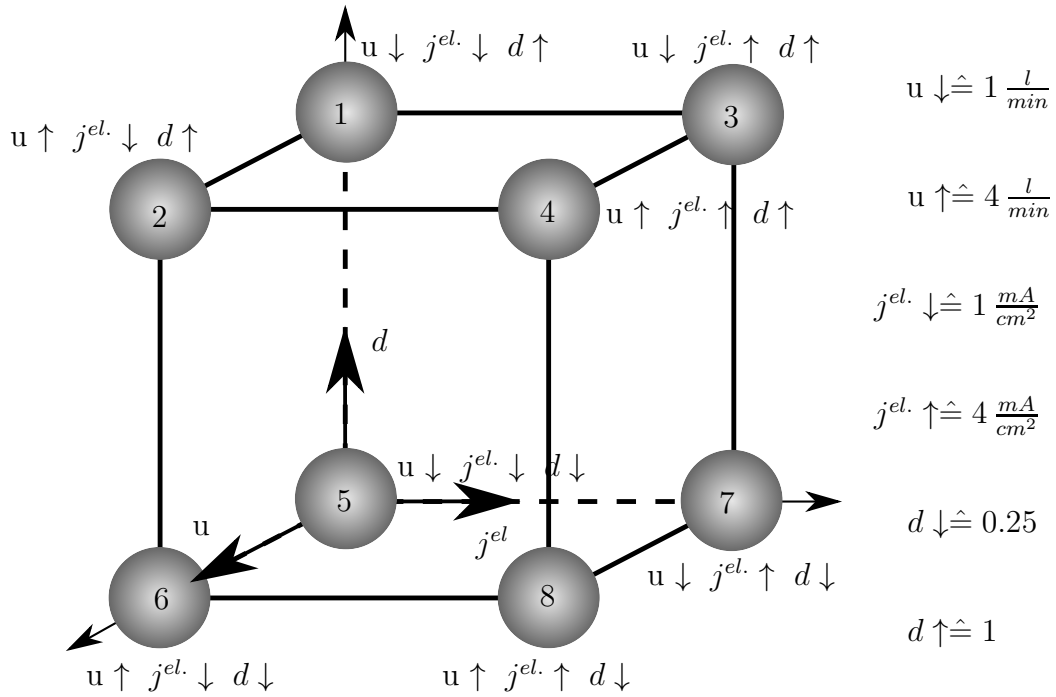

Figure 8.5: Evaluation of the DoE with the presentation of the different experiments, the direction of the change and the choice of parameters

Experiment 1 and 5

The simulated profiles of ion concentration have a parabolic appearance by applying the small velocity and small current density by varying the duty cycle (Figure 8.6). The boundary conditions are met at $x = 0\,\text{mm}$ and $x = 20\,\text{mm}$. Due to convection, the minimum concentration is marginally shifted in the flow direction of the electrolyte. The flow direction equals the x-direction. The simulation results are identical for the experiments with PED for **Version I** and **II**. Both the simulation of experiment 1 and of experiment 5 underestimate the coating thickness in the centre and minimally overestimate the coating homogeneity at the boundary. Overall, the simulation results match the results gained from the experiment very well. The mean error for experiment 1 amounts to 9.3 % for experiment 1 and for experiment 5 to 7.9 %. The exact error for all measuring points for all experiments is summarised in Figure 8.14 and Figure 8.15 in more detail and will be discussed later. The coating homogeneity for experiment 5 with the pulsed sink constant is slightly lower than for the constant sink constant. Even if there are pauses in the ion consumption with the pulsed sink constant and correspondingly an increase in ion concentration in these time steps, there is altogether a higher ion consumption than with the constant sink constant.

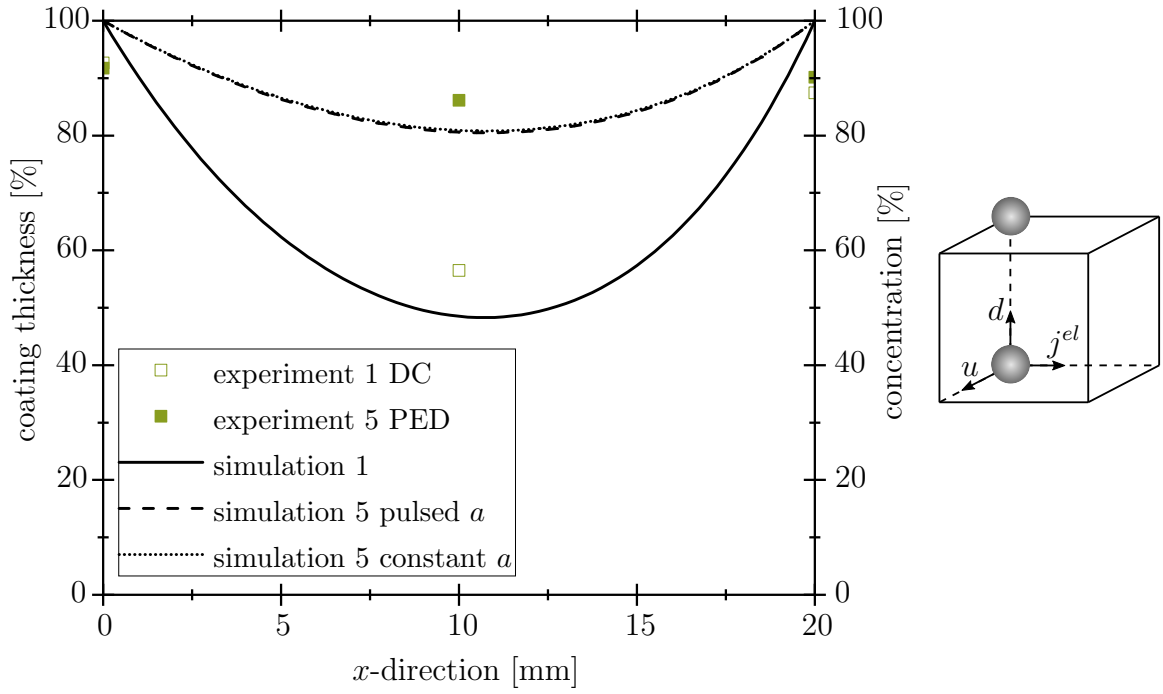

Figure 8.6: Result from the experiment and simulation of experiment 1 and 5 in x-direction, coating thickness for experiment and concentration for simulation

Experiment 2 and 6

For experiments 2 and 6 with a hight velocity and low current density, the trend of the concentration distribution is approximately parabolic, and the boundary conditions are met (Figure 8.7). The simulation results overestimate the coating homogeneity for both the experiment with DC and the experiment with PED. Due to the higher velocity, the minimum of the concentration profile is shifted further to the right than in the previously discussed experiments 1 and 5. Again, the experiment with pulsed current shows a minimally higher ion distribution for the simulation with constant sink constant as opposed to the simulation with pulsed sink constant. The average error over the three measuring points equals 7.4% in experiment 2 and 20.5% in experiment 6. The largest deviation between experiment and simulation is found at the point x=10 mm with 19% in experiment 2 and 33% in experiment 6. The error increase suggests that the assumption of a constant velocity over the entire foam at higher velocities is not accurate.

Experiment 3 and 7

The results of experiments 3 and 7 (Figure 8.8) with a higher current density and thus a larger sink constant compared to experiments 1 and 5 agree with the results of the pre-

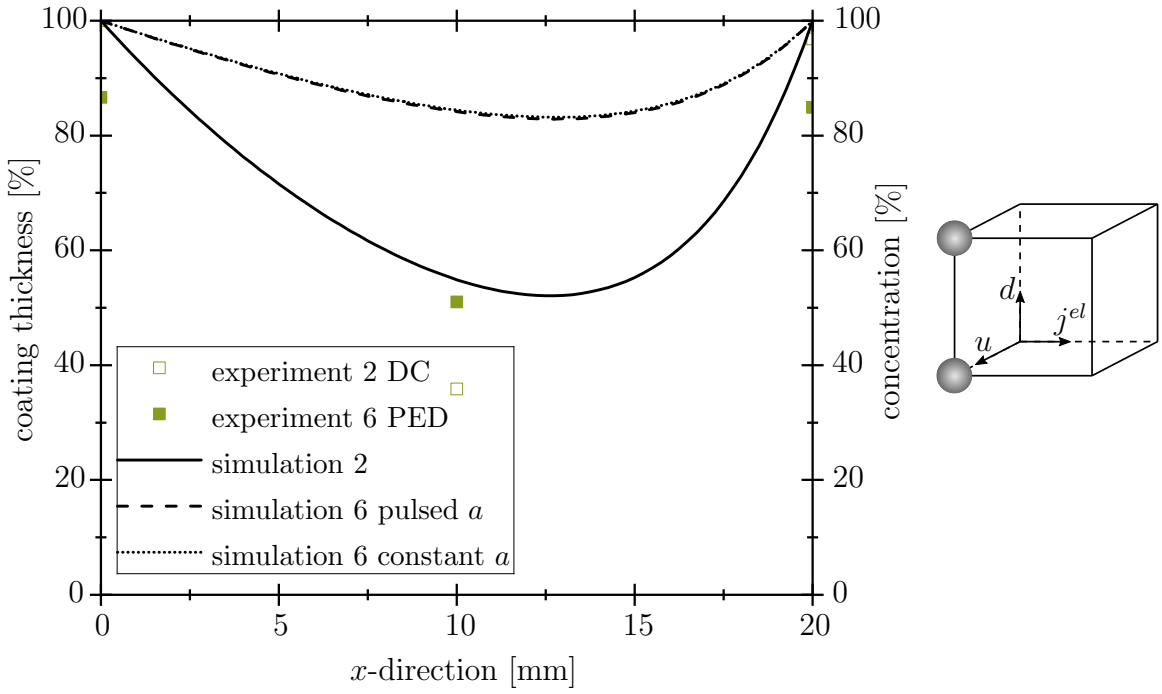

Figure 8.7: Result from the experiment and simulation of experiment 2 and 6 in x-direction, coating thickness for experiment and concentration for simulation

vious experiments. Due to the low flow velocity, the trend is parabolic, and the curve's minimum is minimally shifted to the right. For experiment 3 with DC, the simulation underestimates the coating homogeneity from the experiment; for experiment 7 with PED, the concentration distribution overestimates the coating homogeneity. Again, the experiment with PED leads to a lower concentration distribution for the pulsed sink constant than the experiment with the constant sink constant. The average error equals 29.8% for experiment 3 and 10.3% for experiment 7. The high average error of experiment 3 is caused by the high error at the boundaries at x = 0 mm with 33% and at x = 20 mm with 52%. The error at x = 10 mm equals 5%.

Experiment 4 and 8

In experiments 4 and 8 (Figure 8.9), the coating homogeneity for experiment 8 with PED is lower than the coating homogeneity for experiment 4 with DC. In contrast to this observation, the simulation confirms the results from the previous experiments. Due to the higher velocity compared to experiment 1, the minimum is shifted slightly to the right, and the coating homogeneity is slightly lower. This effect is caused by the higher current density and the associated higher sink constant. As already seen in the other simulations for the PED, the ion concentration for the simulation with the pulsed sink constant is lower than the ion concentration for the simulation with the

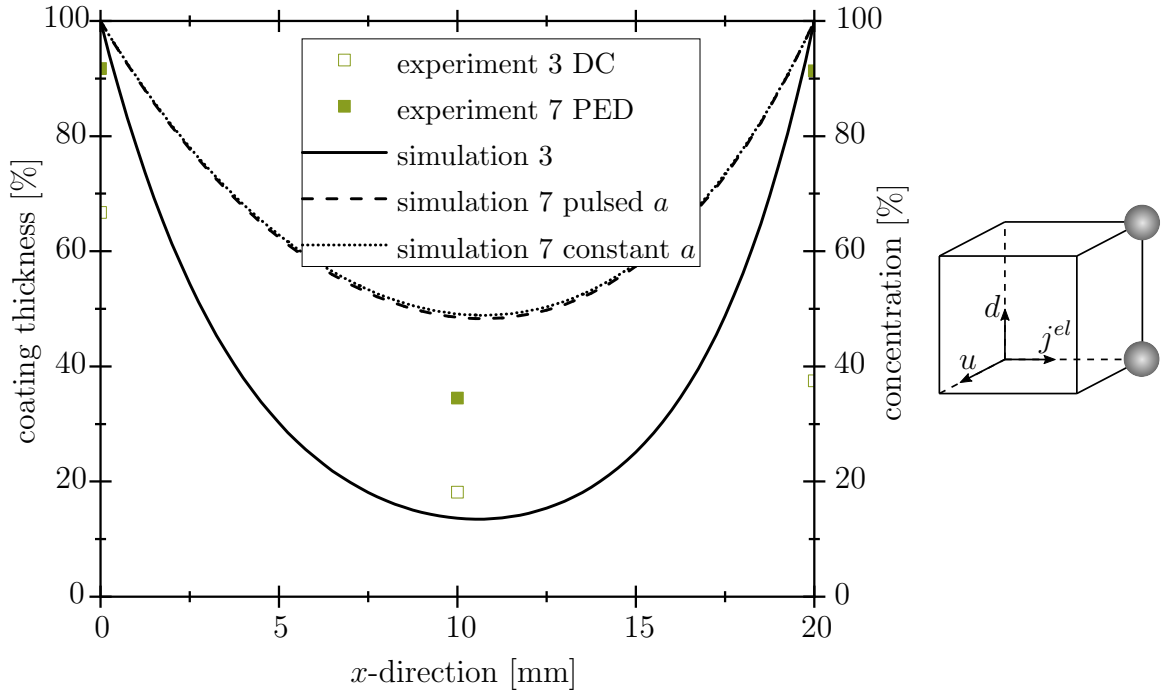

Figure 8.8: Result from the experiment and simulation of experiment 3 and 7 in x-direction, coating thickness for experiment and concentration for simulation

constant sink constant. The average error equals 8.7% for experiment 4 and 23.2% for experiment 8.

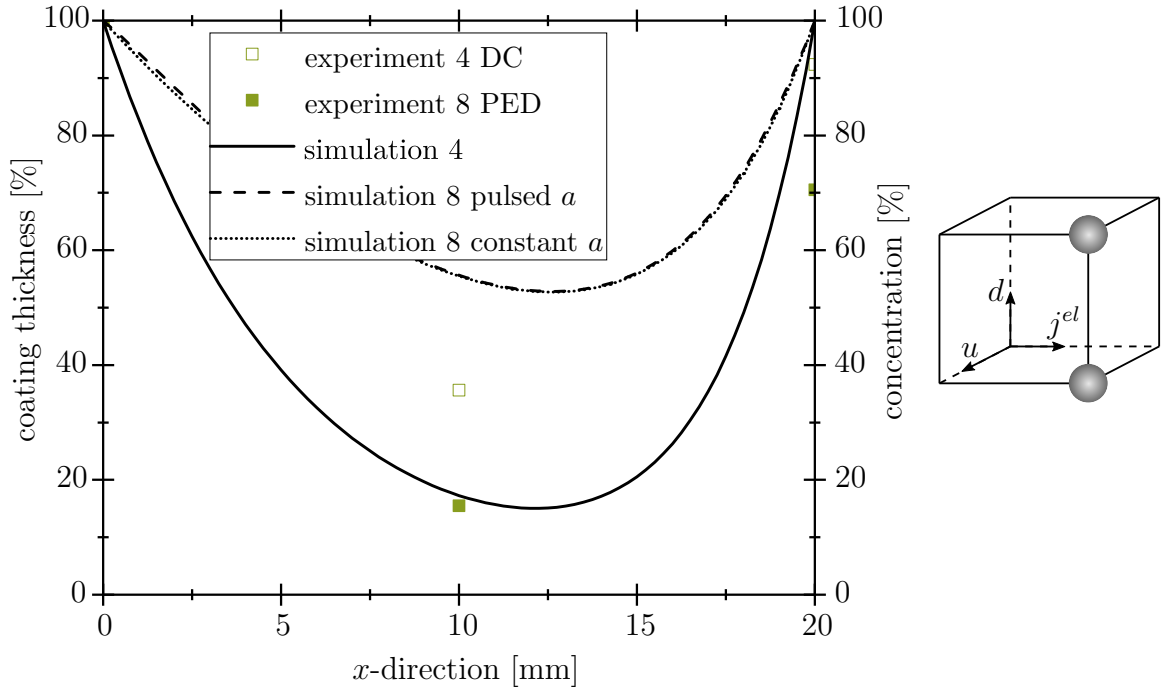

Figure 8.9: Result from the experiment and simulation of experiment 4 and 8 in x-direction, coating thickness for experiment and concentration for simulation

8.2.4 Comparison of Experiment and Simulation in y/z-Direction

Even though the model is designed to optimise the coating homogeneity in the electrolyte flow direction, i.e., in the x-direction and not in the radial y- and z-directions, the results from the simulation may also be compared with the results from the experiment in the radial direction. Since the rotational sample symmetry was used in the simulation, the result corresponds to the experiment's results in the y- and z-directions. Therefore, both directions are shown in the same diagram. As with the results in the x-direction, experiments 1 and 5, 2 and 6, 3 and 7, as well as 4 and 8, are each shown in a single diagram, respectively.

Experiment 1 and 5

The results of experiment 1 with DC show a lower coating and concentration homogeneity than the results of experiment 5 with PED in both experiment and simulation (Figure 8.10). For the simulation results, the implementation version of the PED has no significant influence. However, the ion concentration is minimally higher for a constant sink constant than for a pulsed sink constant. Both simulations are within the results of the experiment. The values of $y = z = 35\,\text{mm}$ correspond to the value of x = 10 mm in Figure 8.6. This value in the simulation is slightly above the other values in Figure 8.10 for both experiments 1 and 5. Accordingly, the simulation matches the results from the experiment very well, tending to be better than expected with regard to Figure 8.6. The average error equals 6.3% for experiment 1 and 8.9% for experiment 5.

Experiment 2 and 6

Experiments 2 and 6 show similar results as experiments 1 and 5 (Figure 8.11). Due to the higher velocity of the electrolyte, the coating homogeneity is slightly higher in the simulation and the experiment. The trend is symmetrical, and in the experiment, as well as in the simulation, the coating and concentration homogeneity is lower for DC than for PED. For experiment 2 and experiment 6, the simulation overestimates the coating homogeneity. The average error equals 16.5% for experiment 2 and 36.7% for experiment 3. These errors underline the results of experiment 2 and 6 in x-direction.

Experiment 3 and 7

For experiment 3, the simulation corresponds to the results from the experiment (Figure 8.12). As seen for experiments 1 and 2, the coating thickness at $x = 35\,\text{mm}$ is slightly higher than the other coating thicknesses. Thus, the coating homogeneity in

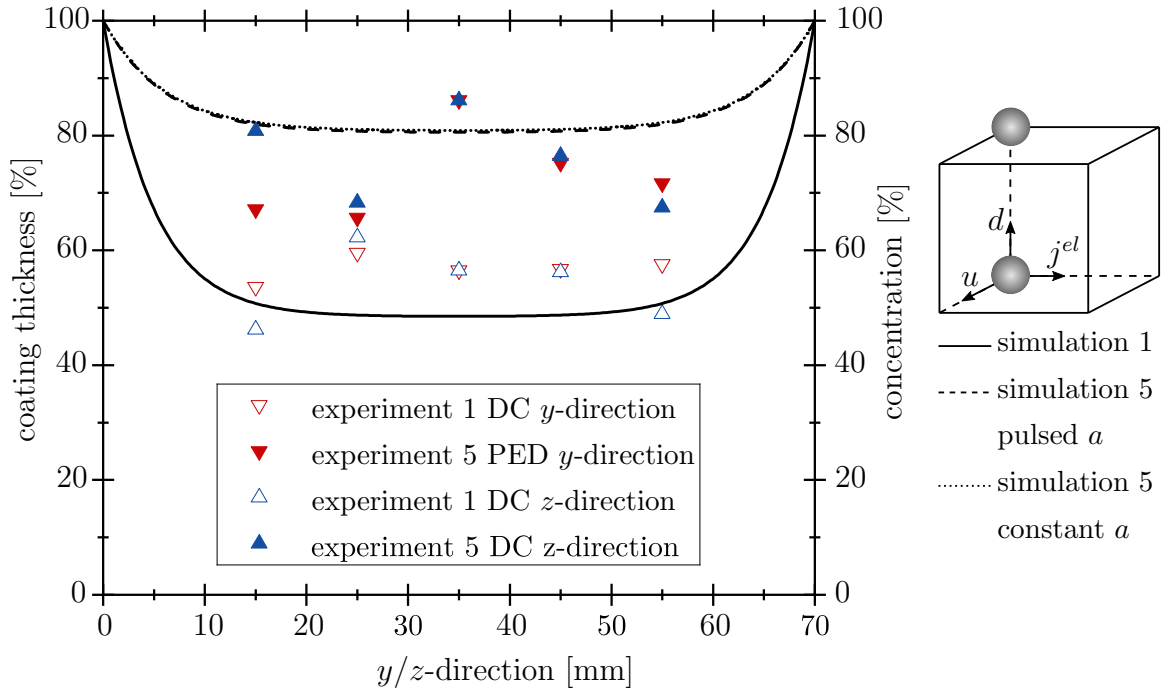

Figure 8.10: Result from the experiment and simulation of experiment 1 and 5 in y/z-direction, coating thickness for experiment and concentration for simulation

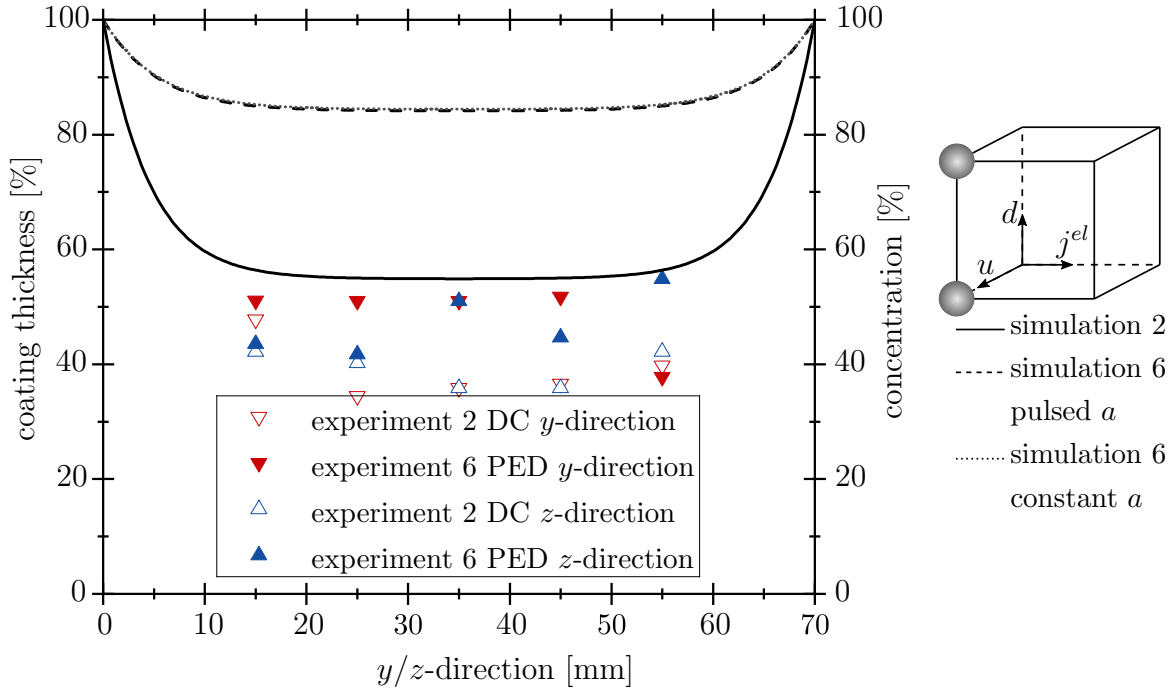

Figure 8.11: Result from the experiment and simulation of experiment 2 and 6 in y/z-direction, coating thickness for experiment and concentration for simulation

the experiment tends to be better than expected, as shown in Figure 8.8. For experiment 7 with PED, the simulation overestimates the coating homogeneity from the

experiment. The average error equals 1.8% for experiment 3 and 15.4% for experiment 7.

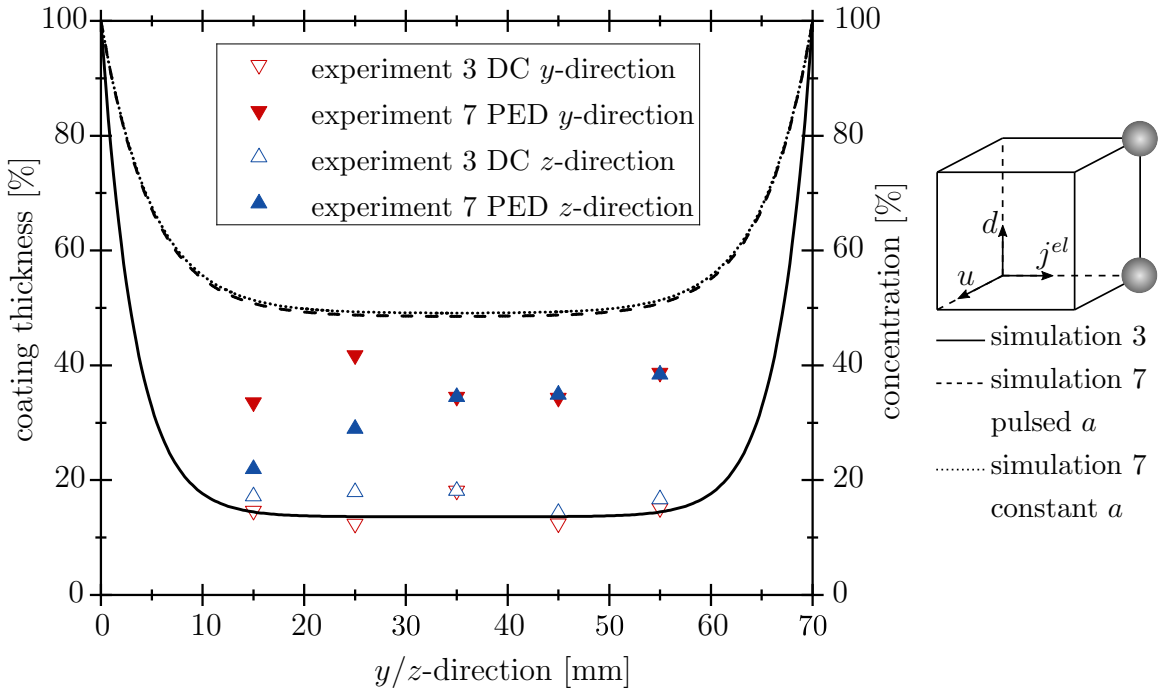

Figure 8.12: Result from the experiment and simulation of experiment 3 and 7 in y/z-direction, coating thickness for experiment and concentration for simulation

Experiment 4 and 8

As with the results in the x-direction, the coating homogeneity in the y/z-direction is also higher for experiment 4 with DC than for experiment 8 with PED (Figure 8.13). For the simulation, however, the results are lower for experiment 4 with DC than for experiment with PED. The results from the simulation overestimated the results from the experiment for experiment 8 and underestimated the results from experiment 4. The average error equals 13.8% for experiment 4 and 41.3% for experiment 8.

Summary of the Comparisons between Experiment and Simulation

In general, the model and thus the simulation describes the coating homogeneity relatively well (Figure 8.14 and 8.15). Especially for the low velocity (grey and light red) and the low current density (grey and black), the results from the simulations and the experiments show almost perfect agreement. For high velocities combined with the PED, however, the error is relatively high. Here, the simulation overestimates the results from the experiment immensely. In general, the simulation overestimates the

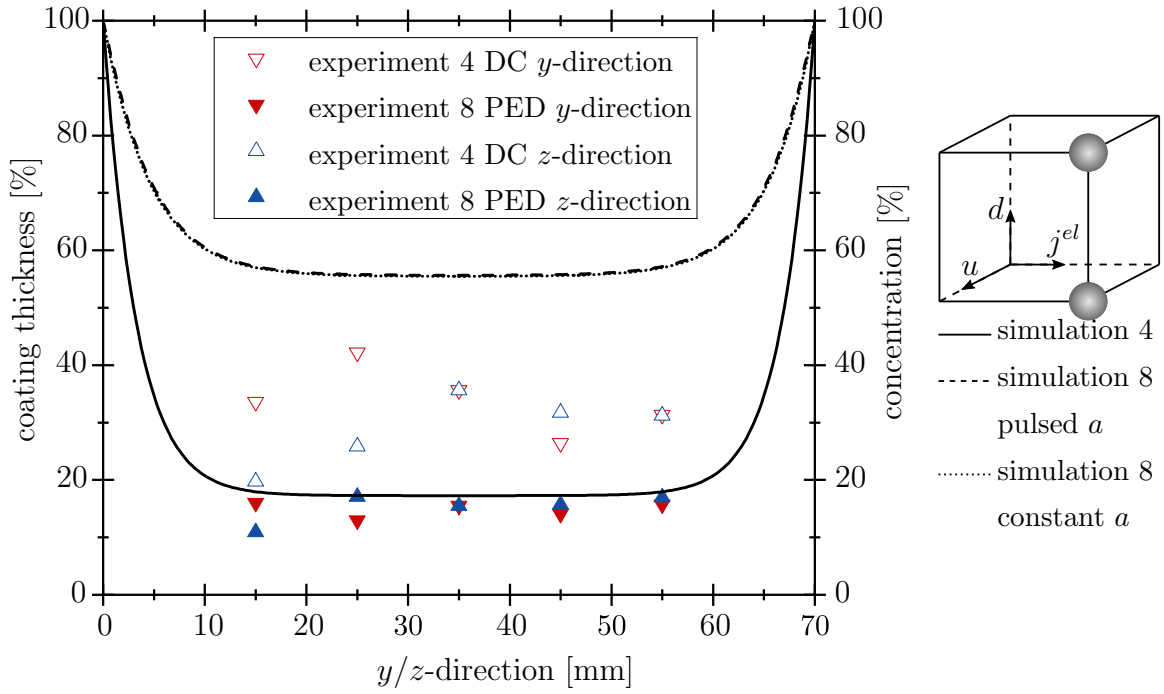

Figure 8.13: Result from the experiment and simulation of experiment 4 and 8 in y/z-direction, coating thickness for experiment and concentration for simulation

coating homogeneity at the boundary, which is related to the given boundary condition of $c = 110\,g/l$ in the simulation.

To determine the influencing factors between simulation and experiment more precise, the DoE will now be evaluated with respect to the target variables:

- difference between coating thickness in experiment and simulation
- difference between the maximum and the minimum coating thickness in the simulation, consequently the coating homogeneity.

Both target variables are examined with respect to the parameters velocity, current density and duty cycle.

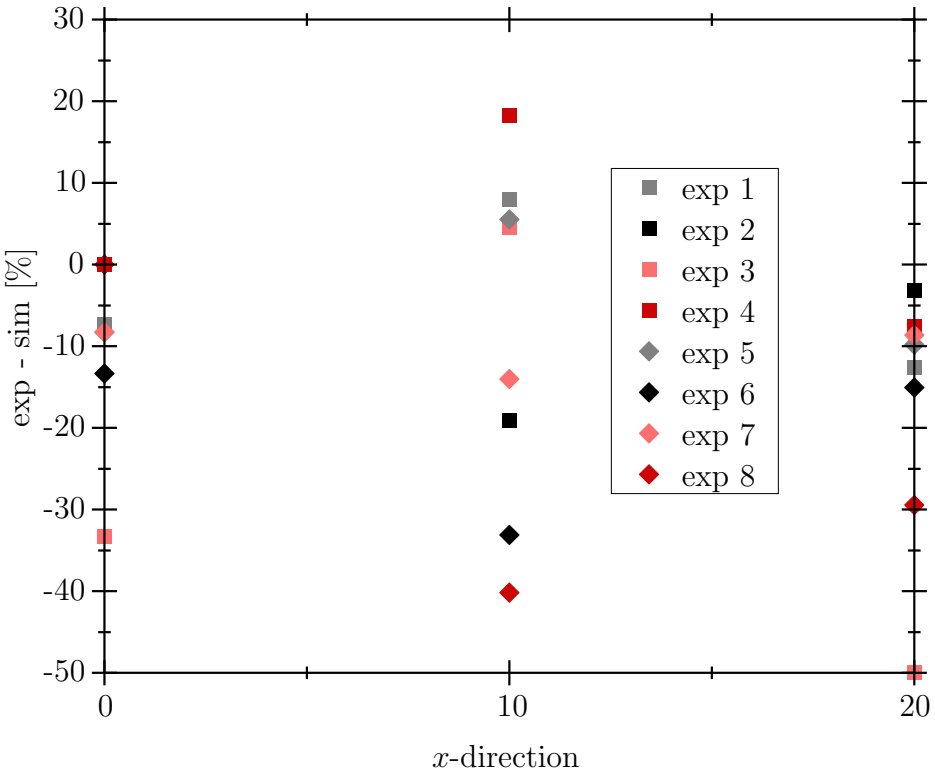

Figure 8.14: Error between experiment and simulation in percent in x-direction, with the variables of the DoE

8.3 Evaluation of the DoE

Following the qualitative and quantitative comparison between experiment and simulation, the DoE will now be evaluated with regard to the effects and interactions of the parameters velocity, current density and duty cycle.

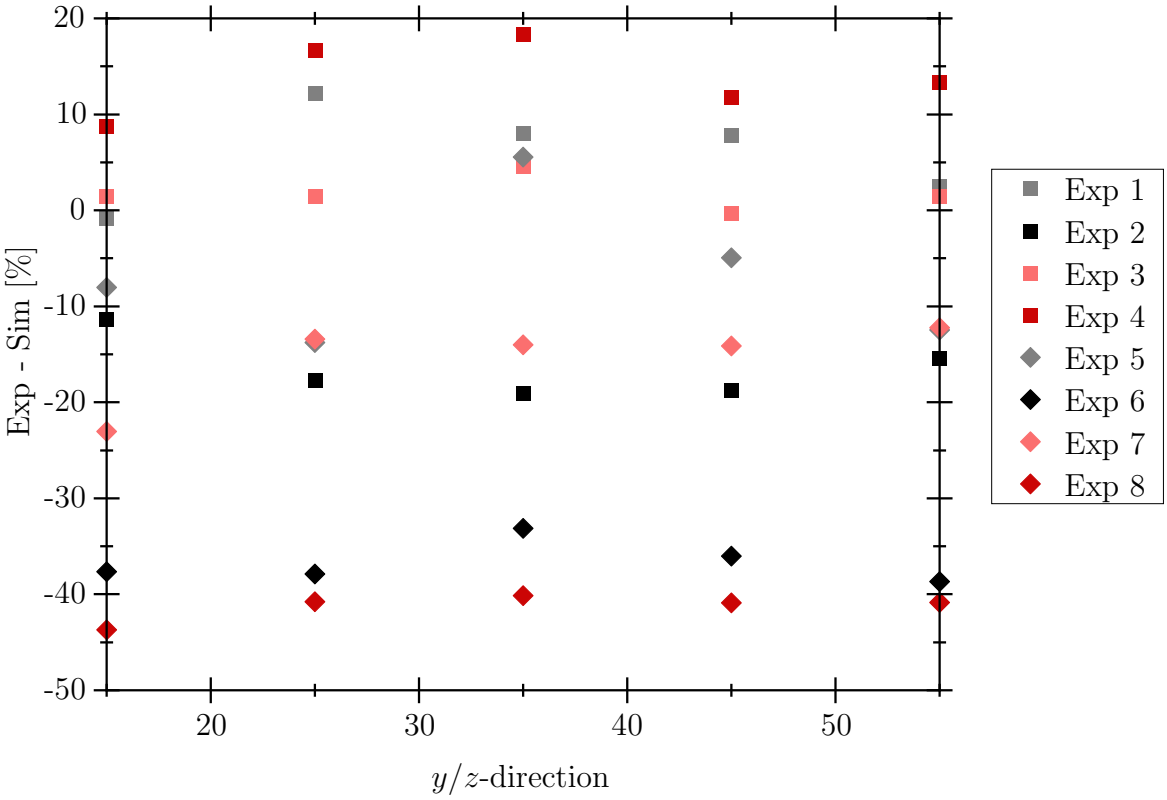

Figure 8.15: Error between experiment and simulation in percent in y/z-direction, with the variables of the DoE

8.3.1 Difference between Simulation and Experiment

Effect

The difference between the coating thickness from the experiment and the concentration from the simulation is calculated to evaluate the DoE with regard to the target variable difference between the experiment and simulation. Figure 8.16 shows the influence of the parameters velocity, current density and duty cycle on this target variable. The higher the slope of the line, the higher the influence of the corresponding variable on the target variable. The duty cycle has the highest influence (m = -13.13). The difference between experiment and simulation decreases as the duty cycle increases. The velocity also has a high influence (m = 8.59). With increasing velocity, the difference between the experiment and simulation increases. The current density has minor influence (m = -1.17).

Interaction

The interaction of the different parameters with each other in relation to the target variable can also be determined by evaluating the DoE. The higher the difference in the slope, the higher the interaction between the two parameters. Here, all parameters

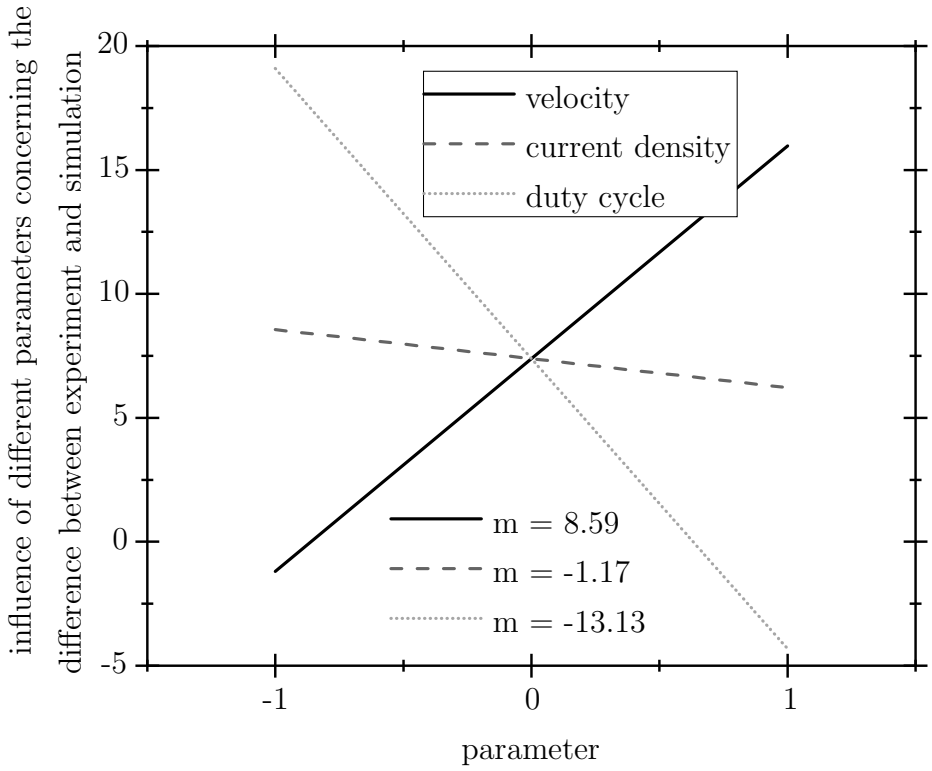

Figure 8.16: Effect of the parameters on coating thickness in the experiment and the ion concentration in the simulation

have similar interactions (Figure 8.17). The highest interaction is between the duty cycle and the current density ($\Delta m_{d\ on\ j} = -14.33$), followed by the interaction between the current density and the velocity ($\Delta m_{j\ on\ u} = -13.80$). The duty cycle and the velocity have the lowest interaction ($\Delta m_{d\ on\ u} = -12.88$).

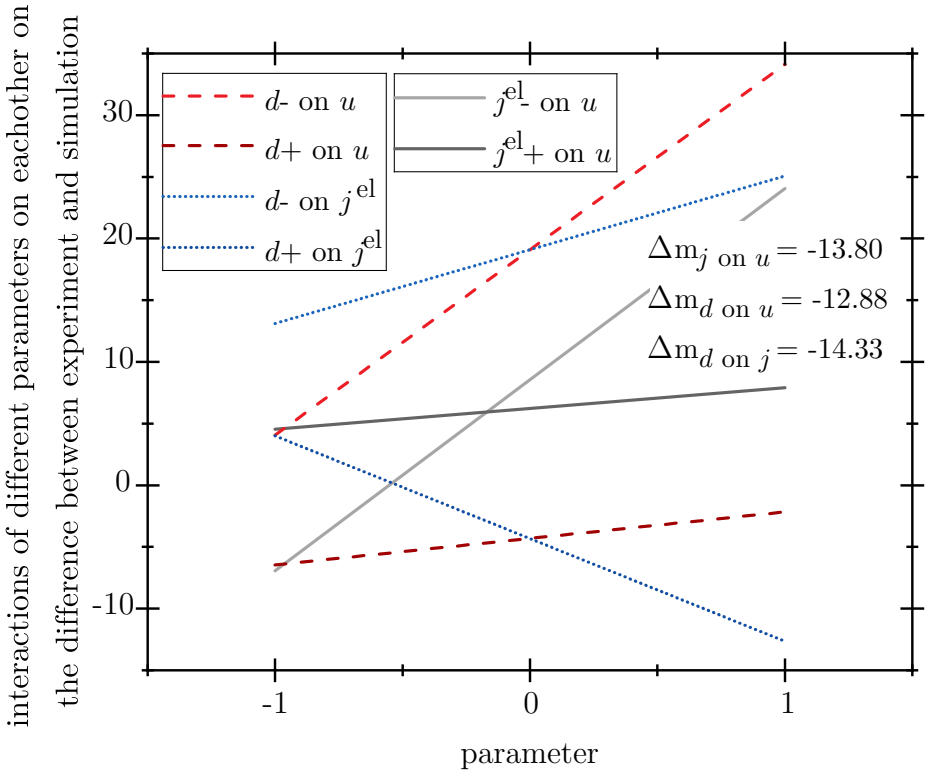

Figure 8.17: Interaction of the parameters on the coating thickness difference between experiment and simulation

Result of the Evaluation of the DoE Regarding the Difference Between Experiment and Simulation

Possible improvements of the model beyond the scope of this work are presented here in addition to the evalutaion of the DoE. The duty cycle strongly influences the difference between simulation and experiment, particularly for the low value of the duty cycle, i.e., the experiments with PED. This influence results in an improvement in the implementation of the duty cycle. In the experiment, the PED repeatedly switches the current on and off. Consequently, the electric field has to be built up and depleted, again and again, resulting in electrical shielding. The simulation can better reproduce the experiment by including electromagnetic shielding in the implementation. The implementation of the velocity should also be improved, and this can be achieved by including Darcy's law in the simulation in order to mimic a non-constant velocity distribution over the foam. Due to the interactions between the current density and both, velocity and duty cycle, the influence of the current density will also change when the parameters duty cycle and velocity are adjusted. For this reason, changing these parameters also affects the current density. Improving the implementation of the current density can therefore be dispensed with in the first step. All considerations made in this section will help to improve the model in further work.

8.3.2 Evaluation of the DoE Difference between Maximum and Minimum Coating Thickness in Simulation

Effect

The DoE can also be evaluated to examine the effect and interactions on the second target value, the difference between the maximum and minimum coating thickness in the simulation. Figure 8.18 shows the influence of the parameters velocity, current density and duty cycle on the coating homogeneity in the simulation. The duty cycle (m = -18.51) has the most substantial influence. With an increase in the duty cycle, the homogeneity in the simulation also increases. The second-highest influence is caused by the current density (m = 16.86). With an increase in current density, the coating homogeneity becomes poorer. The most negligible influence is due to the velocity (m = -2.01). With an increase in velocity, the coating homogeneity increases slightly.

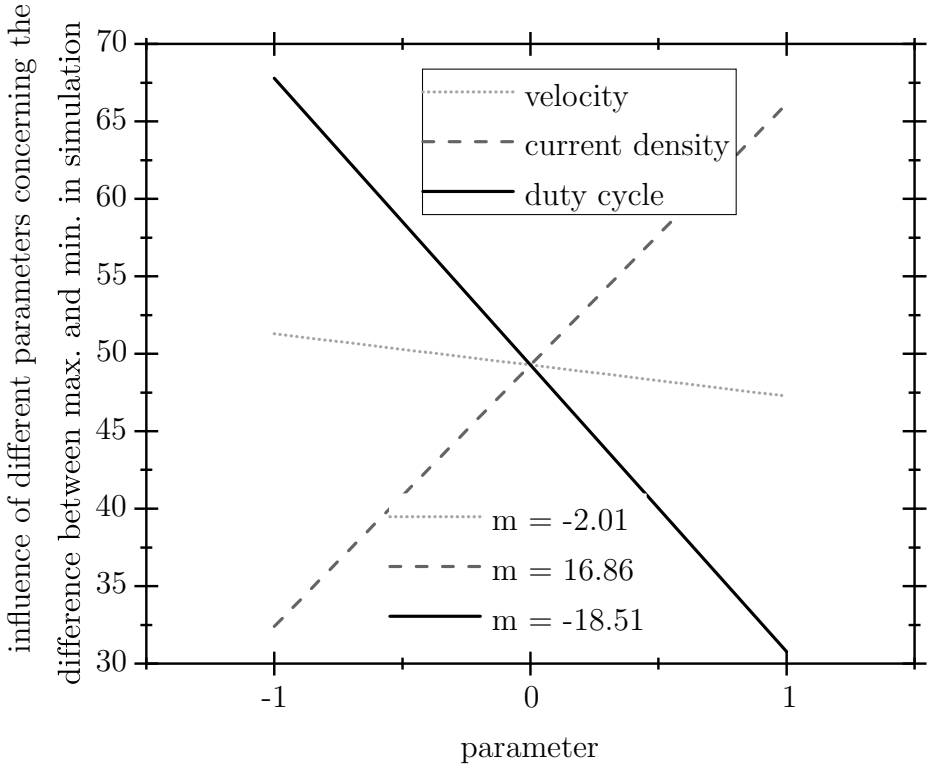

Figure 8.18: Effect of the parameters on the coating thickness homogeneity in simulation

Interaction

The interaction of the parameters with each other is minimal in the simulation. This low level of interaction results from the model choice, which disregards interactions between the parameters of the DoE. A back-coupling would have to be considered to include these interactions. The highest level of interaction is between the current density and

the duty cycle, and the velocity interacts least with the two other parameters duty cycle and current density. The influence of the parameters diffusion constant, electrical field and sink constant also has to be examined separately. Therefore, a sensitivity analysis will be carried out with these parameters in Chapter 8.4.1.

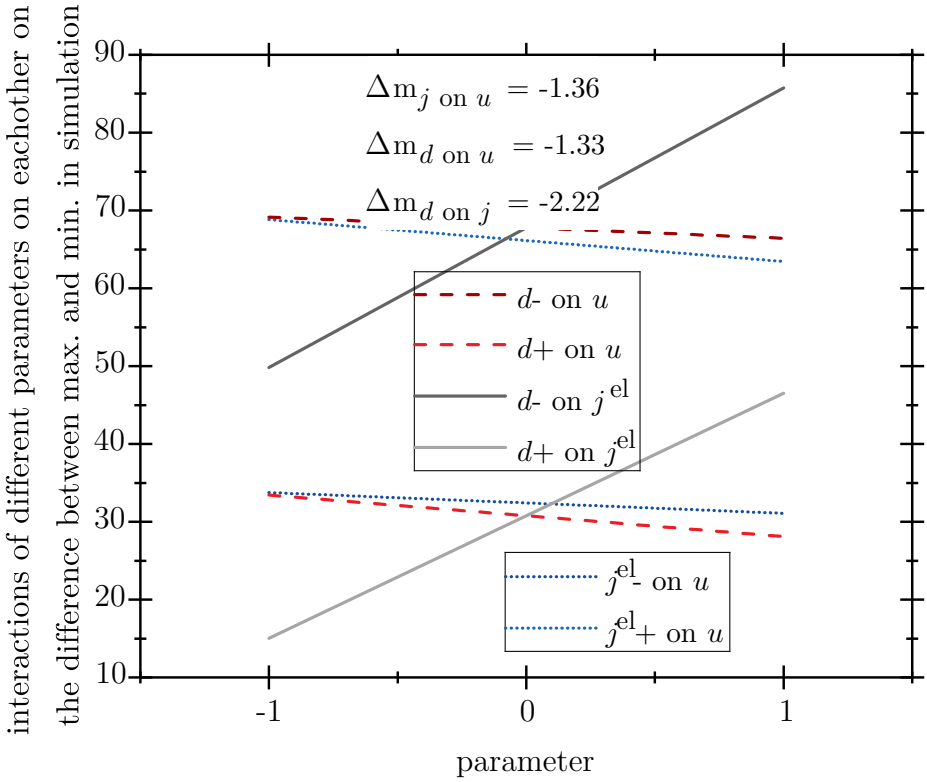

Figure 8.19: Interaction of the parameters on the coating thickness homogeneity in simulation

Result of the Evaluation of the DoE Regarding the Difference Between Minimum and Maximum Coating Thickness in the Simulation

On the one hand, the duty cycle chosen should be as high as possible, i.e., a deposition with DC, in the simulation to achieve a homogeneous coating thickness. However, this does not correspond to the observations made in experiments, where a PED coated foam is more homogeneously coated than a foam, coated with DC. Additionally, the current density chosen should be as low as possible, i.e., with the smallest possible sink constant. This corresponds to the observations that were made in the experiment. Therefore, the current density also has a minor influence on the difference between experiment and simulation. However, lowering the current density and lowering correspondingly the sink constant leads to increased processing time in the experiment. Therefore, a current density variation must always be carefully assessed in terms of pros and cons. The velocity also has a positive influence on the coating homogeneity. This influence is not represented well enough in the simulation, explaining the velocity effect on the

differences between the experiment and the simulation. However, in the experiment, an increase in the velocity can lead to spoiled Ni and thus to poorer material properties [57]. Further experimental test series must examine this effect in more detail.

8.3.3 Results of the Evaluation of the DoE

Considering the simplicity of the model, the simulation reproduces the experiments very well. Especially for low velocities and high duty cycles, the results from experiments and simulations agree to an extraordinary degree. The quality of the simulation can be further enhanced by improving the velocity implementation, with solving the Darcy-law in the context of a back coupling, and by including electrical shielding for the implementation.

8.4 Examination of the Parameter Influence on the Coating Thickness Homogeneity in the Simulation

8.4.1 Sensitivity Analysis

The duty cycle and current density (consequently, the electric field) are linked in the simulation via the sink constant. Thus, no clear statement can be made about which of these parameters has the higher influence. This influence, as well as the influence of other parameters used in the simulation, is not covered by the DoE. Therefore, a sensitivity analysis was carried out to examine the influence of the parameters diffusion constant, electrical field and sink constant on the coating homogeneity in the simulation. In order to compare the results of this research with the results of the DoE, the influence of velocity was also examined. For the sensitivity analysis, each parameter was increased and decreased by a factor of 0.5 respectively. The sensitivity analysis was carried out for experiment 1 for DC and experiment 5 for PED. These experiments can be seen as initial setup, where the coating thickness homogeneity in the executed experiment was the best [57].

Experiment 1

The reduction of the sink constant has the highest influence on the concentration distribution. The increase in the velocity and the diffusion constant have a similar influence. A change in the concentration distribution due to a change in the electric field is not visible (Figure 8.20). This can be explained by the relatively small influence of migration on the electrodeposition process, which has also been described in the relevant

literature [63, 125] and can also be derived analytically. According to **Chapter 6**, the convection and migration model parts have the same appearance and could, therefore, be validated in the benchmark tests with the same methods. The velocity has a value of $0.00466\,{}^{m}/_{s}$ in the simulation, and the equivalent of the migration has a value of $5.86 \times 10^{-7} {}^{m}/_{s}$. Since convection already has no major influence on the coating homogeneity, migration has an even smaller influence by a factor of about 4 orders of magnitude. A reduction by a factor of 0.5 hardly changes the coating homogeneity for the velocity. However, the minimum of the concentration distribution is shifted slightly to the left, so the symmetry of the solution increases. Increasing the sink constant only weakly reduces the ion concentration, and decreasing the diffusion constant reduces the ion concentration the most. This underlines the neither diffusion nor convection dominant experiment that it is.
The velocity should be increased, care should be taken to ensure high diffusivity during the experiment, and the sink constant should be reduced to increase the ion concentration and thus homogenise the coating thickness. However, a reduction in the sink constant is accompanied by an increase in the experimental process duration, which is only desired to a limited extent.

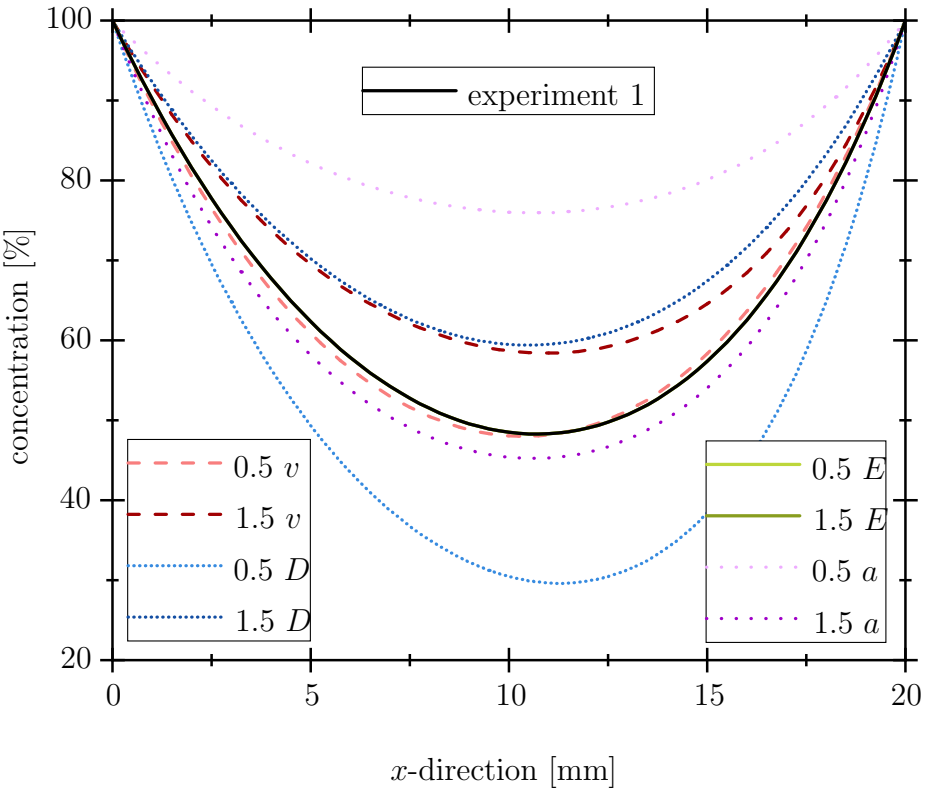

Figure 8.20: Influence of different simulation parameters on the ion concentration of experiment 1

Experiment 5

In the sensitivity analysis of experiment 5 (Figure 8.21), a change in velocity has the most negligible visible influence, and a change in the sink constant has the most substantial influence. The influence of the electric field is not visible. Using the PED in experiment 5, the influence of the sink constant is obviously already so enormous that only the diffusion constant and the sink constant significantly influence the ion concentration within the foam.

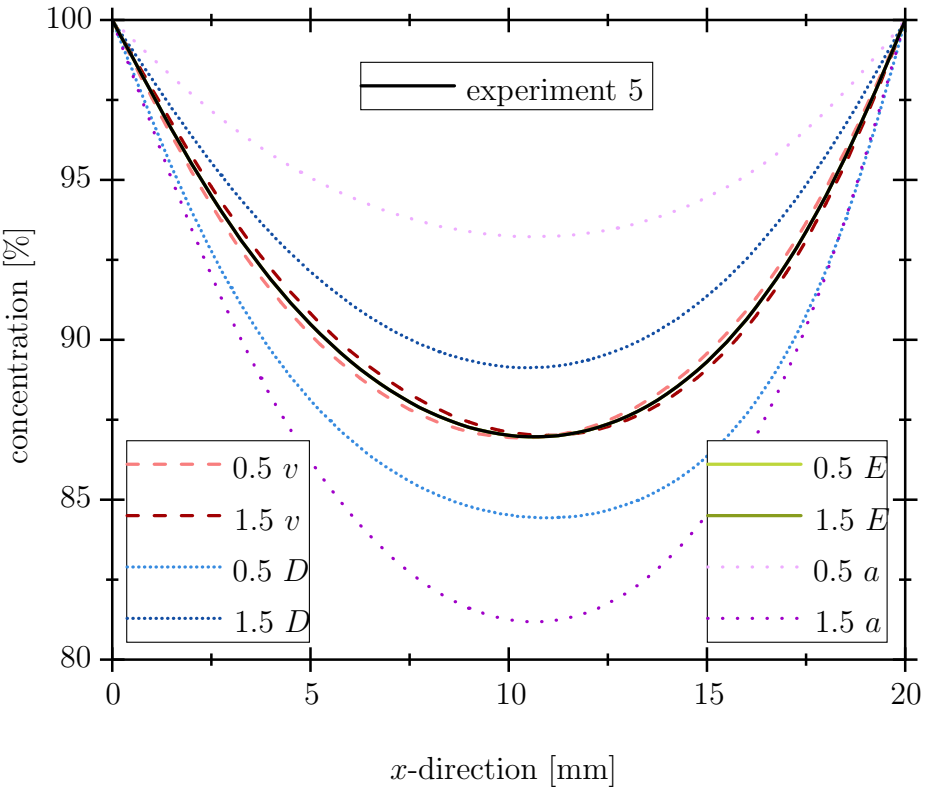

Figure 8.21: Influence of different simulation parameters on the ion concentration of experiment 5

8.4.2 Influence of Further Parameters

An additional parameter not considered in the sensitivity analysis is the frequency of the sink constant for the PED experiments. In experiments 5 to 8, **Version I** and **II** of the sink constant show almost no difference in the results. This observation corresponds to the theoretical observations made from experiments. There, the average current is used to calculate the deposited mass. However, significant differences can be observed in the simulation with a modulation of the frequency between 50 Hz and 2500 Hz (Figure 8.22). For lower frequencies, the concentration distribution runs into a steady state and corresponds to the concentration distribution of the simulation with

a constant sink constant. This observation can be explained by the time steps. The number of time steps with a sink constant with the value 0 decreases with increasing frequency. Since the implementation of the sink term is similar to the well-known compound interest from real life, as shown in **Chapter 6**, the compound interest effect seems to play a role. The more time steps in sequence have a sink constant of the value 0, the better the ion distribution can regenerate. In terms of simulation, a pulsed sink constant does not reliably reflect this effect on the concentration distribution. For this reason, a constant sink constant should be implemented in the simulations in the future.

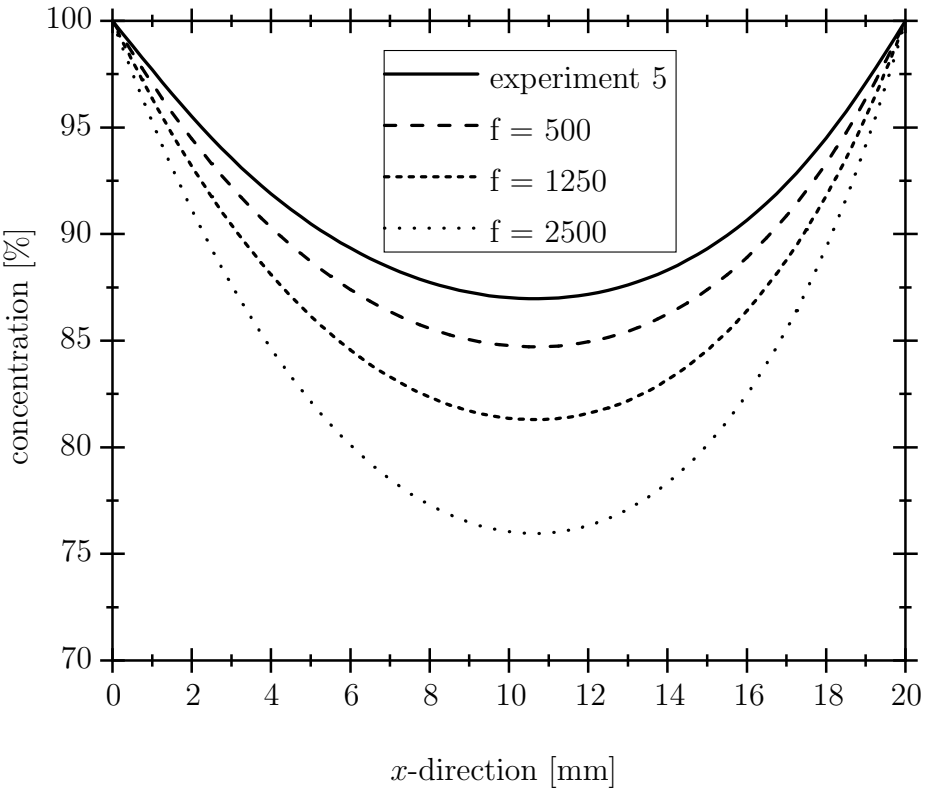

Figure 8.22: Influence of the variation of the frequency of the sink constant a on the coating homogeneity in the electrodeposition process

8.4.3 Stability

Generally, stability analyses are always carried out before the simulation. However, when executing the code developed in **Chapter 5**, the coupling of convection, diffusion, migration, and reaction results in a less stable code than previously assumed. For this reason, a stability analysis of the code in relation to the parameters from experiment 1 was determined for different time and spatial step sizes (Table 8.4). In general, the time and spatial step sizes are related. With an increase in the time step size, the

Table 8.4: CFL_u value and stability (green), instability (yellow) of the implemented code for different time and spatial step sizes for the parameters from experiment 1

		Δx								
		0.001	0.002	0.005	0.01	0.02	0.05	0.1	0.2	0.5
Δt	0.05	0.25	0.125	0.05	0.025	0.0125	0.005	0.0025	0.00125	0.0005
	0.1	0.5	0.25	0.1	0.05	0.025	0.01	0.005	0.0025	0.001
	0.2	1	0.5	0.2	0.1	0.05	0.02	0.01	0.005	0.002
	0.5	2.5	1.25	0.5	0.25	0.125	0.05	0.025	0.0125	0.005
	1	5	2.5	1	0.5	0.25	0.1	0.05	0.025	0.01
	2	10	5	2	1	0.5	0.2	0.1	0.05	0.02

Table 8.5: CFL_D value and stability (green), instability (yellow) of the implemented code for different time and spatial step sizes for the parameters from experiment 1

		Δx								
		0.001	0.002	0.005	0.01	0.02	0.05	0.1	0.2	0.5
Δt	0.05	4.8	1.2	0.192	0.048	0.012	0.00192	0.00048	0.00012	0.00002
	0.1	9.6	2.4	0.384	0.096	0.024	0.00384	0.00096	0.00024	0.000038
	0.2	19.2	4.8	0.768	0.192	0.048	0.00768	0.00192	0.00048	0.0000768
	0.5	48	12	1.92	0.48	0.12	0.0192	0.0048	0.0012	0.000192
	1	96	24	3.84	0.96	0.24	0.0384	0.0096	0.0024	0.000384
	2	192	48	7.68	1.92	0.48	0.0768	0.0192	0.0048	0.000768

spatial step size also has to be increased to fulfil the CFL_u value. However, the code is not stable for a CFL value ≥ 1, and for a time step size of $\Delta t \geq 1$, the explicit method used for the simulation is not stable anymore.

The CFL_D value is also regarded ((Table 8.5)), since the problem as treated here is convection dominant or diffusion dominant depending on the parameter choice. By observing the CFL_D, more combinations of time and spatial step sizes can be excluded in preview. For all CFL_D values $\Delta t \geq 1$ the result diverges. In sum, the implemented code is more instable than the CFL_D and CFL_u would suggest. This instability is caused by combining the upwind scheme with the diffusion part and the reaction term.

9

Summary and Future Work

9.1 Conclusion of the Work

Due to their excellent material properties in relation to their low weight, hybrid foams are a material of the future. However, the coating process has to be fully understood in order to be able to produce foams on a large scale with a homogeneous coating and, thus, homogeneous material properties. The electrodeposition process was modelled and simulated in this work with this in mind. Four dominant mass transport processes were identified for modelling: convection, diffusion, migration, and reaction. The structure of the electrodeposition cell was presented. For an accurate simulation of the given experiments, a DoE was used, and the given experimental results were summarised to examine the effects and interactions of different parameters with as few experiments as possible. By means of a literature review, different models for describing the electrodeposition process were combined to a macroscopic description of the dominating mass transport processes resulting in a one-sided coupled model. Assuming that there is a linear relationship between concentration distribution and coating thickness, a PDE was obtained to describe the electrodeposition process. It was possible to select an approach to discretise the PDE with finite differences. The derivatives were replaced, and the equation was solved using an explicit scheme. Benchmark tests validated each part of the code with respect to its solution at given initial values. The influence of the coating thickness on the geometrical parameters and finally on the mass transport process, called back-coupling, was also examined. Therefore, the RVE was first identified for three foam sizes. Different unit cells found in the relevant literature were further examined for simplification of the microheterogeneous foam structure. The geometry

parameters of the unit cells were examined as a function of the coating thickness. Based on this information the specific inner surface and the specific bulk volume are calculated. The Node Unit with thick triangular struts was then identified as a suitable model for representation the specific bulk volume, and the Kelvin cell with thick nodes and round cross-section of struts for description of the specific surface area. Nevertheless, an offset has to be added for most of the pore sizes. The geometrical parameters also have an influence on the permeability of the foams. Whereby the Ergun-like approach for permeability best describes permeability as a function of coating thickness. Based on the model equation, it is possible to simulate the electrodeposition process. As adjustable parameters differ in experiments and simulations, the parameters used in the experiment were converted into the parameters used for the simulation. Half of the experiments were carried out with a pulsed current, the other half with a constant current. For the simulations with a constant current, the results for the ion concentration run into a steady state. This steady state is reached in all experiments after 4 s at the latest, which supports the assumption that there is a linear relationship between ion concentration and coating homogeneity. For the simulations with a pulsed current, quasi stationary states are reached depending on the implementation of the sink constant. The results of these simulations are very close to each other. Consequently, the assumption that there is a linear relationship between coating homogeneity and ion concentration can also be made for the PED. Comparing to experiment and simulation, the simulation reproduces the experiment very well for low velocities and low current densities. To allow a more precise statement, the DoE was evaluated. According to the evaluation of the DoE with regard to the target size difference between the experiment and simulation, the duty cycle has the highest influence, closely followed by the velocity. The difference between experiment and simulation is exceptionally high for a small duty cycle, i.e., for the experiments with the pulsed current. The applied current signal should be monitored more closely during the experiment to improve the implementation. In reality, a proper square-wave pulse can not always be applied due to the build-up and decay of the electric field. If the square wave pulse is applied correctly during the experiment, the electromagnetic shielding should still be taken into account in the sink constant a. The velocity should not be regarded as constant over the experiment but should be integrated with the help of Darcy's law to improve the results with higher velocities. If these improvements do not lead to the desired success, an extension of Darcy's law by the Brinkman or Forchheimer term is possible. The evaluation of the DoE also shows the highest interaction between the duty cycle and the velocity on the current density. For this reason, an improvement in the implementation of the current density can be omitted in the first step. In general, the model reproduces the experiment very well, for low velocities and high duty cycles. All that

is needed is an improvement in implementing the velocity and duty cycle to improve the results for high velocities and low duty cycles.

9.2 Further Improvement

Even though the results so far are auspicious, there is still room for improvement. Simulation and experiment were only carried out for the pore size 20 ppi. For comprehensive research, the next step is to extend to the pore sizes 10 ppi and 30 ppi. Similarly, implementing the back-coupling of the system would further benefit in identifying the optimal coating parameters. Performing parameter identification to produce a homogeneous coating would result in a high velocity with a low sink constant using the model presented in this thesis. However, experiments at high velocities have shown [57] that this changes the grain structure of the coated Ni, and thus the foams obtain poorer material properties. Integrating the microscopic structure, which has not been considered so far, could also solve this problem. Nevertheless, the work carried out here has laid a comprehensive foundation for further work so that the resource-saving material of hybrid foams can be used on a larger scale in the future.

A

Appendix

In the appendix, additional information on the data discussed within the thesis can be found. In order to improve the overview, the respective results have not been presented in the corresponding chapters.

A.1 Experimental Results

Table A.1: Experimental Results of the DoE

position		experiment 1	experiment 2	experiment 3	experiment 4	experiment 5	experiment 6	experiment 7	experiment 8
3	t	87.82	101.02	200.8	100.72	54.98	70.84	91.78	99.88
	m	54.24	50.5	36.21	35.48	41.06	40.36	34.82	19.38
	b	89.7	104.78	174.00	100.48	53.74	62.72	87.88	79.32
8	t	85.52	99.32	247.42	96.16	57.32	79.04	80.68	102.48
	m	60.24	36.36	30.63	44.52	40.16	40.32	43.32	15.66
	b	92.22	93.84	183.93	68.9	58.2	67.16	95.38	97.74
11	t	81.72	105.06	160.89	98.14	60.88	69.16	76.08	110.12
	m	46.74	44.58	42.52	20.86	49.4	34.44	22.78	13.22
	b	96.86	98.02	126.34	102.36	56.74	61.68	78.66	68.76
12	t	87.88	104.88	196.65	101.86	60.48	68.36	75.74	83.32
	m	63.00	42.5	44.3	27.28	41.76	32.98	30.4	20.7
	b	92.00	98.48	167.87	61.5	49.42	68.56	73.56	116.72
13	t	93.76	105.64	165.09	97.54	55.14	67.12	94.82	121.02
	m	57.16	37.88	44.99	37.6	52.66	40.34	35.84	18.76
	b	88.46	102.32	92.83	105.58	56.08	68.5	95.22	85.38
14	t	95.42	110.14	163.32	103.28	52.3	74.08	94.26	94.02
	m	57.4	38.68	30.77	27.86	46.00	40.9	35.66	17.02
	b	94.64	85.88	152.69	73.86	56.48	62.18	80.4	90.32
15	t	92.48	95.9	143.91	93.74	52.3	56.92	102.3	92.44
	m	58.28	42.00	37.38	33.1	43.8	29.86	40.16	19.02
	b	92.12	101.22	198.43	78.84	47.46	61.98	89.96	103.00
18	t	99.58	99.72	194.21	99.04	61.14	67.58	101.3	109.16
	m	56.9	37.9	35.34	33.52	46.74	35.3	36.24	19.02
	b	94.3	95.4	147.81	73.3	57.94	69.68	94.2	110.84
23	t	101.18	95.32	143.52	102.56	60.18	72.32	103.8	110.26
	m	49.5	44.6	41.25	32.94	41.24	43.36	39.88	20.52
	b	93.04	100.8	220.14	86.9	59.14	62.44	96.06	105.42

A.2 Velocity Benchmark Test

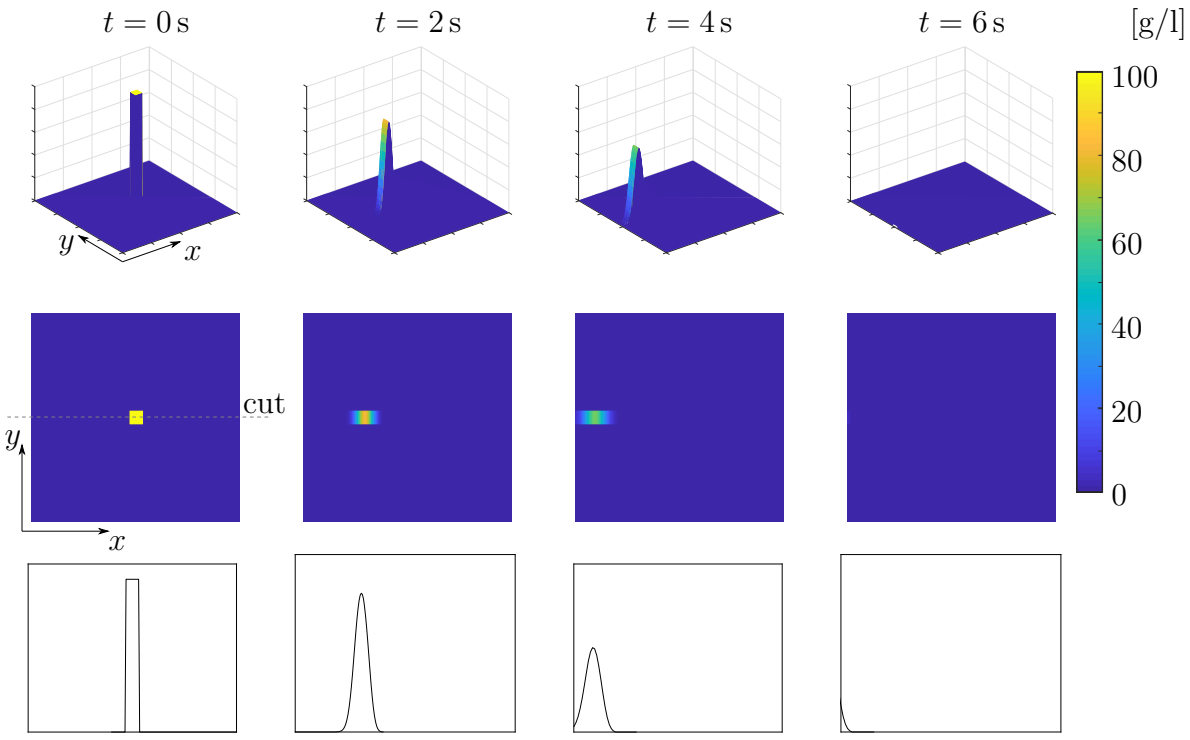

Figure A.1: Appearance and location of the peak for different time steps for a velocity in negative x-direction, top: 3D view, middle: top view, bottom: cut through the top view

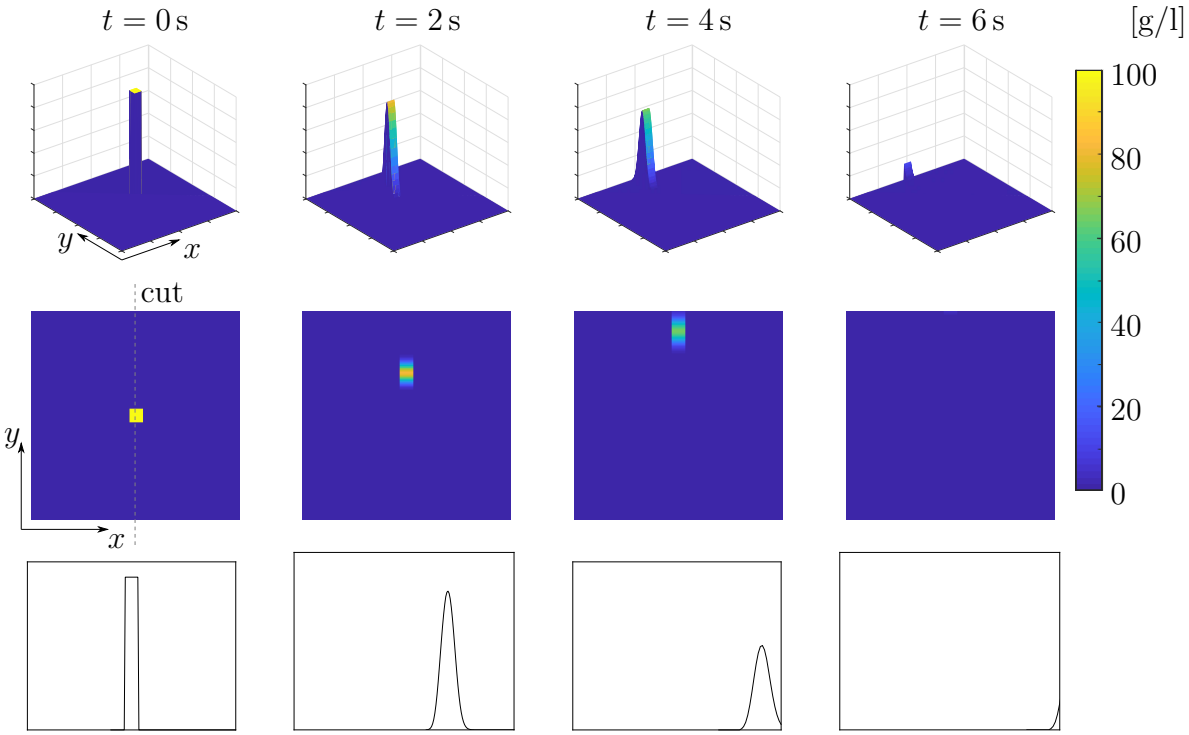

Figure A.2: Appearance and location of the peak for different time steps for a velocity in positive y-direction, top: 3D view, middle: top view, bottom: cut through the top view

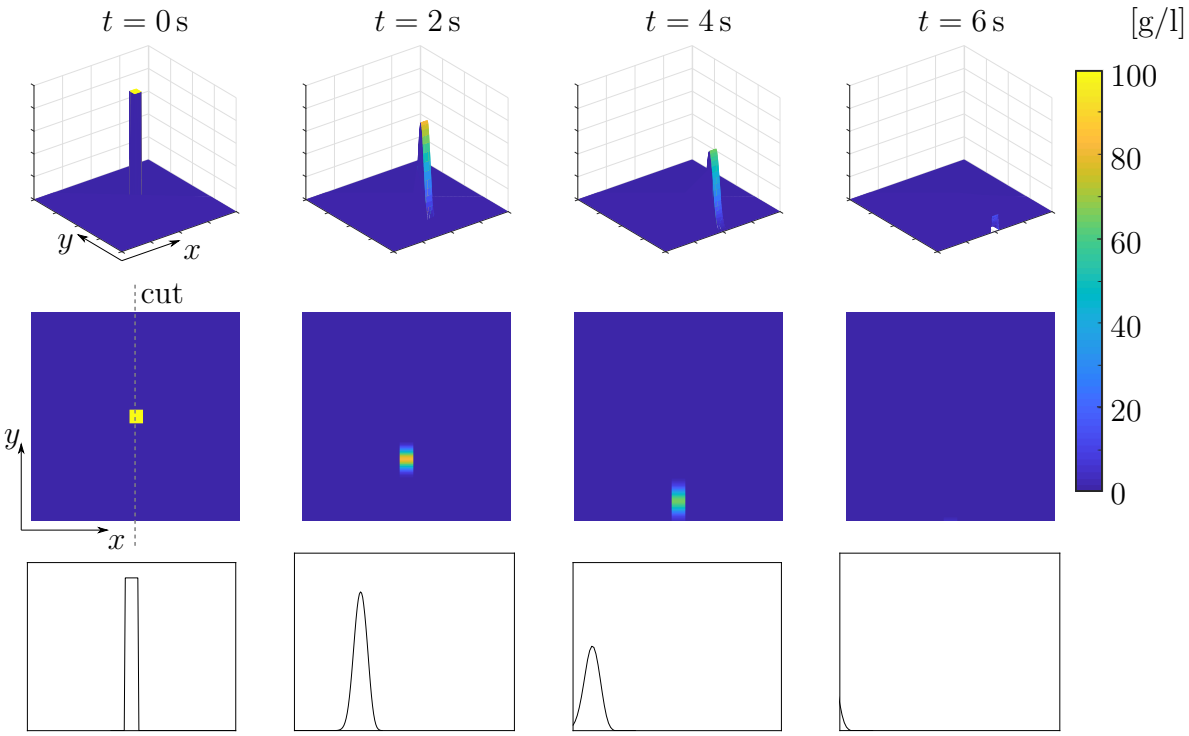

Figure A.3: Appearance and location of the peak for different time steps for a velocity in negative y-direction, top: 3D view, middle: top view, bottom: cut through the top view

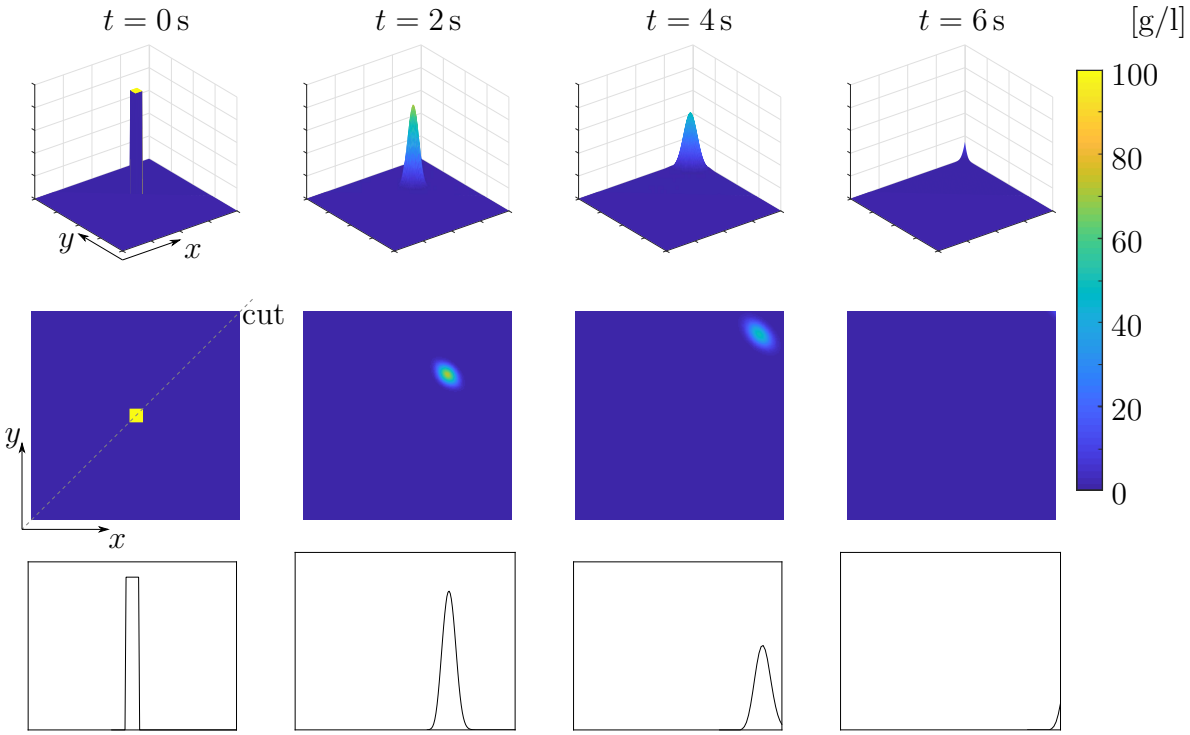

Figure A.4: Appearance and location of the peak for different time steps for a velocity in positive x-direction and positive y-direction, top: 3D view, middle: top view, bottom: cut through the top view

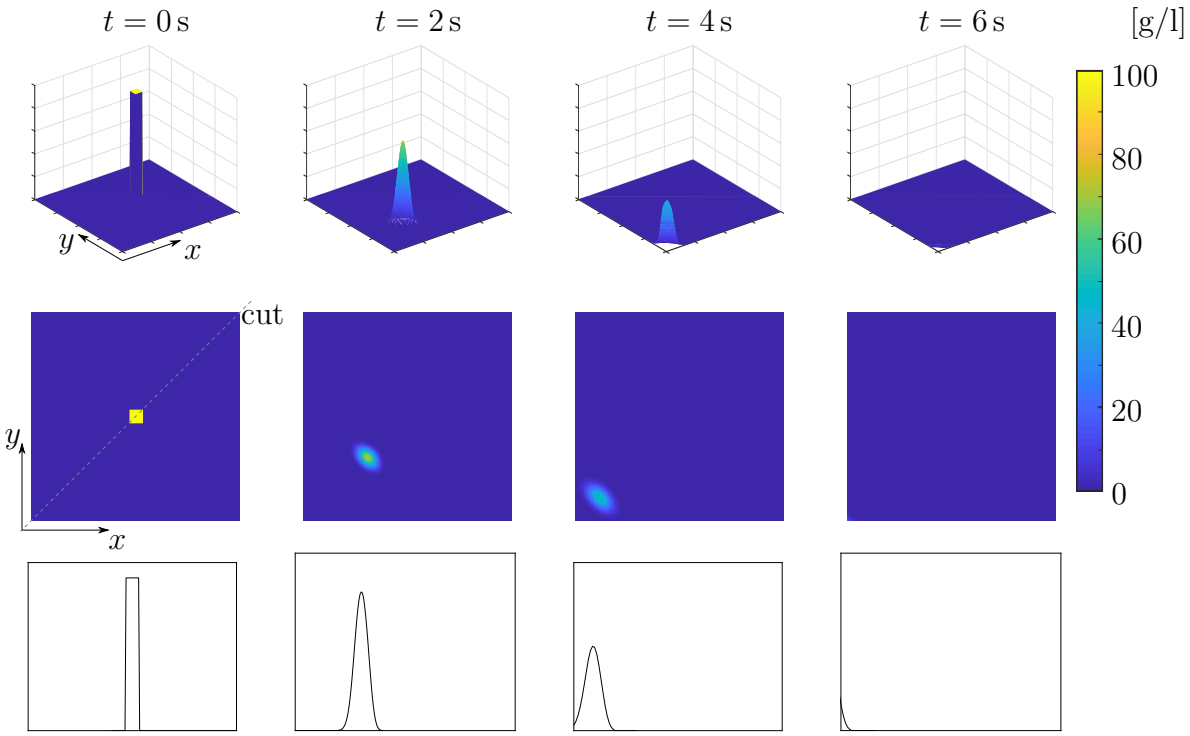

Figure A.5: Appearance and location of the peak for different time steps for a velocity in negative x-direction and negative y-direction, top: 3D view, middle: top view, bottom: cut through the top view

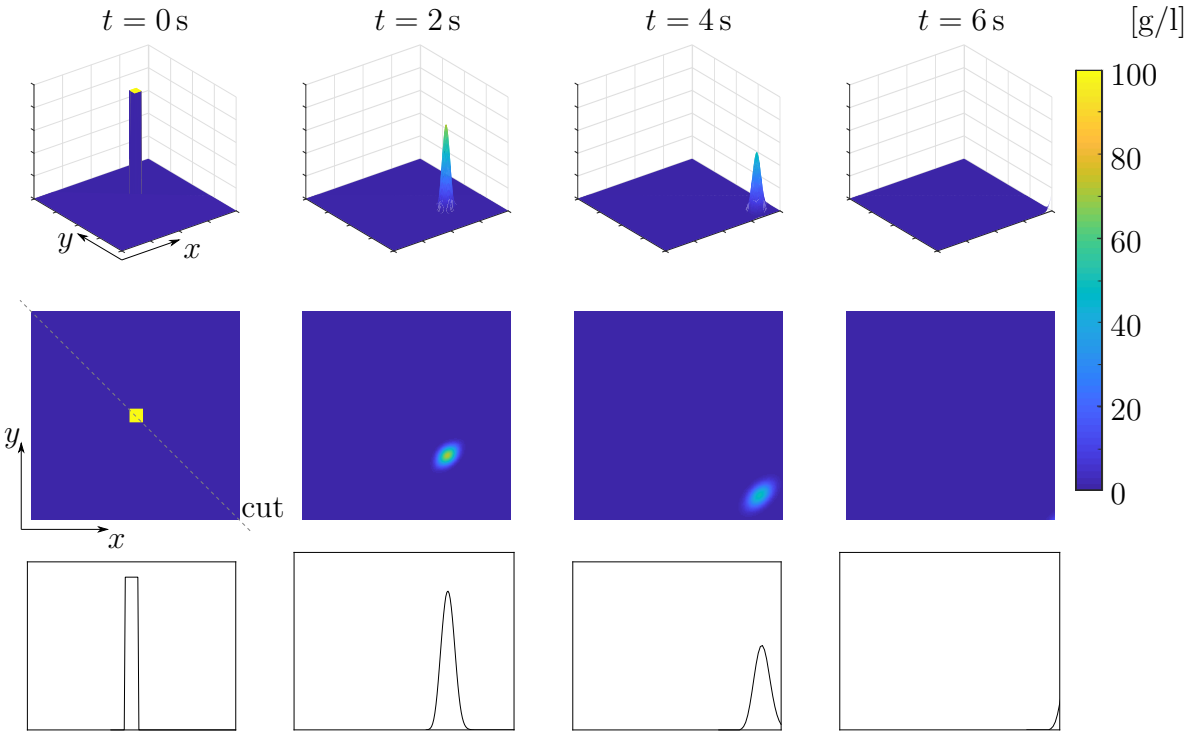

Figure A.6: Appearance and location of the peak for different time steps for a velocity in positive x-direction and negative y-direction, top: 3D view, middle: top view, bottom: cut through the top view

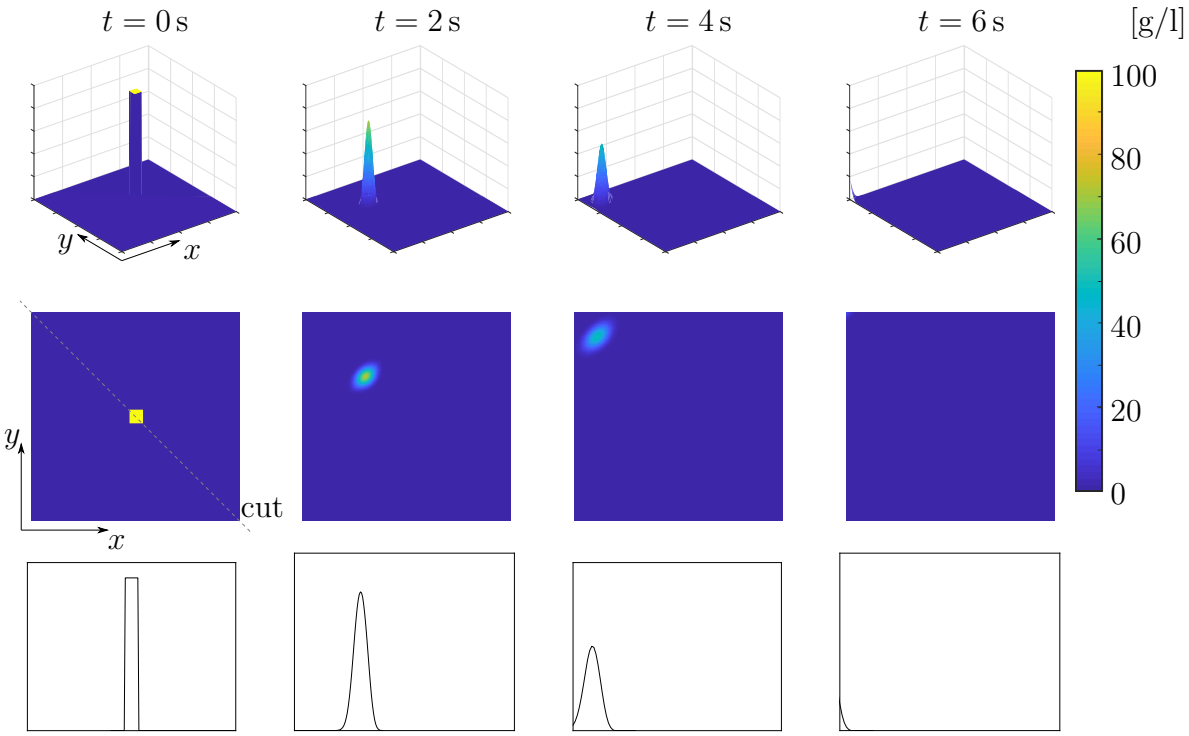

Figure A.7: Appearance and location of the peak for different time steps for a velocity in negative x-direction and positive y-direction, top: 3D view, middle: top view, bottom: cut through the top view

A.3 Permeability

ppi	porosity	permeability [m^2]	medium	experimental setup	literature
5	0.9726	$2.7\ 10^7$	air	horizontal	[15]
5	0.9118	$1.8\ 10^7$	air	horizontal	[15]
10	0.9486	$1.2\ 10^7$	air	horizontal	[15]
10	0.9138	$1.1\ 10^7$	air	horizontal	[15]
10	0.8991	$9.4\ 10^6$	air	horizontal	[15]
20	0.9546	$1.3\ 10^7$	air	horizontal	[15]
20	0.9245	$1.1\ 10^7$	air	horizontal	[15]
20	0.9005	$9.0\ 10^6$	air	horizontal	[15]
40	0.9659	$5.5\ 10^6$	air	horizontal	[15]
40	0.9272	$6.1\ 10^6$	air	horizontal	[15]
40	0.9132	$5.3\ 10^6$	air	horizontal	[15]
5	0.9710	$2.52\ 10^7$	air	horizontal	[15]
5	0.9460	$2.17\ 10^7$	air	horizontal	[15]
5	0.9050	$1.74\ 10^7$	air	horizontal	[15]
10	0.9490	$1.49\ 10^7$	air	horizontal	[15]
10	0.9090	$1.11\ 10^7$	air	horizontal	[15]
20	0.9780	$1.42\ 10^7$	air	horizontal	[15]
20	0.9490	$1.19\ 10^7$	air	horizontal	[15]
20	0.9060	$8.54\ 10^6$	air	horizontal	[15]
40	0.9720	$5.2\ 10^6$	air	horizontal	[15]
40	0.9520	$5.62\ 10^6$	air	horizontal	[15]
40	0.9370	$5.68\ 10^6$	air	horizontal	[15]
5	0.8990	$2.28\ 10^7$	air	horizontal	[16]
5	0.9300	$2.4\ 10^7$	air	horizontal	[16]
10	0.9085	$1.62\ 10^7$	air	horizontal	[16]
10	0.9386	$1.54\ 10^7$	air	horizontal	[16]
20	0.9200	$1.11\ 10^7$	air	horizontal	[16]
20	0.9353	$1.14\ 10^7$	air	horizontal	[16]
40	0.9091	$5.1\ 10^6$	air	horizontal	[16]
40	0.9586	$5.4\ 10^6$	air	horizontal	[16]
10	0.9210	$5.47\ 10^5$	liquid	horizontal	[21]
20	0.9200	$6.75\ 10^5$	liquid	horizontal	[21]
5	0.9726	$2.7\ 10^7$	air	horizontal	[29]
5	0.9118	$1.8\ 10^7$	air	horizontal	[29]
10	0.9486	$1.2\ 10^7$	air	horizontal	[29]
20	0.9546	$1.3\ 10^7$	air	horizontal	[29]
20	0.9005	$9.0\ 10^6$	air	horizontal	[29]
40	0.9272	$6.1\ 10^6$	air	horizontal	[29]
40	0.9132	$5.3\ 10^6$	air	horizontal	[29]

ppi	porosity	permeability [m^2]	medium	experimental setup	literature
10	0.9190	1.0 10^9	air	horizontal	[49]
10	0.9150	8.0 10^8	air	horizontal	[49]
20	0.9190	6.3 10^8	air	horizontal	[49]
20	0.9240	5.4 10^8	air	horizontal	[49]
40	0.9230	4.7 10^8	air	horizontal	[49]
	0.9730	1.77 10^5	liquid		[132]
	0.9750	8.0 10^5	liquid		[132]
	0.9780	1.6 10^6	liquid		[132]
10	0.8180	2.86 10^{10}	air	vertical	[58]
20	0.8040	9.17 10^9	air	vertical	[58]
30	0.8160	7.23 10^9	air	vertical	[58]
45	0.8130	6.23 10^9	air	vertical	[58]
10	0.8520	3.95 10^{10}	air	vertical	[58]
20	0.8580	1.47 10^{10}	air	vertical	[58]
30	0.8520	1.11 10^{10}	air	vertical	[58]
45	0.8480	9.95 10^9	air	vertical	[58]
20	0.7770	6.74 10^9	air	vertical	[58]
10	0.9500	7.5 10^8	air	horizontal	[73]
10	0.9500	2.48 10^7	air	vertical	[90]
20	0.9000	2.18 10^7	air	vertical	[90]
30	0.9200	1.64 10^7	air	vertical	[90]
45	0.9000	4.2 10^6	air	vertical	[90]
10	0.9481	2.48 10^7	air	vertical	[91]
10	0.9417	6.71 10^7	air	vertical	[91]
10	0.9449	3.3 10^7	air	vertical	[91]
20	0.9043	2.18 10^7	air	vertical	[91]
20	0.9294	4.38 10^7	air	vertical	[91]
10	0.8769	1.74 10^7	air	vertical	[91]
10	0.8596	4.78 10^7	air	vertical	[91]
10	0.8683	1.82 10^7	air	vertical	[91]
20	0.8567	2.49 10^7	air	vertical	[91]
20	0.8567	1.17 10^7	air	vertical	[91]
	0.8600	1.62 10^5	air	horizontal	[93]
	0.8300	3.54 10^5	air	horizontal	[93]
	0.9000	5.01 10^5	air	horizontal	[93]
	0.8850	1.53 10^6	air	horizontal	[93]
	0.9000	2.74 10^6	air	horizontal	[93]
10	0.9200	3.66 10^5			[94]
20	0.8900	5.58 10^5			[94]
20	0.9400	8.06 10^5			[94]
20	0.9600	7.19 10^5			[94]
10	0.9200	2.36 10^7			[94]
20	0.9200	1.07 10^7			[94]
40	0.9200	7.15 10^6			[94]
20	0.8900	8.96 10^6			[94]
20	0.9400	1.3 10^7			[94]
20	0.9600	1.16 10^7			[94]

ppi	porosity	permeability [m^2]	medium	experimental setup	literature
10	0.9300	$1.04\ 10^{-7}$		horizontal	[102]
20	0.9300	$7.6\ 10^{-8}$		horizontal	[102]
30	0.9300	$6.3\ 10^{-8}$		horizontal	[102]
5	0.9140	$3.7\ 10^{-6}$	air	horizontal	[110]
10	0.9180	$6.23\ 10^{-6}$	air	horizontal	[110]
20	0.8700	$1.25\ 10^{-6}$	air	horizontal	[110]
20	0.9090	$1.02\ 10^{-6}$	air	horizontal	[110]
20	0.9350	$2.42\ 10^{-6}$	air	horizontal	[110]
20	0.9580	$1.42\ 10^{-6}$	air	horizontal	[110]
40	0.9350	$1.33\ 10^{-6}$	air	horizontal	[110]
5	0.9210	$2.36\ 10^{7}$	air	horizontal	[111]
10	0.9030	$1.9\ 10^{7}$	air	horizontal	[111]
10	0.9340	$1.87\ 10^{7}$	air	horizontal	[111]
10	0.9560	$1.82\ 10^{7}$	air	horizontal	[111]
20	0.9320	$8.24\ 10^{6}$	air	horizontal	[111]
40	0.9300	$6.34\ 10^{6}$	air	horizontal	[111]
5	0.9330	$9.7\ 10^{6}$	air	horizontal	[112]
10	0.9330	$2.09\ 10^{7}$	air	horizontal	[112]
10	0.9050	$1.21\ 10^{7}$	air	horizontal	[112]
20	0.9330	$4.1\ 10^{6}$	air	horizontal	[112]
40	0.9340	$4.4\ 10^{6}$	air	horizontal	[112]
5	0.8990	$1.99\ 10^{-7}$			[130]
5	0.9300	$2.07\ 10^{-7}$			[130]
10	0.9085	$1.08\ 10^{-7}$			[130]
10	0.9386	$1.17\ 10^{-7}$			[130]
20	0.9200	$1.06\ 10^{-7}$			[130]
20	0.9353	$1.17\ 10^{-7}$			[130]
40	0.9091	$5.07\ 10^{-8}$			[130]
40	0.9586	$5.99\ 10^{-8}$			[130]
20	0.8930	$1.71\ 10^{-6}$	air	horizontal	[137]
10	0.8930	$3.47\ 10^{-6}$	air	horizontal	[137]
10	0.9470	$3.26\ 10^{-6}$	air	horizontal	[137]
10	0.8780	$1.93\ 10^{6}$	air	vertical	[138]
30	0.8740	$4.82\ 10^{5}$	air	vertical	[138]
45	0.8020	$3.96\ 10^{5}$	air	vertical	[138]
65	0.8570	$2.39\ 10^{5}$	air	vertical	[138]
10	0.9170	$1.3\ 10^{-7}$	liquid	vertical	[163]
20	0.9330	$2.5\ 10^{-7}$	liquid	vertical	[163]
40	0.9050	$6.6\ 10^{-8}$	liquid	vertical	[163]

ppi	porosity	permeability [m^2]	medium	experimental setup	literature
	0.9000	$2.28\ 10^{-9}$	liquid	horizontal	[166]
	0.9000	$1.85\ 10^{-9}$	air	horizontal	[166]
	0.8700	$2.68\ 10^{-9}$	liquid	horizontal	[166]
	0.8700	$2.13\ 10^{-9}$	air	horizontal	[166]
	0.9100	$6.19\ 10^{-9}$	liquid	horizontal	[166]
	0.9100	$4.44\ 10^{-9}$	air	horizontal	[166]
	0.8800	$2.32\ 10^{-6}$	liquid	horizontal	[166]
	0.8800	$2.81\ 10^{-6}$	air	horizontal	[166]
	0.8900	$2.98\ 10^{-6}$	liquid	horizontal	[166]
	0.8900	$6.02\ 10^{-6}$	air	horizontal	[166]
	0.9500	$1.62\ 10^{-6}$	liquid	horizontal	[166]
	0.9500	$1.22\ 10^{-6}$	air	horizontal	[166]
	0.9200	$8.17\ 10^{-6}$	air	horizontal	[166]

Bibliography

[1] 'DIN 8580:2003-09, Fertigungsverfahren - Begriffe, Einteilung.'

[2] [1990]. 'Ieee standard glossary of software engineering terminology.' *IEEE Std 610.12-1990*, pp. 1–84.

[3] Aal, A. A. & M. S. Aly [2009]. 'Electroless Ni–Cu–P plating onto open cell stainless steel foam.' *Applied Surface Science*, **255**(13-14), pp. 6652–6655.

[4] Ahmed, J., C. Pham-Huu & D. Edouard [2011]. 'A predictive model based on tortuosity for pressure drop estimation in 'slim' and 'fat' foams.' *Chemical Engineering Science*, **66**(20), pp. 4771–4779.

[5] Akolkar, R. [2014]. 'Modeling dendrite growth during lithium electrodeposition at sub-ambient temperature.' *Journal of Power Sources*, **246**, pp. 84–89.

[6] Andrews, E., G. Gioux, P. Onck & L. Gibson [2001]. 'Size effects in ductile cellular solids. part II: experimental results.' *International Journal of Mechanical Sciences*, **43**(3), pp. 701–713.

[7] Antenucci, A., S. Guarino, V. Tagliaferri & N. Ucciardello [2013]. 'Electro-deposition of cu on open cell aluminum foams.' *Materials Sciences and Applications*, **04**(11), pp. 679–682.

[8] Antenucci, A., S. Guarino, V. Tagliaferri & N. Ucciardello [2014]. 'Improvement of the mechanical and thermal characteristics of open cell aluminum foams by the electrodeposition of Cu.' *Materials & Design*, **59**, pp. 124–129.

[9] Armstrong, R. & N. Balasubramanian [2017]. 'Unified hall-petch description of nano-grain nickel hardness, flow stress and strain rate sensitivity measurements.' *AIP Advances*, **7**(8), pp. 085010.

[10] Ashby, M. [2005]. 'The properties of foams and lattices.' *Philosophical Transactions of the Royal Society A: Mathematical, Physical and Engineering Sciences*, **364**(1838), pp. 15–30.

[11] Ashby, M. F., A. Evans, N. A. Fleck, L. J. Gibson, J. W. Hutchinson & H. N. Wadley [2002]. 'Metal foams: a design guide.' *Materials & Design*, **23**(1), pp. 119.

[12] Ashby, M. F. & R. F. M. Medalist [1983]. 'The mechanical properties of cellular solids.' *Metallurgical Transactions A*, **14**(9), pp. 1755–1769.

[13] Bele, E., B. Bouwhuis & G. Hibbard [2009]. 'Failure mechanisms in metal/metal hybrid nanocrystalline microtruss materials.' *Acta Materialia*, **57**(19), pp. 5927–5935.

[14] Berger, C. A. [2016]. *Untersuchungen zur elektrochemischen Metallabscheidung aus ionischen Flüssigkeiten an Lithium, Titan und Dysprosium*. Ph.D. thesis, Universität Ulm.

[15] Bhattacharya, A., V. Calmidi & R. Mahajan [2002]. 'Thermophysical properties of high porosity metal foams.' *International Journal of Heat and Mass Transfer*, **45**(5), pp. 1017–1031.

[16] Bhattacharya, A. & R. L. Mahajan [2005]. 'Metal foam and finned metal foam heat sinks for electronics cooling in buoyancy-induced convection.' *Journal of Electronic Packaging*, **128**(3), pp. 259–266.

[17] Blazek, J. [2001]. 'Principles of solution of the governing equations.' In *Computational Fluid Dynamics: Principles and Applications*, pp. 29–74. Elsevier.

[18] Bockris, J. O., M. A. V. Devanathan, K. Müller & J. A. V. Butler [1963]. 'On the structure of charged interfaces.' *Proceedings of the Royal Society of London. Series A. Mathematical and Physical Sciences*, **274**(1356), pp. 55–79.

[19] Bograchev, D. A., V. M. Volgin & A. D. Davydov [2013]. 'Simulation of inhomogeneous pores filling in template electrodeposition of ordered metal nanowire arrays.' *Electrochimica Acta*, **112**, pp. 279–286.

[20] Bograchev, D. A., V. M. Volgin & A. D. Davydov [2015]. 'Modeling of metal electrodeposition in the pores of anodic aluminum oxide.' *Russian Journal of Electrochemistry*, **51**(9), pp. 799–806.

[21] Boomsma, K. & D. Poulikakos [2001]. 'The effects of compression and pore size variations on the liquid flow characteristics in metal foams.' *Journal of Fluids Engineering*, **124**(1), pp. 263–272.

[22] Boomsma, K., D. Poulikakos & Y. Ventikos [2003]. 'Simulations of flow through open cell metal foams using an idealized periodic cell structure.' *International Journal of Heat and Fluid Flow*, **24**(6), pp. 825–834.

[23] Boonyongmaneerat, Y., C. Schuh & D. Duand [2008]. 'Mechanical properties of reticulated aluminum foams with electrodeposited Ni–W coatings.' *Scripta Materialia*, **59**(3), pp. 336–339.

[24] Bothe, H.-H. [1998]. *Neuro-Fuzzy-Methoden*. Springer Berlin Heidelberg.

[25] Bouwhuis, B., J. McCrea, G. Palumbo & G. Hibbard [2009]. 'Mechanical properties of hybrid nanocrystalline metal foams.' *Acta Materialia*, **57**(14), pp. 4046–4053.

[26] Braun, T. M., D. Josell, J. John & T. Moffat [2019]. 'Simulation of copper electrodeposition in through-hole vias.' *Journal of The Electrochemical Society*, **167**(1), pp. 013510.

[27] Brinkman, H. C. [1949]. 'A calculation of the viscous force exerted by a flowing fluid on a dense swarm of particles.' *Flow, Turbulence and Combustion*, **1**(1).

[28] Buffel, B., F. Desplentere, K. Bracke & I. Verpoest [2014]. 'Modelling open cell-foams based on the Weaire–Phelan unit cell with a minimal surface energy approach.' *International Journal of Solids and Structures*, **51**(19-20), pp. 3461–3470.

[29] Calmidi, V. V. & R. L. Mahajan [2000]. 'Forced convection in high porosity metal foams.' *Journal of Heat Transfer*, **122**(3), pp. 557–565.

[30] Capus, J. M. [2000]. *Metal powders: a global survey of production, applications and markets*. Elsevier.

[31] Carr, N. Z. [2002]. *Simulation and estimation of copper electroplating using level set methods and image processing techniques*. Ph.D. thesis, Texas Tech University.

[32] Chapman, D. L. [1913]. 'A contribution to the theory of electrocapillarity.' *The London, Edinburgh, and Dublin Philosophical Magazine and Journal of Science*, **25**(148), pp. 475–481.

[33] Chen, K. S. & G. H. Evans [2004]. 'Two-dimensional modeling of nickel electrodeposition in LIGA microfabrication.' *Microsystem Technologies*, **10**(6-7), pp. 444–450.

[34] Chen, S., K.-M. Yin & R. E. White [1988]. 'A mathematical model for the electrodeposition of alloys on a rotating disk electrode.' *Journal of The Electrochemical Society*, **135**(9), pp. 2193–2200.

[35] Chung, M.-H. [2000]. 'A numerical method for analysis of tertiary current distribution in unsteady natural convection multi-ion electrodeposition.' *Electrochimica Acta*, **45**(24), pp. 3959–3972.

[36] Cogswell, D. A. [2015]. 'Quantitative phase-field modeling of dendritic electrodeposition.' *Physical Review E*, **92**(1).

[37] Conway, B., J. O. Bockris & R. E. White [1979]. *Modern Aspects of Electrochemistry: No. 13*. Springer.

[38] Conway, B. E., H. Angerstein-Kozlowska & W. B. A. Sharp [1975]. 'Chemical aspects of specific adsorption and underpotential electrodeposition in relation to charge transfer.' *Zeitschrift für Physikalische Chemie*, **98**(1-6), pp. 61–74.

[39] Correia, D., D. Siopa, D. Colombara, S. Tombolato, P. M. Salomé, K. Abderrafi, P. Anacleto, P. J. Dale & S. Sadewasser [2019]. 'Area-selective electrodeposition of micro islands for $CuInSe_2$-based photovoltaics.' *Results in Physics*, **12**, pp. 2136–2140.

[40] Costanza, G., G. Gusmano, R. Montanari, M. E. Tata & N.Ucciardello [2008]. 'Effect of powder mix composition on Al foam morphology.' *Proceedings of the Institution of Mechanical Engineers, Part L: Journal of Materials: Design and Applications*, **222**(2), pp. 131–140.

[41] Courant, R., K. Friedrichs & H. Lewy [1986]. 'On the partial difference equations of mathematical physics.' pp. 96–115. Birkhäuser Boston.

[42] Courant, R., E. Isaacson & M. Rees [1952]. 'On the solution of nonlinear hyperbolic differential equations by finite differences.' *Communications on Pure and Applied Mathematics*, **5**(3), pp. 243–255.

[43] Dahmen, W. & A. Reusken [2022]. *Numerik für Ingenieure und Naturwissenschaftler: Methoden, Konzepte, Matlab-Demos, E-Learning*. Springer Berlin Heidelberg. ISBN 9783662651803.

[44] Darcy, H. [1856]. *Les fontaines publiques de la ville de Dijon: exposition et application*. Victor Dalmont.

[45] Despois, J. & A. Mortensen [2005]. 'Permeability of open-pore microcellular materials.' *Acta Materialia*, **53**(5), pp. 1381–1388.

[46] Dietrich, B., W. Schabel, M. Kind & H. Martin [2009]. 'Pressure drop measurements of ceramic sponges—determining the hydraulic diameter.' *Chemical Engineering Science*, **64**(16), pp. 3633–3640.

[47] Drugan, W. & J. Willis [1996]. 'A micromechanics-based nonlocal constitutive equation and estimates of representative volume element size for elastic composites.' *Journal of the Mechanics and Physics of Solids*, **44**(4), pp. 497–524.

[48] Duan, D. L., R. L. Zhang, X. J. Ding & S. Li [2006]. 'Calculation of specific surface area of foam metals using dodecahedron model.' *Materials Science and Technology*, **22**(11), pp. 1364–1367.

[49] Dukhan, N. [2006]. 'Correlations for the pressure drop for flow through metal foam.' *Experiments in Fluids*, **41**(4), pp. 665–672.

[50] Ebrahimi, F., G. Bourne, M. Kelly & T. Matthews [1999]. 'Mechanical properties of nanocrystalline nickel produced by electrodeposition.' *Nanostructured Materials*, **11**(3), pp. 343–350.

[51] Fabian, C. P., P. Mandin, M. Ridd & M. Sheehan [2019]. 'Hydrodynamic modeling of copper electrodeposition at a vertical rotating cylinder electrode.' *ECS Transactions*, **2**(3), pp. 303–315.

[52] Fang, A. & M. Haataja [2017]. 'Modeling and analysis of electrodeposition in porous templates.' *Journal of The Electrochemical Society*, **164**(13), pp. D875–D887.

[53] Faraday, M. [1834]. 'VI. experimental researches in electricity. - seventh series.' *Philosophical Transactions of the Royal Society of London*, **124**, pp. 77–122.

[54] Fick, A. [1855]. 'V. on liquid diffusion.' *The London, Edinburgh, and Dublin Philosophical Magazine and Journal of Science*, **10**(63), pp. 30–39.

[55] Fisher, R. A. [1992]. *The Arrangement of Field Experiments*, pp. 82–91. Springer New York, New York, NY. ISBN 978-1-4612-4380-9.

[56] Fourie, J. G. & J. P. D. Plessis [2002]. 'Pressure drop modelling in cellular metallic foams.' *Chemical Engineering Science*, **57**(14), pp. 2781–2789.

[57] Fries, M. [2019]. 'Entwicklung eines Durchflussreaktors und systematische Untersuchung der Einflussparameter auf den Elektrodepositionsprozess zur Erzeugung homogener zellulärer Hybridmaterialien.' *Bachelor Thesis*.

[58] Garrido, G. I., F. Patcas, S. Lang & B. Kraushaar-Czarnetzki [2008]. 'Mass transfer and pressure drop in ceramic foams: A description for different pore sizes and porosities.' *Chemical Engineering Science*, **63**(21), pp. 5202–5217.

[59] Gibson, L. J. & M. F. Ashby [1997]. *Cellular Solids*. Cambridge University Press.

[60] Gouy, M. [1910]. 'Sur la constitution de la charge électrique à la surface d'un électrolyte.' *Journal de Physique Théorique et Appliquée*, **9**(1), pp. 457–468.

[61] Grahame, D. C. [1947]. 'The electrical double layer and the theory of electrocapillarity.' *Chemical Reviews*, **41**(3), pp. 441–501.

[62] Grill, C., M. Fries, A. Jung & S. Diebels [2021]. 'Numerical and experimental investigations of the electrodeposition process on open porous foams, determination of the parameter influence on the coating homogeneity.' *International Journal of Heat and Mass Transfer*, **180**, pp. 121791.

[63] Grill, C., A. Jung & S. Diebels [2018]. 'Modelling and simulation of the coating process on open porous metal foams.' *PAMM*, **18**(1), pp. e201800254.

[64] Grill, C., A. Jung & S. Diebels [2019]. 'Investigation of the electrodeposition parameters on the coating process on open porous media.' *PAMM*, **19**(1), pp. e201900106.

[65] Gu, C., J. Lian, J. He, Z. Jiang & Q. Jiang [2006]. 'High corrosion-resistance nanocrystalline Ni coating on AZ91D magnesium alloy.' *Surface and Coatings Technology*, **200**(18-19), pp. 5413–5418.

[66] Guarino, S., M. Barletta, S. Pezzola & S. Vesco [2012]. 'Manufacturing of steel foams by slip reaction foam sintering (SRFS).' *Materials & Design*, **40**, pp. 268–275.

[67] Guyer, J. E., W. J. Boettinger, J. A. Warren & G. B. McFadden [2004]. 'Phase field modeling of electrochemistry. II. kinetics.' *Physical Review E*, **69**(2).

[68] Hadamard, J. [1902]. 'Sur les problèmes aux dérivées partielles et leur signification physique.' *Princeton university bulletin*, pp. 49–52.

[69] Helmholtz, H. [1853]. 'Über einige Gesetze der Vertheilung elektrischer Ströme in körperlichen Leitern mit Anwendung auf die thierisch-elektrischen Versuche.' *Annalen der Physik und Chemie*, **165**(6), pp. 211–233.

[70] Hill, R. [1963]. 'Elastic properties of reinforced solids: Some theoretical principles.' *Journal of the Mechanics and Physics of Solids*, **11**(5), pp. 357–372.

[71] Hooman, K. & N. Dukhan [2013]. 'A theoretical model with experimental verification to predict hydrodynamics of foams.' *Transport in Porous Media*, **100**(3), pp. 393–406.

[72] Huu, T. T., M. Lacroix, C. P. Huu, D. Schweich & D. Edouard [2009]. 'Towards a more realistic modeling of solid foam: Use of the pentagonal dodecahedron geometry.' *Chemical Engineering Science*, **64**(24), pp. 5131–5142.

[73] Hwang, J.-J., G.-J. Hwang, R.-H. Yeh & C.-H. Chao [2001]. 'Measurement of interstitial convective heat transfer and frictional drag for flow across metal foams.' *Journal of Heat Transfer*, **124**(1), pp. 120–129.

[74] Iasiello, M., S. Cunsolo, N. Bianco, V. Naso, M. Oliviero, W. M. Harris & W. K. Chiu [2014]. 'Forced convective heat transfer in metal foams: the characteristic length issue.' *THODS FOR*, p. 117.

[75] Ibl, N. [1981]. 'Nomenclature for transport phenomena in electrolytic systems.' *Pure and Applied Chemistry*, **53**(10), pp. 1827–1840.

[76] Ibl, N., J. Puippe & H. Angerer [1978]. 'Electrocrystallization in pulse electrolysis.' *Surface Technology*, **6**(4), pp. 287–300.

[77] Inayat, A., H. Freund, A. Schwab, T. Zeiser & W. Schwieger [2011]. 'Predicting the specific surface area and pressure drop of reticulated ceramic foams used as catalyst support.' *Advanced Engineering Materials*, **13**(11), pp. 990–995.

[78] Innocentini, M., V. Salvini, J. Coury & V. Pandolfelli [1999]. 'Permeability of ceramic foams.' *American Ceramic Society Bulletin*, **78**(9), pp. 78–84.

[79] Jaeger, P. D., C. T'Joen, H. Huisseune, B. Ameel & M. D. Paepe [2011]. 'An experimentally validated and parameterized periodic unit-cell reconstruction of open-cell foams.' *Journal of Applied Physics*, **109**(10), pp. 103519.

[80] John, K. [2020]. 'Durchflussversuche zur Ermittlung der Permeabilität von Schäumen.'

[81] Jung, A. [2016]. *Cellular Materials: Structure-Property Relationships and Mechanical Modelling*. Ph.D. thesis, Universität des Saarlandes.

[82] Jung, A. & S. Diebels [2015]. 'Synthesis and mechanical properties of novel Ni/PU hybrid foams: A new economic composite material for energy absorbers.' *Advanced Engineering Materials*, **18**(4), pp. 532–541.

[83] Jung, A. & S. Diebels [2017]. 'Microstructural characterisation and experimental determination of a multiaxial yield surface for open-cell aluminium foams.' *Materials & Design*, **131**, pp. 252–264.

[84] Jung, A., D. Klis & F. Goldschmidt [2015]. 'Experiments, modeling and simulation of the magnetic behavior of inhomogeneously coated nickel/aluminum hybrid foams.' *Journal of Magnetism and Magnetic Materials*, **378**, pp. 178–185.

[85] Jung, A., H. Natter, S. Diebels, E. Lach & R. Hempelmann [2010]. 'Nanonickel coated aluminum foam for enhanced impact energy absorption.' *Advanced Engineering Materials*, **13**(1-2), pp. 23–28.

[86] Jung, A., H. Natter, R. Hempelmann, S. Diebels, M. R. Koblischka, U. Hartmann & E. Lach [2010]. 'Electrodeposition of nanocrystalline metals on open cell metal foams: Improved mechanical properties.' *ECS Transactions*, **25**(41), pp. 165–172.

[87] Jung, A., H. Natter, R. Hempelmann, S. Diebels, M. R. Koblischka, U. Hartmann & E. Lach [2010]. 'Study of the magnetic flux density distribution of nickel coated aluminum foams.' *Journal of Physics: Conference Series*, **200**(8), pp. 082011.

[88] Jung, A., H. Natter, R. Hempelmann & E. Lach [2009]. 'Nanocrystalline alumina dispersed in nanocrystalline nickel: enhanced mechanical properties.' *Journal of Materials Science*, **44**(11), pp. 2725–2735.

[89] Jung, A., M. Weinmann & H. Natter [2016]. 'Electroforming and electrodeposition on complex 3d geometries: special requirements and new methods.' In *Handbook of Nanoelectrochemistry*, pp. 941–970. Springer.

[90] Kamath, P. M., C. Balaji & S. Venkateshan [2011]. 'Experimental investigation of flow assisted mixed convection in high porosity foams in vertical channels.' *International Journal of Heat and Mass Transfer*, **54**(25-26), pp. 5231–5241.

[91] Kamath, P. M., C. Balaji & S. Venkateshan [2013]. 'Convection heat transfer from aluminium and copper foams in a vertical channel – an experimental study.' *International Journal of Thermal Sciences*, **64**, pp. 1–10.

[92] Keck, S. [2017]. *Elektrochemische Beschichtung offenporiger Schäume*. Ph.D. thesis.

[93] Khayargoli, P., V. Loya, L. Lefebvre & M. Medraj [2004]. 'The impact of microstructure on the permeability of metal foams.' In *CSME forum*, volume 2004, pp. 220–228.

[94] Kim, S. Y., J. W. Paek & B. H. Kang [2000]. 'Flow and heat transfer correlations for porous fin in a plate-fin heat exchanger.' *Journal of Heat Transfer*, **122**(3), pp. 572–578.

[95] Koch, C. C. [2007]. 'Structural nanocrystalline materials: an overview.' *Journal of Materials Science*, **42**(5), pp. 1403–1414.

[96] Köhl, M., M. Bram, H. P. Buchkremer & D. Stoever. 'Damping elements, and production and use thereof.'

[97] Koster, T., W. Peelen, J. Larbi, M. de Rooij & R. Polder [2009]. 'Numerical model of $Ca(OH)_2$ transport in concrete due to electrical currents.' *Materials and Corrosion*, **61**(6), pp. 518–523.

[98] Krause, T., L. Arulnayagam & M. Pritzker [1997]. 'Model for nickel-iron alloy electrodeposition on a rotating disk electrode.' *Journal of The Electrochemical Society*, **144**(3), pp. 960–969.

[99] Krishnan, S., J. Y. Murthy & S. V. Garimella [2006]. 'Direct simulation of transport in open-cell metal foam.' *Journal of Heat Transfer*, **128**(8), pp. 793–799.

[100] Kumar, K., H. Van Swygenhoven & S. Suresh [2003]. 'Mechanical behavior of nanocrystalline metals and alloys.' *Acta materialia*, **51**(19), pp. 5743–5774.

[101] Kumar, P. & F. Topin [2017]. 'State-of-the-art of pressure drop in open-cell porous foams: Review of experiments and correlations.' *Journal of Fluids Engineering*, **139**(11).

[102] Kurtbaş, İ., N. Celik & İ. Dinçer [2010]. 'Exergy transfer in a porous rectangular channel.' *Energy*, **35**(1), pp. 451–460.

[103] Kusner, R. & J. M. Sullivan [1996]. 'Comparing the Weaire-Phelan equal-volume foam to Kelvin's foam.' *Forma*, **11**(3), pp. 233–242.

[104] Laursen, A. B., K. R. Patraju, M. J. Whitaker, M. Retuerto, T. Sarkar, N. Yao, K. V. Ramanujachary, M. Greenblatt & G. C. Dismukes [2015]. 'Nanocrystalline Ni_5P_4: a hydrogen evolution electrocatalyst of exceptional efficiency in both alkaline and acidic media.' *Energy & Environmental Science*, **8**(3), pp. 1027–1034.

[105] Lausic, A., B. Bouwhuis, J. McCrea, G. Palumbo & G. Hibbard [2012]. 'Mechanical anisotropy in electrodeposited nanocrystalline metal/metal composite foams.' *Materials Science and Engineering: A*, **552**, pp. 157–163.

[106] Lefebvre, L.-P., J. Banhart & D. Dunand [2008]. 'Porous metals and metallic foams: Current status and recent developments.' *Advanced Engineering Materials*, **10**(9), pp. 775–787.

[107] Legland, D., I. Arganda-Carreras & P. Andrey [2016]. 'MorphoLibJ: integrated library and plugins for mathematical morphology with ImageJ.' *Bioinformatics*, **32**(22), pp. 3532–3534.

[108] Leong, K. & H. Li [2011]. 'Theoretical study of the effective thermal conductivity of graphite foam based on a unit cell model.' *International Journal of Heat and Mass Transfer*, **54**(25-26), pp. 5491–5496.

[109] Li, J., J. Yan, Q. Deng, G. Cheng & S. Dong [1997]. 'Viologen-thiol self-assembled monolayers for immobilized horseradish peroxidase at gold electrode surface.' *Electrochimica Acta*, **42**(6), pp. 961 – 967.

[110] Liu, J., W. Wu, W. Chiu & W. Hsieh [2006]. 'Measurement and correlation of friction characteristic of flow through foam matrixes.' *Experimental Thermal and Fluid Science*, **30**(4), pp. 329–336.

[111] Mancin, S., C. Zilio, A. Cavallini & L. Rossetto [2010]. 'Pressure drop during air flow in aluminum foams.' *International Journal of Heat and Mass Transfer*, **53**(15-16), pp. 3121–3130.

[112] Mancin, S., C. Zilio, A. Diani & L. Rossetto [2012]. 'Experimental air heat transfer and pressure drop through copper foams.' *Experimental Thermal and Fluid Science*, **36**, pp. 224–232.

[113] Mandin, P., J. Cense, C. Fabian, C. Gbado & D. Lincot [2007]. 'Electrodeposition process modeling using continuous and discrete scales.' *Computers & Chemical Engineering*, **31**(8), pp. 980–992.

[114] Mandin, P., T. Pauporté, P. Fanouillère & D. Lincot [2004]. 'Modelling and numerical simulation of hydrodynamical processes in a confined rotating electrode configuration.' *Journal of Electroanalytical Chemistry*, **565**(2), pp. 159–173.

[115] Marcus, R. A. [1992]. 'Electron transfers across interfaces.' In *Extended Abstracts of the Electrochemical Society Fall Meeting, Toronto, Ontario, Canada, Oct. 11-16, 1992*, p. 338. Electrochemical Society.

[116] Meller, M. [1925]. 'Produit métall. pour l'obtention d'objets laminés.' French Patent 615.147.

[117] Meyers, M., A. Mishra & D. Benson [2006]. 'Mechanical properties of nanostructured materials.' *Prog. Mater. Sci*, **51**, pp. 427–556.

[118] Mitchell, C. E. J., A. Howard, M. Carney & R. G. Egdell [2001]. 'Direct observation of behaviour of Au nanoclusters on TiO_2 (1 1 0) at elevated temperatures.' *Surface science*, **490**(1-2), pp. 196–210.

[119] Mohanty, G., J. M. Wheeler, R. Raghavan, J. Wehrs, M. Hasegawa, S. Mischler, L. Philippe & J. Michler [2014]. 'Elevated temperature, strain rate jump microcompression of nanocrystalline nickel.' *Philosophical Magazine*, **95**(16-18), pp. 1878–1895.

[120] Moreira, E., M. Innocentini & J. Coury [2004]. 'Permeability of ceramic foams to compressible and incompressible flow.' *Journal of the European Ceramic Society*, **24**(10-11), pp. 3209–3218.

[121] Moreira, E. A. & J. R. Coury [2004]. 'The influence of structural parameters on the permeability of ceramic foams.' *Brazilian Journal of Chemical Engineering*, **21**(1), pp. 23–33.

[122] Motz, C. & R. Pippan [2001]. 'Deformation behaviour of closed-cell aluminium foams in tension.' *Acta Materialia*, **49**(13), pp. 2463–2470.

[123] Nelson, L. S. [1994]. 'Engineering, quality and experimental design.' *Journal of Quality Technology*, **26**(3), pp. 241–242.

[124] Neuman, S. P. [1977]. 'Theoretical derivation of Darcy's law.' *Acta Mechanica*, **25**(3-4), pp. 153–170.

[125] Newman, K. E. T.-A., John S. [2004]. *Electrochemical Systems*. Wiley-Interscience. ISBN 0471477567.

[126] Nilsson, A. O. [2007]. 'Substitution of rechargeable NiCd batteries: a background document to evaluate the possibilities of finding alternatives to NiCd batteries.'

[127] Ortlieb, C. P. [2001]. *Mathematische Modelle und Naturerkenntnis*. Universität Hamburg, Fachbereich Mathematik.

[128] Pan, D., T. G. Nieh & M. W. Chen [2006]. 'Strengthening and softening of nanocrystalline nickel during multistep nanoindentation.' *Applied Physics Letters*, **88**(16), pp. 161922.

[129] Perrot, C., R. Panneton & X. Olny [2007]. 'Periodic unit cell reconstruction of porous media: Application to open-cell aluminum foams.' *Journal of Applied Physics*, **101**(11), pp. 113538.

[130] Phanikumar, M. & R. Mahajan [2002]. 'Non-darcy natural convection in high porosity metal foams.' *International Journal of Heat and Mass Transfer*, **45**(18), pp. 3781–3793.

[131] Phelan, R., D. Weaire & K. Brakke [1995]. 'Computation of equilibrium foam structures using the surface evolver.' *Experimental Mathematics*, **4**(3), pp. 181–192.

[132] Plessis, P. D., A. Montillet, J. Comiti & J. Legrand [1994]. 'Pressure drop prediction for flow through high porosity metallic foams.' *Chemical Engineering Science*, **49**(21), pp. 3545–3553.

[133] Pliny the Elder & H. Rackham [1938]. *Natural history*. Harvard University Press, Cambridge, Mass.

[134] Popov, K. I., D. N. Keča, S. I. Vidojković, B. J. Lazarević & V. B. Milojković [1976]. 'Mathematical model and digital simulation of pulsating overpotential copper electrodeposition.' *Journal of Applied Electrochemistry*, **6**(4), pp. 365–370.

[135] Qi, Z., H. Geng, X. Wang, C. Zhao, H. Ji, C. Zhang, J. Xu & Z. Zhang [2011]. 'Novel nanocrystalline PdNi alloy catalyst for methanol and ethanol electro-oxidation in alkaline media.' *Journal of Power Sources*, **196**(14), pp. 5823–5828.

[136] Ramasubramanian, M., S. Popova, B. N. Popov, R. E. White & K.-M. Yin [1996]. 'Anomalous codeposition of Fe-Ni alloys and Fe-Ni-SiO_2 composites under potentiostatic conditions: Experimental study and mathematical model.' *Journal of the Electrochemical Society*, **143**(7), pp. 2164.

[137] Ribeiro, G., J. Barbosa & A. Prata [2012]. 'Performance of microchannel condensers with metal foams on the air-side: Application in small-scale refrigeration systems.' *Applied Thermal Engineering*, **36**, pp. 152–160.

[138] Richardson, J., Y. Peng & D. Remue [2000]. 'Properties of ceramic foam catalyst supports: pressure drop.' *Applied Catalysis A: General*, **204**(1), pp. 19–32.

[139] Rienstra, S. W. [2002]. 'Modelling and perturbation methods.' **24**, pp. 2016.

[140] Rocca, A. L. & H. Power [2005]. 'Free mesh radial basis function collocation approach for the numerical solution of system of multi-ion electrolytes.' *International Journal for Numerical Methods in Engineering*, **64**(13), pp. 1699–1734.

[141] Sato, A., H. Sakai, T. Hatakeyama & T. Nakagawa [2007]. 'Porous conductive material and its manufacturing method, electrode and its manufacturing method, fuel cell and its manufacturing method, and apparatus, moving object, power generation system, co-generation system, and electrode reaction utilization apparatus.' *JP 2007035437*.

[142] Scheffler, M. & P. Colombo, editors [2005]. *Cellular Ceramics*. Wiley.

[143] Schindelin, J., I. Arganda-Carreras, E. Frise, V. Kaynig, M. Longair, T. Pietzsch, S. Preibisch, C. Rueden, S. Saalfeld, B. Schmid, J.-Y. Tinevez, D. J. White, V. Hartenstein, K. Eliceiri, P. Tomancak & A. Cardona [2012]. 'Fiji: an open-source platform for biological-image analysis.' *Nature Methods*, **9**(7), pp. 676–682.

[144] Schmidt, V. M. [2003]. *Elektrochemische Verfahrenstechnik*. Wiley.

[145] Schneider, C. A., W. S. Rasband & K. W. Eliceiri [2012]. 'NIH image to ImageJ: 25 years of image analysis.' *Nature Methods*, **9**(7), pp. 671–675.

[146] Schuh, C., T. Nieh & T. Yamasaki [2002]. 'Hall–Petch breakdown manifested in abrasive wear resistance of nanocrystalline nickel.' *Scripta Materialia*, **46**(10), pp. 735–740.

[147] Schürch, P., R. Ramachandramoorthy, L. Pethö, J. Michler & L. Philippe [2020]. 'Additive manufacturing by template-assisted 3D electrodeposition: Nanocrystalline nickel microsprings and microspring arrays.' *Applied Materials Today*, **18**, pp. 100472.

[148] Seguin, D., A. Montillet & J. Comiti [1998]. 'Experimental characterisation of flow regimes in various porous media—I: Limit of laminar flow regime.' *Chemical Engineering Science*, **53**(21), pp. 3751–3761.

[149] Shibuta, Y., Y. Okajima & T. Suzuki [2007]. 'Phase-field modeling for electrodeposition process.' *Science and Technology of Advanced Materials*, **8**(6), pp. 511–518.

[150] Siebertz, K., D. van Bebber & T. Hochkirchen [2010]. 'Versuchspläne.' In *Statistische Versuchsplanung*, pp. 25–56. Springer.

[151] Siebertz, K., D. van Bebber & T. Hochkirchen [2017]. 'Grundlagen.' In *Statistische Versuchsplanung*, pp. 1–25. Springer Berlin Heidelberg.

[152] Smith, B., S. Szyniszewski, J. Hajjar, B. Schafer & S. Arwade [2012]. 'Steel foam for structures: A review of applications, manufacturing and material properties.' *Journal of Constructional Steel Research*, **71**, pp. 1–10.

[153] Sochnikov, V. S. & S. Efrima [2002]. 'Simulation of interfacial metal electrodeposition: the electrochemical model and the numerical implementation.' *The Journal of Physical Chemistry B*, **106**(46), pp. 11993–11999.

[154] Solbrå, A., A. W. Bergersen, J. van den Brink, A. Malthe-Sørenssen, G. T. Einevoll & G. Halnes [2018]. 'A Kirchhoff-Nernst-Planck framework for modeling large scale extracellular electrodiffusion surrounding morphologically detailed neurons.' *PLOS Computational Biology*, **14**(10), pp. e1006510.

[155] Song, H.-W., Z.-J. Fan, G. Yu, Q.-C. Wang & A. Tobota [2005]. 'Partition energy absorption of axially crushed aluminum foam-filled hat sections.' *International Journal of Solids and Structures*, **42**(9-10), pp. 2575–2600.

[156] Srinivasan, S. [2006]. *Fuel Cells*. Springer-Verlag GmbH. ISBN 9780387354026.

[157] Steiner, H.-G. [1976]. 'Zur Methodik des mathematisierenden Unterrichts.' *Anwendungsorientierte Mathematik in der Sekundarstufe II*, pp. 211–246.

[158] Sterck, H. D. & P. Ullrich [2009]. 'Introduction to computational PDEs.'

[159] Stern, O. [1924]. 'Zur Theorie der elektrolytischen Doppelschicht.' *Zeitschrift für Elektrochemie und angewandte physikalische Chemie*, **30**(21-22), pp. 508–516.

[160] Suleiman, A. S. & N. Dukhan [2014]. 'Forced convection inside metal foam: Simulation over a long domain and analytical validation.' *International Journal of Thermal Sciences*, **86**, pp. 104–114.

[161] Suleiman, A. S. & N. Dukhan [2014]. 'Long-domain simulation of flow in open-cell mesoporous metal foam and direct comparison to experiment.' *Microporous and Mesoporous Materials*, **196**, pp. 104–114.

[162] Ta, K., R. Zhang, M. Shin, R. T. Rooney, E. K. Neumann & A. A. Gewirth [2019]. 'Understanding Ca electrodeposition and speciation processes in nonaqueous electrolytes for next-generation Ca-ion batteries.' *ACS Applied Materials & Interfaces*, **11**(24), pp. 21536–21542.

[163] Tadrist, L., M. Miscevic, O. Rahli & F. Topin [2004]. 'About the use of fibrous materials in compact heat exchangers.' *Experimental Thermal and Fluid Science*, **28**(2-3), pp. 193–199.

[164] Tenno, R. & A. Pohjoranta [2012]. 'Control of diffusion limited electrochemical redox processes: Simulation study.' *Journal of Process Control*, **22**(1), pp. 228–235.

[165] Thomson, W. [1887]. 'On the division of space with minimum partitional area.' *Acta Mathematica*, **11**(0), pp. 121–134.

[166] Topin, F., J.-P. Bonnet, B. Madani & L. Tadrist [2006]. 'Experimental analysis of multiphase flow in metallic foam: Flow laws, heat transfer and convective boiling.' *Advanced Engineering Materials*, **8**(9), pp. 890–899.

[167] Tournassat, C., C. I. Steefel & T. Gimmi [2020]. 'Solving the Nernst-Planck equation in heterogeneous porous media with finite volume methods: Averaging approaches at interfaces.' *Water Resources Research*, **56**(3).

[168] Verbrugge, M. W. & C. W. Tobias [1985]. 'A mathematical model for the periodic electrodeposition of multicomponent alloys.' *Journal of The Electrochemical Society*, **132**(6), pp. 1298–1307.

[169] Vishnugopi, B. S., F. Hao, A. Verma & P. P. Mukherjee [2020]. 'Surface diffusion manifestation in electrodeposition of metal anodes.' *Physical Chemistry Chemical Physics*, **22**(20), pp. 11286–11295.

[170] Vizcaino, A., A. Carrero & J. Calles [2007]. 'Hydrogen production by ethanol steam reforming over Cu–Ni supported catalysts.' *International Journal of Hydrogen Energy*, **32**(10-11), pp. 1450–1461.

[171] Wang, Y., Y. Cao, M. Wang, S. Zhong, M.-Z. Zhang, Y. Feng, R.-W. Peng, X.-P. Hao & N.-B. Ming [2004]. 'Spontaneous formation of periodic nanostructured film by electrodeposition: Experimental observations and modeling.' *Physical Review E*, **69**(2).

[172] Wehrs, J., G. Mohanty, G. Guillonneau, A. A. Taylor, X. Maeder, D. Frey, L. Philippe, S. Mischler, J. M. Wheeler & J. Michler [2015]. 'Comparison of in situ micromechanical strain-rate sensitivity measurement techniques.' *JOM*, **67**(8), pp. 1684–1693.

[173] Westermann, T. [2010]. *Modellbildung und Simulation*. Springer Berlin Heidelberg, Berlin, Heidelberg. ISBN 9783642054600.

[174] Whitaker, S. [1996]. 'The Forchheimer equation: A theoretical development.' *Transport in Porous Media*, **25**(1), pp. 27–61.

[175] Xiao, H., H. He, X. Ren, P. Zeng & F. Wang [2017]. 'Numerical modeling and experimental verification of copper electrodeposition for through silicon via (TSV) with additives.' *Microelectronic Engineering*, **170**, pp. 54–58.

[176] Xu, X., Y. Liu, J.-Y. Hwang, O. O. Kapitanova, Z. Song, Y.-K. Sun, A. Matic & S. Xiong [2020]. 'Role of Li-ion depletion on electrode surface: Underlying mechanism for electrodeposition behavior of lithium metal anode.' *Advanced Energy Materials*, **10**(44), pp. 2002390.

[177] Yang, X., T. J. Lu & T. Kim [2014]. 'An analytical model for permeability of isotropic porous media.' *Physics Letters A*, **378**(30-31), pp. 2308–2311.

[178] Yin, K.-M. & R. E. White [1990]. 'A mathematical model of pulse plating on a rotating disk electrode.' *AIChE Journal*, **36**(2), pp. 187–196.

[179] Ying, R. Y., P. K. Ng, Z. Mao & R. E. White [1988]. 'Electrodeposition of copper-nickel alloys from citrate solutions on a rotating disk electrode: II. mathematical modeling.' *Journal of the Electrochemical Society*, **135**(12), pp. 2964.

[180] Zeidan, D., S. Padhi, A. Burqan & P. Ueberholz [2020]. *Computational Mathematics and Applications*. Springer. ISBN 9811584974.

[181] Zheng, Z., R. M. Stephens, R. D. Braatz, R. C. Alkire & L. R. Petzold [2008]. 'A hybrid multiscale kinetic monte carlo method for simulation of copper electrodeposition.' *Journal of Computational Physics*, **227**(10), pp. 5184–5199.

[182] Zierep, J. [2015]. *Grundzüge der Strömungslehre Grundlagen, Statik und Dynamik der Fluide*. Springer Fachmedien Wiesbaden, Wiesbaden. ISBN 9783658117962.

B

Publications, Proceedings, Presentations and Posters

B.1 Publications and Proceedings

- Grill, C., A. Jung, S. Diebels [2018]
  'Modeling and Simulation of the Coating Process on Open Porous Metal Foams'
  Proc. Appl. Math. Mech. (PAMM), 18-1, pp. e201800254

- Grill, C., A. Jung, S. Diebels [2019]
  'Influence of Electrodeposition Parameters on the Coating Process on Open Porous Media'
  Proc. Appl. Math. Mech. (PAMM), 19-1, pp. e201900106

- Grill, C., M. Fries, A. Jung, S. Diebels [2021]
  'Influence of Electrodeposition Parameters on the Coating Process on Open Porous Media'
  International Journal for Heat and Mass Transfer, 180, pp. 121791

- Grill, C., S. Diebels, A. Jung [2023]
  'Determination of an RVE and identifying a representative idealised model for specific surface and volume of metal foams'
  International Journal of Solids and Structures, *to be submitted*

B.2 Presentations

- Grill, C., A. Jung, S. Diebels
  'Anfänge zur Modellierung der elektrochemischen Beschichtung offenporiger zellulärer Materialien'
  10. Workshop Kontinuumsmechanik, Bad Tölz, 2017

- Grill, C., A. Jung, S. Diebels
  'Modellierung and Simulation of the Coating Process on Open Porous Metal Foams'
  89th GAMM Annual Meeting, München, 2018

- Grill, C., A. Jung, S. Diebels
  'Influence of electrodeposition parameters on the coating process on open porous media', 90th GAMM Annual Meeting, Wien, 2019

- Grill, C., A. Jung, S. Diebels
  'Simulation of the Electrochemical Coating Process on open-cell Foams'
  COUPLED 2019, Sitges, Barcelona, 2019

- Grill, C., A. Jung, S. Diebels
  'Parameter Influence on the Electrodeposition Coating Process on Open Porous Foams'
  12. Workshop Kontinuumsmechanik, Schwarzenborn, 2019

- Bleistein, T., S. Diebels, C. Grill, A. Jung
  'Hybrid Foams: Manufacturing, Microstructure and Mechanical Properties'
  Kolloquium der Mechanik, TU Darmstadt, 2019

- Grill, C., M. Fries, A. Jung, S. Diebels
  'Simulation of the Electrodeposition Coating Process on Open Porous Foams'
  Mechanik Seminar, Val-d'Illiez, Schweiz, 2020

- Grill, C., M. Fries, F. Kunz, S.Diebels, A. Jung
  'Ni/PU Hybrid Foams – From Simulation of the Electrodeposition Process up to Mechanical Characterisation'
  ACEX2021, Malta, 2021

B.3 Posters

- Grill, C., A. Jung, S. Diebels
  'Modellierung und Simulation der Beschichtung offenporiger Metallschäume mittels Elektrodeposition'
  Tag der Chemie der Universität des Saarlandes, Saarbrücken, 2017

- Grill, C., A. Jung, S. Diebels
  'Modellierung und Simulation der Beschichtung offenporiger Metallschäume mittels Elektrodeposition'
  Doktorandentag der Universität des Saarlandes, Saarbrücken, 2017